SIMULATION OF BEHAVIOURAL MODIFICATION EFFECTS AND DEPOSITION IN SUSPENSION WASTE PIPE FLOWS

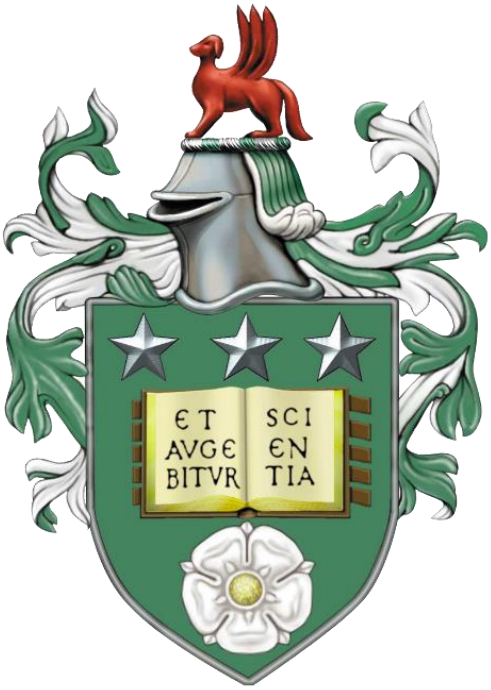

Bisrat Wolde

The University of Leeds

School of Chemical and Process Engineering

Submitted in accordance with the requirements for the degree of

Doctor of Philosophy

October 2023

DECLARATION

The candidate confirms that the work submitted is his own, except where work which has formed part of jointly authored publications has been included. The contribution of the candidate and the other authors to this work has been explicitly indicated below. The candidate confirms that appropriate credit has been given within the thesis where reference has been made to the work of others.

Chapters 4 and 6 results:

B. Wolde, L. F. Mortimer and M. Fairweather. (2022). Effects of Stokes number on particle deposition in particle-laden turbulent pipe flows. *Proceedings of the Conference on Modelling Fluid Flow (CMFF'22), Budapest, Hungary, 30th August-2nd September 2022, Vad, J. (Ed.), Budapest University of Technology and Economics, Budapest, pp. 149-156.*

B. Wolde, L. F. Mortimer and M. Fairweather. (2023*)* Stokes Number Effects on Deposition in Particle-Laden Turbulent Pipe Flows *Chemical Engineering and Technology, Vol. 46, No. 7, pp. 1351-1361.*

B. Wolde, L. F. Mortimer and M. Fairweather. (2023). Prediction of critical deposition velocities in particle-laden horizontal turbulent pipe flows. *Turbulence, Heat and Mass Transfer 10, Proceedings of the Tenth International Symposium on Turbulence, Heat and Mass Transfer, Rome, Italy, 11th-15th September 2023, Hanjalic, K., Borello, D., Suga, K., and Venturini, P. (Eds.), Begell House Inc., New York, pp. 457-460.*

Chapters 4 and 5 results:

T. N. Hunter, P. K. Allan, C. L. Corkhill, F. J. Currell, M. Fairweather, R. Harrison, J. Hartley, J. A. Hriljac, A. Kozlowski, M. Kuman, L. Leay, L. F. Mortimer, A. Nearchou, B. O'Driscoll, D. Parkes, J. Reed, G. Singh, B. Wolde, and T. Zagyva. (2022). The TRANSCEND University Consortium: Integrated Waste Management, *Proceedings of the 2022 Waste Management Conference WM2022, Phoenix, USA, 6th-10th March 2022, WM Symposia, Tempe, Paper 22109.*

B. Wolde, L. F. Mortimer and M. Fairweather. (2023). Impact of behavioural modification techniques on agglomeration dynamics in particle-laden turbulent pipe flows. *Proceedings of the 14th International ERCOFTAC Symposium on Engineering Turbulence Modelling and Measurements – ETMM14, Barcelona, Spain, 6th-8th September.*

For publications that were co-authored, the other authors contributed to supervisory meetings every week or two weeks, providing guidance, and sharing ideas for progression. Prior to publishing, they additionally edit and proofread the papers. The simulation, data processing, analysis, and writing of the original drafts and revisions are attributed to myself.

ACKNOWLEDGEMENTS

Glory be to God in the highest heaven and to Holy Mary, the Theotokos.

Dedicated to my late beloved sister Feseswork Wolde, who passed away far too soon and was a strong and inspiring role model!

I would like to take the chance to express my sincere gratitude to everyone who has supported and advised me throughout my PhD.

First and foremost, I would like to thank my supervisor, Professor Michael Fairweather, for providing me with this opportunity and for his invaluable guidance, advice, and constant support to see the project through to the end. I doubt I would have been able to complete this research without his unwavering encouragement, patience, and guidance along the way. I'd also like to express my gratitude to Dr. Lee Mortimer for his numerous comments, recommendations, and support throughout my PhD. Their endless advice, patience, and support are genuinely appreciated.

Dr. Hugh Rice deserves special thanks for his advice and for always being available when I needed him during the first years of my PhD. I'd like to thank the students and research fellows in Office 2.22 for being so pleasant and helpful.

I'm grateful for funding from the UK Engineering and Physical Sciences Research Council and the University of Leeds through the TRANSCEND (Transformative Science and Engineering for Nuclear Decommissioning) project.

I owe my family a heartfelt debt of gratitude for their unwavering support during my PhD. My appreciation is extended to my father, Wolde Gafat, as well as to my mothers, Zerfenish Bezani and Getanish Mersha. Finally, I am eternally grateful to my sisters, brothers, nieces, nephews, and friends for their unending emotional support.

ABSTRACT

The development of fundamental understanding through modelling and simulation of important phenomena related to turbulent multiphase flows, such as particle deposition and agglomeration, is of interest to a wide range of industrial and natural processes. These include chemical engineering, mineral processing, agriculture, oil and gas, and nuclear waste management among many others. In the present study, particle-laden turbulent pipe flows are studied using direct numerical simulation of the fluid phase in combination with Lagrangian particle tracking, with a particular focus on predicting and elucidating the dynamics of particle-particle interactions. The models used, which have been developed and validated in the present study, enhance our understanding of these flows, particularly surrounding the processes which lead to particle collisions and agglomeration, as well as deposition and bed-formation. An energy-balance based agglomeration determination technique is used along with four-way coupling to predict particle aggregation due to collision interactions within the flow. The impact of behavioural modification effects is investigated by varying influential parameters such as the reduced surface potential, temperature, inverse Debye length, Hamaker constant, coefficient of restitution, and Reynolds number. It is discovered that the electric double layer repulsion dynamics exerts little effect on collision and agglomeration behaviour, attributed to the large particle diameters examined in comparison to the effective range of those forces. However, this study demonstrated that the restitution coefficient has a significant influence on the behaviour of particle-particle agglomeration, with a decrease in the coefficient resulting in higher aggregation rates. The Hamaker constant and Reynolds number variations both lead to major impacts on particle-particle interaction. It is determined that collisions and agglomeration events occur more frequently for increased Hamaker constants and Reynolds numbers.

Finally, a novel empirical correlation has been developed to predict the critical deposition velocity, at which the onset of particle deposition in particle-laden turbulent pipe occurs. The results indicate that at high Stokes numbers, the particle dispersion function and mean vertical displacement values fall quickly, and the formation of beds is observed. However, at lower Stokes numbers thinner dune-like structures are formed on the lower pipe wall. Using a volume-coverage percentage in the near-wall region of the lower half of the pipe as an identifier to define of the onset of deposition provides strong agreement with experimental predictions as well as the novel empirical correlation for prediction the critical deposition velocity.

Table of Contents

NOMENCLATURE

Symbol	Definition	Units
Roman and Greek Symbols		
A_{flow}	Cross-sectional area of the flow	m^2
d^*	Particle diameter	-
dr	Total error in distance along the radial direction	m
dy	Total error in the wall-normal distance, y	m
$d\overline{U}$	Total error in mean axial velocity	m
D	Pipe inner diameter	m
e_n	Coefficient of restitution	-
$\boldsymbol{g}$	Acceleration due to gravity	ms^{-2}
H	Hamaker constant	zJ
H^*	Hamaker constant in bulk units	-
I	Turbulence intensity	-
k	Turbulence kinetic energy	m^2s^{-2}
k_B	Boltzmann's constant	-
L	General characteristic length	m
N_{agg}	Particle-particle agglomerations	-
N_{col}	Particle-particle collisions	-
N_P	Total number of particles	-
n	Number of Samples	-
P	Pressure	$kgm^{-1}s^{-2}$
r	Distance from pipe centreline or Radial coordinate	m
R	Pipe radius	m
T_f	Temperature	K
t	Time	s
t^*	Time in bulk units	-
U_B	Bulk mean velocity	ms^{-1}
$\boldsymbol{u}^+$	Dimensionless instantaneous velocity in wall units	-
$u'_{r,rms}$	Root mean square (rms) of radial turbulent velocity	ms^{-1}
$\boldsymbol{u}_S^*$	Particle-fluid slip velocity in bulk units	-
u^*_z	Mean streamwise velocity	ms^{-1}

$u'_{z,rms}$	Root mean square (rms) of axial turbulent velocity	ms^{-1}
$u'_{\theta,rms}$	Root mean square (rms) of azimuthal turbulent velocity	ms^{-1}
V_c	Critical deposition velocity	-
y^+	Dimensionless distance from pipe wall in wall units	-
z	Axial or streamwise coordinate/distance	m
ν	Kinematic viscosity	m^2s^{-1}
ρ	Fluid density	kgm^{-3}
μ	Dynamics viscosity	$kgm^{-1}s^{-1}$
ε	Dissipation rate of turbulent kinetic energy per unit mass	m^2s^{-3}
η	Kolmogorov Length scale	m
θ	Azimuthal coordinate	-
Θ	Reduced surface potential	mV
ϕ	Particle volume fraction	-
κ	Inverse Debye length	m
β	General angle	-
ρ_f	Density of fluid	kgm^{-3}
ρ_s	Density of solid phase	kgm^{-3}
ρ_P^* or s	Particle-fluid density ratio	-
τ	Shear stress	$kgm^{-1}s^{-2}$
τ_η	Kolmogorov time scale	-

Subscripts and superscripts

f	Fluid-phase
s	Solid phase
$*$	Non-dimensional bulk units
$+$	Non-dimensional shear units

Dimensionless numbers

ϕ	Volume fraction
Fr	Froude number
Re_B	Bulk Reynolds number
Re_τ	Shear stress Reynolds number
St_B	Bulk Stokes number
St^+	Shear Stokes number

Abbreviations and acronyms

ADV	Acoustic doppler velocimetry
CFD	Computational fluid dynamics
DNS	Direct numerical simulation
EDL	Electric double layer
HPIV	Holographic particle image velocimetry
HLW	High level waste
HWA/HFA	Hot-wire anemometry/film
LDA/LDV	Laser Doppler anemometry/velocimetry
LES	Large eddy simulation
LLW	Low level waste
LPT	Lagrangian particle tracking/tracker
MPS	Micro-pillar sensor
NDA	Nuclear Decommissioning Authority
PDF	Probability density function
PIV	Particle image velocimetry
POCO	Post-operational clean-out
RMS	Root mean square
SEM	Spectral element method
SGS	Sub-grid scale
UDV	Ultrasonic doppler velocimetry
VDV	van der Waals
VILW	Very low-level waste

1 INTRODUCTION

Accurate simulation of multiphase turbulent flows is of fundamental importance for many industrial and scientific research applications. The term multiphase refers to the simultaneous flow of a fluid phase containing either a secondary phase such as bubbles, droplets or particles. The generation of understanding through accurate numerical modelling of turbulent multiphase flows is valuable across numerous industries such as chemical engineering, agriculture, pharmaceuticals, and nuclear waste processing (Lee et al., 2013; Guha et al., 2007). Many industries use knowledge obtained from high fidelity simulations to control and optimise unwanted behaviour such as particle deposition, erosion, and agglomeration. Of relevance to this study, flows prevalent in the nuclear waste processing are often difficult to investigate in situ and may result in safety concerns and system breakdowns, highlighting the need for non-invasive studies such as through computational simulation.

In the past, multiphase direct numerical simulation (DNS) investigations have been performed mainly using one-way coupling between the particles and the fluid, and at low Reynolds numbers and particle concentrations. To obtain better insight into flows relevant to the legacy ponds and silos in which nuclear waste is stored, such as how sludges (in this case a liquid containing high particle concentrations) and slurries (a mixture of dense solids suspended in a liquid) containing dense particulates interact, these systems need to be investigated thoroughly. The ability to predict and generate ways of controlling particle dispersion, particle-particle interaction, deposition, and agglomeration in turbulent pipe flows, in particular, is of value in improving the transport and process efficiency of high concentration particulate flows, and especially in the retrieval of such waste and post-operational clean-out (POCO) operations (carried out after final shutdown that prepares a plant for decommissioning and aimed at reducing the risk and hazard in a facility by removing the nuclear inventory and reducing the lifetime costs of the redundant plants). To elucidate the dynamics and generate knowledge surrounding such systems, characterisation of particle-laden turbulent flows is performed here using first-principles mathematical modelling. The variation of influential parameters is also investigated to determine the impact of behavioural modification effects, i.e., studying the impact of key parameters on particle interactions to obtain a desired flow behaviour. This will

be achieved by implementing additives or manipulating the fluid phase and particle physical and chemical properties to enable improved flow, mixing and separation of wastes during retrieval and POCO activities.

To investigate behavioural modification effects in suspension waste flows, wall-bounded pipe flows are simulated. Modifications of fluid and solid mechanical and chemical properties present in the inventory can be implemented practically by changes in temperature, ionic strength and pH of the liquid phase, or by injecting additives such as polymers and nanoparticles into the liquid phase that will attach to the particles, modifying their surface properties. These are capable of improving flow rates, as well as the mixing and separation of waste in POCO activities. The impact of particle coatings is also be investigated. These modifications change the way particles interact by affecting van de Waals forces, the collision restitution coefficient and electric double layer repulsion forces.

In the present work, by using high-accuracy and robust simulation techniques, the impact of behavioural modification techniques on particle dispersion and agglomeration is investigated using a fully coupled DNS-Lagrangian particle tracking (LPT) approach. These techniques are used to predict particle-laden turbulent pipe flows at a shear Reynolds number, $Re_\tau = 720$, based on the pipe diameter. An energy balance-based agglomeration determination technique is used along with four-way coupling between the particles and the fluid to predict particle aggregation due to collision interactions within the flow. The variation of influential parameters such as the Hamaker constant, coefficient of restitution, Reynolds number, temperature of the suspension, reduced surface potential and inverse Debye length is investigated to determine the impact of potential behavioural modification techniques (Mortimer and Fairweather, 2021). These modifications change the way particles interact by affecting various terms in the Derjaguin-Landau-Verwey-Overbeek (DLVO) theory of interaction potentials (Derjaguin and Landau, 1941; Verwey and Overbeek, 1955).

Rice (2013) investigated the settling and deposition behaviour of suspensions of dense particles in closed cylindrical pipes using ultrasonic methods, with the onset of particle deposition and resuspension from beds studied. In his experiments, a range of parameters were considered, although pipe diameter was not. Parameters that were difficult to vary and excluded from his studies included the influence of pipe diameter, D, and the role of particle size

distribution or polydispersity and packing fraction. Nevertheless, Rice (2013) proposed two ways of evaluating the critical deposition velocity, i.e. the velocity at which particles first start to deposit out in a flow: first by measuring particles depositing within a flow and secondly by measuring particles resuspending from the pipe floor, arguing that these were equivalent and represented different ways to obtain the critical deposition velocity. The author then established the critical deposition velocity of particles through experiments that monitored their resuspension from a particle bed.

The Stokes number is used to characterise how particles behave in a fluid flow. It facilitates comprehension of the reaction of particles to the surrounding fluid motion, and is defined as the ratio of the characteristic time of a particle to a characteristic time of the flow. In present study, several particle-laden turbulent pipe flows are studied using DNS and large eddy simulation (LES) of the continuous phase in combination with LPT to determine critical deposition velocities at various particle Stokes numbers. All the work was carried out using the computational fluid dynamic solver, Nek5000, enhanced with a four-way coupled LPT to enable high-fidelity modelling of particle-laden pipe flows. The deposition of particles over the course of a simulation in which the flow rate is slowly reduced from a range of initial bulk Reynolds numbers $Re_b = 11{,}700$ to $600{,}000$ is studied, with a focus on determining a method for critical deposition velocity identification, as well as the analysis of deposition out of the flow to form solid beds. Furthermore, it is worthy of note that no previous modelling studies have examined the onset of deposition, or the critical deposition velocity, in such flows, with most deposition studies being experimental.

A brief review of radioactive nuclear waste processing in the UK is presented in Section 1.1. With the characterisation of nuclear waste sludge flows and slurries present in POCO operations in mind, the motivation and objectives of the project are discussed in Section 1.2.

1.1 Radioactive nuclear waste processing in the UK

Nuclear energy plays an important role in providing reliable, low pollutant emission (such as carbon dioxide) and affordable electricity. There are drawbacks in delivering an affordable nuclear energy future however – the waste products of most nuclear energy operations are radioactive. Radioactive wastes occur in many different types of physical and chemical forms.

Safely disposing of these radioactive materials requires expertise, and the implementation of scientifically robust, innovative approaches to decommissioning and waste management (Ozcan et al., 2016). Improved processing methods are vital for both legacy and new nuclear build wastes. To better understand the characteristics of slurries and sludges currently held on nuclear sites, it is imperative to investigate and be able to predict the properties of the particles found in the waste inventory. Radioactive waste management involves a series of steps. In planning and preparation, the site aims to limit the amount of waste products generated wherever possible and plans ahead of time on how to handle the waste. The waste treatment process usually begins soon after it is generated. The method varies according to the type of the waste and the desired disposal route which includes the decontaminating, shredding, compacting, drying, and hardening of the waste. These wastes must be packaged in specially designed containers for safe storage in interim storage facilities until a suitable disposal route becomes available where they will remain permanently, i.e., a geological disposal facility. Some waste can be treated for reuse or recycling; hence packaging or disposal is not required (Nuclear Decommissioning Authority, 2022).

An integrated and effective waste management system is an essential part of the UK Nuclear Decommissioning Authority (NDA) programme. An NDA report published in 2022 on the radioactive waste inventory sets out its integrated waste management strategy. Five key steps are presented hierarchically for dealing with waste management. The first and preferred approach is waste prevention, then followed by waste minimization where possible. Following that the re-use of materials and recycling of these materials is suggested if these approaches are safe and there are opportunities to do so. Finally, if the waste cannot be managed by any other means it should be disposed of carefully. This strategy is employed for existing radioactive wastes generated within the NDA estate and will, most likely, be adopted in relation to waste materials produced in the future. Safety is always a priority, and a multisite approach is generally applied in implementing this strategy. Environmental impacts were the main factor of consideration in the development and deployment of the waste hierarchy. Producing low waste volumes, and re-using or recycling, is clearly more desirable than disposal (NDA, 2022)

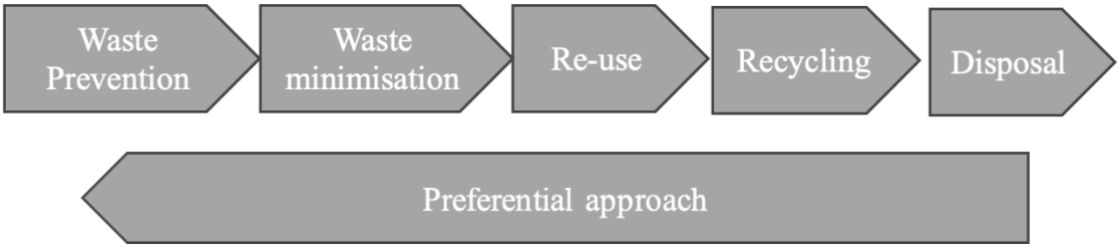

Figure 1.1: The waste hierarchy (source NDA, 2022).

The NDA classifies radioactive wastes into two main categories, and then two further subcategories according to amount of radioactive material and type of activity:

I. Higher activity wastes (HAW)
   a. High level waste (HLW)
   b. Intermediate level waste (ILW)
II. Low level waste (LLW)
   a. Low level waste
   b. Very low level waste (VLLW)

According to the 2022 NDA report and data included therein, as of 1st of April 2022 the total mass of all existing wastes in stock and future arisings from all sources is 5.1 million tonnes. HLW is the lowest volume of all radioactive wastes, accounting for less than 1% of the total volume. It is usually transformed into a glass waste form in order to immobilize and shield it. Due to its high radioactivity, its temperature may increase significantly, therefore its storage environment must take this into account. ILW accounts for around 4.4% of the total volume of radioactive waste. Figure 1.2 shows the composition of waste types classified as ILW. It consists of a variety of forms, though approximately 41% by volume is comprised of graphite (26%) and plutonium contaminated material (15%) (NDA, 2022).

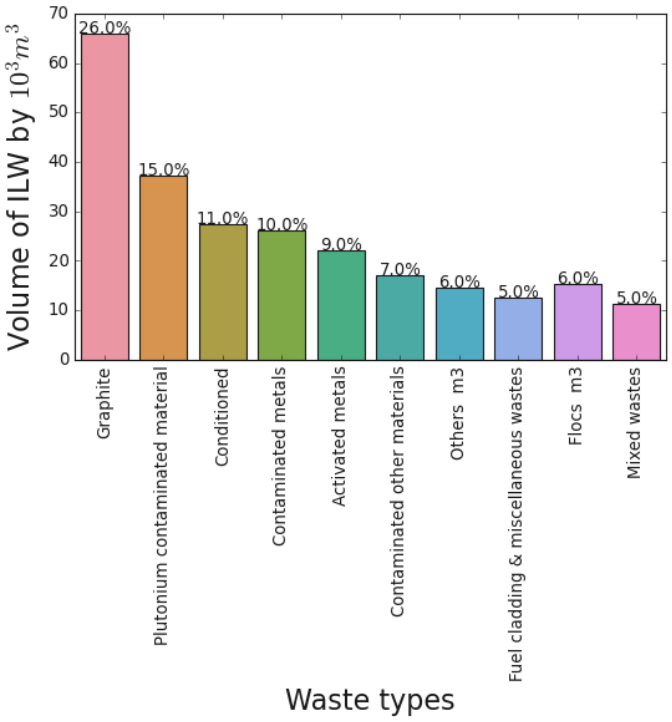

Figure 1.2: Composition of ILW by waste types (NDA, 2022).

LLW is defined as possessing an activity of less than 4 GBq of alpha radiation and/or 12GBq per tonne of gamma and beta activity – one Becquerel (Bq) being equivalent to one radioactive decay event per second (NDA, 2022). Approximately 95% of radioactive waste products by volume are in the LLW category. Figure 1.3 illustrates the composition of waste types for both low level waste (left) and very low-level waste (right.) Miscellaneous contaminated materials and concrete and rubble make up to about 76% of the volume of LLW. Activated and contaminated metals comprise around 19%. VLLW has the lowest radioactivity and can be disposed of in permitted landfill facilities. Concrete and rubble (debris) make up roughly 90% of the volume of VLLW (NDA, 2022).

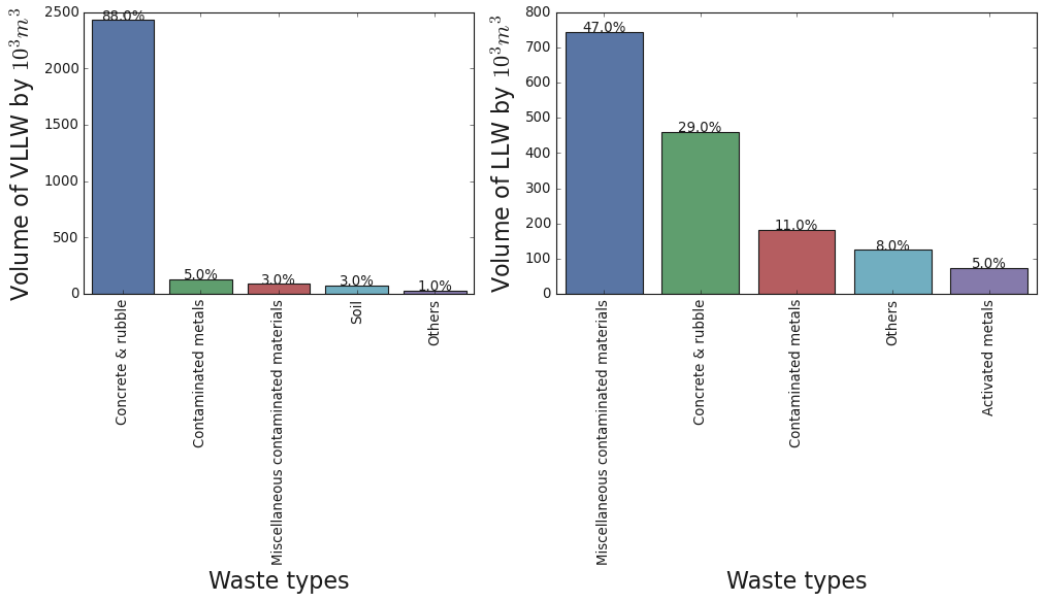

Figure 1.3: Composition of LLW (left) and VLLW (right) by waste types (NDA, 2022).

1.2 Aims and objectives

In this thesis, the development of a methodology based on direct numerical simulation and large eddy simulation to study the details of turbulent pipe flows is described. A readily available computational fluid dynamic solver, Nek5000, is utilised and extended to simulate particle-laden turbulent pipe flows. The solver is based on the spectral element method with a high-order residual technique. It is favourable for its high spectral accuracy, parallel process scaling and low numerical dispersion and dissipation. The code is further linked with a fully-coupled Lagrangian particle tracker (LPT) to allow simulation of particle-laden flows.

The overall aim of this study is to address some of the fundamental technical difficulties that are encountered within the nuclear industry. Developing and facilitating approaches for safer, more cost-efficient waste management and decommissioning is the ultimate application of the research. Understanding and modelling pond and silo sludge behaviour is essential to the management of radioactive wastes. In the legacy ponds and silos, for example at Sellafield, characterising how sludges and slurries containing dense particulates will behave is vital for post-operational clean-out operations. In this project the aim is to establish a predictive tool to support POCO operations through improvements in the flow, mixing and separation of wastes during retrieval and POCO operations.

Behavioural modification effects in suspension waste pipe flows are simulated, i.e., the use of modifications to fluid and solid particle properties to promote a desired outcome such as reducing particle agglomeration which in turn helps to prevent particle deposition and potential pipe blockages. The primary goal of this aspect of the research is to investigate different behavioural modification techniques and deposition in particle laden flows, with an energy-based deterministic agglomeration model used to predict particle interaction and aggregation.

The onset of particle deposition in particle-laden turbulent pipe flows is also studied using a four-way coupled DNS-LPT approach. A wide range of particle Stokes numbers is considered, and comparisons of critical particle deposition velocities derived from the simulations with those obtained experimentally from both particle deposition and resuspension approaches are made. Results for the concentration of particles forming dune-like structures and beds in the near-wall region are used to determine a method for predicting the critical deposition velocity.

Below is a list of project's main objectives:

- Develop and obtain statistically settled single-phase flows in a circular pipe at three different shear Reynolds numbers, Re_τ=277, 360 and 720, using the DNS computational fluid dynamics (CFD) code, Nek5000.
    - Validate and analyse the single-phase turbulent pipe flow predictions against available experimental data and previous DNS results.
    - Perform four-way coupled DNS at $Re_\tau = 277$, 360 and 720, accounting for momentum-transfer between the particles and the fluid, and interparticle collisions.
    - Using the fully-developed flows, implement and validate a one-way and four-way coupled multiphase DNS with LPT for horizontal turbulent pipe flows.
    - Gather four-way and inter-particle collision statistical results for analysis after sufficient response time for the particles to adjust to the surrounding fluid and compare the results against previous DNS results.
- Extend existing the deterministic inter-particle agglomeration model to include electric double layer repulsion.

- Use extended the agglomeration model to investigate particle collision and agglomeration in a horizontal pipe flow at shear Reynolds number, $Re_\tau = 720$, and particle volume fraction, $\phi_p = 1 \times 10^{-3}$.
    - Study system sensitivity to mechanical and chemical parameters to develop behavioural modification techniques. The behavioural modification effects to be studied include variations to Hamaker constant, coefficient of restitution, Reynolds number, fluid temperature, ionic strength, reduced surface potential and inverse Debye length.
    - Analyse results from the behavioural modification techniques study to determine their ability to promote desired outcomes such as reducing particle agglomeration, and hence, the likely deposition of particles during processing.
- Develop a framework to predict the critical deposition velocity in particle-laden turbulent pipe flows.
    - Perform simulations of depositing particle-laden flows, using the above developed framework, to predict the onset of particle deposition in turbulent pipe flows.
    - Develop and perform an LES-LPT approach to study the details of particle deposition for high Reynolds number systems, in line with those present in many experimental studies.

1.3 Numerical simulation background

Numerical studies of single- and multiphase turbulent flows entail the use of high-performance computer simulations to predict fluid flow and particle dispersion behaviour. These simulations can be used to gain a better understanding of the complex dynamics of particles in a turbulent flow, and to predict complex multiphase systems under a variety of scenarios.

The Reynolds-averaged Navier-Stokes (RANS) method is one of the most extensively used approaches for numerical simulations of turbulent flow. This method involves solving for averaged quantities in the fluid flow governing equations that describe the mean flow. These averaged equations are closed using various turbulence models that are used to predict the effects of turbulent fluctuations, rather than resolving them directly. RANS simulations can be

used to analyse a wide range of fluid flow conditions and provide precise prediction of the mean velocity profiles and turbulence intensity fields, though only averaged information is generated. However, time-dependent information is imperative to particle dispersion and interaction prediction, and the motion of small turbulent eddies, not predicted by RANS, is important since they lead to many migratory and interaction behaviours observed in particle-laden turbulent flows.

The large-eddy simulation approach is another method available for the numerical simulation of turbulent flows. This method involves directly resolving the largest energy-containing scales motion in the turbulent flow while modelling the impact of smaller scales using sub-grid scale models. LES simulations can be used to analyse a wide range of fluid flow conditions while also providing precise predictions of turbulent variations in the flow.

In recent years, high-resolution direct numerical simulation of turbulent flows has gained in popularity due to its ability to provide comprehensive details of turbulent flows and their associated energy spectrum. The DNS computational method solves the Navier-Stokes equations for a flow over all length and time scales, without the use of approximate turbulence or sub-grid scale modelling. This approach provides a realistic description of the turbulent flow, but it is computationally intensive and only applicable to less complex flows and low turbulent Reynolds numbers. Nevertheless, DNS is an important tool for understanding the complex dynamics of fluid flow.

The use of various numerical methods, such as RANS, LES, and DNS, allows for the prediction of fluid flow behaviour in a wide range of conditions and can be used to improve the design of industrial processes, predict the behaviour of natural systems, and optimise fluid flow in pipes and other systems. These simulations are also of value in evaluating and supplementing experimental research, resulting in a more complete picture of fluid flow behaviour.

1.4 Project background and thesis structure

A collaborative approach to nuclear energy research and development across academia, industry and government is of benefit to the UK economy in many ways, and this research was carried out as part of the ESPRC-supported TRANSCEND (Transformative Science and Engineering for Nuclear Decommissioning) project. TRANSCEND is a collaborative research

consortium of 11 universities and 8 industry partners, with the £9.4M research programme comprising 40 projects which address some of the key challenges within the areas of nuclear decommissioning and waste management. Overall, this project is of value in establishing the UK nuclear industry as a leading global competitor in end-to-end radioactive waste management and decommissioning, i.e., in processing and waste treatment to reduce active radiation, packaging waste in specially engineered containers for safe storage and transportation, storage in interim facilities, and final disposal at sites where the nuclear waste remains permanently (NDA, 2022).

The thesis's structure is as follows:

Chapter 2 forms a review of the relevant literature. Experimental and simulation studies of single-phase and multiphase flows, particle deposition and behavioural modification research to date are reviewed in their respective sections.

Chapter 3 describes the basis of the mathematical approaches and numerical algorithms utilised in this study. The methodology for the DNS, LES and LPT techniques used for each simulation is also thoroughly discussed.

Chapter 4 provides a validation of the unladen turbulent pipe flow simulation predictions as well as multiphase validation results, and discussion and analysis of the key features of such flow.

Chapter 5 presents simulations of potential behavioural modification techniques, used to promote desirable outcomes such as reduced/improved aggregation.

Chapter 6 develops a model to predict the critical deposition velocity in particle-laden turbulent pipe flows. This model is then compared with experimental results on the onset of deposition to assess the value of the predictions.

Chapter 7 summarises the main conclusions and findings of the study and details suggestions for further investigations.

2 BACKGROUND AND LITERATURE REVIEW

2.1 Introduction

This literature review examines in detail experimental as well as numerical findings surrounding the main continuous phase phenomena and particle behaviour in turbulent pipe flows studied to date, as well as flows in similar wall-bounded geometries. Single-phase and multiphase experimental and numerical simulations in channels, ducts, and pipes are reviewed. The review also covers previous experimental and numerical simulation studies that are used later to validate that the developed and deployed codes were performing as intended.

2.2 Background

There have been various notations adopted for describing the geometry of turbulent pipe flows. In the mathematical literature, most commonly, the radial distance is represented by r, the angular position or azimuthal location by θ and the axial distance by z for cylindrical geometries, and in Cartesian coordinate systems by x, y, z (Riley et al., 2006). In most engineering research papers, the radial (or distance from the origin), azimuthal or circumferential, and axial or streamwise coordinates are defined as r, θ and z, respectively. In this research, common engineering notations have been adopted when deriving the governing fluid dynamic equations.

2.2.1 Turbulence

Turbulence is considered as one of the unresolved phenomena of physics and engineering due to its irregularity, mixing, dissipation and three-dimensional vorticity fluctuations. The velocities, $\boldsymbol{u}(\mathbf{r}, \mathrm{t})$, where $\boldsymbol{r}$ is the position, and t is time, fluctuate erratically and irregularly. These kinematic characteristics make it hard to obtain a generalised turbulence model, in RANS approaches at least, that can be used in all scenarios. Hence, one has to develop a model

and/or a solution depending on the geometrical configuration and scales of the flow to obtain a specific solution.

In the late nineteenth century, Reynolds (1895) experimented by steadily injecting dye into a long pipe. In that study, he established a dimensionless parameter used to characterize the behaviour of the flow, now known as the Reynolds number, $Re = UD/\nu$, where U is the bulk velocity, D is the diameter of the pipe and ν is the kinematic viscosity of the fluid. It was observed that the main features of turbulent flows are the capability to transport kinetic energy and rapid mixing (diffusivity) due to energy exchange in the flow. As the flow behaviour mainly depends on the forces that dominate the flow, i.e., viscous, inertia, surface tension or other forces, turbulent flows are chaotic and velocity profiles vary significantly, hence the inertial forces are dominate (Pope, 2000).

2.2.2 The Reynolds number

In fluid dynamics, the Reynolds number is one of the most fundamental parameters that can be used to determine how turbulent flows behave. Given a Reynolds number, a flow can be classified as either laminar, transitional or turbulent. This dimensionless quantity represents the ratio of two of the forces which arise in a flow, namely, inertial forces (ρU) and viscous forces (μ/D). Here, ρ is the density of the fluid phase and μ is the dynamic viscosity of the fluid. The ratio of these two forces gives the Reynolds number, $Re = \rho U/(\mu/D)$ (Munson et al., 2002). This dimensionless quantity is directly proportional to the characteristic velocity, U. As the Reynolds number increases, the inertial forces increase, and the flow destabilizes and subsequently forms turbulence (Ahmari and Kabir, 2020).

2.2.3 Reynolds decomposition and turbulence kinetic energy

Reynolds decomposition refers to the mathematical technique used to split a turbulent flow field, $\boldsymbol{u}_F(\boldsymbol{x}, t)$, into mean and time dependent fluctuating terms:

$$\boldsymbol{u}(\boldsymbol{r}, t) = \overline{\boldsymbol{u}}(\boldsymbol{r}) + \boldsymbol{u}'(\boldsymbol{r}, t) \tag{2.1}$$

Here, $\boldsymbol{u}(\boldsymbol{r}, t)$ is the instantaneous velocity at position vector, $\boldsymbol{r}$, and time, t, $\overline{\boldsymbol{u}}(\boldsymbol{r})$ is the timewise mean velocity and $\boldsymbol{u}'(\boldsymbol{r}, t)$ is the fluctuating velocity term (about the mean) due to

turbulence. The fluctuation term is defined as the instantaneous velocity subtracted from the instantaneous quantity, $\boldsymbol{u}(\boldsymbol{r}, t)$, such that the temporal average is equal to zero. The root mean square (rms) fluctuating term is defined as:

$$u_{rms}(\boldsymbol{r}) = \sqrt{\overline{\boldsymbol{u}'(\boldsymbol{r}, t)^2}} \tag{2.2}$$

Equation (2.2) can be used to measure the magnitude of the dispersion of errors or residuals in any calculation. It refers to the discrepancy between results that were expected and actual results. Often, this is used to quantify the level of turbulence in a flow. The turbulence kinetic energy, k, can be derived using the fluctuating velocity terms as follows:

$$k = \frac{1}{2}\langle \boldsymbol{u}'.\boldsymbol{u}' \rangle = \frac{1}{2}\left(\overline{u'^2} + \overline{v'^2} + \overline{w'^2}\right) \tag{2.3}$$

2.2.4 Kolmogorov microscales and the energy cascade

The smallest scale in turbulent flows of a fluid are referred to as the Kolmogorov microscales. The Kolmogorov scale is dominated by viscosity and at these scales the kinetic energy is dissipated into local heat. The rate of energy dissipation is given by ϵ. According to Kolmogorov (1941), turbulence becomes isotropic such that $\overline{u'^2} = \overline{v'^2} = \overline{w'^2}$ at small scales. The Kolmogorov length and time scale are then defined as:

$$\eta = \left(\frac{\nu^3}{\epsilon}\right)^{\frac{1}{4}} \tag{2.4}$$

$$\tau_\eta = \left(\frac{\nu}{\epsilon}\right)^{\frac{1}{2}} \tag{2.5}$$

Here, η is the Kolmogorov length scale, ϵ is the average rate of dissipation of turbulence kinetic energy per unit mass, ν the kinematic viscosity of the fluid, and τ_η the Kolmogorov time scale.

2.2.5 Energy spectra

The energy spectrum of turbulence is an important component in characterizing the distribution of energy between different eddy sizes. It represents an association between an eddy

wavenumber, κ, which is equivalent to $2\pi/l$ where l is eddy length scale, and the energy associated with that particular eddy size, $E(\kappa)$. The research by Pao (1965), Lin (1972), and Hill (1978) shows that there is strong agreement across different energy spectrum regions.

2.2.6 Particle flow regimes

For monodispersed flows, it is useful to classify the flow regime that is expected to be observed based on bulk parameters such as volume fraction, density and particle size. The volume fraction, ϕ_P, is defined as:

$$\phi_P = N_P \frac{V_P}{V_F} \tag{2.6}$$

Here, N_P is the number of dispersed particles, and V_P and V_F are the volume of each particle, and the volume of the flow topology, respectively. A particle-laden flow regime can be characterized using Eq. (2.6) along with the particle Stokes number based on the Kolmogorov time scale, St_K, which is the ratio of the particle timescale to the Kolmogorov timescale. This was first suggested by Elghobashi (1991) in the early 1990s and later improved, with Fig. 2.1 showing the regime classification for particle-laden turbulent flows (Elghobashi, 2007). Large particles refers to a group of particles that exhibit specific traits or actions, including having more inertia than microparticles, responding more slowly to changes in the fluid flow, or settling at higher velocities. In the regime where $1 > St_K \geq 10$, large particles respond far more slowly than particles on the Kolmogorov time scale. Particles are referred to as ghost particles in the regime where $0.1 > St_K \geq 1$ because the effects of both large and microparticles, which increase or decrease turbulence kinetic energy, respectively, are cancelled out and, as a result, such particles have little effect on the turbulent flow field. Finally, particles in the regime where $St_K \leq 0.1$, referred to as microparticles, function as flow tracers because of their low Stokes numbers; nevertheless, at high volume fractions, these particles accelerate energy dissipation and slow the rate at which turbulence kinetic energy decays.

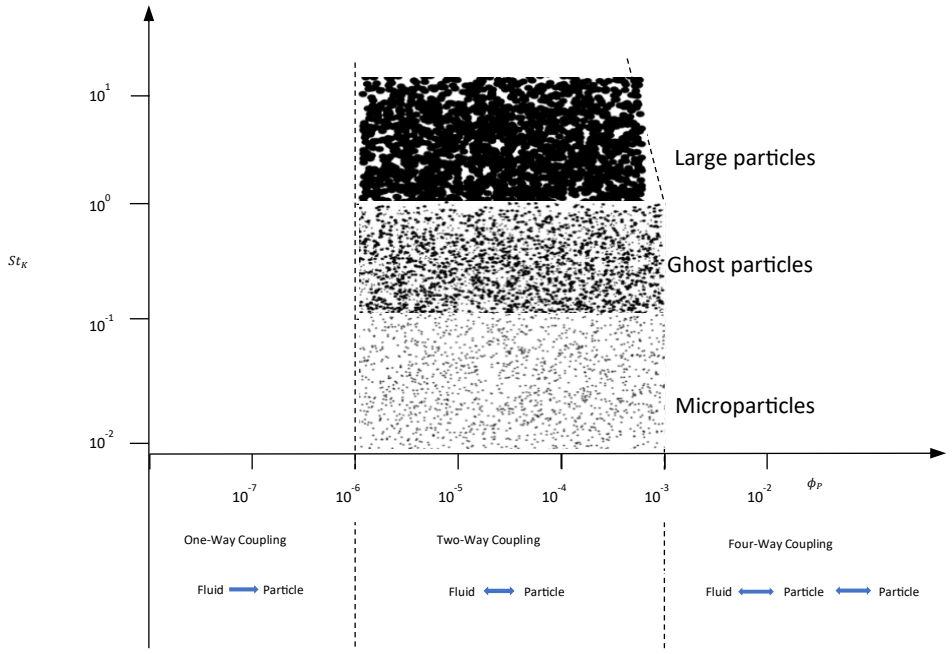

Figure 2.1: Regime classification for particle-laden turbulence, in line with Elghobashi (2007).

2.3 Single-phase turbulent fluid flows

Single phase turbulent fluid flow refers to the movement of a fluid in which there is only one phase present. The flow for high Reynolds numbers is characterized by turbulent motion. This type of flow is observed in many industrial and natural systems, including rivers, oceans, and pipes in power plants and other industrial facilities. Turbulent flow is distinguished by the chaotic and uneven motion of fluid particles. It is caused by the presence of large-scale eddies and vortices that form and disintegrate all the time, transferring energy to ever smaller scales. Because of the chaotic nature of turbulent flow, it is difficult to anticipate and model, and it is frequently represented using statistical rather than deterministic methods. In the fluid mechanics of multiphase flows, the study of single-phase flow is the primary step in any simulation as additional phases are usually injected into a statistically stationary fluid phase. There have been many single-phase experimental as well as numerical studies of turbulent flows in wall-bounded pipes, ducts and channel geometries carried out over time. In this section, the more recent and important experimental and numerical simulation work is reviewed.

2.3.1 Experimental techniques

Hot-wire and/or hot-film anemometry (HWA/HFA) is one of the earliest methods widely used to measure the turbulent velocity profiles and the direction of the fluid, utilising heat loss to the surrounding fluid. In this method, a thermal transducer is heated by an electrical current and placed in the fluid stream. The principle of heat transfer from the hot-wire to the fluid is used to analyse and measure the velocity profiles. Hot-film anemometry is implemented to measure the wall shear stress. In 1979, Kreplin and Eckelmann (1979) conducted an experiment using a low bulk Reynolds number, $Re_B = 7700$, to study the fluctuating velocity fields and wall shear stress in a fully developed turbulent channel flow using a hot film. This method offered a high spatial and temporal resolution plus a good frequency response characteristic. Despite this, the technique is less favoured today due to ambient temperature variation errors and its intrusive nature. More details surrounding this technique are available in Perry (1982). Table 2.1 lists further hot-wire experimental literature.

Laser Doppler velocimetry (LDV/LDA) is a popular non-invasive velocity measurement technique. The method uses the Doppler shift in a laser beam light to measure fluid velocity and turbulence distribution. It can provide high-resolution velocity field measurements which are, nevertheless, often limited to small scale flows. This technique was initially developed in the 1960s to allow more accurate measurement of low-velocity fields (Yeh and Cummins, 1964; Durst et al., 1976).

2.3.2 Experimental studies in pipes

In the past, many single-phase experiments have been performed in pipes and a wide range of variables and phenomena have been studied. Pipe topology is popular for experimental investigation of complex flow behaviours near the wall regions of these wall-bounded flows. These experiments have focused on measuring mean velocities, as well as velocity fluctuations in order to determine normal and Reynolds stresses within the flow.

In the mid 1950s, Laufer (1954) used HWA to gather mean and other statistical quantities such as Reynolds stresses, turbulence dissipation and energy spectra in a fully developed turbulent 10-inch pipe flow. The author discovered that the viscous sublayer had the highest turbulence

energy production, dissipation, and diffusion rates. However, Lawn (1971) later found inconsistencies in Laufer's (1954) measurements of the energy dissipation rate.

Patel and Head (1968) conducted similar research, observing a deviation from the predicted inner-law mean velocity distributions when strong pressure gradients exist within the boundary layer. They also noticed that these conditions tended to cause the boundary layer to revert to a laminar state. The authors used these findings to develop a set of criteria for the mean shear-stress gradients found in the wall region, which indicate when the layer is likely to transition to a laminar state. The authors suggested that the key factor in starting the reverse transition is the distribution of shear stress in the wall region as opposed to the overall Reynolds number.

Lawn (1971) conducted additional measurements of the turbulence energy dissipation rate and the spectral distributions of the stress components, building on Laufer's (1954) work on this subject. By assuming isotropy while calculating quantities with few data, Laufer's (1954) results on dissipation are inconsistent with those of Lawn (1971), and the latter author underlined and discussed these discrepancies, arguing that they were due to limitations of the hot-wire technique at increased Reynolds numbers, $Re_\tau > 105$.

Bremhorst and Walker (1973) provided measurements of the spectral components of turbulence momentum transfer in fully developed pipe flow with emphasis on the region near the solid wall. They identified that two types of momentum transfer occur near the wall. These mechanisms are linked to the frequency range of the energy containing part of the turbulence spectrum and the lower end of the spectrum. The authors demonstrate an inverse relationship between frequency magnitude and net momentum transfer.

In 1976, Comte-Bellot conducted research on the occurrence of turbulent structures within the core region of a turbulent pipe flow. This generated a better understanding of the turbulent structures by measuring the cross-sectional shear stress fluctuations and explored the existence of both spatial and temporal processes that can occur in this region, in comparison to closer to the wall. In this work, both hot-wire and hot-anemometer devices were used to measure the fluctuating velocity components.

Eggels et al. (1994) conducted HWA, LDA and particle image velocimetry (PIV) experiments in a cylindrical geometry in 1994, using a Reynolds number based on the centreline velocity

of $Re_c \cong 7000$ and a characteristic length, $L = 5D$, where D is the pipe diameter. The results exhibited agreement with each other as well as with direct numerical simulations carried out by Eggels et al. (1994).

Westerweel et al. (1996) used a digital version of the previously mentioned PIV technique to measure flow velocities within a turbulent pipe at a bulk Reynolds number of 5300. The author's results were used to determine the accuracy of the new method when compared to other well-established techniques such as standard PIV and LDA. When analysed, digital PIV provided the same accuracy level as standard PIV, however, the interrogation of the images was much faster for digital PIV and so this technique was shown to be less time-consuming making it more efficient.

Den Toonder and Nieuwstadt (1997) used the two-dimensional LDV method to measure the effect of Reynolds number on the mean flow statistics. Reynolds numbers ranging from 5000 to 25,000 were investigated in a water flow. Their results matched prior studies for the lowest Reynolds number experiments, and the non-dimensionalised mean velocity profiles were found to be Reynolds number dependent. The turbulence statistics were shown to be in good agreement with equivalent direct numerical simulations (Eggels et al., 2004).

Zagarola and Smits (1998) studied the turbulence statistics and pressure drop in a fully developed pipe flow by considering a considerably greater range of bulk Reynolds numbers, ranging from 31,000 to 35,000,000. Their findings were utilised to expand on the theory to explain the mean flow scaling. There was some uncertainty in these results due to the velocity gradient corrections utilised, thus McKeon and Smits (2002) worked on determining this correction factor. In the latter work, the authors argue that the velocity gradient correction term scales with Reynolds number, which was not considered in prior investigations.

Recently, machine learning algorithms, called convolutional neural networks, and deep learning have been implemented to estimate particle motion as part of the PIV method. These are alternatives to the image cross-correction methods used in PIV to rebuild fluid velocity profiles from the raw experimental data (Cai et al., 2020).

2.3.3 Experimental studies in ducts and channels

Several non-pipe experimental turbulent flow systems have also been investigated such as fully developed channel and duct flows. The channel flow is one of the most common flow geometries employed by researchers to measure both single and two-phase turbulent flows due to its simplicity in that mean statistical quantities are generally related solely to the distance from the channel wall. Nikuradse (1926, 1929) was one of the first to investigate flow measurements in a fully developed channel flow. However, due to their periodic characteristics in two directions, channel flow investigations are challenging to set up and undertake experimentally.

Nikuradse (1926) observed that above a certain Reynolds number, the mean velocity contours for duct flows differ from those of pipe flows. Since that time, there has been a lot of interest in studying flows in a duct topology in which the flow is completely confined by four perpendicular walls. Prandtl (1927) observed that the mean streamwise velocity contours in a duct flow were distorted towards the duct corners. Prandtl believed that this was due to secondary turbulent motions, which caused the fluid to behave differently and move from the duct centre to the corners in the cross-sectional plane of the duct. These corner vortices are categorised as Prandtl's secondary flows, which emerge from turbulence rather than from skewing of the cross-stream vorticity. Hoagland (1960) examined this type of phenomena in further depth. The author used the HWA method to gain more precise and quantitative profiles of secondary velocities in duct flow.

Brundrett and Bains' (1964) work provided a more thorough understanding of these secondary turbulent motions. In their research, the HWA technique was used to quantify all six components of the Reynolds stress and the mean flow velocity distribution. This was achieved by positioning the hot-wire probes in various orientations across a duct flow apparatus. Normal-stress gradients were discovered to be the most important in the formation of the cross-stream velocities.

Gessner and Jones (1965) used the same experimental technique to study the effect of Reynolds number on secondary flows in ducts. They studied secondary flow velocities at various Reynolds numbers, and discovered that when the Reynolds number increased, the non-dimensionalised secondary flow velocities reduced.

2.3.4 Numerical studies in pipes

The first direct numerical simulation in a smooth circular pipe was carried out by Eggels et al. (1994) to study a fully developed turbulent flow. The simulation was performed using a finite-volume technique at low Reynolds number, $Re_B \cong 5300$, based on the bulk velocity and diameter of the pipe. The results obtained were compared with experimental datasets and a channel DNS. Their research found that the mean axial velocity profile in the pipe, at such low Reynolds number, did not follow the usual log law. The law of the wall states that the velocity profile of the fluid close to the pipe wall exhibits a logarithmic relationship with distance from the wall. Their work emphasised the importance of direct numerical simulation to scientific research and to the further understanding of turbulent flow.

In early 2000, many researchers conducted numerical simulations of turbulent flows in cylindrical geometries, with notable works utilising direct numerical simulation including those of Orlandi and Fatica (1997), Wagner et al. (2001), and Fukagata and Kasagi (2002). Although these works improved our understanding of such flows, they were simulated at low Reynolds numbers. For example, Wagner et al. (2001) used a pipe length of $L = 10R$ and at shear Reynolds number, $Re_\tau \cong 320$.

Wu and Moin (2008) employed DNS to investigate turbulent pipe flow at a bulk Reynolds number of 44,000 based on the bulk velocity and diameter of the pipe. 630 million grid points were used, and they employed a second-order finite-difference integration approach to solve the governing fluid dynamic equations. Their mean flow and second-order turbulence statistics showed good agreement with experimental data. When measured in wall units, the authors' flow visualisations and two-point correlations demonstrate that large-scale turbulent structures have similar near-wall azimuthal sizes at Re_B= 44000 and 5300.

In recent years, moderately high Reynolds number simulations have been carried using high performing computers. El Khoury et al. (2013) used a high-order spectral element method to predict flows at four different shear Reynolds numbers, based on pipe radius, of $Re_\tau \cong 360, 7200, 1100$ and 2000 in a smooth pipe with a characteristic length $L \cong 12.5D$. When comparing their findings to previous DNS results in various geometries, the authors discovered that pressure is the primary quantity that fluctuates in the geometry of pipes, channels, and boundary layers. Furthermore, the authors found that the turbulence kinetic energy budgets

were practically indistinguishable close to the wall, and Reynolds number dependencies for numerous statistical parameters were also observed.

Table 2.1 summarises both experimental and DNS studies carried out for single-phase turbulent pipe flows at various Reynolds number. The present DNS results obtained in this study are compared with various DNS and experimental dataset available in the literature at, or approximately equal to, the Reynolds numbers of the simulations performed. For each simulation the mean velocity profiles, and the root mean square of velocity fluctuations and shear stress, are compared. Only literature data with incompressible and Newtonian fluid flows has been used for validation.

Table 2.1: Summary of single-phase turbulent pipe flow experimental and numerical simulation studies at various Reynolds numbers.

Methods	**Pipe diameter, D / mm**	**Bulk Reynolds number, $Re_B / 10^3$**	**Validated for:**	**Reference**
LDA	123	6.95-7.37	360	Eggels et al. (1994)
	40	4.9 -25.3	360, 720	Den Toonder et al. (1997)
PIV	123	6.95-7.37	360	Eggels et al. (1994)
HWA	123	6.95-7.37	360	Eggels et al. (1994)
DNS – finite volume technique	123	6.95-7.37	360	Eggels et al. (1994)
DNS – spectral element technique		10-28	720	Singh et al. (2018)
		5.3-11.7	360, 720	El Khoury et. al (2013)
		3.97	277	Vreman (2007)

2.3.5 Numerical studies in ducts and channels

Beginning in the late 1960s, efforts were made to explore turbulent flows in-depth using computational models. As processing performance improved, realistic turbulent flow simulation times became possible. The sub-grid scale model introduced by Smagorinsky (1963) and improved by Lilly (1967) is the most frequently utilised model in LES. Through the work of Deardorff (1970), this model was made applicable to engineering simulation flows. For a three-dimensional channel flow, the author used 6720 grid points to carry out an LES at a high Reynolds number. The Smagorinsky model makes a mixing length assumption, which means that the eddy viscosity is assumed to be proportional to a sub-grid scale (SGS) characteristic length and a typical turbulent velocity. As suggested in Smagorinsky's (1963) paper on LES methods, eddy coefficients were used to estimate the SGS Reynolds stresses.

The Smagorinsky model has the disadvantage of being too dissipative in near-wall regions, and it has been proven to be less accurate when compared to other more advanced SGS models.

Demuren and Rodi (1984) reviewed experimental results and turbulent flow models that described secondary motions in ducts. They utilised a Reynolds stress model within a RANS approach, and also performed their own LES computations. Madabhushi and Vanka (1991) performed an LES at a Reynolds number of Re_B = 5810. They used a spectral finite-difference method in conjunction with the Smagorinsky eddy viscosity model for the SGS to undertake an LES analysis of turbulence driven secondary flows in a square duct. The simulations were able to predict the statistics of mean flow velocities and all turbulence quantities.

Kajishima and Miyake (1992) provided a detailed explanation for how the secondary flows are produced in their LES analysis of turbulent square duct flows. Similar results were observed in the LES simulations of Su and Friedrich (1994) who asserted that reasonably high resolution is needed to capture the secondary flows.

Gavrilakis (1992) conducted a DNS of a turbulent duct flow using a bulk Reynolds number of 4410. A comprehensive analysis of the mean flow characteristics and turbulence statistics was performed. Using an approximately equal Reynolds number ~ 4,440, secondary flows in a duct were also examined by Joung et al. (2007). These authors observed that the momentum transfer between the duct's corner and its centre was entirely dependent on the secondary flows.

2.4 Multiphase turbulent fluid flows

For several decades, researchers have investigated the interaction of a flow consisting of more than one phase, with materials with different phases (i.e. solid, liquid or gas) having been studied. For instance, liquid-liquid flows such as oil droplets in water. These simultaneous flows could also include bubbles, as well as polydispersed or irregular shaped particles. In this thesis, spherical particle-laden turbulent pipe flow simulations are carried out and studied in the context of deposition and flow behavioural modification.

2.4.1 Experimental techniques

In the 1970s, the LDA/LDV technique was widely employed to generate understanding of fluid flow and its properties. Tsuji and Morikawa (1982) used this technique in a horizontal multiphase pipe flow with an inner diameter of 30 mm. The authors discovered that different particle sizes had different impacts on the flow turbulence, with larger particles enhancing it and smaller particles attenuating it. Tsuji et al. (1984) also conducted studies utilising this technology for vertical pipes. Air-solid two-phase flows were used in both these LDA-based experiments. The authors again found that larger particles increased turbulence whereas smaller particles flattened the mean fluid velocity profile. Additionally, they also discovered that for medium-sized particles, simultaneous turbulence increase and attenuation were seen in different sections of the pipe flow. The advantage of laser Doppler velocimetry is associated with its extremely high spatial and temporal resolution. Also, it is a non-intrusive measurement with no need for calibration, resulting in low errors in velocity measurements.

Particle image velocimetry is a more recent, widely utilised technology for investigating multiphase flows that again uses a non-intrusive laser optical measurement. The displacement of particle tracer images are measured to determine the velocity distribution. This method relies on digital image processing. PIV has evolved to be the dominant technique for use in complex turbulent flow experiments as more data processing power has become available. An extension to PIV is holographic particle image velocimetry (HPIV). This is a high spatial resolution three-dimensional velocity profile capturing technique.

2.4.2 Experimental studies in pipes

In the late 1970s, Zisselmar and Molerus (1979) studied undisturbed suspension pipe flows close to the wall using laser doppler anemometry with a mean particle diameter, $d_p = 53\ \mu m$, and solid-phase concentration below 5.6%. Their experimental study concluded that solid particles at this volume fraction have a significant effect on the intensity of the turbulence. The solid particles either increase or dampen the intensity of turbulence, based on the concentration and wall distance. Their experimental study also demonstrated how fluid-particle interaction can be used to interpret heat transfer modifications, and this was applied to further understand the turbulent heat transfer process. In particular, they observed a strong increase of

turbulence at the location which the maximum heat transfer was reached (Zisselmar and Molerus, 1979).

Den Toonder et al. (1997) investigated drag reduction by polymer additives in turbulent pipe flow. They carried out both experimental and direct numerical simulation investigations. In their DNS work, a constitutive equation which was based on Batchelor's theory and Maxwell's model was implemented to understand the effect of polymers. The Maxwell model is an extension to the constitutive equation with an elastic component. They also carried out laser Doppler velocimetry experiments using a periodic (re-circulating) condition using a very dilute polymer solution (20 wppm), Superfloc A110 in water. The mean, variance, skewness, kurtosis and power spectra of the velocity profiles was measured and they compared the results with similar friction velocity turbulent flows at a shear Reynolds number $Re_\tau \cong 1035$. According to their research, the viscoelastic polymer model demonstrated less drag reduction, indicating that elastic effects have an adverse impact on it.

Other experimental multiphase simulations in pipes includes that of Varaksin (2000) who studied the effect of particle concentration using glass particles with a mean diameter of $d_p \cong 50$ μm, and Choi and Chung (1983) who conducted a gas-solid flow in a fully developed pipe, extending Prandtl's mixing length model to include first-order closure and predicted velocity fields, as well as friction factors.

Table 2.2: Summary of particle-laden turbulent wall-bounded flow experimental studies.

Geometry	Method	Particle properties, d / μm	Bulk Reynolds number, $\mathbf{Re_B \times 10^3}$	Reference
Pipe flow(s)	HWA	–	50 – 500	Laufer (1954)
	–	0.8 – 2.63, brass/iron	2	Friedlander and Johnstone (1957)
	–	19.5 – 48.5 pollen, etc.	4 – 60	Forney and Spielman (1974)
	–	–	10 – 50	Liu and Agarwal (1974)
	LDV	100 – 800, glass	N/A	Lee and Durst (1982)
		200, 3400, plastic	$Re_+ = 470$	Tsuji and Morikawa (1982)
		200, 3400, plastic	16 – 32	Tsuji et al. (1984)
	PDA	30-100, glass	5.3	Caraman et al. (2003)
		90, 270, and	134 – 3 9	Gillies et al. (2004)
		60-90, glass	5.3	Borée and Caraman (2005)
Duct flow(s)	LDA	–	42	Melling and Whitelaw (1976)
	HWA	–	53 – 107	Aly et al. (1978)
	LDA	–	250	Gessner et al. (1979)
		–	3.5	Cenedese et al. (1991)
		–	3.5	Cenedese et al. (1992)
	HPIV	3 – 15, tracers	123	Zhang et al. (1997)
	HPIV	20, tracers	120	Tao et al. (1999)
	MPS-3		15	Gnanamanickam et al. (2013)
	LDV	–	1.203 – 2.205	Owolabi et al. (2016)
Channel flow(s)	HWA	–	50	Tracy (1965)
	HFA	–	5.6 – 8.2	Eckelmann (1974)
		–	7.7	Kreplin and Eckelmann (1979)
	PIV	60, polythene	6.385	Li et al. (2012)

2.4.3 Experimental studies in ducts and channels

Compared to simulation-based studies, significantly less experimental research on particle-laden flows in duct and channel geometries has been performed, with the majority of such work focused on pipe and tube geometries. Alexander and Coldren (1951) carried out one of the earliest experiments on particle-laden duct flows where they investigated droplet transfer from air flows to duct walls. Friedlander and Johnstone (1957) evaluated concentrations of depositing particles on the inner surface of glass and brass tubes to investigate particle-laden turbulent flows. Section 2.3.3 describes additional work on deposition-related experiments. Table 2.2 summarises the major experimental studies performed in wall-bounded flows.

2.4.4 Numerical studies in pipes

Uijttewaal and Oliemans (1996) studied the motion of a dense, dispersed particle-phase in a vertical turbulent pipe flow. The single-phase was simulated at three different Reynolds numbers, $5300, 18300$ and 42000 using both DNS and LES techniques. This study demonstrated that LES is a viable alternative approach to study dispersed systems. Their simulation results suggested that it is possible to predict experimental two-phase flows characteristics using numerical simulations.

Rani and Vanka (2000) performed DNS to investigate two-way coupling effects in particle-laden turbulent pipe flows at a shear Reynolds number, $Re_\tau \cong 360$, volume fraction, $\phi_p = 6.84 \times 10^{-5}$ and particle sizes, $d_p^+ = 0.432, 0.648, 0.864$, based on the shear length scale. The Eulerian method was used to solve the continuous phase while the dispersed phase was modelled using LPT. The Navier-Stokes equations were solved using a second-order, finite-volume technique. In this study, only the drag force was considered in the particle equation of motion which was solved using a fourth-order Runge-Kutta method. Their study has shown that the longitudinal energy spectra exhibits a high degree of turbulence in the radial direction close to the pipe centre.

In 2002, Portela et al. (2002) studied near-wall behaviour of small, heavy particles in a cylindrical geometry using the one-way point-particle LPT method. Fluid-particle and particle-particle interactions were neglected in this study. Their results indicated that elastic-bouncing walls produced different behaviour than absorbing ones. The researchers also observed that near to the wall, the radial particle-velocity is correlated with the local particle concentration.

Rani et al. (2004) performed simulations at shear Reynolds number, $Re_\tau \cong 360$, based on the friction velocity, u_τ, pipe diameter, D, and pipe length, $L = 5D$. In this study, various particle response times, τ_p, volume fractions, ϕ_p, and particle settling velocities were considered. The Navier-Stokes equations were solved using a finite-volume technique. In the circumferential and axial directions, a periodic boundary condition was used, and in the radial direction a no-slip boundary condition was deployed. The numerical simulations were conducted with and without gravity. The mean and RMS velocity profiles and turbulence kinetic energy budget were discussed. According to their findings, when particles are not gravitationally influenced,

changes in either the volume fraction or the response time have relatively little impact on the fluid streamwise mean velocity profile. The present work at shear Reynolds, $Re_\tau = 360$, was validated against this study, with the results presented in Chapter 4.

Vreman (2007) performed DNS studies simulating glass-beads of 60 μm and 90 μm in a vertical air-solid pipe flow at Reynolds number 5300 based on centreline velocity, U_c and pipe diameter, D. Several cases were simulated at different volume fractions, ranging from $\phi_p = 0.5 \times 10^{-4}$ to 0.015, with two different lengths of pipe, $L = 5D$ and $L = 10D$, and particle diameters, $d_p = 60\ \mu$m and $d_p = 90\ \mu$m. Two Stokes number, $St = 4$ and 9, based on the bulk fluid timescale D/U_B were considered. The particle equation of motion was solved by a Lagrangian approach. The wall roughness was also considered in this study. The author observed that for low volume fractions the largest particle concentration occurs along the wall, but as the volume fraction increases, the concentration profile becomes more uniform, and for high volume fractions, particles accumulate towards the centre of the pipe. The present work for shear Reynolds $Re_\tau = 360$ was compared with this research, presented in Chapter 4.

Table 2.3: Summary of DNS particle-laden turbulent pipe flow studies used for validation.

Method	Pipe diameter, D / mm	Particle properties, d_P / μm	Bulk Reynolds number, $Re_B \times 10^3$	Shear Reynolds number, Re_τ	Reference
DNS	-	90	5.3	360	Rani et al. (2004)
	20	60	3.975	277	Vreman (2007)

Table 2.3 provides a summary of the multiphase work used for validation purposes in this thesis. These simulations were both conducted in cylindrical geometries using the DNS-LPT technique. Due to the lack of previous relevant research, and computational power at the time, most earlier particle-laden flow characterisation studies were carried out at low shear Reynolds number and particle concentrations.

2.4.5 Numerical studies in ducts and channels

Winkler et al. (2004) investigated particle-laden vertical duct flows at a shear Reynolds number of Re_τ = 5,810 using a fully-developed LES. The simulation was conducted using one-way coupling, so that the simulations did not account for inter-particle interactions and the particles'

influence on the carrier phase. However, the force contributions from lift, drag, and gravity were taken into account when predicting the motion of the particles. Probability density function (PDF) plots for the preferential concentrations of the particles, and a correlation between particle locations and low-vorticity areas, was provided. The authors went on to conduct a further study that concentrated on wall deposition (Winkler et al., 2006). They discovered that when Stokes numbers were large, average non-streamwise velocities would increase and an overall increase in deposition was also observed when compared with a pipe flow under identical Stokes and Reynolds numbers. Sharma and Phares (2006) investigated the first turbulent transport of particles in a square duct at a bulk Reynolds number of 4,410 using DNS and LPT. The authors considered only the effect of the drag force when computing the forces on the particles and observed that at higher inertia, particles were discovered to accumulate towards the wall regions and mix more effectively in these regions as a result.

Fairweather and Yao (2009) investigated particle dispersion in a turbulent duct flow at a bulk Reynolds number of 250,000. The authors considered a wide range of particle sizes from 5 to 1000 μm, and the study was performed using the LES-LPT approach. Gravity was shown to have the greatest influence on larger particles, causing deposition, while the secondary flows were determined to be the major factor responsible for smaller particle dispersion. Particle resuspension, or the migration of particles from the duct wall to the bulk flow, was also examined by Yao and Fairweather (2010), using similar parameters to those used by Fairweather and Yao (2009). Particle sizes ranged from 5 μm to 500 μm. The force contributions from lift, drag, buoyancy and gravity were taken into account when analysing the motion of the particles, and the authors demonstrated that secondary flows have significant effects on particle resuspension.

Vreman et al. (2009) used the LES approach to investigate the effect of four-way coupling in a vertical turbulent multiphase channel flow. The authors concluded that four-way coupling must be taken into account in order to accurately simulate particle phases with volume fractions of approximately $\phi_P \sim 10^{-2}$ which affirmed Elghobashi's (2007) suggestion. Additionally, in 2012, using a bulk Reynolds number, $Re_B = 11{,}900$, Breuer et al. (2012) carried out a four-way coupled LES-LPT of a turbulent channel flow. The authors provided an effective deterministic search technique that lowers the computational time from $O(N_P^2)$ to $O(N_P)$ for

interparticle collisions, for number of particles N_P. An illustration of this search algorithm which is also used in this study is provided in Chapter 3.

In order to predict collisions and agglomeration in an LES of a turbulent channel flow, Njobuenwu and Fairweather (2017) deployed a deterministic approach. The authors incorporated the van der Waals force and energy-balance based agglomeration condition. They conducted parametric simulations on the effect of the restitution coefficient, $e_n = 0.2$ to 0.8, particle size, $d_p = 60$ to 316 μm, shear Reynolds number, $Re_\tau = 150$ to 590, and particle concentration, 5×10^{-4} to 5×10^{-3}, on the predictions. They observed an increase in aggregation with decreasing restitution coefficient, and that collisions amongst smaller particles were most frequent and efficient in forming agglomerates. Particle-particle interactions also showed a strong dependency on the Reynolds number, with increases in particle concentration enhancing agglomeration.

Table 2.4: Summary of particle-laden turbulent wall-bounded flow simulation studies.

Geometry	Methods	Coupling / Particle properties, d_p / µm	Bulk Reynolds number, $\mathbf{Re_B}$ / $\mathbf{10^3}$	Reference
Pipe	DNS	1W	$Re_\tau = 337$	Marchioli et al. (2003)
		–	7	Eggels et al. (1993)
	LES/DNS	1W	$5.3 - 42$	Uijttewaal and Oliemans (1996)
	RANS	2W	10	Adams (2011)
	DNS	–	$5.3 - 61$	Boersma (2011)
		–	$Re_\tau = 180 - 1000$	El Khoury et al. (2013)
Duct	LES	–	5.81	Madabhushi and Vanka (1991)
	DNS	–	4.41	Gavrilakis (1992)
	LES	–	49	Su and Friedrich (1994)
		1W	$Re_\tau = 360$	Winkler et al. (2004)
		1W, 5-1000 µm	250	Fairweather and Yao (2009)
	DNS	1W drag only	$Re_\tau = 300$	Sharma and Phares (2006)
		–	$Re_\tau = 600$	Zhu (2009)
	LES	1W, 5-500 µm	250	Yao and Fairweather (2010)
Channel	DNS	4W	70	Li et al. (2001)
		1W ellipsoidal	8	Zhang et al. (2001)
		1W	$Re_\tau = 150$	Marchioli and Soldati (2002)
		–	$Re_\tau = 100 - 300$	Morinishi and Tamano (2005)
		1W	$Re_\tau = 150 - 300$	Marchioli and Soldati (2007)
		1W ellipsoidal	$Re_\tau = 360$	Mortensen et al. (2008)
	LES	4W high ϕ_P	–	Vreman et al. (2009)
	DNS	1W fibres	$Re_\tau = 150$	Marchioli et al. (2010)
		2W	$Re_\tau = 180$	Zhao et al. (2010)
	DNS/LES	2W	125	Zamansky et al. (2011)
	LES	4W	11.9	Breuer et al. (2012)
		4W with agglomeration	11.9	Breuer and Almohammed (2015)
	DNS	4W	$Re_\tau = 150$	Kuerten and Vreman (2015)
		2W	$Re_\tau = 180$	Lee and Lee (2015)
		1W non-spherical	$Re_\tau = 300$	Njobuenwu and Fairweather (2015a)
	DNS/LES	4Wnon-spherical	42.585	Van Wachem et al. (2015)
	DNS	4W	$Re_\tau = 642$	Vreman (2015)
		4W	$Re_\tau = 150$	Zhao et al. (2015)
	LES (with neural network)	–	$Re_\tau = 160 - 610$	Prat et al (2020)

Mortimer et al. (2020) extended the Njobuenwu and Fairweather (2015b) deterministic model for DNS. The authors investigated particle-particle agglomeration using a fully coupled turbulent channel flow simulation at shear Reynolds number, $Re_\tau = 180$. They also studied the effect of particle size, $d_p = 202, 286$ and 405 μm at a fixed volume fraction, $\phi_P = 10^{-3}$ and a number of injected primary particles of 109,313. Their findings show that collision rates rise with particle size at a certain particle number but remain similar for all particle sizes at a set volume fraction. They also observed that smaller particles tend to agglomerate faster to form bigger particles more quickly, and an that increased collision occurrences were observed close to the walls.

The model developed by Njobuenwu and Fairweather (2015b) which was extended by Mortimer et al. (2020) for DNS was used in the present research. As part of this research, the model has been altered for the pipe geometry, with the full DLVO theory incorporated. Behavioural modification techniques are investigated by modifying key parameters of interest in order to obtain a desired flow property.

Table 2.4 provides a summary of the key numerical particle-laden turbulent wall-bounded flow studies performed to date.

2.5 Particle deposition

Pakzonka et al. (1981) reviewed the effects of solid concentration and particle size on depositing flows using three different pipe diameters, $D = 50.8$ mm, 103 mm and 202 mm. The authors claim that the deposition velocity exhibits a concentration-dependent maximum and starts to decline above approximately 15% by solid phase volume fraction. They also observed that the presence of fine particles (< 75 μm) has a substantial impact on deposition velocity reduction for larger concentrations.

A numerical simulation was performed by Ekambara et al. (2009) to investigate the behaviour of solid-liquid, slurry flow in a pipe using the commercial computational fluid dynamics code, ANSYS-CFX. This simulation was conducted using high particle-fluid volume fractions, $\phi_p = 8\% - 45\%$, with particle sizes ranging from, $d_p = 90$ μm to 500 μm, bulk velocities, $U_B = 1.5 - 5.5$ m s^{-1}, and pipe diameters, $D = 50 - 500$ mm. The authors claim that the CFD model developed could predict particle concentration profiles for smaller particle slurries. Solid

concentration profile-dependent variables were also investigated such as velocity, pipe diameter, particle size and pressure drop. They noted that the distribution of the particles in the vertical plane is uneven, with the degree of asymmetry rising with increasing particle size, according to the experimental and numerical simulation data. In addition, they discovered that concentration profiles depend solely on the volume fraction of in situ solids for particles that are sufficiently large.

Rice (2020) investigated the behaviour of suspensions of solid particles using different particle species. Small and large glass, and small and large plastic, particles were considered. Using ADV, the critical deposition velocity of particles was established through experiments that investigated their resuspension from a particle bed. The particle concentration was measured using acoustic attenuation. The author considered four different particle types to determine the critical deposition velocity. The four particle species (with particle diameter d_P) were Honite-16 (large glass, $d_P = 41$ μm), Honite-22 (small glass, $d_P = 77$ μm), Guyblast 40/60 (small plastic, $d_P = 468$ μm) and Guyblast 30/40 (large plastic, $d_P = 691$ μm). For all particle species considered, the experiments were conducted at volume fractions $\phi_p = 0.5\%, 1\%$ and 3%, with an inner diameter of the pipe, $D = 42.6$ mm. These nominal concentrations were plotted against their respective critical velocity results. The author suggested that one can evaluate the deposition velocity from either resuspension or deposition experiments.

To test the author's contention, in present work, an empirical correlation was developed based on Rice's (2020) experimental resuspension datasets in conjunction with other available resuspension and deposition datasets. A dimensional analysis was then performed to collapse the resuspension and deposition data into a single empirical correlation. The DNS-LPT and LES-LPT codes developed were then tested in terms of their ability to predict critical deposition velocities. Further details are given in Chapter 6.

2.6 Numerical simulation

Conventional CFD and the lattice Boltzmann method (LBM) are two popular methods for simulating fluid flows, each having their own set of benefits and drawbacks. In some flow regimes, such as high Reynolds number flows or flows with intricate boundary conditions, CFD methods, particularly since they rely on directly solving the Navier-Stokes equations, can provide greater accuracy. Even though LBM is effective, it might not be able to fully capture some of the most important physics associated with these flow. In order to precisely represent turbulent flows in simulations, CFD offers a large variety of turbulence models and simulation approaches. LBM has the ability to simulate turbulence; however, creating and utilizing turbulence models inside the LBM framework can be more difficult. Because it is more frequently used in both industry and by academics, CFD methods have also been around for longer and are more highly developed. This has led to the availability of numerous well-known, feature rich, and supported commercial and open-source CFD software programs. Although LBM is becoming more and more popular, there are not as many well-developed software solutions.

In numerous scientific and engineering applications, a numerical technique known as the discrete element method (DEM) is utilized to simulate the behaviour of granular materials, such as particles. It enables the investigation of the interactions and motions of individual particles within a system by modelling each one as a separate entity, although it must be coupled with a fluid flow solver in order to predict particle-laden flows. We have opted to use a widely accessible DNS solver because the research described in this thesis heavily depends on our ability to comprehend the physics at micro-particulate sizes. Nek5000, a CFD code with good scaling for parallel processing and great accuracy, was accordingly selected. The reason for this is that a wide variety of Reynolds numbers have been studied in depth in the past, allowing the results to be appropriately validate against other solutions. The LPT algorithm, which was developed in-house, was used to precisely simulate particles within the multi-phase fluid flow. This approach was adopted, rather than DEM, because of the latter's high computational cost, which limits the number of particles that can be studied, and the requirement of a relatively coarse CFD numerical solution grid since DEM particles must fit within the fluid elements.

2.7 Conclusions

In this chapter, single-phase and multiphase flow studies within the literature have been reviewed and summarised, with the major findings identified and discussed. It is apparent that very little DNS has been performed to investigate turbulent pipe flows at moderately high Reynolds numbers, and even less in the presence of an additional particulate phase.

In the past, multiphase DNS investigations have been performed in the main with only one-way coupling between the particles and the fluid, and at low Reynolds numbers. There is also a noticeable absence of four-way coupled simulations (i.e. both particle-fluid and particle-particle interactions taken into account) especially when combined with particle agglomeration DNS-based work in cylindrical geometries is more common, but four-way coupling and agglomeration are again neglected despite most industrial scale systems exhibiting both collisions and aggregation due to high volume fractions. Further, very few previous studies have considered particle deposition in such flows, and simulation of critical deposition velocities. As computational power advances it is now possible to perform such particle-laden flow simulations. The effects of particles on the fluid, interparticle collisions and particle agglomeration in turbulent pipe flows at moderately high Reynolds numbers are therefore investigated with the emphasis placed on the analysis of results to determine particle dispersion, collision and agglomeration, as well as particle deposition out of the flow and the formation of solid beds and dune-like structures.

In addition, behavioural modification effects such as changes in temperature, ionic strength and pH of the liquid phase, as well as particle coating and polymer addition to the flow, have not been studied in any detail in the past, with no applications to date in practically relevant cylindrical geometries. This is another identified gap in the literature which will be considered through numerical simulations.

3 RESEARCH METHODOLOGY

3.1 Introduction

This chapter provides an overview of the research methodologies used to perform the simulations within this thesis. The governing equations for simulating both the continuous phase (the Navier-Stokes equations), and the particulate phase (through Lagrangian particle tracking) are considered in detail, along with the appropriate simulation domain setup, initial conditions and boundary conditions.

3.2 Fluid phase modelling

3.2.1 Navier-Stokes equations

The laws of conservation of energy, momentum and mass for a small volume of fluid are applied in order to derive the governing Navier-Stokes equations. In this study, all simulations are performed under the assumption that the fluid is Newtonian and incompressible, i.e., the density does not change as the pressure changes along the pipe. For a pressure-driven, incompressible flow within a long, straight pipe of circular cross-section with an internal diameter, D, the time-dependent governing equations, expressed in Cartesian form, can be derived. Assuming that mass is conserved within a small control volume, we obtain:

$$\frac{d\rho}{dt} + \rho\left(\frac{\partial u}{\partial x} + \frac{\partial v}{\partial y} + \frac{\partial w}{\partial z}\right) = \frac{d\rho}{dt} + \rho(\nabla \cdot \boldsymbol{u}) = 0. \tag{3.1}$$

While the density, ρ, is constant, $d\rho/dt = 0$. Hence, for incompressible flow the continuity equation can be simplified to:

$$\rho(\nabla \cdot \boldsymbol{u}) = 0, \tag{3.2}$$

where, $\nabla \cdot \boldsymbol{u}$ is the sum of $\frac{\partial u}{\partial x}, \frac{\partial v}{\partial y}, \frac{\partial w}{\partial z}$, i.e., the partial differential of the velocity field in the x, y and z directions respectively. Eq. (3.2) ensures that mass is conserved. Applying the same logic to the conservation of momentum, we obtain that:

$$\rho \frac{d\boldsymbol{u}}{dt} = m\boldsymbol{a} = f_{total} = f_{body} + f_{surface}, \tag{3.3}$$

with m the mass of the fluid control volume and $\boldsymbol{a}$ the local fluid instantaneous acceleration. One can expand the full derivative, $\frac{d\boldsymbol{u}}{dt}$, using chain rule to obtain $\frac{\partial \boldsymbol{u}}{\partial t} + (\boldsymbol{u} \cdot \nabla)\boldsymbol{u}$. The Navier-Stokes equation conservation of momentum component can hence be expressed as follows for constant density:

$$\frac{\partial \mathbf{u}}{\partial \mathrm{t}} + (\boldsymbol{u} \cdot \nabla)\boldsymbol{u} = -\nabla p + \frac{1}{Re_B}\nabla^2 \boldsymbol{u} + \rho \boldsymbol{g}, \tag{3.4}$$

where $Re_B = U_B D/\nu$ represents the bulk Reynolds number, U_B is the bulk flow velocity, D is the pipe diameter and ν is the kinematic fluid viscosity. Here we note that the viscous force component, $\frac{1}{Re_B}\nabla^2 \boldsymbol{u}$, scales inversely with the bulk Reynolds number. Hence, viscosity has fewer effects for flows with increased turbulence levels. The velocity vector, $\boldsymbol{u}$, is defined at Cartesian co-ordinate points (x, y, z) with velocity components (u, v, w), respectively. These unknown components are a function of both position and time. For velocity component u, the Navier Stokes equation can be expressed as follows:

$$\begin{aligned}
\rho\left\{\frac{\partial u}{\partial t} + u\frac{\partial u}{\partial x} + v\frac{\partial u}{\partial y} + w\frac{\partial u}{\partial z}\right\} &= -\frac{\partial p}{\partial x} + \mu\left\{\frac{\partial^2 u}{\partial x^2} + \frac{\partial^2 u}{\partial y^2} + \frac{\partial^2 u}{\partial z^2}\right\} \\
\rho\left\{\frac{\partial v}{\partial t} + u\frac{\partial v}{\partial x} + v\frac{\partial v}{\partial y} + w\frac{\partial v}{\partial z}\right\} &= -\frac{\partial p}{\partial x} + \mu\left\{\frac{\partial^2 v}{\partial x^2} + \frac{\partial^2 v}{\partial y^2} + \frac{\partial^2 v}{\partial z^2}\right\} \\
\rho\left\{\frac{\partial w}{\partial t} + u\frac{\partial w}{\partial x} + v\frac{\partial w}{\partial y} + w\frac{\partial w}{\partial z}\right\} &= -\frac{\partial p}{\partial x} + \mu\left\{\frac{\partial^2 w}{\partial x^2} + \frac{\partial^2 w}{\partial y^2} + \frac{\partial^2 w}{\partial z^2}\right\}
\end{aligned} \tag{3.5}$$

A solution for the unknowns (p, u, v, w) as a function of time is sought using the continuity equation, alongside appropriate initial and boundary conditions. The general form of the Navier-Stokes equations, based on the bulk Reynolds number and without the influence of other body forces is:

$$\nabla \cdot \boldsymbol{u} = 0 \tag{3.6}$$

$$\frac{\partial \boldsymbol{u}}{\partial t} + (\boldsymbol{u} \cdot \nabla)\boldsymbol{u} = -\nabla p + \frac{1}{Re_B}\nabla^2 \boldsymbol{u} \tag{3.7}$$

3.2.2 Direct numerical simulation

For fluid flow, the governing motion laws are represented by the aforementioned Navier-Stokes equations. Analytical solutions of the Navier-Stokes equations are not generally viable due to the inherent non-linearity in the partial differential equations (PDE). A viable approach in recent years to solve these equations is through numerical computation. The experimental investigation of turbulent flows is time-consuming and expensive. As discussed in Section 2, turbulent flows are chaotic and the velocity profiles fluctuate randomly, containing a range of spatial and temporal scales. Solutions (computational or otherwise) to the Navier-Stokes equations provide a thorough description of the velocity field in great detail. There is a growing body of literature that recognises the importance of DNS in solving for incompressible fluid flow, as discussed in the literature review. This computational technique solves the Navier-Stokes equation without using turbulence modelling, obtaining resolutions down to the lowest length and timescales present within such flows, the Kolmogorov scales. Despite being computationally expensive and generally only practical for small-scale flows at moderate Reynolds numbers, this approach can accurately depict a comprehensive view of the behaviour of the fluid flow. The results obtained by DNS can also support and validate the experimental research carried out in the past.

3.2.3 The Nek5000 solver

To solve the descriptive equations covered above in a DNS environment, the CFD solver Nek5000 has been used. This solver is based on the spectral element method and employs a high-order weighted residual technique. Nek5000 is favourable due to its high accuracy and low numerical dispersion and dissipation and is easily and efficiently parallelisable. It was developed by Fischer et al. (2008) and has been used widely throughout the DNS literature in recent decades (e.g. El Khoury et. Al, 2013; Njobuenwu and Fairweather, 2015b; Njobuenwu and Fairweather 2017; Mortimer et al., 2020).

Nek5000 solves the Navier-Stokes equations in non-dimensional form. Below, the non-dimensional variables are defined which are used to obtain the non-dimensional version of the Navier-Stokes equation in Nek5000:

$$\boldsymbol{x}^* = \frac{\boldsymbol{x}}{D},\ \boldsymbol{u}^* = \frac{\boldsymbol{u}}{U_B},\ t^* = \frac{t}{D/U_B},\ p^* = \frac{p}{\rho {U_B}^2}. \tag{3.8}$$

Using the above, Eqs. (3.6) and (3.7) can be non-dimensionalised as follows:

$$\nabla \cdot \boldsymbol{u}^* = 0 \tag{3.9}$$

$$\frac{\partial \boldsymbol{u}^*}{\partial t^*} + (\boldsymbol{u}^* \cdot \nabla)\boldsymbol{u}^* = -\nabla p^* + \frac{1}{Re_B}\nabla \cdot \boldsymbol{\tau}^* + \boldsymbol{f}_i \tag{3.10}$$

Here, $\boldsymbol{u}^*(\boldsymbol{x}^*, t^*)$ is the fluid velocity vector, non-dimensionalised using the bulk velocity, U_B, and the position vector, $\boldsymbol{x}^*$, and time, t^*, are non-dimensionalised as $x^* = \frac{x}{D}$ and $t^* = \frac{t}{D/\mathrm{u_b}}$, respectively. The term p^* is the non-dimensionalised pressure for high-velocity flows, with $p^* = \frac{p}{\rho {U_B}^2}$. The bulk Reynolds number Re_B is already non-dimensional and defined as $Re_B = U_B D/\nu$. Finally, $\boldsymbol{\tau}^*$ is the non-dimensionalised stress tensor, $\boldsymbol{\tau}^* = \nabla \boldsymbol{u}^* + \nabla {\boldsymbol{u}^*}^T$, and f_i is a generic body forcing term, in the context of pipe flows representing both the driving pressure gradient and the two-way interaction between the fluid and the particles, detailed later.

Equations (3.9) and (3.10) are solved numerically using the spectral element method along with appropriate boundary conditions. In three-dimensional space, these equations are discretised as grid points by the Lagrange-Galerkin approximation method. N^{th}-order Lagrange polynomial interpolants on Gauss-Lobatto-Legendre (GLL) points are implemented as a basis for velocity space, and Lagrangian interpolants of order N-2 on Gauss-Legendre quadrature points are employed for pressure space.

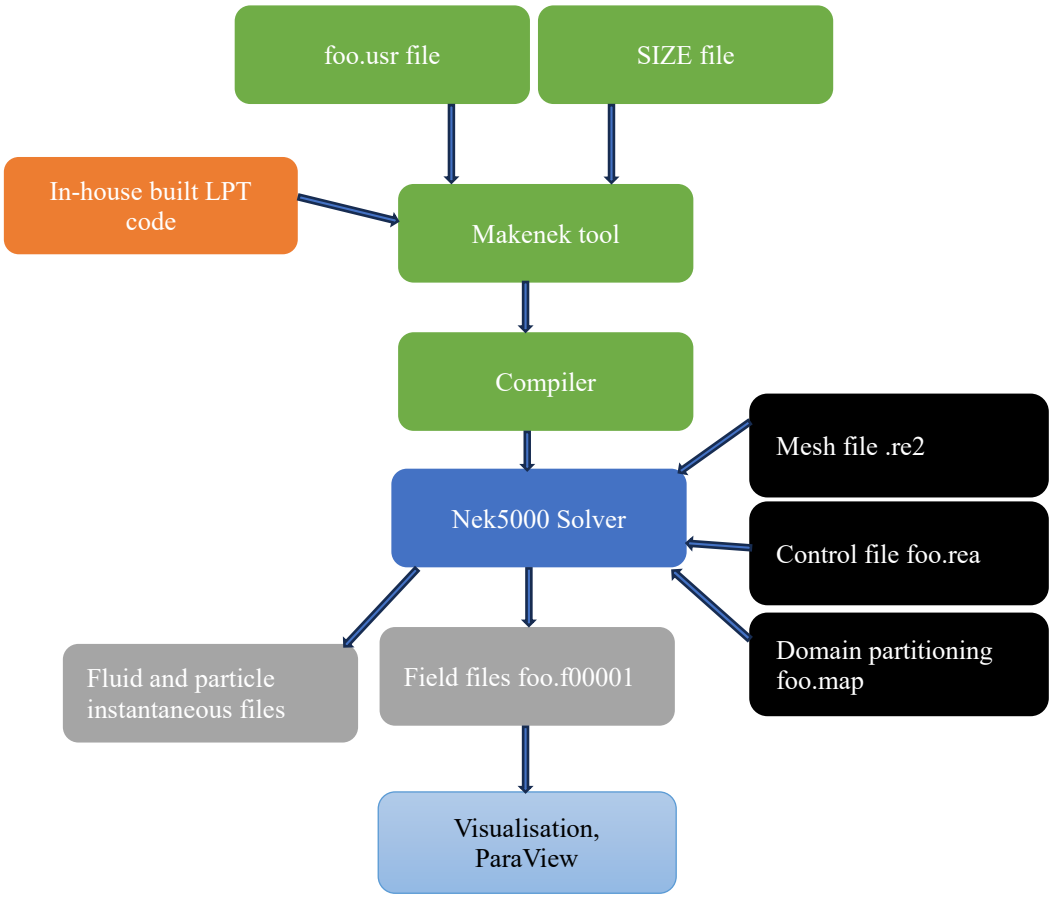

Figure 3.1: Nek5000 solver and LPT code overview.

The setup and solver process is as follows. As shown in Fig. 3.1, the foo.usr file, the foo.rea file, and SIZE files are the three main components for each simulation. A user-defined set of FORTRAN subroutines are contained in the foo.usr file. These include functions such as boundary and initial conditions, variable properties, forcing functions for the fluid and/or particle phases, geometry initialisation, as well as user-defined ad hoc subroutines. The foo.rea file is used to adjust runtime characteristics such as the Reynolds number, density, viscosity, number of timesteps, flow rate and restart conditions. This file also contains the mesh and boundary condition data. The primary parameters for allocating static memory are defined in the SIZE file.

The incompressible fluid flow solver, Nek5000, does not provide a three-dimensional (3D) mesh generator for complex domains. For the simulations performed in this thesis, the 3D spectral element mesh was generated by extruding a two-dimensional (2D) circular mesh by using the tool, preNek. Once the code was compiled, a recursive spectral bisection technique

was utilised to partition the flow domain. This generates the foo.map file with the correct processor decomposition.

3.2.4 Pipe flow domain

The computational domain consisted of a circular pipe of diameter, D, and characteristic length, L=$12.5D \approx 4\pi D$, partitioned into 36,576 spectral elements. Within each element, the velocity is represented by high-order tensor-product Gauss–Lobatto–Legendre (GLL) polynomial expansions of order *N*. The flow in the streamwise direction was driven by a prescribed pressure gradient term in Eq. (3.10). The shear Reynolds number, based on the shear velocity, was used to characterise each pipe flow studied. In the present work, $Re_\tau \approx$ 277, 360 and 720 turbulent flows were studied. The spectral elements method is a high-order weighted residual technique that splits the domain into several hexahedral subdomains or elements that comprise the entire system. For all simulations, the same mesh topology and number of spectral elements was used, ensuring sufficient elements such that the Kolmogorov scale conditions required for DNS were met. GLL quadrature points ($N = 7$, which corresponds to 8^3 grid-points per element) were used to distribute the vertices in each element. Periodic boundary conditions were applied in the streamwise direction, and no-slip conditions at the wall for the radial velocity components. The total number of elements and equivalent GLL grid points used for the DNS simulations are given in Table 3.1 while Figure 3.2 illustrates the mesh topology implemented in all simulations. In Chapter 6, the LES method is used with the same computational mesh to investigate particle deposition in flows with bulk Reynolds numbers ranging from 11,700 to 600,000.

Table 3.1: The present turbulent pipe flow fluid phase configuration.

Re_B	Re_τ	Elements	GLL grid points
3,975	277	36,576	18,726,912
5,300	360	36,576	18,726,912
11,700	720	36,576	18,726,912

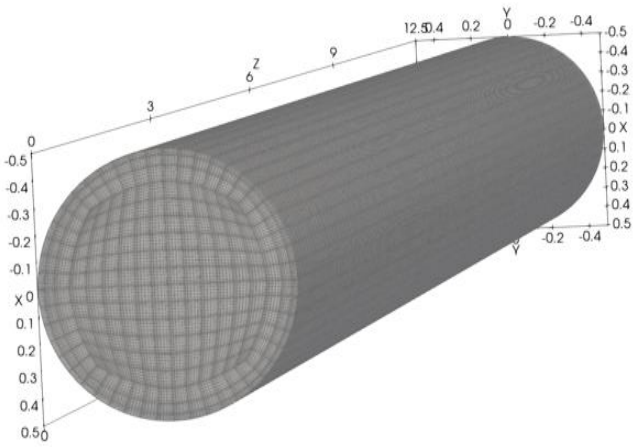

Figure 3.2: The computational mesh topology with Gauss–Lobatto–Legendre quadrature points (N = 7) for all simulations.

3.2.5 Extensions to the DNS and LPT solvers

An in-house developed LPT code was used in conjunction and interfaced with the Nek5000 core fluid solver (Njobuenwu and Fairweather 2017; Mortimer et al., 2020), further details of which are given below. This code has been validated and employed by multiple researchers within the University of Leeds and other collaborative institutions. It is now a well-established algorithm used in a variety of studies in channel and duct flows. For this project, the LPT algorithm was extended for cylindrical geometries. Given that the LPT algorithm for the pipe and its topology were created specifically for this project, validation and testing were required. Intensive unit, integration, system, and acceptance (validation) tests were performed and are reported in Chapter 4 and Chapter 6. Two LPT modules were also developed and deployed from scratch, one for injecting particles randomly throughout the computational domain and the other for determining particle collisions with the wall using projection vectors and dot products. This is described in more detail in Section 3.3.8. Furthermore, the LPT code was extended to include the full DLVO (Derjaguin and Landau, 1941; Verwey and Overbeek, 1955) theory. This is the first study to investigate electric double layer repulsion in a pipe geometry using a deterministic inter-particle agglomeration model. The LPT code includes modules for particle statistics input, advection, particle-fluid coupling and inter-particle collision and agglomeration.

3.2.6 Large eddy simulation

Large eddy simulation employs a low-pass filter to exclude the smallest turbulence scales from the Navier-Stokes equations, thereby lowering the computational cost of a simulation while keeping the most relevant flow details by focusing primarily on large, energy containing turbulence structures. A filtered version of the Navier-Stokes equations is then solved, and a sub-grid scale model is used to estimate effect of the filtered-out turbulence scales on the resolved scales. This corrects model solutions for not explicitly resolving the small scales (Smagorinsky 1963). This entails taking advantage of the fact that the smallest length scales in most flows are isotropic, as opposed to the anisotropic large-scale motions. Although such simulations are not as precise as when solving the full Navier-Stokes equations directly over all length and time scales, as in DNS, the LES approach nevertheless offers more accurate flow information than the RANS method. The Nek5000 algorithm was utilised for all LES simulations which were employed for high Reynolds number flows which could not be feasibly performed using DNS. One of the key features of this algorithm is its ability to handle unstructured meshes which can incorporate a variety of turbulent flow simulation and modelling approaches such as LES. A detailed description of Nek5000 method is given in Section 3.2.3.

The dynamic sub-grid scale stress model of Germano et al. (1991) was employed in this study. For the implementation of the SGS stress model, the approximate localisation approach of Piomelli and Liu (1995) was adopted.

3.3 Particle phase modelling

To investigate the bulk behaviour of high concentration dispersions of particles within turbulent pipe flows, a Lagrangian particle tracker was developed, capable of modelling large quantities of dispersed, spherical solids which runs concurrently with Nek5000. A fourth-order Runge-Kutta method was also implemented to solve the Newtonian equation of motion for each particle at every time-step. The derivation of all the forces implemented in the particle equation of motion is discussed in this section.

To initialise the computations, particles were injected at random positions within the fully developed fluid flow domain and assigned the fluid velocity at that location. Figure 3.3

illustrates the randomly injected particles and the assigned velocity upon injection. Particle collisions with the pipe wall were considered to be elastic, i.e., the total kinetic energy remains the same before and after the collision. Periodic boundary conditions were applied at the extremes of the streamwise direction and no-slip conditions at the wall at a radial distance $r^* = 0.5$. Statistical data was gathered for analysis a certain response times ($t^* = 20$) to allow the particles to adjust to the surrounding fluid. The algorithm for performing particle collisions with the wall is explained in detail in Section 3.3.8.

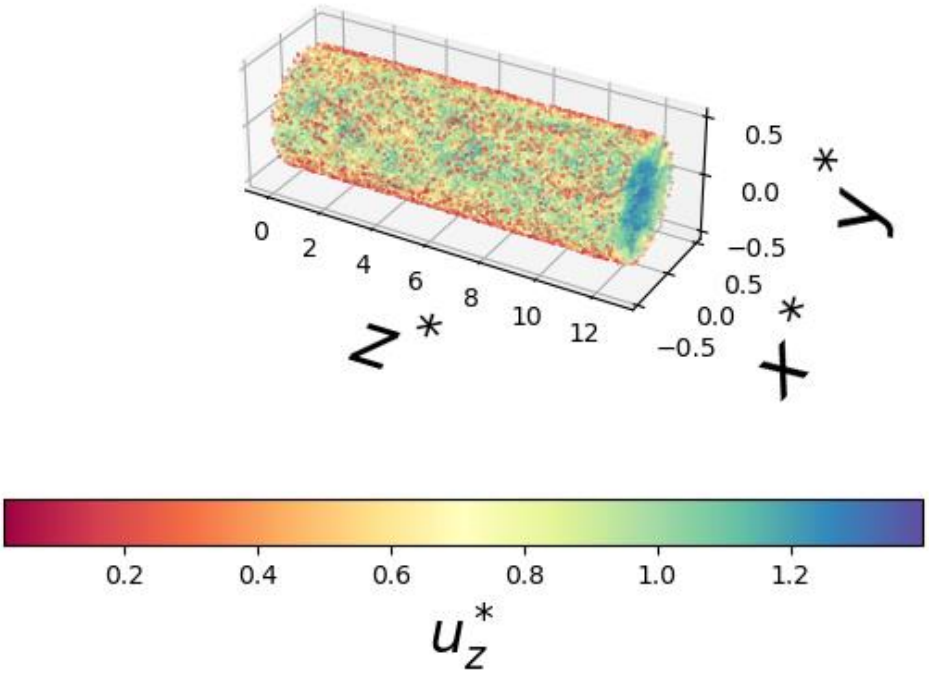

Figure 3.3: A 3D instantaneous plot of particle positions after injection. The colour represents the particle streamwise velocity. Particles are injected at a random position within the fully developed fluid flow domain and assigned the instantaneous local fluid velocity at that location, interpolated spectrally.

3.3.1 Particle equations of motion

The particle equation of motion for all forces considered in the flows encountered in this study is described below. For the work presented in this thesis, a modified Maxey and Riley (1983) equation is used. The particle equation motion in the turbulent flow is obtained by solving Newton's second law of motion for each spherical particle. Equation (3.11) is the sum of all the forces applied in the force equation:

$$\sum \boldsymbol{F}_N = \boldsymbol{F}_D + \boldsymbol{F}_G + \boldsymbol{F}_L + \boldsymbol{F}_V + \boldsymbol{F}_P + \boldsymbol{F}_A. \tag{3.11}$$

Here, $\boldsymbol{F}_N$ is the sum of all hydrodynamic and body forces on each particle. $\boldsymbol{F}_D$ is the drag force, $\boldsymbol{F}_G$ the gravitational/buoyancy force, $\boldsymbol{F}_L$ the lift force, $\boldsymbol{F}_V$ the virtual added mass force, $\boldsymbol{F}_p$ the pressure gradient force and $\boldsymbol{F}_A$ represents any additional forces present. In Nek5000, equations are solved in non-dimensional form. As such, each component of the particle equation needs to be converted, such that the solver deals with solely non-dimensional variables for both the fluid and particle phase. The particle Stokes numbers, representing the ratio of the particle time scale to a particular fluid timescale, based on the bulk and shear velocities, are given by Eqs. (3.12) and (3.13), respectively:

$$St_B = \frac{\tau_p}{\tau_{f,B}} = Re_B \frac{\rho_p^* {d_p^*}^2}{18 f_D} \tag{3.12}$$

$$St_\tau = \frac{\tau_p}{\tau_{f\,\tau}} = Re_\tau^2 \frac{\rho_p^* {d_p^*}^2}{18 f_D} \tag{3.13}$$

Here, f_D is the non-dimensional Stokes drag function, which is defined below and, using Eqs. (3.12) and (3.13), one can obtain the following expression:

$$\frac{St_\tau}{St_B} = \frac{Re_\tau^2}{Re_B} \tag{3.14}$$

The LPT solves a force-balance equation for each particle in the system, represented as an impenetrable computational sphere under the assumption of point particles. The particle equations of motion for all forces considered are presented in Eqs. (3.15) and (3.16), such that the non-dimensional form of the equations of motion for spherical particles, as implemented in the simulations, is:

$$\boldsymbol{u}_p^* = \frac{\partial \boldsymbol{x}_p^*}{\partial t^*} \tag{3.15}$$

$$\frac{\partial \boldsymbol{u}_P^*}{\partial t^*} = \frac{1}{M_{VM}} \left[\underbrace{\frac{3 C_D |\boldsymbol{u}_s^*|}{4 d_p^* \rho_P^*} \boldsymbol{u}_s^*}_{Drag} + \underbrace{\frac{1}{Fr}\left(1 - \frac{1}{\rho_p^*}\right) \widehat{\boldsymbol{g}^*}}_{\text{Gravity}} + \underbrace{\frac{3}{4} \frac{C_L}{\rho_P^*} (\boldsymbol{u}_s^* \times \boldsymbol{\omega}_F^*)}_{Lift} + \underbrace{\frac{1}{2\rho_P^*} \frac{D' \boldsymbol{u}_F^*}{D t^*}}_{Virtual\ Mass} + \underbrace{\frac{1}{\rho_P^*} \frac{D \boldsymbol{u}_F^*}{D t^*}}_{Pressure\ Gradient} \right] \tag{3.16}$$

In Eqs. (3.15) and (3.16), $\boldsymbol{u}_p^*$ is the particle velocity vector, $\boldsymbol{x}_p^*$ the particle position vector, C_D the drag coefficient, and $\boldsymbol{u}_s^*$ the slip velocity given as $\boldsymbol{u}^* - \boldsymbol{u}_p^*$. Also, Fr is the Froude number, defined as $\mathrm{F}r = u_b^2/gD$, where g is gravitational acceleration and $\underline{\widehat{g^*}}$ is a unit vector in the direction of gravitational attraction. The term, $\boldsymbol{\omega}_F^*$, represents the vorticity of fluid which is given by $\boldsymbol{\omega}_F^* = \nabla \times \boldsymbol{u}^*$, and the full equation is divided by $M_{VM} = (1 + 1/2\ \rho_p^*)$ to account for the virtual mass force. The drag force occurs due to particle movement through a resistive fluid phase and is the dominant force in fluid-particle flows (Schiller and Naumann, 1934), while the lift force arises due to shear across the particle. Saffman (1965) studied the strength and direction of the lift force for low particle Reynolds numbers and later Dandy and Dwyer (1990) extended this work to high particle Reynolds numbers. The virtual mass and pressure gradient forces were based on the fluid acceleration and local pressure gradient, respectively (Stokes, 1851). A gravitational force was also applied in the vertical direction in all simulations apart from validation cases. A detailed derivation of these forces is discussed below.

3.3.2 Drag force

The Stokes drag force is often the most dominant force in fluid-particle systems. For spherical particles, this can be expressed as:

$$F_D = \frac{3\rho_f m_p C_D(\boldsymbol{u}_f - \boldsymbol{u}_p)|\boldsymbol{u}_f - \boldsymbol{u}_p|}{4\rho_p d_p}. \tag{3.17}$$

Here, m_p is the particle mass, ρ_p and ρ_f are the density of the particle-phase and fluid-phase respectively, C_D is the drag coefficient, d_p is the particle diameter, and $\boldsymbol{u}_F$ and $\boldsymbol{u}_P$ are the fluid and particle-phase velocities, respectively. The particle Reynolds number, Re_p, is used to calculate the drag coefficient, C_D, which is given by:

$$Re_p = \frac{\rho_f d_p}{\mu_f}|\boldsymbol{u}_f - \boldsymbol{u}_p|, \tag{3.18}$$

with μ_f the kinematic viscosity of the fluid phase. Substituting the slip velocity, $\mathbf{u}_s$:

$$\mathbf{u}_s = \mathbf{u}_f - \mathbf{u}_p, \tag{3.19}$$

the particle Reynolds number can be written using non-dimensional variables as:

$$Re_p = Re_b \mathrm{d}_p^* \left|\mathbf{u}_p^*\right| , \tag{3.20}$$

Schiller (1934) and Clift et al. (2005) defined the Stokes drag function at different particle Reynolds number as:

$$f_D = \begin{cases} 1 & if\ 0 < Re_p \leq 0.5 \\ 1 + 0.15 Re_p^{0.687} & if\ 0.5 < Re_p \leq 1000 \\ \dfrac{0.44}{24} Re_p & if\ 1000 < Re_p \leq 250{,}000 \end{cases} . \tag{3.21}$$

These enable us to define the drag coefficient, C_D:

$$C_D = \frac{24}{Re_p} f_D . \tag{3.22}$$

Using the above equations, the equation of motion using the non-dimensional drag force can be expressed as:

$$F_D = m_p \frac{\partial u_p^*}{\partial t^*} = m_p \frac{3 C_D |\boldsymbol{u}_s^*|}{4 d_p^* \rho_p^*} \left(\frac{U_B^2}{D}\right) \boldsymbol{u}_s^* , \tag{3.23}$$

If we consider only the drag force, we obtain the following equation of motion:

$$\frac{\partial u_p^*}{\partial t^*} = \frac{3 C_D |\boldsymbol{u}_s^*|}{4 d_p^* \rho_p^*} \left(\frac{U_B^2}{D}\right) \boldsymbol{u}_s^* . \tag{3.24}$$

3.3.3 Lift force

The lift force arises due to velocity gradients over the particle. Saffman (1965) studied the strength and direction of the lift force for low particle Reynolds numbers and later Dandy and Dwyer (1990) extended it to high particle Reynolds numbers. The equation can be expressed as:

$$F_L = \frac{\pi}{4}\frac{\rho_f}{2} d_p^2 \, C_L d_p(\boldsymbol{u}_f \times \boldsymbol{\omega}_f), \tag{3.25}$$

Where,

$$\mathrm{C_L} = \frac{4.1126}{\mathrm{Re_s}^{0.5}} f\left(\mathrm{Re_p}, \mathrm{Re_s}\right), \tag{3.26}$$

and $\boldsymbol{\omega}_\mathrm{f}$ is the vorticity of fluid which is defined as:

$$\boldsymbol{\omega}_f = \nabla \times \boldsymbol{u}_f \tag{3.27}$$

The local particle Reynolds number based on the vorticity is given by:

$$Re_s = \frac{\rho_f \, d_p^2}{\mu_f} |\boldsymbol{\omega}_\mathrm{f}|. \tag{3.28}$$

The coefficient for the lift force is expressed as:

$$\mathrm{C_L} = \begin{cases} \left(1 - 0.3314\beta^{\frac{1}{2}} e^{-\frac{Re_P}{10}}\right) + 0.3314\beta^{\frac{1}{2}} & 0 < Re_P \leq 40 \\ 0.0524(\beta Re_P)^{\frac{1}{2}} & Re_P > 40 \end{cases} \tag{3.29}$$

with

$$\beta = 0.5\frac{Re_s}{Re_p}. \tag{3.30}$$

Considering only the lift force the non-dimensional equation of motion can be expressed as:

$$\frac{\partial u_p^*}{\partial t^*} = \frac{3C_L}{4\rho_p^*}(\boldsymbol{u_s^*} \times \boldsymbol{\omega_f^*}). \tag{3.31}$$

3.3.4 Gravitational and buoyancy force

The force due to gravity and buoyancy upon a particle with mass, m_p, with non-dimensional density ratio, ρ_p^*, is given by:

$$F_G = \boldsymbol{g}\left(1 - \rho_p^*\right)m_p. \tag{3.32}$$

Here, $\boldsymbol{g}$ is the gravitational acceleration vector, where the direction depends on the geometry. The non-dimensional form is given as:

$$\frac{\partial u_p^*}{\partial t^*} = \frac{1}{Fr}\left(1 - \frac{1}{\rho_{\boldsymbol{p}}^*}\right)\widehat{\boldsymbol{g}} \tag{3.33}$$

where $\widehat{\boldsymbol{g}}$ is the unit vector in the direction of gravitational attraction and Fr is the Froude number which is defined as:

$$Fr = \frac{U_B^2}{|g|D} \tag{3.34}$$

The gravitational force was applied in the same direction as the fluid flow streamwise direction for the validation case simulations to predict vertical pipe flows, and in the vertical direction in all deposition runs to simulate horizontal pipe flows.

3.3.5 Pressure gradient force

The force exerted on the local fluid flow field around the particles due to differences in pressure over a given distance is given below. The fluid field motion often moves from places of high pressure to areas of low pressure when there is a variation in pressure throughout a region (Mortimer, 2019):

$$F_P = \rho_f V_p \left(\frac{D\boldsymbol{u}_f}{Dt}\right), \tag{3.35}$$

where $\frac{D}{Dt}$ is the material derivative, given by:

$$\frac{D}{Dt} = \frac{\partial}{\partial t} + u_p . \nabla, \tag{3.36}$$

which can be expressed in non-dimensional form as:

$$\frac{\partial u_p^*}{\partial t *} = \frac{1}{\rho_p^*} \frac{Du_f^*}{Dt^*}. \tag{3.37}$$

3.3.6 Virtual mass force

The virtual mass force, which is caused by the inertia of the displaced fluid and consideration of the local accelerating or decelerating fluid flow field, generates unstable forces on a submerged particle. The unstable forces given to the particle by these processes were initially discovered by Friedrich Bessel and were later quantified by Stokes (1851). This force is defined as:

$$F_V = \frac{1}{2} \rho_f V_p \left(\frac{D\boldsymbol{u}_f}{Dt} - \frac{\partial \boldsymbol{u}_p}{\partial t} \right), \tag{3.38}$$

which can be expressed in non-dimensional form as:

$$\frac{\partial u_p^*}{\partial t^*} = \frac{1}{2\rho_p^*} \frac{D\boldsymbol{u}_f^*}{Dt^*}, \tag{3.39}$$

If the simulation includes the effects of the virtual mass force, the code ensures that the added mass is divided in the full equation of motion. For simulations where the virtual mass force is negligible, the term M_{VM} in the full equation is set to unity, otherwise:

$$M_{VM} = \left(1 + \frac{1}{2\rho_p^*} \right). \tag{3.40}$$

3.3.7 Two-way momentum coupling

Studies involving the effects of two-way coupling and interparticle collisions (Elghobashi, 2007) demonstrate that modelling of the forces exerted by the dispersed phase on the

continuous phase is required at increased volume-fractions to ensure accuracy. One-way coupling is insufficient to replicate the interaction between fluid and particles at higher volume fraction, $\phi_P \geq 10^{-6}$. For two-way coupling a volume fraction of $10^{-6} \leq \phi_P \leq 10^{-3}$ is suggested. Hence, the impact of the fluid flow on the particles and the particles on the fluid flow was considered in this study. This is achieved by introducing an additional term in the Navier-Stokes equation which is given in Eq. (3.41):

$$\mathbf{f}_{2\mathrm{W}}^{*\mathrm{i}} = \frac{1}{V_i^*} \sum_{i=1}^{N} \frac{\partial \boldsymbol{u}_{p_i}^*}{\partial t^*} \tag{3.41}$$

where V_i^* is the volume of the computational cell, and i is the number of particles present in that cell (Mortimer et al. 2020).

3.3.8 Particle-wall collisions

Particle collisions with the wall are considered to be elastic, i.e., the kinetic energy remains the same. As illustrated in Fig. 3.4 (left), for a particle at position, P_i, with translational velocity, u, when a collision occurs with the wall, the normal component of the velocity is computed and then the new location of the particle. A vector projection method is applied to calculate the particle rebound velocity (Peterson, 2020). The projection vector of u onto N, $\mathrm{proj}_{\mathrm{N}}^{(u)}$, can be computed using the dot product, $\mathrm{proj}_N^{(u)} = \left(\frac{N \cdot u}{N \cdot N}\right) N = \left(\frac{N \cdot u}{|N|^2}\right) N$, which represents the normal component of the vector u. The tangential component is then $u - \mathrm{proj}_N^{(u)}$. The rebounded velocity vector, u', is finally calculated by inverting the projection vector and keeping the tangential component the same, $u' = u - 2\mathrm{proj}_N^{(u)}$.

Figure 3.4 (right) shows a single particle tracked through time. The particle is injected at the blue point, and the red dot is the final position of the particle. It is demonstrated colliding with the wall multiple times at different locations and rebounding back into the domain at the correct angle as intended.

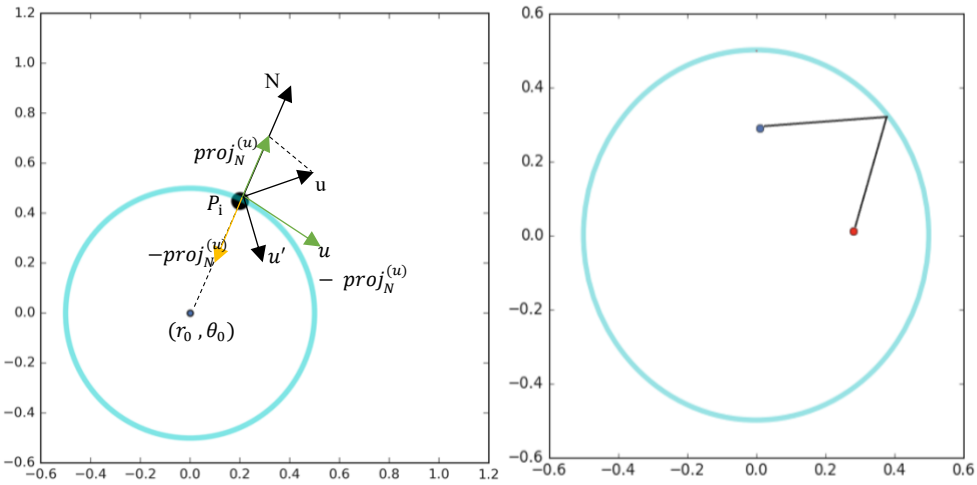

Figure 3.4: Illustration of the rebounding algorithm (left) and (right) shows a single particle colliding with the wall and bouncing back into the flow within a circular boundary.

3.3.9 Collision algorithm

The simulations were also performed four-way coupled, accounting for collisions between particles. The term four-way coupling describes how each component phase interacts in a multiphase flow – fluid-particle, particle-fluid and particle-particle interactions. The hard-sphere collision model simplifies particle collisions by assuming they are fully rigid spheres. When two particles contact in this model, their velocities change quickly in accordance with the fundamental rules of momentum and energy conservation. There are no concerns about particle deformation or collision time. In contrast, the full impulse-resolved soft-sphere model technique takes into account the particles' softness or deformability. It entails resolving the impulses exchanged during particle contact over time, while accounting for characteristics such as particle elasticity and collision duration. We utilize a hard-sphere collision model rather than a full impulse-resolved soft-sphere model in this work since we anticipate that the collision occurs much faster than the timestep. Furthermore, we assume that any other interparticle forces operating during the impact are minimal, or, in the case of agglomeration, are treated independently. Therefore, a deterministic, hard-sphere, elastic collision model was utilised. A deterministic grid-based binary collision search algorithm was also used to reduce computational cost. As the particles are rigid and undeformable, it is reasonable to assume that the particle collision contact time is shorter than the LPT time-step, and this was ensured, and particle collisions not missed, by reducing the time step such that the distance travelled by a particle in a single time step was less than the diameter of the particle. By comparing the relative collision velocities of the particles upon impact, the code can identify which have

collided and calculate rebound velocities. Other particle-particle forces acting on the collision were considered insignificant, and agglomeration was modelled separately (described in more detail in Section 3.3.10). To examine hard-sphere elastic collisions more precisely under four-way coupling conditions, a volume fraction, $\phi_P \geq 10^{-3}$, was utilised, as discussed earlier (Mortimer et al. 2020). Collisions were detected using virtual search grids, as illustrated in Figure 3.5. A first virtual search grid (left) and a second coarser virtual search grid (right) were used, as depicted in this figure. Here, the particles are divided into user-specified numbers of cells within a primary and subsequently secondary coarse mesh (red dotted) at each timestep. The use of two grids enables all collisions to be detected, as illustrated in the figure, with the collision between two particles missed by the initial grid identified within the secondary gird.

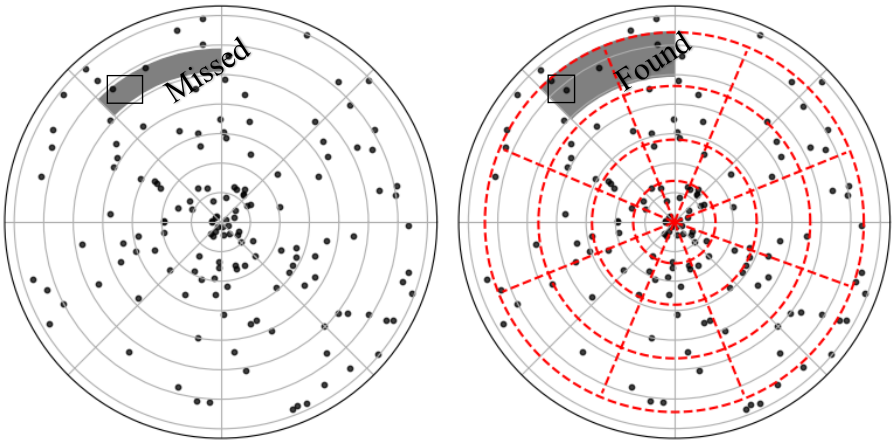

Figure 3.5: Initial (left) and secondary (right) virtual search grids for deterministic binary collision identification (see, also, Mortimer et al. (2020) and Breuer et al. (2012)).

3.3.10 DLVO interaction forces and agglomeration

Inter-particle collisions can be further extended to include the agglomeration of colliding particles. In this research, a simple agglomeration computational framework is utilised to model the process of particles combining to form larger clusters or aggregates. Usually, this model implies that particles collide and adhere to one another without taking into account the particular morphology or shape of the particles. Although these models provide a useful foundation for researching particle aggregation, further work must be done to consider the effects of particle morphology. A detailed recommendation for additional works is provided in Section 7.2.

A deterministic hard sphere collision model, as implemented in Njobuenwu and Fairweather (2015) and Breuer and Almohammed (2015), was used to predict particle agglomeration. In

this model, particles and their agglomerates are modelled as constituent-equivalent-volume point spheres. Particle agglomeration is assumed to occur if the total kinetic energy of the collision is insufficient to overcome the attractive van der Waals potential of the DLVO force between the two colliding particles, taking into account the energy dispersed upon particle compression as the two particles collide (Derjaguin and Landau, 1941; Verwey and Overbeek, 1955). The equation for the full DLVO attraction and/or repulsion caused by a spherical particle, p_1, on spherical particle p_2, is given by:

$$\mathrm{F}_{TOT} = \mathrm{F}_{vdW} + \mathrm{F}_{EDL}. \tag{3.42}$$

Here, F_{vdW} is the attractive van der Waals term and F_{EDL} is the electric double layer term in the DLVO equation. The van der Waals attraction is as follows:

$$\mathrm{F}_{vdW} = \frac{H}{12\delta_0^2} f, \tag{3.43}$$

where H is the Hamaker constant, δ_0 the inter-surface distance between spheres, and f is a factor depending on the geometry of the colliding surfaces. For two spheres of diameter, $d_1 \gg \delta$ and $d_2 \gg \delta$ in contact at a small distance δ, f is equal to $\frac{2d_1d_2}{d_1+d_2}$. The electric double layer repulsion is:

$$\mathrm{F}_{\mathrm{p_1p_2}}^{\mathrm{EDL}} = \frac{64\pi \mathrm{r}_p n \mathrm{k}_B \mathrm{T}_f \Theta^2 \mathrm{e}^{-\mathrm{k}h_1}}{k} \hat{n} \tag{3.44}$$

with

$$\Theta = \tanh\left(\frac{ze\varphi}{4k_B \mathrm{T}_f}\right) \tag{3.45}$$

$$k = \sqrt{\frac{2nz^2e^2}{\varepsilon_0 \varepsilon_r k_B \mathrm{T}_f}} \tag{3.46}$$

In the above equations, r_p is the particle radius, n is the number density of electrolyte ions, k_B is Boltzmann constant, T_f is the temperature of suspension, Θ is the reduced surface

potential, and κ is the inverse Debye length. Additionally, z is the electrolyte ionic valency, e is the elementary electric charge, φ is the zeta potential, ε_0 is permittivity of vacuum and ε_r is the relative permittivity of solvent and $\hat{n}$ is a unit vector on the particles.

One can obtain the van der Waals energy between two spheres by integrating Eq. (3.42) with respect to the distance between the spheres:

$$\triangle E_{vdW} = \frac{H}{12\pi}\frac{A}{\delta_0^2} \tag{3.47}$$

Here, A is the contact area. For small deformations, $d_1 \gg h_1$ and $d_2 \gg h_2$, the contact area can be expressed as:

$$A = \pi d_1 h_1 = \pi d_2 h_2 \tag{3.48}$$

where h_1 *and* h_2 are the depths of the deformation. The expressions for h_1 and h_2 are determined by the work required to deform a ductile material (Breuer and Almohammed, 2015):

$$h_1 = d_1 d_2^2 |\boldsymbol{u}_2^- - \boldsymbol{u}_1^-| \left[\frac{\rho_1\rho_2(1-e_n^2)}{6\bar{\sigma}(d_1+d_2)(\rho_1 d_1^3 + \rho_2 d_2^3)}\right]^{\frac{1}{2}} \tag{3.49}$$

Similarly, the electrical double layer caused by the spherical particles can be expressed as:

$$\Delta E_{EDL} = \frac{2\sigma^2}{\varepsilon_0 \varepsilon_r k} e^{-kh_1} \tag{3.50}$$

The energy-balance based non-dimensional agglomeration condition is given in Eq. (3.44), where, if the particle-particle resultant collision energy is sufficiently low then an agglomeration occurs, otherwise the particles recoil using an inelastic hard-sphere calculation:

$$\boldsymbol{u}_{p,r}^{*^2} - \frac{(1-e_n^2)(\boldsymbol{u}_{p,r}^* \cdot \hat{\boldsymbol{n}})^2}{|\boldsymbol{u}_{p,r}^* \cdot \hat{\boldsymbol{n}})|} \leq \frac{H^*}{6\delta_0^{*^2}}\left[\frac{6(1-e_n^2)}{\pi^2 \rho_p^* \bar{\sigma}^*}\left(\frac{d_{p,1}^{*^3} + d_{p,2}^{*^3}}{d_{p,1}^{*^2} d_{p,2}^{*^2}(d_{p,1}^* + d_{p,2}^*)}\right)\right]^{\frac{1}{2}} + \frac{2}{\varepsilon_r k^*}\left(\frac{\Theta^2}{\varepsilon_0}\right)^* e^{-k^* {h_1}^*} \tag{3.51}$$

Here, superscript * represents dimensionless quantities using bulk flow parameters. Additionally, $\boldsymbol{u}_{p,r}^*$ is the relative particle collision velocity, e_n is the normal coefficient of restitution, $H^* = H/\rho U_B^2 D$ is Hamaker constant (where U_B is the bulk velocity and D is the pipe diameter), $\delta_0^* = \delta_0/D$ is the minimum contact distance, $\rho_p^* = \rho_p/\rho$ is the particle-fluid density ratio, $\bar{\sigma}^* = \bar{\sigma}/(\rho U_B^2)$ is the yield pressure and $d_{p,1}^*$ and $d_{p,2}^*$ are the first and second colliding particle diameters. Also, $\hat{\boldsymbol{n}}$ is the unit vector, $k^* = kD$ the inverse Debye length, ${h_1}^* = d_{p,1}^* d_{p,2}^{*^2} |\boldsymbol{u}_{p,r}^*| \left[\rho_{p,1}^* \rho_{p,2}^* (1-e_n^2)/6\bar{\sigma}^* (d_{p,1}^* + d_{p,2}^*)(\rho_{p,1}^* d_{p,1}^{*^3} + \rho_{p,2}^* d_{p,2}^{*^3})\right]^{1/2}$ is the depth of the deformation and $[\Theta^2/\varepsilon_0]^* = \Theta^2/\varepsilon_0 \rho_f U_B$ is the square of the reduced surface potential to permittivity of vacuum.

Agglomerates formed are given new diameters based on the volume of a larger sphere equal to that of the sum of the volume of the constituent colliding particles (Mortimer et al., 2020; Breuer and Almohammed, 2015).

The two particles form a new spherical particle with the sum of the volumes of the two original particles if the requirements of Eq. (3.44) are met. The agglomerates' new velocity, u_{agg}^* and position r_{agg}^* are given, by conservation of momentum, as:

$$u_{agg}^* = \frac{1}{{d_{agg}^*}^3}\left({d_{p,1}^*}^3 u_1^* + {d_{p,2}^*}^3 u_2^*\right) \tag{3.52}$$

where $$d_{agg}^* = \sqrt[3]{{d_{p,1}^*}^3 + {d_{p,2}^*}^3}$$

$$r_{agg}^* = \frac{1}{2}(r_1^* + r_2^*) + t_{col} u_{agg}^* \tag{3.53}$$

where $d_{p,1}^*$ and $d_{p,2}^*$ are the non-dimensional diameters of the first and second colliding particles, u_1^* and u_2^* are the collision velocities, r_1^* and r_2^* are the collision positions and t_{col} is the overlap time collision (Mortimer, 2019).

3.3.11 Fourth order Runge-Kutta algorithm

The particle equations of motion were solved using a fourth order Runge-Kutta algorithm. This method imitates the Taylor series method without requiring differentiation of the original differential equation. Fourth order method yields accurate results and a low error term with a larger step size. Mathematically it can be represented as follows:

$$y_{i+1} = y_i + \frac{1}{6}(K_1 + 2K_2 + +2K_3 + +K_4) \tag{3.54}$$

Where,

$$K_1 = hf(x_i,\ y_i) \tag{3.55}$$

$$K_2 = hf\left(x_i + \frac{1}{2}h,\ y_i + \frac{1}{2}K_1\right) \tag{3.56}$$

$$K_3 = hf\left(x_i + \frac{1}{2}h,\ y_i + \frac{1}{2}K_2\right) \tag{3.57}$$

$$K_4 = hf(x_i + h,\ y_i + K_3) \tag{3.58}$$

The advantage of using this method is that, being a one-step method, it uses only information from the last step computed. Additionally, it is more accurate than Euler's and modified Euler's methods. The additional information available from the previously computed data can be used in the multistep method to construct a polynomial which estimates the derivative functional and extrapolates into the next intervals.

4 VALIDATION RESULTS AND PARTICLE-FLUID COUPLING EFFECTS

4.1 Introduction

In this chapter, the DNS and LPT codes implemented to simulate particle-laden flow systems are first validated against experimental data and numerical simulation results in the literature to build confidence in the techniques, and to demonstrate the reliable prediction of turbulent flow statistics. Various simulations of particle-laden turbulent pipe flows are performed to validate the DNS-LPT approach being used. For each simulation, several statistical quantities were gathered for analysis. The present DNS-implemented method is compared with various DNS and experimental datasets available in the literature at, or approximately equal to, the Reynolds numbers of the simulations performed. For each simulation, predictions of the mean axial velocity (u_z^*), axial ($u'^*_{z,rms}$), radial ($u'^*_{r,rms}$) and azimuthal ($u'^*_{\theta,rms}$) normal stresses, and the primary Reynolds shear stress ($< u'_z\, u'_r >^*$) are compared. Only literature data with incompressible and Newtonian fluid flow conditions has been used for validation and, where possible, multiple experiments and DNS datasets have been compared with the current simulations. There are no multiphase turbulent DNS investigations in the literature at the relatively high Reynolds number $Re_B = 11{,}700$ considered later, hence the multiphase code was validated against lower Reynolds number flows, $Re_B = 3{,}975$ and 5,300. The DNS flow properties were obtained at three different shear Reynolds numbers, $Re_\tau \approx 277$, 360 and 720, using the same numerical mesh topology and configurations. It is clear from the results given in Sections 4.2.3 to 4.2.5, generated using approximately 19 million grid points, that the results obtained are in strong agreement with the literature results. El Khoury (2013), for example, simulated the pipe flow using a large number of grid points, up to ≅ 121.4 million, compared to the 19 million used in the current simulation. Nevertheless, good agreement with the latter's results is obtained, and all the simulations produced results that are in-line with the DNS and experimental datasets of others.

Using these fully developed single-phase flows, the second half of the chapter entails the simulation of spherical particles with properties of relevance to nuclear waste processing. As discussed in the Methodology chapter, particles are initially injected at random locations within the computational domain and assigned the local surrounding fluid velocity through spectral interpolation. Various LPT algorithms were modified for the pipe topology since they were originally written for a channel flow geometry. A number of new modules were also added to the model, including an algorithm for collisions with walls, a module that dynamically handles periodic conditions and a module that controls the flow by maintaining a constant pressure gradient in the axial direction while maintaining a constant bulk velocity. The model also included an algorithm for injecting particles randomly throughout the pipe domain at the beginning of the simulation. The validation therefore also acts to demonstrate the effectiveness of all these algorithms. To better understand such flows, probability density functions and the near-wall particle concentration of particle properties for each flow are also analysed. Finally, the impact of one-way and four-way coupling on turbulent statistics is examined. The mean and shear stress profiles of one-way and four-way coupled particle data for $Re_B \approx 11{,}700$, with and without agglomeration, are also investigated.

4.2 Single-phase turbulent pipe flow validation

4.2.1 Simulation parameters and setup

The Methodology chapter provided a full description of the pipe flow's computational domain used in all simulations throughout this chapter. El Khoury et al.'s (2013) earlier work generated outstanding results when compared to experimental data, hence in the current work, we selected to closely reproduce a mesh with GLL points based on his simulations using the lowest number of grid points, which is roughly 19 million. The grid spacings (in wall units) employed in this work, for the comparison cases of Vreman (2007) and El Khoury et al. (2013), are shown in Table 4.1. Compared to Vreman (2007), a resolution with greater precision was employed for the $Re_\tau \approx 277$ flow, whilst the present $Re_\tau \approx 360$ resolution is roughly comparable to that of El Khoury et al. (2013), with a little less precision in the radial direction. The current $Re_\tau \approx 720$ case is less refined than that of El Khoury et al (2013). Despite the significant differences in the resolution used for the $Re_\tau \approx 720$ and 277 cases, however, the turbulence statistics will be shown to exhibit great agreement with the literature datasets.

The flow in the streamwise direction was maintained by a constant pressure gradient, chosen to obtain the desired flow Reynolds number. In this chapter, turbulent pipe flows with Reynolds numbers based on shear velocities, $Re_\tau \approx 277$, 360 and 720, are studied. Periodic boundary conditions were applied at the extents of the streamwise direction and no-slip conditions were enforced at the wall at radial distance $r^* = 0.5$. The instantaneous pressure fluctuation (I), instantaneous streamwise profile (II) and the cross-sectional view of the computational mesh (III) with instantaneous axial velocity pseudo-colour at $Re_\tau \approx 360$ are all presented in Fig. 4.1. This figure reveals the full nature of the turbulence fields presents in the pipe flow.

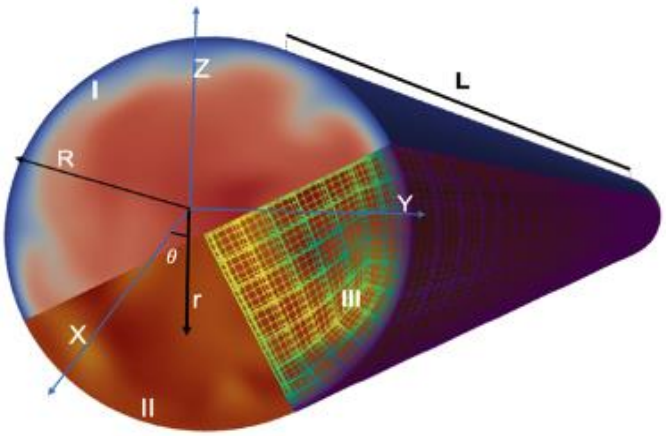

Figure 4.1: I –Instantaneous streamwise pressure, II – instantaneous streamwise velocity field and III – the cross-sectional view of a quarter of the computational mesh with mean axial velocity pseudo-colour at $Re_\tau \approx 360$.

Table 4.1: Single-phase pipe flow computational grid points and maximum mesh spacing. Comparisons with literature are demonstrated for DNS simulations.

Re_B	Re_τ	GLL points	$\Delta r^+ max$	$\Delta\theta^+ max$	$\Delta z^+ max$	References
3,975	277	607k	3	9	20	Vreman (2007)
3,975	277	18.7m	4.77	4.93	7.42	Present DNS
5,300	360	18.7m	4.44	4.93	9.91	El Khoury et al. (2013)
5,300	360	18.7m	4.77	4.93	7.42	Present DNS
11,700	720	121m	4.44	4.93	9.91	El Khoury et al. (2013)
11,700	720	18.7m	4.77	4.93	7.42	Present DNS

4.2.2 Instantaneous flow analysis

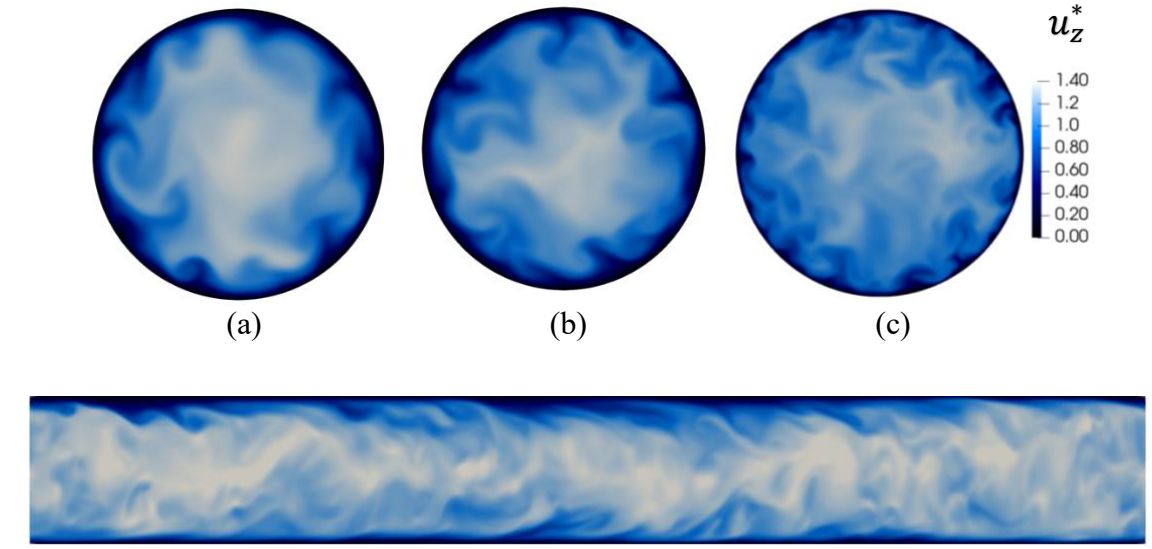

(a) (b) (c)

(d)

(e)

(f)

Figure 4.2: Pseudo-colour visualisation of the instantaneous streamwise velocity for (a) and (d): $Re_\tau \approx$ 277, (b) and (e): $Re_\tau \approx$ 360 and (c) and (f): $Re_\tau \approx$ 720, normalised by the bulk velocity, U_B.

Figure 4.2 (a), (b), and (c) show the computational domain clipped at the centre of the streamwise direction to visualise the streamwise instantaneous velocities within the cross-section of the pipe flow. Figure 4.2 (d), (e) and (f) show the corresponding fluid velocities in the streamwise direction as pseudo-colour contour plots for $Re_\tau \approx$ 277, 360 and 720, respectively. These plots provide a detailed representation of the turbulent velocity field present in the pipe flows, as well as the influence of Reynolds number on the structure of turbulence

and its variation throughout the domain. For all Reynolds numbers, the highest streamwise velocities occur close to the centre of the pipe and exhibit a strong positive motion that is homogenous along the pipe. This is evident in Fig. 4.3, which is sliced along the central plane and cross-section of the pipe to visualise the axial velocity in three dimensions.

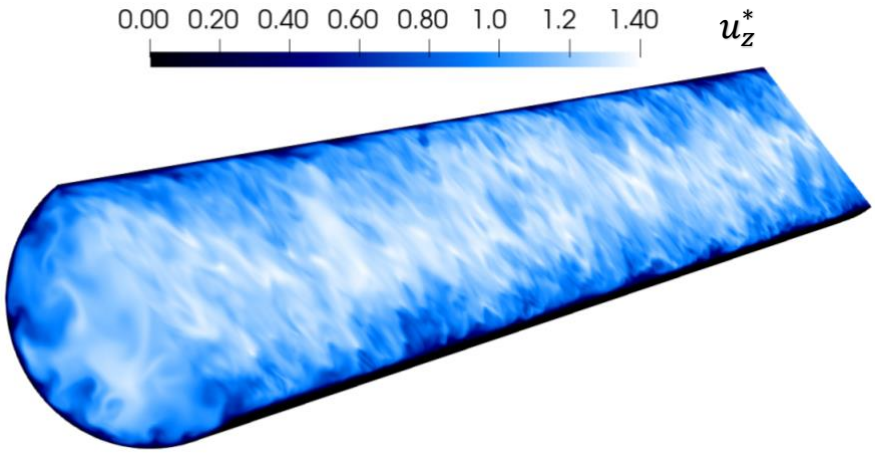

Figure 4.3: Computational domain sliced along the central plane and cross-section of the pipe with pseudo-colour visualisation of the instantaneous streamwise velocity in 3D, $Re_\tau \approx 720$, normalised by bulk velocity, U_B.

4.2.3 Single-phase validation at $Re_\tau \approx 277$

A single-phase simulation was first performed at a shear Reynolds number of $Re_\tau \approx 277$ in order to validate the DNS approach being used. Figure 4.4 shows the mean streamwise velocity profile of that flow compared with the DNS predictions of Vreman (2007), which were performed at the same shear Reynolds number. The technique used in this work to predict the flow is similar to that of Vreman's (2007), except in the latter case a lower number of grid-points were used. Despite the grid-point number difference, the results are in very strong agreement. Figure 4.4 (b) shows the same quantity on a logarithmic scale, which provides extra detail surrounding the mean axial velocity profile close to the wall, again with acceptable agreement between the two sets of results.

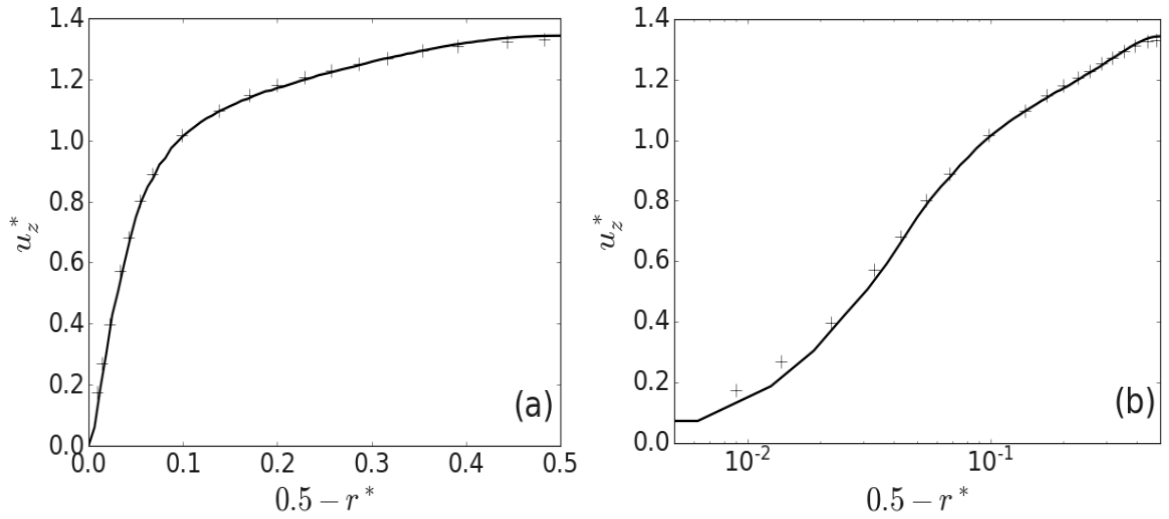

Figure 4.4: Mean streamwise velocity profiles with DNS validation at $Re_\tau \approx 277$. —: present DNS, +: Vreman (2007) DNS. (a): linear scale, (b): log scale.

Also of importance is the magnitude of the fluid velocity fluctuations throughout the pipe flow, which is an indication of the level of turbulence. The root mean square (rms) velocity fluctuations are obtained using the definition:

$$u'^* = u^* - \bar{u}^* \tag{4.1}$$

Once a mean was established, the velocity fluctuations were measured and gathered throughout the flow, before being used to obtain rms values. Figure 4.5 shows the rms of the axial, radial and azimuthal fluctuating velocities, as well as the Reynolds shear stress, $< u'_z\, u'_r >^*$, at $Re_\tau \approx 277$, together with the results of Vreman (2007). Close to the pipe centreline, the present simulation results and those of Vreman (2007) are in good agreement. It is noted that there are some discrepancies inside the bulk flow region of the axial $u^*_{z,rms}$ normal stresses and the Reynolds shear stress $< u'_z\, u'_r >^*$, which can be attributed to the present work's substantially higher numerical resolution. Overall, however, satisfactory comparisons of the mean streamwise velocity, as well as the normal and shear stresses, as a function of wall distance give confidence in the present continuous phase predictions.

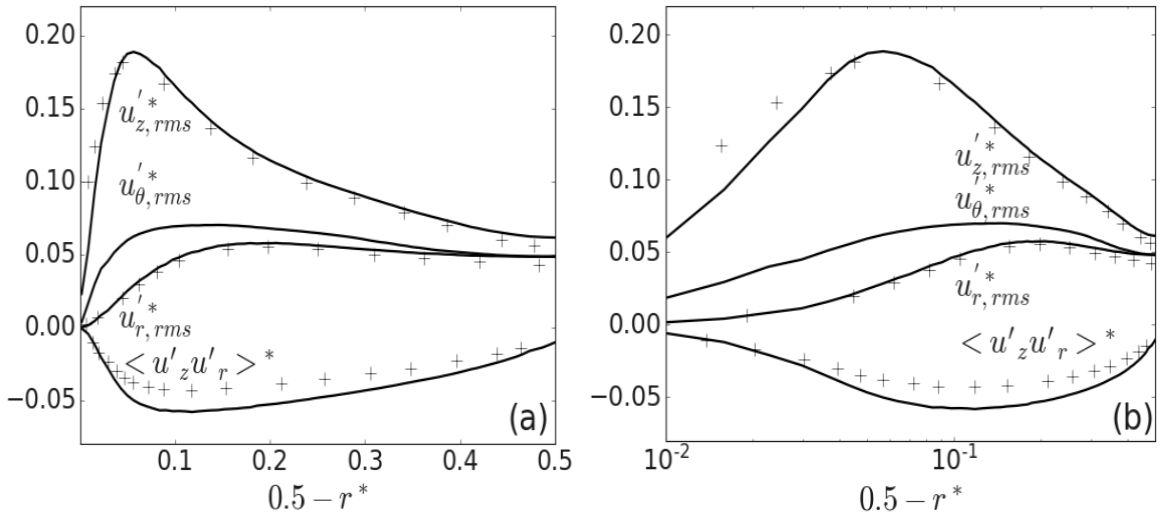

Figure 4.5: Validation of rms fluctuating velocity and shear stress profiles at $Re_\tau \approx 277$. The axial, $u'^{*}_{z,rms}$, radial, $u'^{*}_{r,rms}$, azimuthal, $u'^{*}_{\theta,rms}$, normal stresses and Reynolds shear stress, $< u'_z\, u'_r >^*$ are compared against DNS. —: present DNS, +: Vreman (2007). (a): linear scale, (b): log scale.

4.2.4 Single-phase validation at $Re_\tau \approx 360$

Figure 4.6 shows the mean streamwise velocity profiles of the present flow at shear Reynolds number $Re_\tau \approx 360$ compared with the DNS results of El Khoury et al. (2013), performed at the same shear Reynolds number. The configuration is similar except that in El Khoury et al. (2013), a higher number of mesh elements was used. The results are also compared with the experimental datasets of den Toonder et al. (1997) and Eggels et al. (1994) at shear Reynolds numbers of 340 and 360, respectively. The present results are demonstrated to be in good agreement with both the literature DNS and experimental datasets, with some minor deviations close to the wall.

Figure 4.7 displays the root mean square of the axial, radial and azimuthal velocity fluctuation profiles, as well as the Reynolds shear stress, $< u'_z\, u'_r >^*$, at $Re_\tau \approx 360$. These are compared with the DNS results of El Khoury et al. (2013) at the same shear Reynolds number. Data from the Eggels et al. (1994) and den Toonder et al. (1997) experiments are provided for comparison at $Re_\tau \approx 360$. Both El Khoury et al. (2013) and Eggels et al. (1994) agree with the current root mean square velocity fluctuation predictions in the axial, radial and azimuthal directions. Furthermore, the present axial rms values agree well except near to the wall when contrasted with the inner scaled rms values from Den Toonder's et al. (1997) experiment, though this was performed at a slightly lower Reynolds number, $Re_\tau \approx 338$. The present Reynolds shear stress

predictions strongly agree with all the alternative results. All results are also plotted on a logarithmic scale, in Figs. 4.6 and 4.7, and these figures add further detail regarding the mean streamwise velocity profile and normal and shear stresses close to the wall. The discrepancy between den Toonder et al.'s (1997) LDV data and the present DNS predictions near the wall in the log plot of Fig. 4.7 is likely due to the spatial and temporal resolution limitations of LDV close to solid surfaces, as well as the small difference in shear Reynolds number between the two flows. Overall, however, comparison of the axial, $u'^{*}_{z,rms}$, radial, $u'^{*}_{r.rms}$, azimuthal, $u'^{*}_{\theta,rms}$ and Reynolds shear stress, $< u'_z\, u'_r >^{*}$ as a function of wall distance against literature DNS and experimental data is very good.

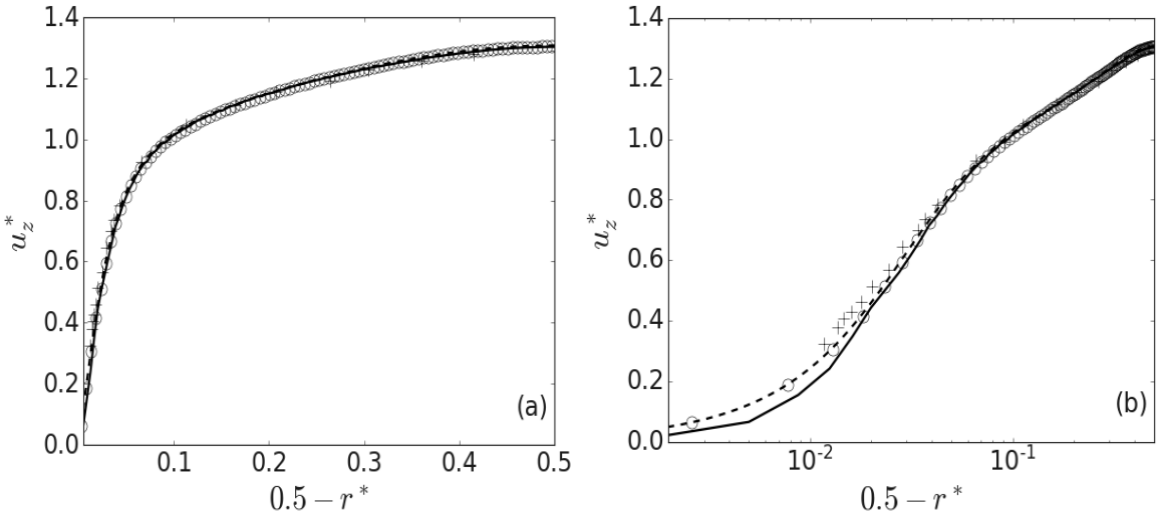

Figure 4.6: Mean streamwise velocity profiles with DNS and experimental data validation at $Re_\tau \approx 360$. —: present DNS, − −: El Khoury et al. (2013) DNS, +: den Toonder et al. (1997) experimental dataset at $Re_\tau \approx 338$, and ○: Eggels et al. (1994) experimental dataset at $Re_\tau \approx 360$. (a): linear scale, (b): log scale.

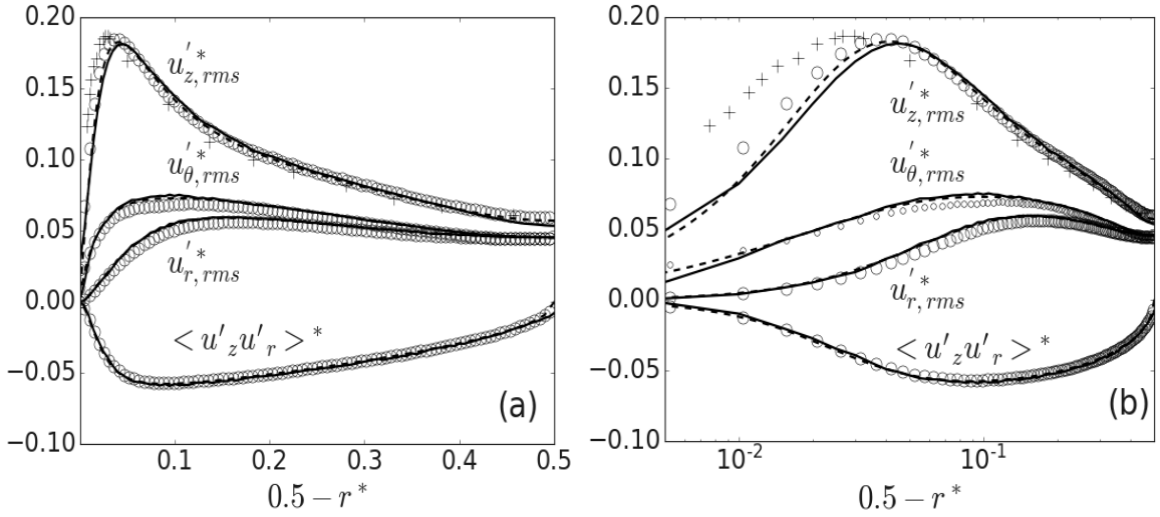

Figure 4.7: Validation of rms fluctuating velocity and shear stress profiles at Re_τ ≈360. The axial, $u'^*_{z,rms}$, radial, $u'^*_{r,rms}$, azimuthal, $u'^*_{\theta,rms}$, normal stresses and Reynolds shear stress, $< u'_z\, u'_r >^*$ profiles are compared against DNS and experimental datasets. −: present DNS, − −: El Khoury et al. (2013) DNS, +: den Toonder et al. (1997) experimental dataset at Re_τ≈ 338, and ○: Eggels et al. (1994) experimental dataset at Re_τ≈ 360. (a): linear scale, (b): log scale.

4.2.5 Single-phase validation at $Re_\tau \approx 720$

Figure 4.8 shows the mean streamwise velocity profile of the present prediction at an increased shear Reynolds number, $Re_\tau \approx 720$. This is compared with the results of El Khoury et al.'s (2013) DNS findings at $Re_\tau \approx 720$ as well as with Singh at al.'s (2018) DNS predictions at $Re_\tau \approx 640$. The present work agrees with the predictions of El Khoury et al. (2013) but slightly deviates when contrasted with Singh et al.'s (2018) results, although this is likely due to the difference in Reynolds number, with Singh et al.'s (2018) simulations using a lower shear Reynolds than the present work. The result are additionally compared with the Den Toonder et al.'s (1997) experimental dataset at $Re_\tau \approx 629$. This correlates well with the present work given the difference in Reynolds number.

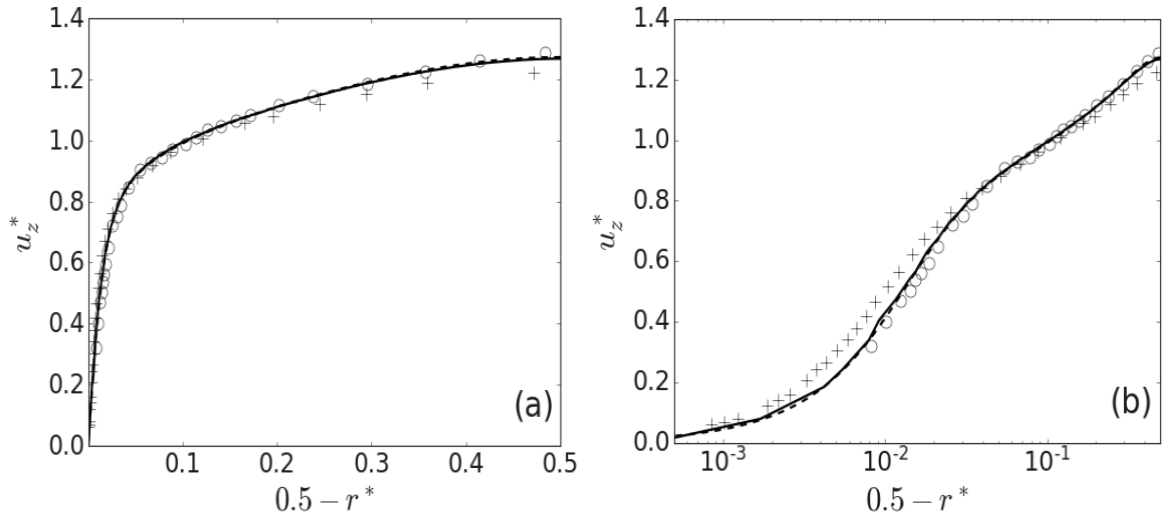

Figure 4.8: Mean streamwise velocity profiles with DNS and experimental data validation at $Re_\tau = 720$. −: present DNS, − −: El Khoury et al. (2013) DNS, ○: den Toonder et al. (1997) experimental dataset at $Re_\tau \approx 629$, +: Singh et al. (2018) DNS at $Re_\tau \approx 640$. (a): linear scale, (b): log scale.

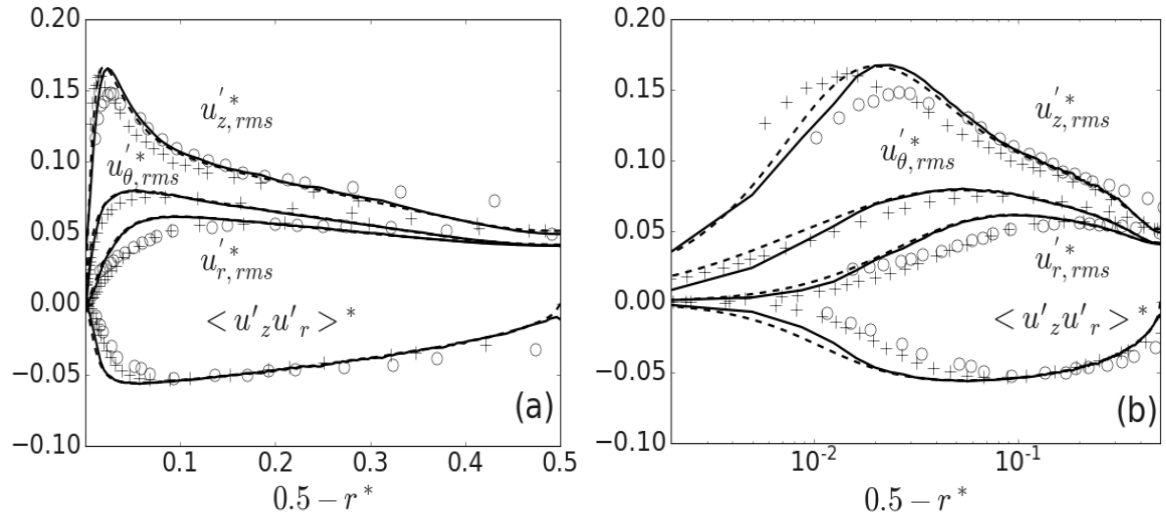

Figure 4.9: Validation of rms fluctuating velocity and shear stress profiles at $Re_\tau = 720$. The axial, $u'^*_{z,rms}$, radial, $u'^*_{r,rms}$, azimuthal, $u'^*_{\theta,rms}$ normal stresses and Reynolds shear stress, $< u'_z\, u'_r >^*$ profiles are compared against DNS and experimental datasets. −: present DNS, − −: El Khoury et al. (2013) DNS, ○: den Toonder et al. (1997) experimental dataset at $Re_\tau \approx 629$ and +: Singh et al. (2018) DNS at $Re_\tau \approx 640$. (a): linear scale, (b): log scale.

Figure 4.9 shows variations in the axial, radial and azimuthal normal stress profiles, and the Reynolds shear stress, $< u'_z\, u'_r >^*$, at $Re_\tau \approx 720$ together with the results of El Khoury et al. (2013), Singh et al. (2018) and den Toonder et al. (1997), with good agreement found throughout. In the bulk flow region of the pipe, all the alternative simulations and experimental

data compared with are in good agreement with the profiles of the present DNS, although some slight deviation from the results of den Toonder et al. (1997) is apparent. Nevertheless, overall the comparisons of normal and shear stresses as a function of wall distance against literature DNS and experimental data gives confidence in the present predictions. Figures 4.8(b) and 4.9(b) provide further details regarding the mean streamwise velocity and stresses by plotting the same variables on a logarithmic scale.

4.3 Particle-laden turbulent pipe flow simulation validation

In all validation cases considered in this section, the effects of drag and gravitational forces were considered when calculating the particle trajectories. The gravitational force was applied in the axial flow direction. Tables 4.2 and 4.3 contain detailed configuration information as well as additional simulation information for each case. The particle mean streamwise, and rms of velocity fluctuation and shear stress, profiles are compared and contrasted with available literature datasets. The probability density functions of particle dynamic properties for each wall-normal region are also analysed to further understand the local behaviour of the particles.

The instantaneous mean streamwise velocity is shown in Fig. 4.10 (left) which shows lines representing fluid streamwise tracers, with fluid velocities tending to be greater close to the centre of the pipe as would be expected. Figure 4.10 (right) illustrates randomly injected particles with different initial spectrally interpolated velocity values. At the initialisation of the particle-laden flow, particles were injected into a fully developed turbulent flow and distributed randomly within the domain. At each particle point, the local fluid velocity was set as the instantaneous fluid velocity. The highest particle velocities were obtained near the centreline of the pipe once more.

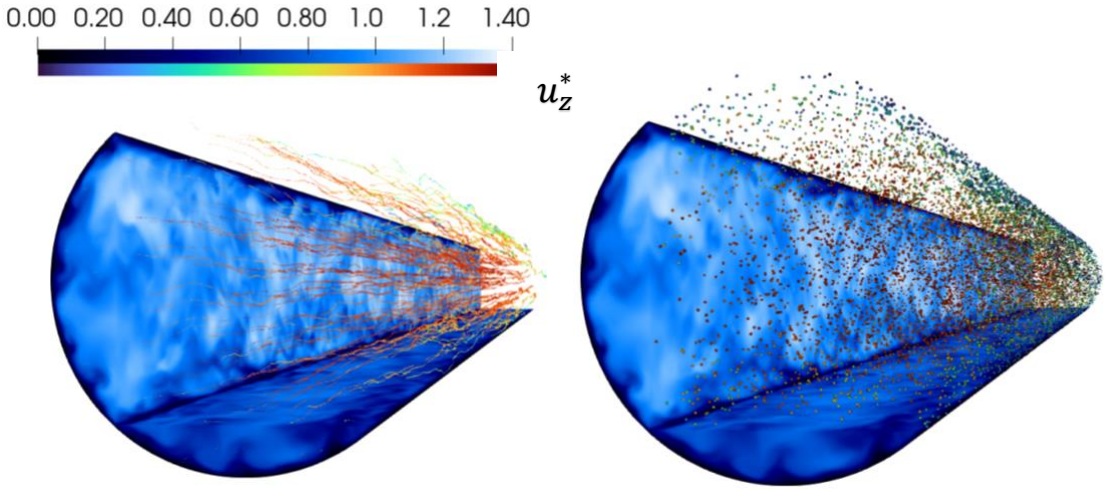

Figure 4.10: Pseudo-colour visualisation of instantaneous mean axial velocity with fluid flow tracer lines (left) and initial particle distribution and instantaneous velocities (right) for $Re_\tau \approx 360$ flow.

4.3.1 Particle-laden flow simulation configuration at $Re_\tau \approx 277$

Table 4.2 shows the simulation details used with the present LPT solver for the validation with the DNS-based results of Vreman (2007). This case was chosen because it was the closest available particle flow simulation at the Reynolds number of interest, $Re_\tau \approx 277$. The same number of particles $N_p = 29{,}400$, particle diameter $d_p = 60$ μm, and density ratio $\rho_p^* = 2058$ as used by the latter author were employed in the current study.

Table 4.2: Particle-laden turbulent pipe flow validation parameters for comparisons between present work and Vreman (2007) at $Re_\tau = 277$.

Parameter	$Re_\tau = 277$	
	Present work	Vreman (2007)
Particle diameter, $d_p[\mu m]$	60	60
Particle diameter, d_p^*	0.003	0.003
Axial length	12.5D	10D
Number of particles, N_p	29,400	29,400
Shear Stokes number, St^+	78.97	78.96
Bulk Stokes number, St_B	4.09	4.0
Density ratio, ρ_p^*	2058	2058
Volume fraction, ϕ_p	0.0000424	0.000053

4.3.2 Multiphase validation at $Re_\tau \approx 277$

The particulate phase mean streamwise velocity, rms velocity fluctuations and shear stress profiles were computed and compared against the DNS findings of Vreman (2007) at $Re_\tau \approx 277$. It should be noted that four-way coupled simulations were considered by Vreman (2007). In the present work, the particles were injected at random locations within the computational domain and assigned the surrounding fluid velocity at the start of the simulation. A spherical 60 μm particle diameter was chosen with 29,400 particles used in the simulation. Drag and gravitational forces were used when calculating the particle trajectories, with the impact of the lift force considered negligible. The gravitational force was applied in the streamwise direction; hence a vertical pipe was simulated. These assumptions are in line with those made by Vreman (2007). The only difference was that in the present simulation a much larger number of numerical grid nodes were used, as detailed earlier. One-way and four-way coupled simulations with the same particle size and number were performed in the present work, with the mean streamwise and normal and shear stress profiles analysed.

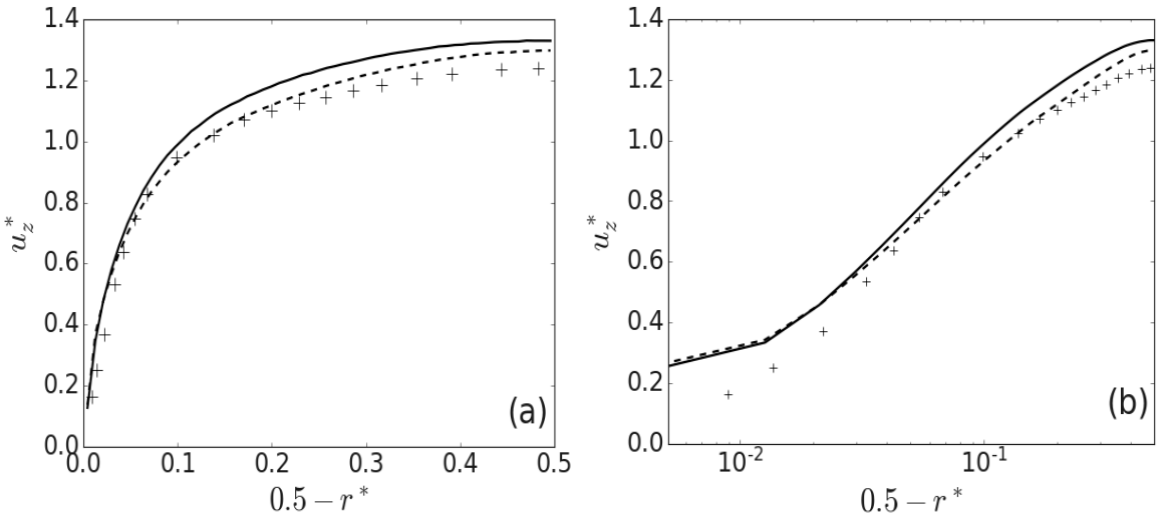

Figure 4.11: Mean particle streamwise velocity profiles for DNS at $Re_\tau \approx 277$. —: one-way coupled and − −: four-way coupled present DNS, +: DNS predictions of Vreman (2007). (a): linear scale, (b): log scale.

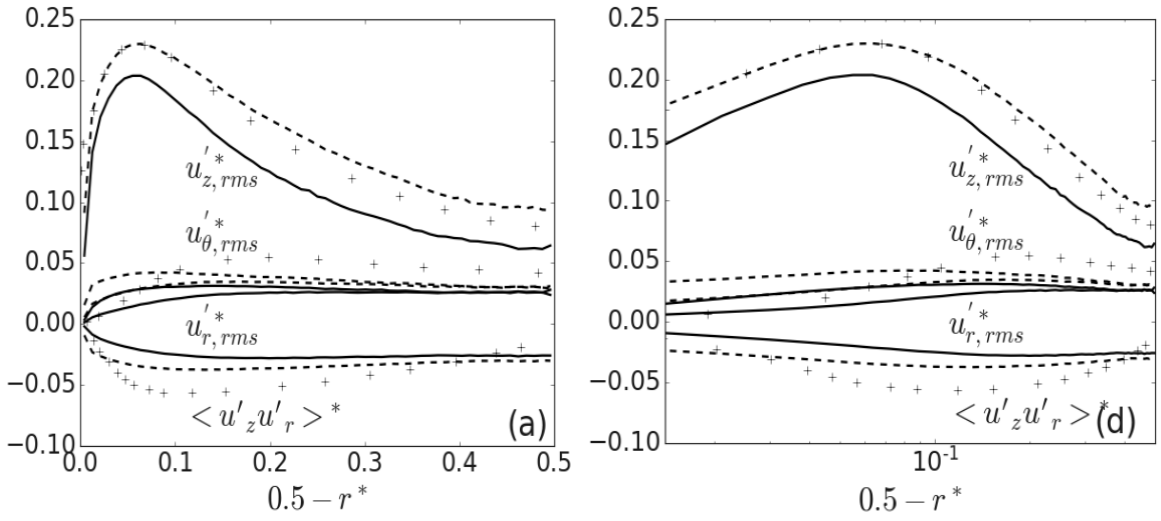

Figure 4.12: Validation of rms fluctuating velocity and shear stress profiles at $Re_\tau \approx 277$. The axial, $u'^{*}_{z,rms}$, radial, $u'^{*}_{r,rms}$, azimuthal, $u'^{*}_{\theta,rms}$ normal stresses and Reynolds shear stress, $< u'_z\, u'_r >^*$ profiles are compared against DNS results. —: one-way coupled and − −: four-way coupled present DNS, +: DNS predictions of Vreman (2007). (a): linear scale, (b): log scale.

The particle mean velocity profile and stresses are compared with the results of Vreman's (2007) DNS in Figs. 4.11 and 4.12, again showing reasonable agreement despite the previously noted lack of computational nodes in the latter's computations. Clearly the present one-way coupled simulations are significantly different from those using four-way coupling, with the latter required to simulate the impact of particles on the continuous phase flow field. There is reasonable agreement between the four-way DNS predictions of Vreman (2007) and the present four-way coupled results, although some differences do occur within the bulk flow region, this likely being due to the significantly increased numerical resolution used in the present work (18.7M nodes as opposed to 607k in Vreman (2007)). One-way coupled results are also included in Fig. 4.12 to demonstrate the impact of four-way coupling relative to the system without collisions or particle-fluid interaction. The four-way coupling method more accurately estimates the mean velocity and stresses of both the fluid phase and particle phase by capturing inter-particle interaction and feedback effects between the two phases, namely from the particles to the fluid.

Figure 4.13 shows mean particle concentration profiles in the streamwise direction for both the one-way and four-way coupled cases, with the concentration normalised by the initially injected concentration, C_0. The statistics on particle concentration were collected over $100 \leq t^* \leq 150$. Due to the high Stokes number, $St^+ \cong 79$, utilised in the simulation, more particles

were observed close to the wall in the one-way coupled case than in the four-way coupled simulation. This has been observed many times in previous work, with the effects of turbophoresis more pronounced for increased Stokes numbers (Mortimer, 2019). Interestingly, the effects of four-way coupling tend to hinder the wall-accumulation process, likely due to particle collisions near the wall leading to increased rms velocity fluctuations, as observed in Figure 4.12. More turbulent particle behaviour in these regions will be detrimental to the preferential concentration of particles in low-speed streaks in the near-wall region.

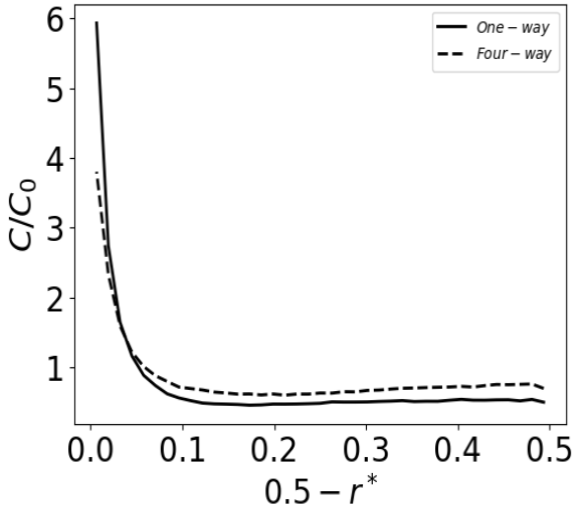

Figure 4.13: Near-wall concentrations of $St^+ \cong 79$ particles in $Re_\tau \approx 277$ pipe flow normalised by initial bulk concentration. —: one-way coupled, − −: four-way coupled.

To further examine the local behaviour of the particles in various regions of the pipe flow, probability density functions (PDFs) of dynamic quantities were also generated. Figure 4.14 compares both one-way and four-way coupled PDFs for the shear Reynolds number $Re_\tau \approx 277$ simulation in the viscous sublayer ($0 \leq 0.5 - r^* < 0.0135$), buffer layer ($0.0135 \leq 0.5 - r^* < 0.083$), log-law ($0.083 \leq 0.5 - r^* < 0.1$) and bulk flow ($0.1 \leq 0.5 - r^* \leq 0.5$) regions of the pipe. The top-left plot displays radial velocity PDFs, which have a wider spread for the one-way coupled particle velocities. The top-right plot depicts PDFs for both one-way and four-way coupled particle velocities in the azimuthal direction, again demonstrating a wide dispersion of negative azimuthal velocities for both particle simulations.

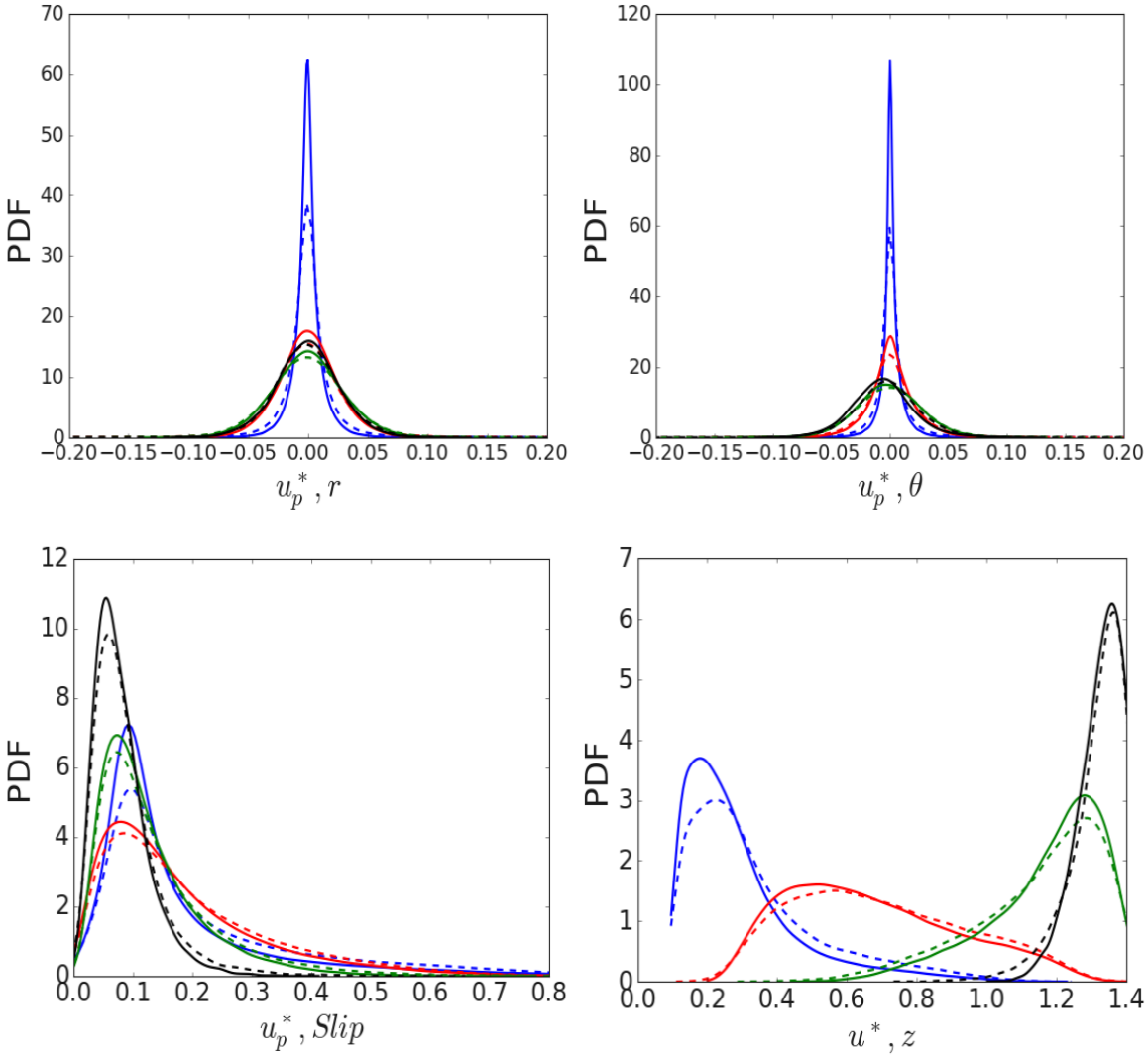

Figure 4.14: Probability density functions of particle dynamic properties within the viscous, buffer, log-law and bulk flow regions of the pipe with $St^+ \cong 79$ particles. Top-left: radial velocity, top-right: azimuthal velocity, lower-left: slip velocity, lower-right: axial velocity. —: one-way coupled, – –: four-way coupled. Blue: viscous sublayer, red: buffer layer, green: log-law region, black: bulk flow.

Due to the influence of gravity, there is also a slight skew towards negative velocities in both cases. PDFs of the slip velocity are also given in the lower-left plot, and these tend to increase in the four-way case, as would be expected for more inertial particles due to inter-particle collisions. Finally, PDFs of the particles' streamwise velocity are given in the lower-right plot, in the viscous sublayer, buffer layer, log-law and bulk flow regions of the pipe. One-way coupled results exhibit a larger spread in velocities in the viscous sublayer, which suggests greater particle concentrations close to the wall which confirms the findings of Fig. 4.13. The buffer and bulk flow regions exhibit a slight change in the velocity distribution for the one-way

and four-way coupled simulations, however, the dispersion is larger for the one-way results in the log-law region.

4.3.3 Particle-laden flow simulation configuration at $Re_\tau \approx 360$

In this section, an additional particle species has been simulated at an increased Reynolds number in order to further validate the particle solver. The configuration of the simulation at $Re_\tau \approx 360$ is given in Table 4.3 below.

Table 4.3: Particle-laden turbulent pipe flow validation parameters for comparisons between present work and Rani et al. (2004) at $Re_\tau \approx 360$.

Parameter	$Re_\tau = 360$	
	Present work	Rani et al. (2004)
Particle diameter, d_p^+	0.72	0.72
Particle diameter, d_p^*	0.002	0.002
Axial length	12.5D	-
Number of particles, N_p	420,000	420,000
Shear stokes number, St^+	57.6	57.6
Bulk stokes number, St_B	2.36	-
Density ratio, ρ_p^*	2,000	2,000
Volume fraction, ϕ_p	0.000179	0.000448

4.3.4 Multiphase validation at $Re_\tau \approx 360$

A separate simulation was performed at $Re_\tau \approx 360$, with the findings directly compared with the DNS results of Rani et al. (2004), who also considered particles within the same flow configuration, to validate the coupled DNS and LPT solver. At the start of the simulation, 420,000 particles were randomly injected, and each particle was assigned its surrounding fluid velocity. Figures 4.15 and 4.16 demonstrate the coupling effects of the particles on the continuous phase flow (note that Rani et al. (2004) do not provide results for the particle species). The mean streamwise velocity profiles of the present work are compared against the DNS results of Rani et al. (2004) at a particle Stokes number based on the shear timescale of $St^+ \cong 58$. The mean streamwise velocity results are in very good mutual agreement. This simulation used the highest concentration of particles present in the validation cases, which had a volume fraction equivalent to 1.79×10^{-4}. Generally, the rms velocity fluctuation

profiles are in good agreement, with slight discrepancies attributable to differences in volume fraction between the two cases.

Figure 4.16 displays the root mean square of the axial, radial and azimuthal fluctuating velocity profiles, along with the mean Reynolds shear stress $< u'_z \, u'_r >^*$, at $Re_\tau = 360$. These results are compared to the DNS results of Rani et al. (2004), with both sets of results showing good agreement. Turbulence attenuation, particularly in the bulk flow region, is also observed upon switching to four-way coupling and is found to be similar in magnitude to that of the comparison study.

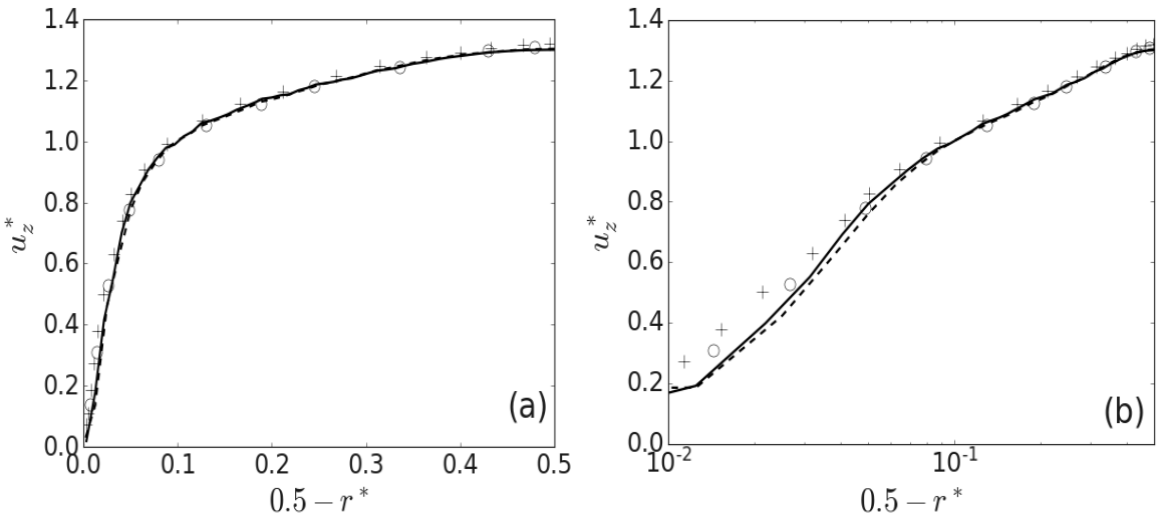

Figure 4.15: Particle-laden flow validation and effects of coupling on continuous-phase dynamics. Fluid mean streamwise velocity profiles are compared, —: one-way coupled and − −: four-way coupled present work. Symbols represent findings of Rani et al. (2004), +: one-way and ○: four-way coupled. (a): linear scale, (b): log scale.

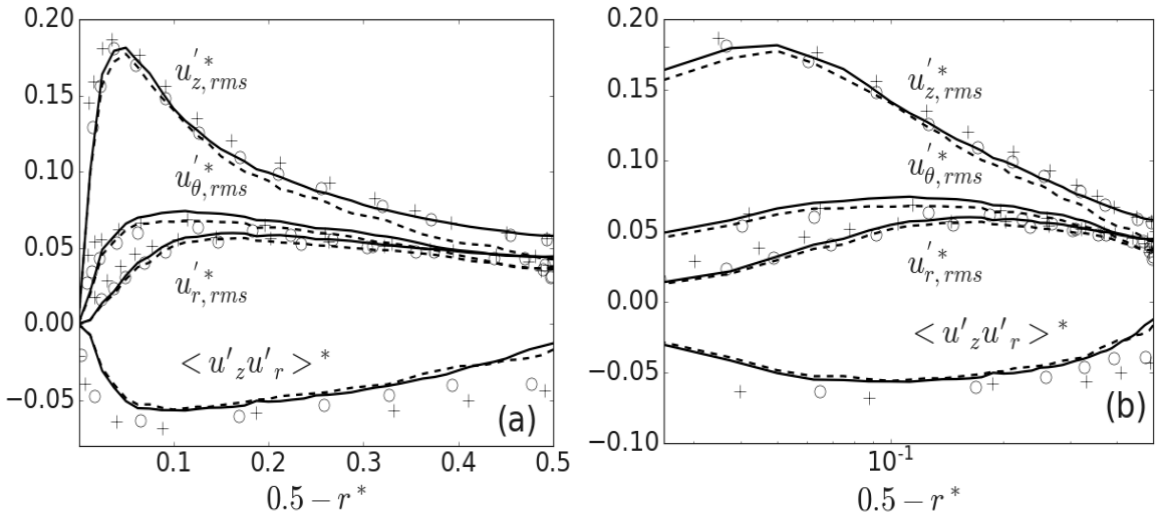

Figure 4.16: Particle-laden flow validation and effects of coupling on continuous-phase dynamics. The axial, $u'^*_{z,rms}$, radial, $u'^*_{r,rms}$, azimuthal, $u'^*_{\theta,rms}$ normal stresses and Reynolds shear stress, $< u'_z\, u'_r >^*$ are compared, —: one-way coupled and − −: four-way coupled present work. Symbols represent findings of Rani et al. (2004), +: one-way and ○: four-way coupled. (a): linear scale, (b): log scale.

Figure 4.17 shows the one-way and four-way coupled mean particle velocity profiles. The particle statistics were not presented by Rani et al. (2004), but the results are nonetheless of interest and so have been included here. The present four-way coupled simulations, which are necessary to simulate the impact of particles on the continuous phase flow field, clearly differ considerably from the one-way coupled simulations. Although there are some variances within the bulk flow regions, the logarithmic plot in Fig. 4.17 (b) also exhibits more obvious differences close to the wall. The one-way coupled findings highlight the not insignificant influence of four-way coupling in comparison to computations performed without particle collisions or particle-fluid interaction. In particular, in the near-wall region, these differences are due to interactions between the particles and the wall boundary which, in the case of four-way coupling, can result in momentum transfer as the particles bounce off the wall, affecting the particles' mean velocity. Additionally, small differences between the two levels of coupling are observed throughout the flow.

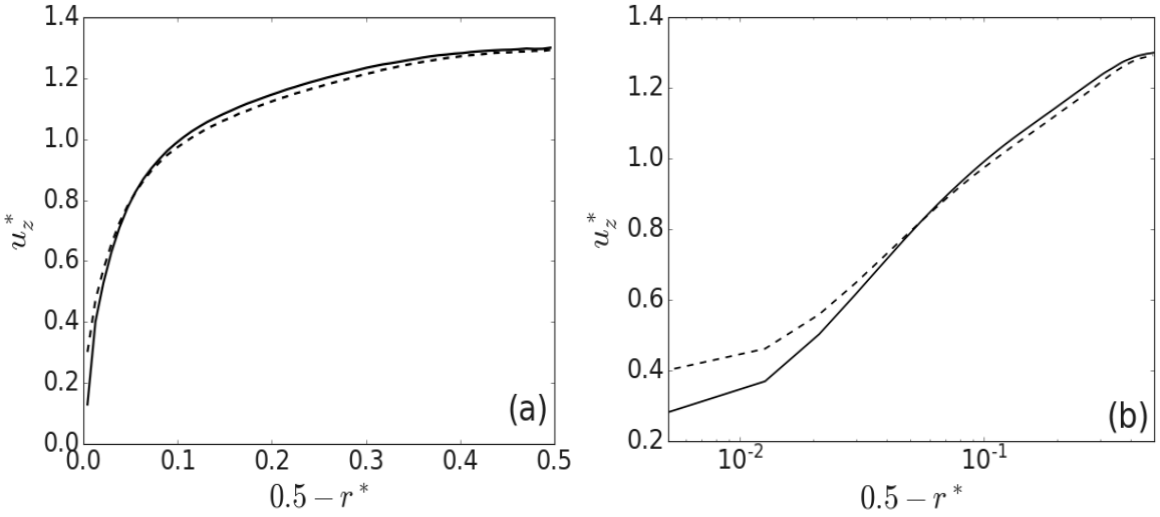

Figure 4. 17: Effect of coupling on the mean streamwise particle velocity profiles at $Re_\tau \approx 360$. —: one-way coupled and − −: four-way coupled.

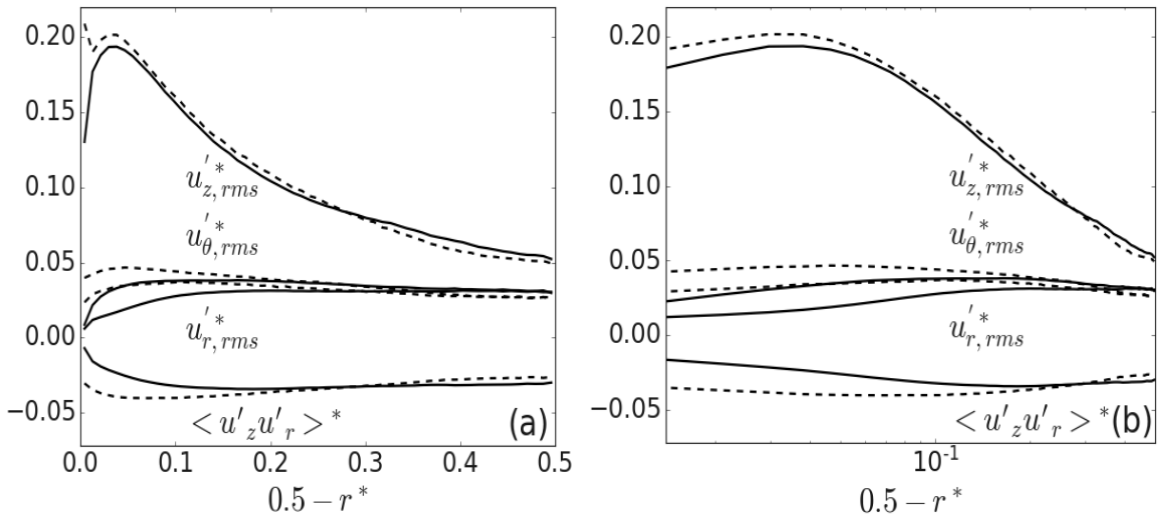

Figure 4.18: Effect of coupling on the rms particle velocity fluctuation and Reynolds shear stress profiles at $Re_\tau \approx 360$. —: one-way coupled and − −: four-way coupled.

Figure 4.18 shows the rms of the axial, radial, and azimuthal fluctuating velocity profiles, as well as the mean Reynolds shear stress, $< u'_z\, u'_r >^*$, of the particles at $Re_\tau = 360$ for one-way and four-way coupled flows. The same particle size and number of particles were used in both the one-way and four-way coupled simulations. The large particle Stokes number is the reason why the rms of fluctuating velocity profiles, and the shear stress, for the four-way simulations deviate significantly from those of the one-way simulations, demonstrating the impact of the particles on the fluid. This is in line with the findings for the Vreman et al. (2007) validation noted earlier, the mean particle concentration profiles are shown in Figure 4.19,

normalised by the initial injected concentration, C_0, for both one-way and four-way particle coupling. Data on particle concentration was again gathered over $100 \leq t^* \leq 150$. This plot again demonstrates, in line with the results of Fig. 4.13, that one-way coupling produces the highest near-wall concentration of particles for the reasons previously noted.

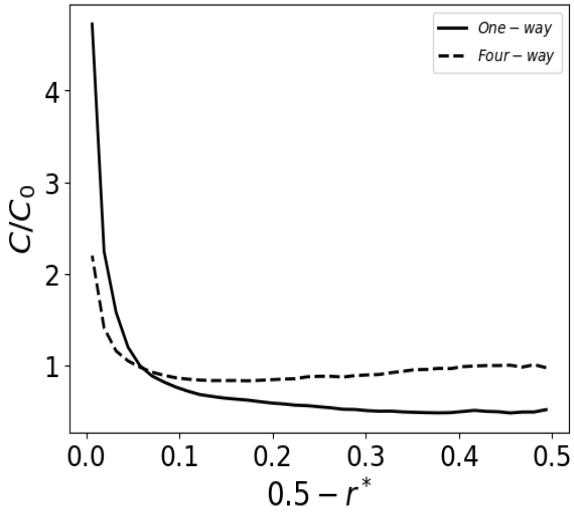

Figure 4.19: Near wall particle concentration of $St^+ \cong 58$ particle in $Re_\tau \approx 360$ pipe flow normalised by initial concentration. —: one-way coupled and – –: four-way coupled.

PDFs of particle dynamic quantities for each flow region were again analysed to further understand the local behaviour of particles. Figure 4.20 shows the PDFs in the viscous, buffer, log-law and bulk flow regions of the pipe flow for particles Stokes number, $St^+ \cong 58$. The top-left plot is for the particle velocity in the radial direction, whilst the top-right plot considers the azimuthal direction. The lower-left plot is the particle slip velocity and the lower-right is the axial direction particle velocity. The radial component PDFs demonstrate a wider spread of velocities in the four-way case compared to the one-way case. A broader spread of azimuthal velocities is also observed when particle collisions are considered. In both cases, there is a minor bias towards negative velocities due to the influence of gravity. PDFs of the slip velocity are also show and, due to inter-particle collision, these PDFs tend to increase in the four-way coupled case, with particle interactions leading to a redistribution of velocities based on local collisions rather than being influenced predominantly by the local flow field. Lastly, the PDFs of the particle's streamwise velocity are provided, with the four-way coupled case again exhibiting a wider range of velocities, which tend to increase throughout the domain.

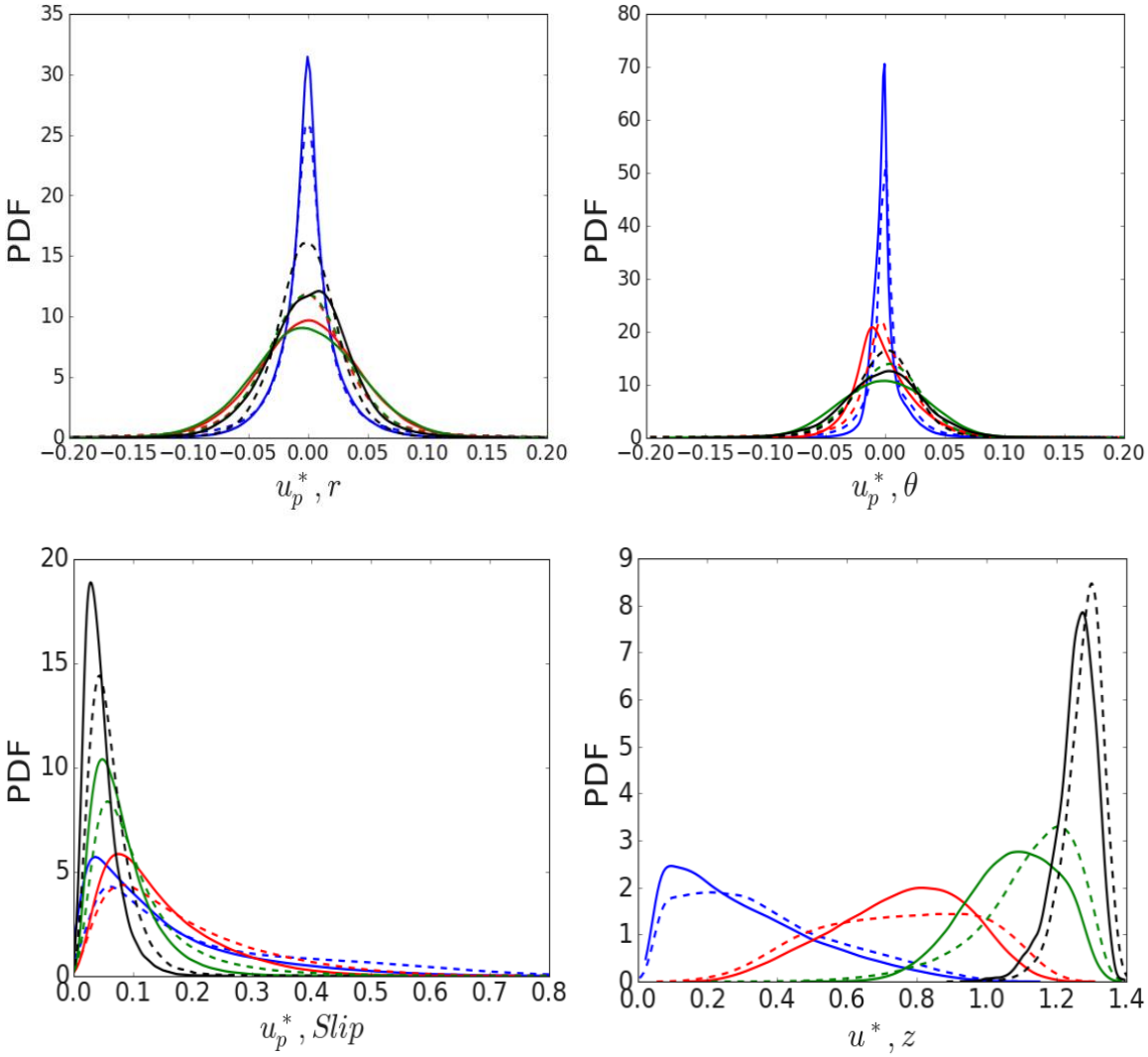

Figure 4.20: Probability density functions of particle dynamic properties within the viscous, buffer, log-law and bulk flow regions of the pipe with $St^+ \cong 58$ particles. Top-left: radial velocity, top-right: azimuthal velocity, lower-left: slip velocity, lower-right: axial velocity. —: one-way coupled, − −: four-way coupled. Blue: viscous sublayer, red: buffer layer, green: log-law region, black: bulk flow.

4.4 LES validation at $Re_\tau \approx 720$

In Chapter 6, a correlation of experimental data is developed for predicting the critical deposition velocity of particles in a flow, based on particle resuspension data from a bed within a pipe, as is used to collapse both deposition and resuspension experimental datasets. Using the numerical models described, depositing pipe flows are run over the range of this correlation to assess whether the numerical model is able to successfully predict the onset of particle

deposition, in line with the developed correlation. High Reynolds number flows were necessary to cover the range of this correlation, and this was not feasible with the DNS-based approach since, due to time constraints, the total number of particles used with the DNS-LPT coupled simulations was limited to 2 million and new high-resolution meshes would need to be generated which would significantly increase compute times. As an alternative, it was decided use a less computationally demanding LES-LPT approach. We chose the latter approach since there are already thoroughly validated and tested algorithms for LES within NEK5000 and, as noted, the computing times are substantially less than those of DNS-based methods. The results of an overlapping LES at $Re_\tau \approx 720$, at which a DNS-based method could also be run, are here validated against the equivalent DNS run and experimental datasets.

The pseudo-colour contour plots in Figure 4.21 show the instantaneous fluid velocity in the streamwise direction as predicted by the LES technique at $Re_\tau \approx 720$. These depict the turbulent velocity field present in the pipe flow. The streamwise direction in the pipe's centre is typically where the highest velocities occur, and they exhibit a strong positive conveying motion.

Figure 4.22 shows the predicted LES mean streamwise velocity profile at a shear Reynolds number, $Re_\tau \approx 720$. In order to validate this, it was compared with the results of the present DNS at the same shear Reynolds number, as well as El Khoury et al.'s (2013) DNS results, at $Re_\tau \approx 720$, and Singh's et al.'s (2018) DNS at $Re_\tau \approx 640$. The present LES simulation is ween to agree well with the present DNS and that of El Khoury et al. (2013), but slightly differs from Singh's et al. (2018) predictions. This slight deviation is most likely caused by the difference in Reynolds number, as Singh's et al. (2018) simulation used a lower shear Reynolds number than in the present work. The results are also compared with the den Toonder et al. (1997) experimental dataset at $Re_\tau \approx 630$. Given the difference in Reynolds number, this again provides a reasonable validation of the present LES simulation.

Figure 4.23 displays the LES predicted axial, $u'^*_{z,rms}$, radial, $u'^*_{r,rms}$ and azimuthal, $u'^*_{\theta,rms}$ normal stress profiles, and the Reynolds shear stress profile, $< u'_z\, u'_r >^*$, at $Re_\tau \approx 720$. These all exhibit good agreement with the results of the present DNS, and the results of El Khoury et al. (2013), Singh et al. (2018) and den Toonder et al. (1997). Some minor deviations occur towards the wall, and there is some deviation with the results of den Toonder et al. (1997) in

the inner regions of the flow, as previously observed in Fig. 4.9. Overall, however, these results generate confidence in the present LES technique. Figures 4.212(b) and 4.23(b) provide further details regarding the mean axial velocity profile and normal and shear stresses by plotting the same variables on a logarithmic scale.

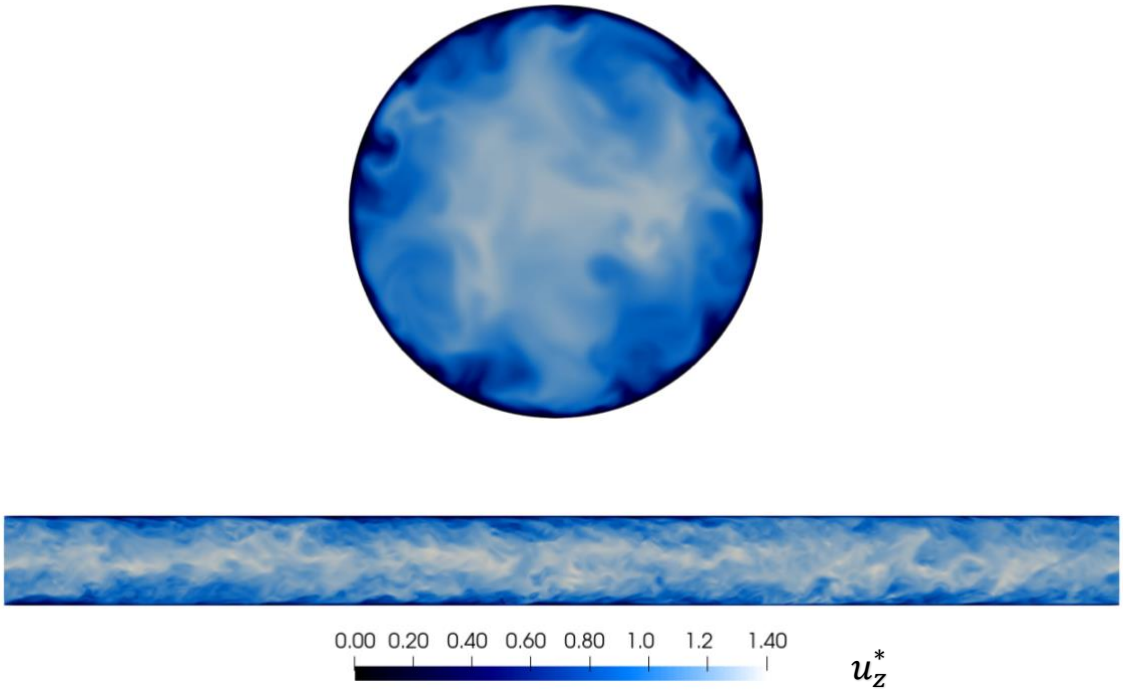

Figure 4.21: LES pseudo-colour visualisation of the instantaneous axial velocity normalised by the bulk velocity, U_B, at $Re_\tau \approx 720$.

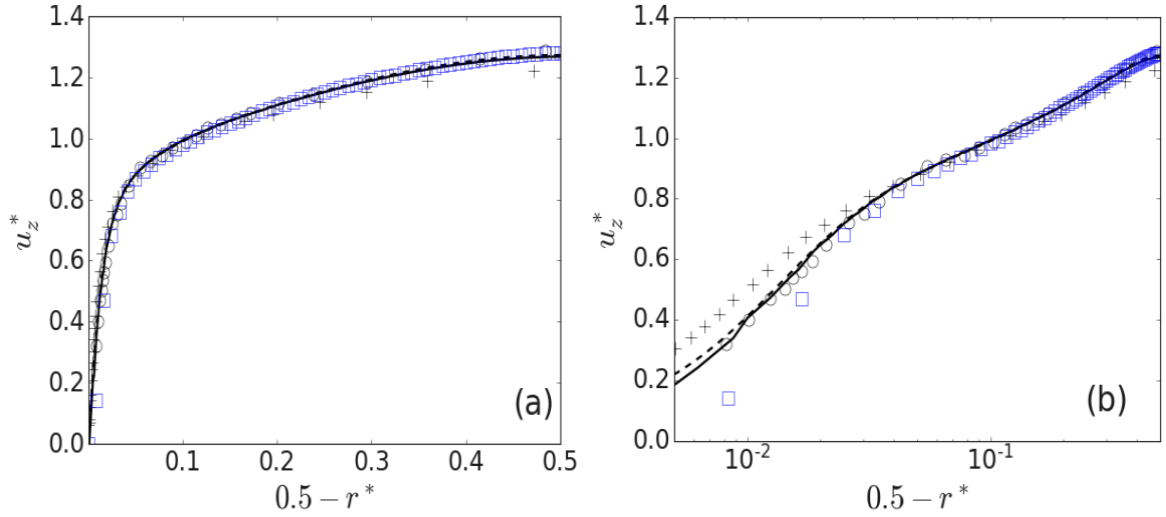

Figure 4.22: Mean streamwise velocity profiles for LES at $Re_\tau \approx 720$. —: present DNS, ⊡: present LES, − −: El Khoury et al. (2013) DNS, ○: den Toonder et al. (1997) experimental dataset at $Re_\tau \approx 629$, +: Singh et al. (2018) DNS at $Re_\tau \approx 640$. (a): linear scale, (b): log scale.

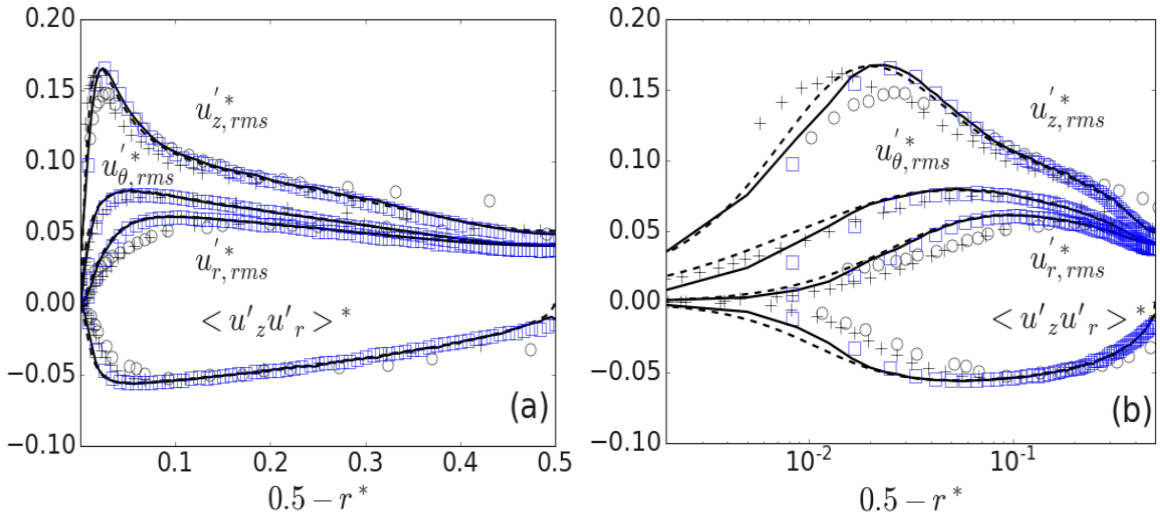

Figure 4.23: Validation of rms fluctuating velocity and shear stress profiles at Re_τ ≈720. —: present DNS, ⊡: present LES, − −: El Khoury et al. (2013) DNS, ○: den Toonder et al. (1997) experimental dataset at $Re_\tau \approx 629$, +: Singh et al. (2018) DNS $Re_\tau \approx 640$. (a): linear scale, (b): log scale.

4.5 Effect of one-way and four-way coupling on particle-laden turbulent pipe flow statistics

Having observed some interesting effects due to four-way coupling in the validation section, as compared to one-way coupled results, here we perform and investigate in more detail simulations at a high Reynolds number in order to elucidate the effects of coupling in more detail. A fully resolved particle-laden turbulent pipe flow with a shear Reynolds number based on the pipe diameter, $Re_\tau \approx 720$, is used for the simulations. This time, the four-way coupled approach also includes the effects of particle agglomeration, with simulations at a high concentration with a volume fraction, $\phi_P \geq 10^{-3}$ in order to represent more realistic industrially relevant flows. Such a high concentration has been demonstrated to be required in order to encourage particle collisions and ensure sufficient agglomeration of particles (Ferrante and Elghobashi, 2003; Njobuenwu and Fairweather, 2017). The values of the particle-phase parameters represent those of calcite in water, a system often used to simulate nuclear waste transport flows, and the details are presented in Table 4.4. These parameters were utilised for both the one-way and four-way coupled simulations, as well as for all simulation cases in Chapter 5. The one-way, four-way and four-way coupled with agglomeration results were all obtained using 150,000 randomly injected particles initially assigned the local fluid velocity. 100 μm particles with a density ratio (relative to the fluid density) of 2.71 were used in all the

simulations to resemble calcite in water. In the case of four-way coupling with agglomeration, once significant numbers of collisions had occurred statistical data was gathered to examine the influence of agglomeration on mean and normal and shear stress profiles.

Table 4.4: Particle phase parameters used in high concentration one-way, four-way and four-way with agglomeration simulations.

Parameter	$Re_\tau \approx 720$
Particle diameter, d_p	100 μm
Particle diameter, d_p^*	0.005
Axial length	12.5D
Number of particles, N_p	150,000
Bulk Stokes number, St_B	0.044
Shear Stokes number, St^+	1.951
Density ratio, ρ_p^*	2.71
Volume fraction, ϕ_p	0.001
Particle and fluid timestep, Δt^*	0.001

Figures 4.24 through 4.27 compare the one-way and four-way coupled velocity profiles of the fluid flow and the particles. At first glance, the difference in the fluid and particle velocities caused by the one-way and four-way coupling appears to be minimal. However, the four-way mean velocity profile is slightly higher than the one-way profiles due to inter-particle interaction, e.g. Fig. 4.24 and Fig. 4.26. This is to be expected as the bulk particle Stokes number, $St_B = 0.044$, is low, therefore particles are greatly influenced by the local flow, and due to their low inertia, struggle to impart momentum back to the fluid. Moving forward, the validation simulations as well as the present results do demonstrate that it is vital to utilise four-way coupled simulations since the impact of such coupling on the fluid dynamics of the flow cannot be disregarded. The number of particle collisions also increases significantly when particle concentrations are high enough. For these reasons, four-way coupling is used in all of the simulations performed in Chapters 5 and 6. The logarithmic scales are shown on the right side of the above plots to indicate whether any near-wall impacts are more noticeable, and it is clear from Fig. 4.25 and Figure 4.27 that the rms radial velocity fluctuations are reduced.

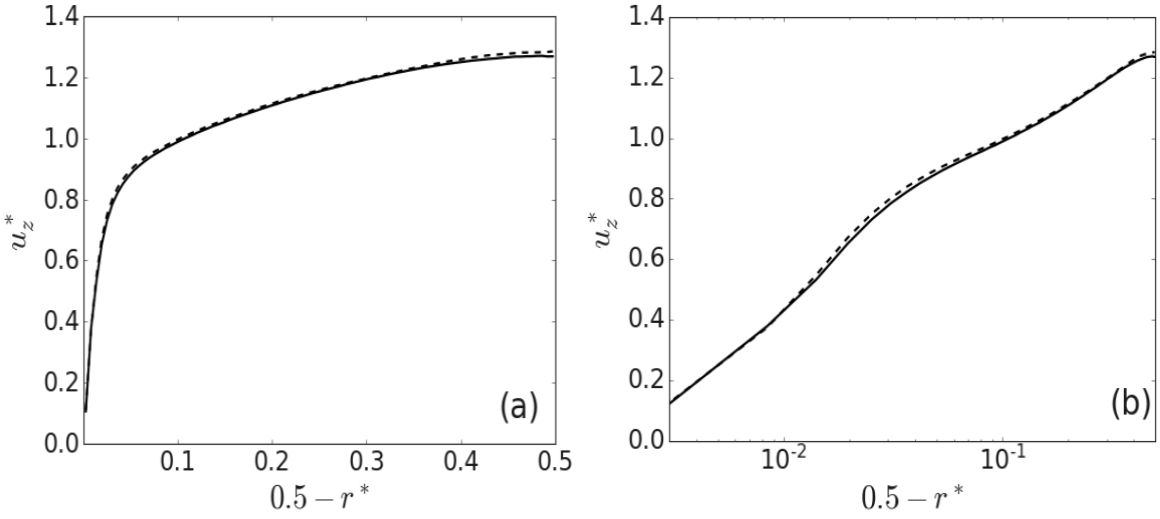

Figure 4.24: Fluid mean streamwise velocity profiles for particle-laden turbulent pipe flow at Re_τ ≈720 representing calcite in water. —: one-way coupled and − −: four-way coupled. (a): linear scale, (b): log scale.

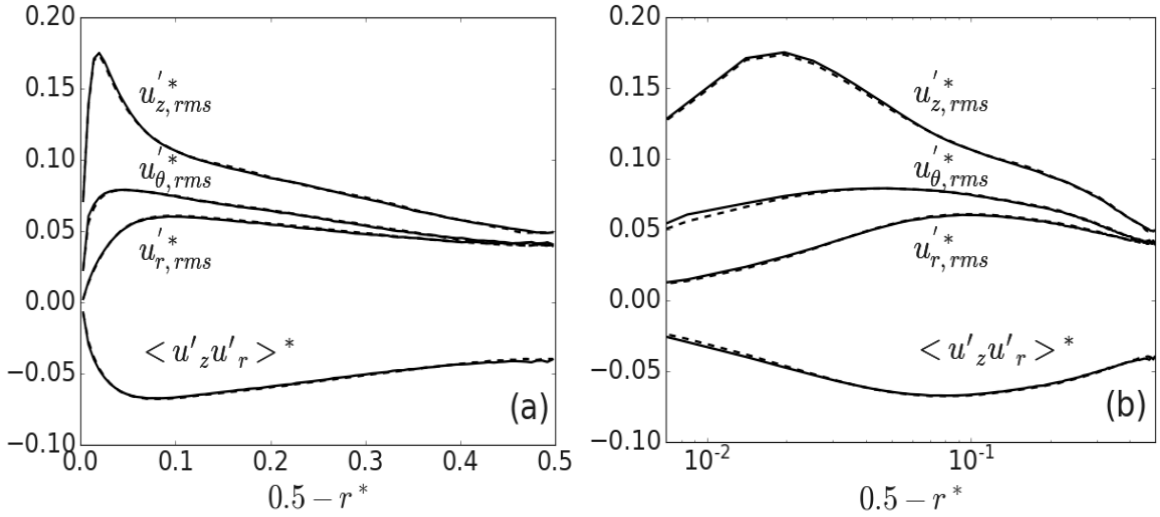

Figure 4.25: Fluid rms of velocity fluctuations and Reynolds shear stress profiles for particle-laden turbulent pipe flow at $Re_\tau \approx 720$ representing calcite in water. —: one-way coupled and − −: four-way coupled. (a): linear scale, (b): log scale.

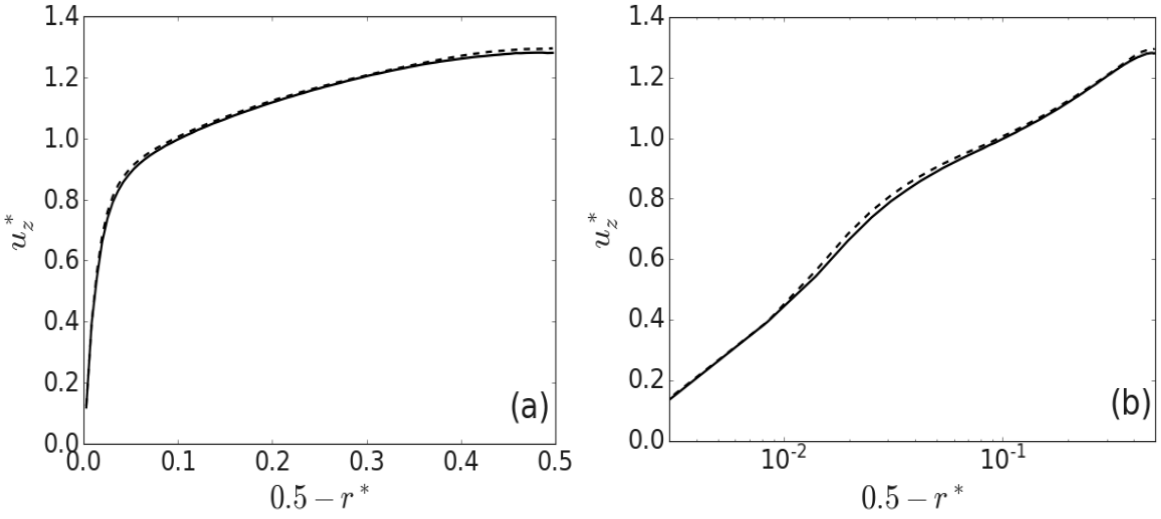

Figure 4.26: Particle mean streamwise velocity profiles for particle-laden turbulent pipe flow at $Re_\tau \approx 720$ representing calcite in water. —: one-way coupled and − −: four-way coupled. (a): linear scale, (b): log scale.

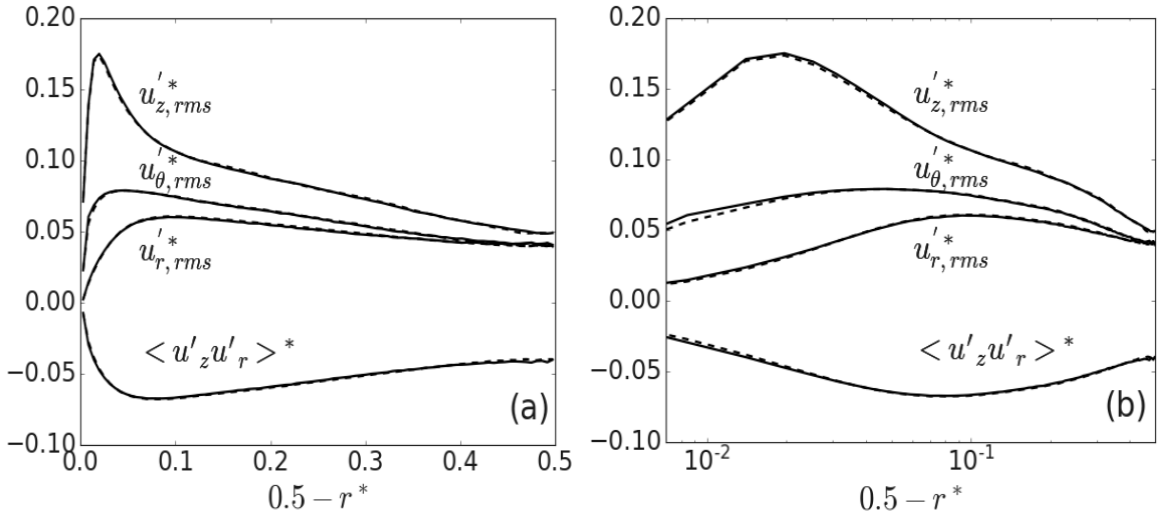

Figure 4.27: Particle rms of velocity fluctuations and Reynolds shear stress profiles for particle-laden turbulent pipe flow at $Re_\tau \approx 720$ representing calcite in water. —: one-way coupled and − −: four-way coupled. (a): linear scale, (b): log scale.

Figures 4.28 through 4.31 show the mean streamwise velocity, and normal and shear stress profiles, for the four-way and four-way coupled with agglomeration simulations for calcite-water flows at shear Reynolds number, $Re_\tau = 720$. To make these predictions, the same configuration was employed as before, and for the four-way with agglomeration case, a restitution coefficient, $e_n = 0.4$, and a Hamaker constant, H = 22.3 zJ, were used. The mean streamwise fluid velocity component of the four-way coupled with and without agglomeration

comparison exhibits negligible difference, however with agglomeration it is shown to have an influence on the particle velocity component. These effects are observable in the flow's buffer, log-law, and bulk flow regions in Fig. 4.31, reducing the velocity in each case. As particles agglomerate, therefore, they grow larger and heavier, increasing their inertia and make it more difficult for them to accelerate, resulting in a lower the overall velocity. Since the Stokes number is low in this case, the effect anticipated by Winkler et al. (2006) that higher Stokes number particles increase mean non-streamwise velocities was not observed. Figures 4.29 and 4.31 display the four-way and four-way with agglomeration comparisons of the fluid and particle normal and shear stresses. As noted, when the concentration of particles increases, the impact of the particles on the turbulent flow should become more noticeable. However, the fluid's rms of velocity fluctuations and shear stress results in Fig. 4.29, and the corresponding particle values in Fig. 4.31 appear largely unaffected by the influence of agglomeration apart from close to the wall. This is again due to the relatively low particle Stokes number used in these simulations.

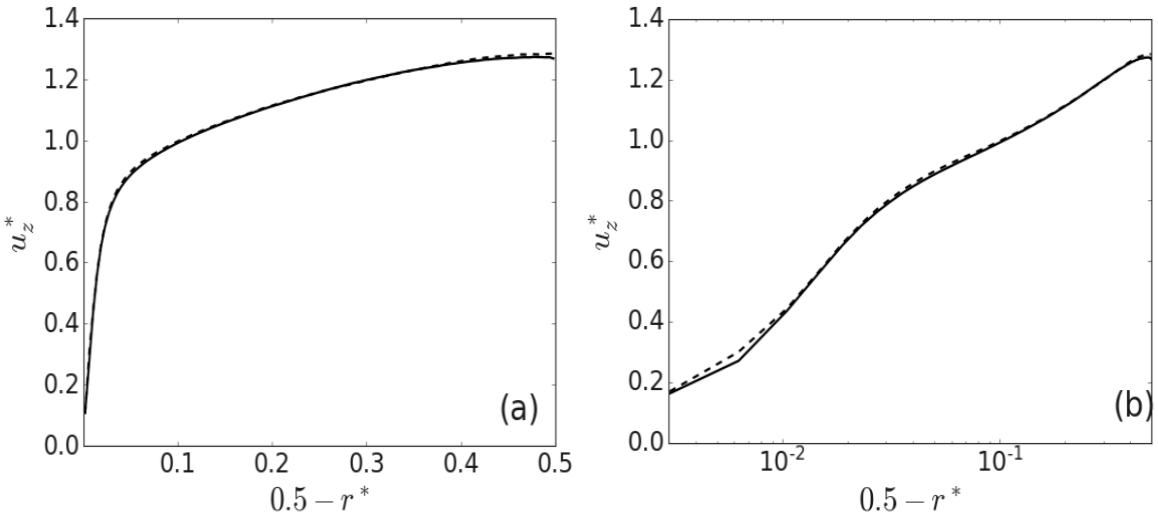

Figure 4.28: Fluid mean streamwise velocity profiles for particle-laden turbulent pipe flow at $Re_\tau \approx$ 720 representing calcite in water. − −: four-way coupling and —— : four-way coupling with agglomeration. (a): linear scale, (b): log scale.

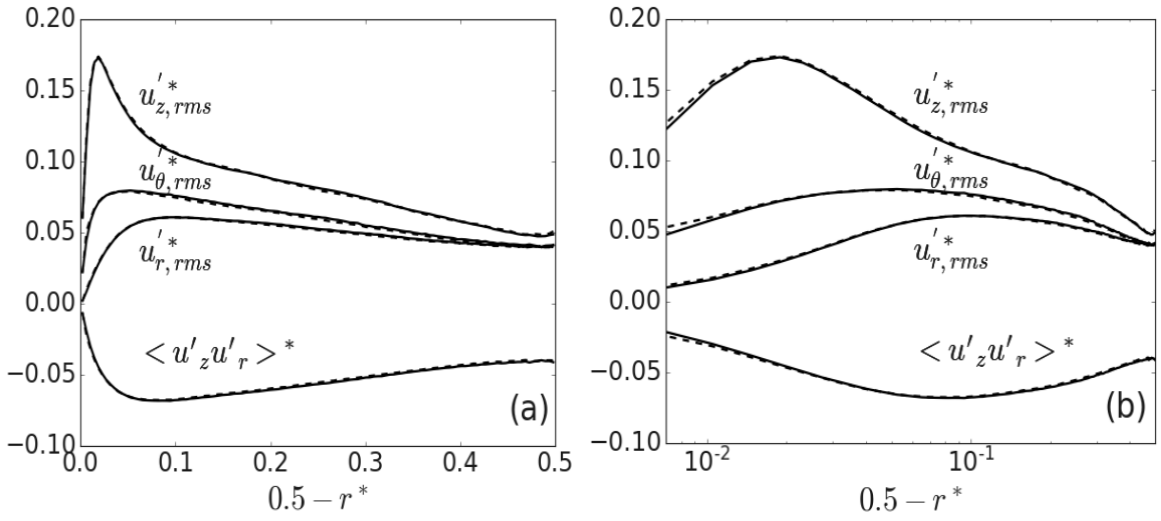

Figure 4.29: Fluid mean rms velocity fluctuations and Reynolds shear stress profiles for particle-laden turbulent pipe flow at $Re_\tau \approx 720$ representing calcite in water. − −: four-way coupling and —: four-way coupling with agglomeration. (a): linear scale, (b): log scale.

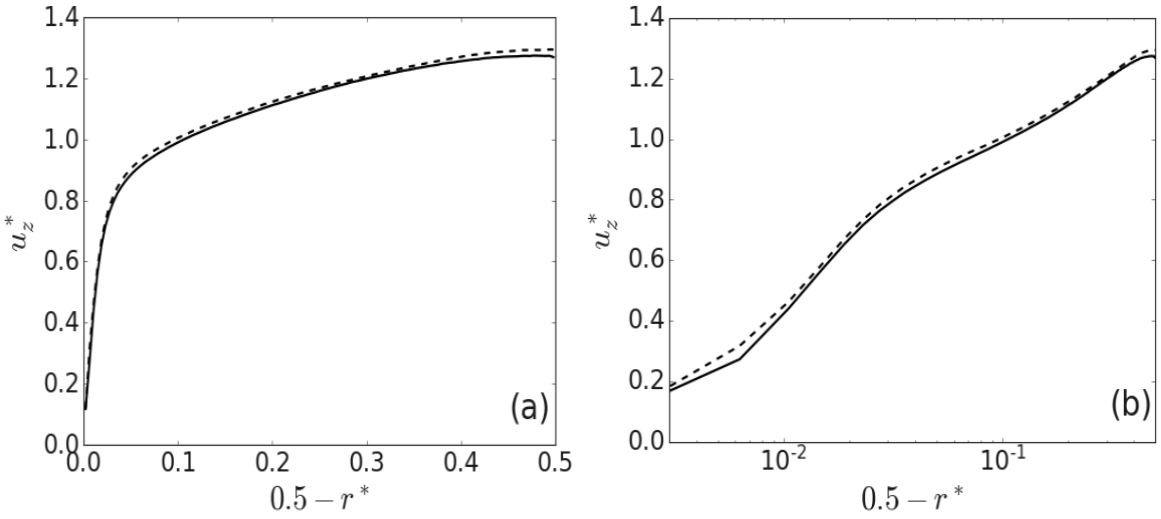

Figure 4.30: Particle mean streamwise velocity profiles for particle-laden turbulent pipe flow at $Re_\tau \approx 720$ representing calcite in water. − −: four-way coupling and —: four-way coupling with agglomeration. (a): linear scale, (b): log scale.

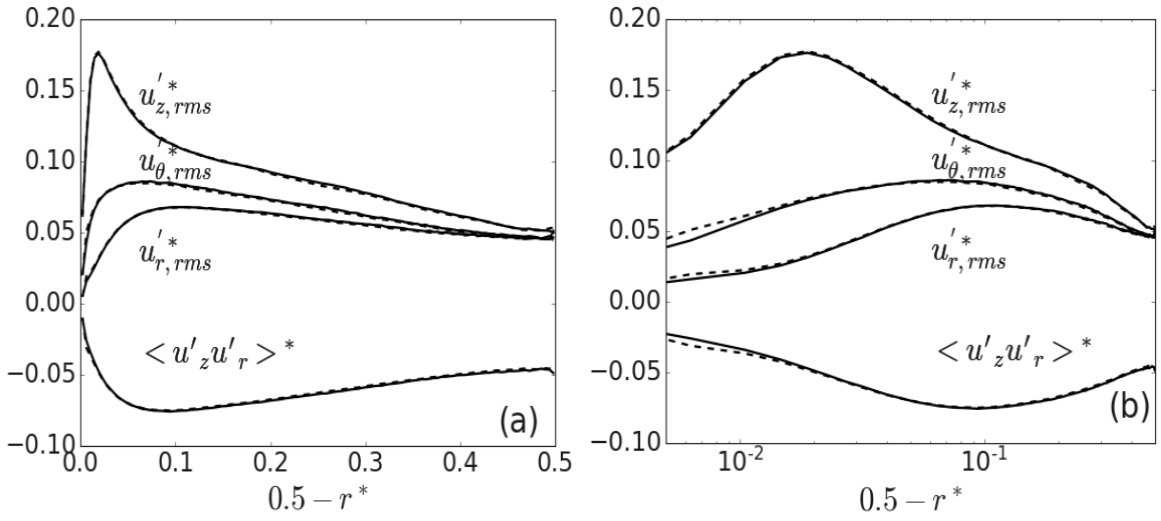

Figure 4.31: Particle mean rms velocity fluctuations and Reynolds shear stress profiles for particle-laden turbulent pipe flow at $Re_\tau \approx 720$ representing calcite in water. − −: four-way coupling and —: four-way coupling with agglomeration. (a): linear scale, (b): log scale.

4.6 Conclusions

The results of single-phase direct numerical simulations for a fully-developed turbulent pipe flow at three distinct turbulent bulk Reynolds numbers, $Re_B \approx$ 3,975, 5,300, and 11,700, have been detailed in this chapter. The results were used as a validation and compared to literature DNS and experimental datasets to demonstrate the effectiveness of the implemented Nek5000 simulation. All results of turbulent pipe flows obtained using the continuous phase solver, Nek5000, at various shear Reynolds numbers were in good agreement with those of earlier high-accuracy DNS and experimental data. Profiles of mean streamwise velocity, and normal and shear stress profiles, within the flow were gathered to validate the code implemented. Overall, the agreement obtained given confidence in the accuracy of the present numerical approach to predicting turbulent single-phase flows.

A further DNS-based study was carried out, coupled with Lagrangian particle tracking, for fully developed turbulent particle-laden pipe flows, with mean velocity, and normal and shear stress, profiles within the flows generated. The fully-developed pipe flows were performed with one-way and four-way coupling between the particles and the flow field, carried out at different particle Stokes numbers and flow Reynolds numbers. A constant pressure gradient along the pipe was maintained and the gravitational force was applied in the streamwise direction for

both validations. The results obtained were again demonstrated to be in good agreement with other simulation results in the literature and experimental datasets.

The mean particle concentration profiles for one-way and four-way coupled simulations within the turbulent pipe flow were also investigated. It was evident that higher particle Stokes numbers led to a larger concentration of particles near the wall, as the particles migrate towards the wall over time through the effects of turbophoresis. One-way coupling was found to lead to higher near-wall concentrations than for four-way coupled results, since four-way coupling tends to hinder the wall-accumulation process, likely due to particle collisions near the wall leading to increased rms velocity fluctuations. Subsequently, and to further understand the local behaviour of particles, PDFs of particle dynamic quantities in the viscous, buffer, log-law and bulk flow regions of the pipe were also examined. The radial direction showed a larger spread in velocities when four-way coupling was included which suggests that collisions lead to anisotropy of local velocities and a redistribution of particle momenta, decoupling the particles from the local fluid velocity field.

Finally, the effect of one-way and four-way coupling with and without particle agglomeration was also investigated. Overall, the influence of one-way and four-way coupling with and without agglomeration on fluid and particle-laden turbulent pipe flows statistics was shown to be small for low particle Stokes numbers. These results do, however, give insights into particle behaviour which will be considered further in relation to the work reported in Chapters 5 and 6.

5 ASSESSMENT OF BEHAVIOURAL MODIFICATION TECHNIQUES

5.1 Introduction

Very few DNS-based studies have been performed in the past to investigate turbulent pipe flows in the presence of a particulate phase. In those limited cases, multiphase DNS investigations have mainly used one-way coupling between the particles and the fluid, and the simulations have generally been at low Reynolds numbers. There is also a noticeable absence of four-way coupling and particle agglomeration studies, particularly in cylindrical geometries, despite most industrial flows possessing high volume fractions where the interactions between particles are of importance to emergent phenomena such as deposition and preferential concentration. As computational power advances it is now possible to perform such complex particle-laden flow simulations which are important in predicting the long-term dispersive and aggregation behaviour of industrial flows. In this chapter, by using high-accuracy and robust simulation techniques, the impact of behavioural modification techniques on particle dispersion and agglomeration has been investigated using a fully coupled DNS-LPT approach.

A fully resolved particle-laden turbulent pipe flow with shear Reynolds number based on pipe diameter, $Re_\tau = 720$, is used to simulate four-way coupled flows with agglomeration at high concentration with a volume fraction, $\phi_P \geq 10^{-3}$, except for when studying the influence of Reynolds number. Such a high concentration is required to encourage particle collisions and ensure sufficient agglomeration of particles (Ferrante and Elghobashi, 2003; Njobuenwu and Fairweather, 2017).

In order to predict collisions and agglomeration in a large eddy simulation of a turbulent channel flow, Njobuenwu and Fairweather (2017) deployed a deterministic approach, with the authors incorporating a van der Waals force and energy-balance-based agglomeration

condition. They observed that there was an increase in particle aggregation with decreasing restitution coefficient in their results. Mortimer et al. (2020) extended the Njobuenwu and Fairweather (2017) deterministic model for use with DNS. These authors investigated particle-particle agglomeration using a fully coupled turbulent channel flow simulation at shear Reynolds number, $Re_\tau = 180$. They also studied the effect of particle size at a fixed volume fraction, $\phi_P \geq 10^{-3}$. It was observed that smaller particles tend to agglomerate faster to form larger particle clusters more quickly. These techniques are here extended to pipe flow geometries, more accurately representing industrial flows.

In this chapter, the effects of interparticle collisions and particle agglomeration in turbulent pipe flows at a moderately high Reynolds number, $Re_\tau = 720$, are investigated with the emphasis placed on the analysis of results to determine particle dispersion, collision, and agglomeration behaviour. It is crucial to comprehend the fundamental mechanisms of particle collision and agglomeration since these processes are important to many different scientific and industrial domains. Understanding the forces that regulate these processes is crucial for controlling particle interactions and providing the ability to either encourage or discourage particle interactions and eventual agglomerations. When discrete particles collide and interact with one another, particle collisions and agglomeration may occur. Accurately predicting the effects of these events is essential for optimising nuclear waste transport operations.

The variation of important parameters in DLVO theory is also investigated to determine the impact of behavioural modification effects, i.e. studying the impact of key parameters on particle interactions to obtain a desired flow behaviour. These modifications change the way particles interact by varying different terms in the DLVO interactions potentials, as well as the kinematics of the collisions themselves. The reduced surface potential ($\Theta = 16$, 20 and 24 mV), inverse Debye length, ($\kappa = 3.04 \times 10^{-9}$, 3.04×10^{-8}, and 3.04×10^{-10} m), ambient temperature of the suspension (T_f =264, 293 and 322 K), the coefficient of normal restitution ($e_n = 0.2$, 0.4 and 0.6), the Hamaker constant ($H = 7.84$, 22.3 and 36.76 zJ) and the shear Reynolds number ($Re_\tau = 360$ and 720) are some of the parameters which are examined. According to the work of Mortimer and Fairweather (2021), these variables, particularly those associated with the van der Waals interaction (Hamaker constant) and collision kinematics (coefficient of restitution), were found to have the greatest influence on collision dynamics in particle-laden channel flow simulations and are therefore being further studied in the current pipe geometry.

5.2 Modelling and simulation of energy balance-based agglomeration using DLVO theory

5.2.1 Influence of electric double layer

Simulations were performed with and without the electric double layer (EDL) repulsion term in the agglomeration determination algorithm to investigate the impact of EDL on the rate of agglomeration in a pipe geometry. For these simulations, a shear Reynolds number of $Re_\tau = 720$ was utilized along with the restitution coefficient, e_n = 0.4, and the Hamaker constant, H =22.3 zJ, to represent 100 μm diameter calcite particles in water. To account for the influence of the EDL, the key parameters incorporated were the reduced surface potential, $\Theta = 20$mV, inverse Debye length, κ = 3.04 x 10^{-9} m, and the temperature of the suspension, $T_f = 293$K. Table 5.1 shows the values of the particle-phase characteristics representing calcite in water for the simulations performed using both forces in DLVO theory. Calcite is a simulant that is frequently utilised in nuclear waste transport process investigations (Sadowski, 1994).

To initialize the simulations, 150,000 randomly injected particles were assigned a spectrally interpolated fluid velocity. Four-way coupling was used throughout, with both solely van der Waals and full DLVO theory terms used to determine agglomeration as described in the Chapter 3 Research Methodology. In each simulation a particle volume fraction of $\phi_p = 1 \times 10^{-3}$ and a density ratio of 2.71 were used. Once a considerable number of collisions had occurred (chosen for each simulation such that the collision statistics were smooth and statistically stationary), data on collision and agglomeration location and frequency was obtained to investigate the impact of including the effects of the electric double layer. Mortimer et al. (2020) investigated particle agglomeration over $0 \leq t^* \leq 100$ and obtained favourable findings. The particle agglomeration processes in this thesis were studied using simulations that were performed for a total time of t^*=120, calculated across 120,000 timesteps.

The electric double layer effect occurs as a result of interactions between interfacial pairs of ion layers or at the interface between a particle surface and a surrounding electrolyte solution. Here we aim to determine the extent of these interactions by studying agglomeration both with and without these effects considered. The time evolution of agglomerates of various sizes, from singlets to quintuplets, is shown in Figure 5.1, along with the effect of the electric double layer

on the overall number of agglomerates of size N_p as a function of t^*. The findings show that there is no significant difference in the rate of agglomeration formation when the electric double layer model is included. The singlet and doublet particles in particular are not significantly affected by the electric double layer effect. For triplets, it appears that there are more agglomerates without the electric double layer interaction starting at around t^* = 8, but at about t^* = 60, the number of agglomerates with and without EDL coincides. Quadruplet particles exhibit the same behaviour. For the base case, the impact of an electric double layer on calcite particles suspended in water is therefore negligible. The collision (upper and lower left) and agglomeration (upper and lower right) event locations from the final 20,000 timesteps of the base-case with EDL simulation are shown in Figure 5.2. The development of particle collision streaks is mostly influenced by the collisions that take place as particles move through the medium of the flow. Particle size, volume fraction, velocity, Van der Waals forces, and electrostatic forces all play significant roles in determining the strength and frequency of particle collisions.

Table 5.1: Particle phase parameters used in base case study with and without the effects of electric double layer repulsion.

Parameter	**Value**
Particle diameter, d_p (μm)	100
Particle diameter, d_p^*	0.005
Number of particles, N_p	150,000
Bulk Stokes number, St_B	0.044
Shear Stokes number, St^+	1.951
Restitution coefficient, e_n	0.4
Hamaker constant, $H\ (zJ)$	22.3
Shear Reynolds number, Re_τ	720
Reduced surface potential, Θ (mV)	20
Inverse Debye length, κ (m)	3.04×10^{-9}
Temperature of suspension, T_f (K)	293
Density ratio, ρ_p^*	2.71
Volume fraction, ϕ_p	0.001
Simulation timestep, Δt^*	0.001

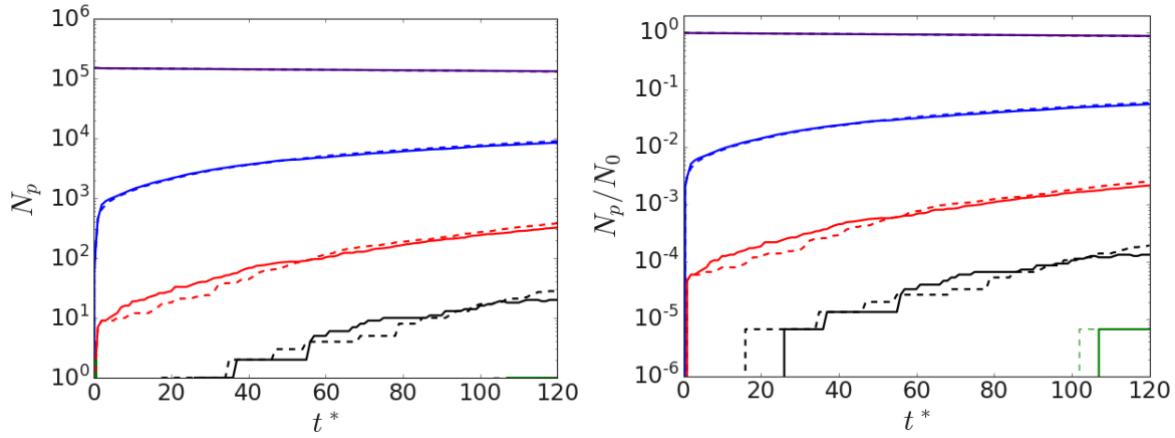

Figure 5.1: Influence of electric double layer on total number of agglomerates of size N_p, normalised by total number of particles as function of time, t^*. Indigo: singlets; blue: doublets; red: triplets; black: quadruplets and green: quintuplets. The number of particles is normalised by the total number of particles in the domain (left). —: base case with EDL, − −: without EDL.

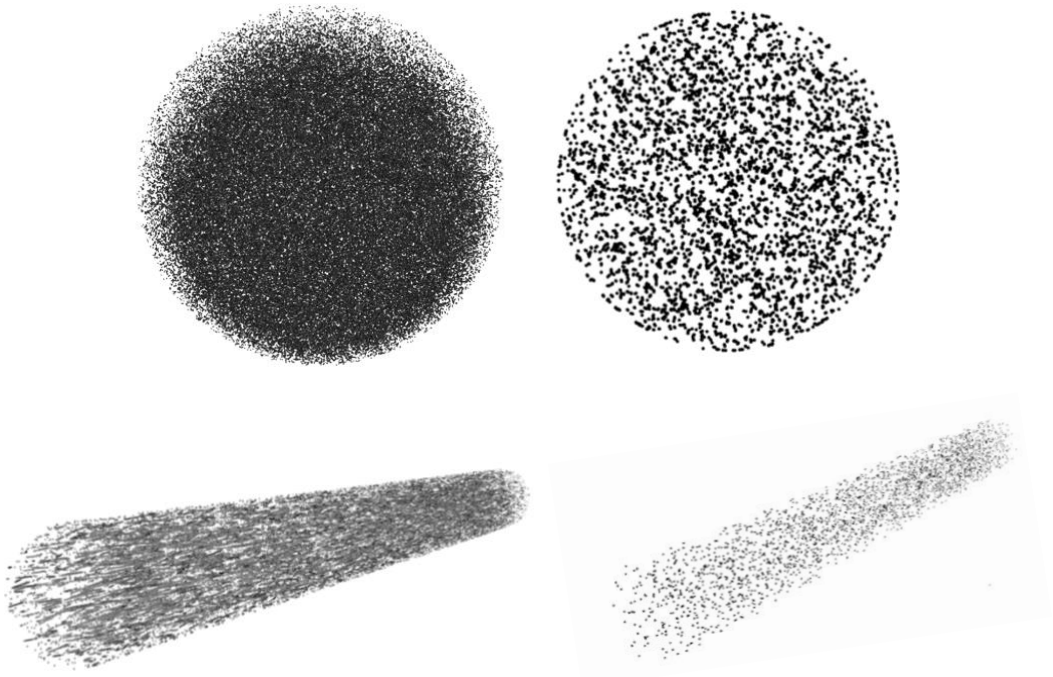

Figure 5.2: Position of locations of collision (left) and agglomeration (right) events captured throughout a full simulation – base case with EDL.

5.2.2 Effect of variation of temperature

Though the base case shows a negligible effect of EDL, it is important to determine whether modifications to EDL-related parameters will cause the term to cause a more pronounced influence. Temperature plays a critical role in electric double layer repulsion, as explained in the Chapter 3 Research Methodology, Section 3.3.10. Here, we explore the effect of temperature on agglomeration rate, and the outcomes are then compared to the base case with EDL. The effects of a 10% temperature increase (T_f = 322K) and decrease (T_f = 264K) were studied. Figure 5.3 shows the influence of the temperature on the total number of agglomerates of size N_p as a function of t^*. Agglomerates with singlets to quintuplets of particles are monitored as they change over time. When examining the formation of triplets and quadruplets, it can be seen that the lower temperatures encourage particle collisions and the possibility for agglomeration, although this impact is negligible, and temperature change exhibits little impact on the dynamics of the particle interactions. Mortimer et al. (2021) also found that there is relatively little effect of temperature on particle interaction dynamics for micron-scale particles.

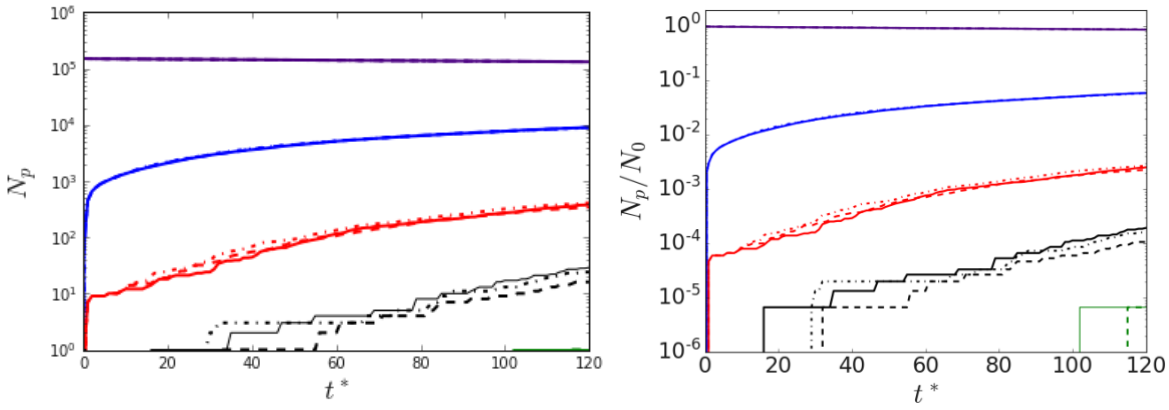

Figure 5.3: Influence of the temperature on total number of agglomerates of size N_p, normalised by total number of particles as function of time, t^*. Indigo: singlets; blue: doublets; red: triplets; black: quadruplets and green: quintuplets. The number of particles normalised by total number of particles in the domain (left). —: (Θ=20; T_f = 293), − −: $T_f = 322$, and −·−: $T_f = 264$.

5.2.3 Effect of reduced surface potential

The reduced surface potential is another important parameter in the electric double layer repulsion force. This term refers to the electrical potential differential between a particle's surface and its surroundings. This can be caused by a variety of factors that impact the charge distribution and interactions at the particle's surface. A higher temperature can promote charge mobility and diffusion, which reduces surface potential and redistributes charges. Reduced surface potential is also a result of the interaction of various elements, including the zeta potential, the elementary electric charge, and the ionic valency of the electrolyte. The effect of changing the potential on the number of agglomerates of size N_p is depicted in Figure 5.4. Again, for the base case with EDL, Θ =20 mV, and higher reduced surface potential, the production of agglomerates with constituent numbers ranging from singlets to quintuplets is observed, whereas only quadruplets are seen for the lower reduced surface potential. For all three reduced surface potential simulations, the formation of doublet particles or the tendency of singlets to form larger agglomerates stays roughly the same during the course of the simulation. Furthermore, the influence on triplet or quadruplet particle formation is equally negligible. Generally, the modifications to the reduced surface potential lead to negligible effects on the agglomeration rate for calcite particles in water.

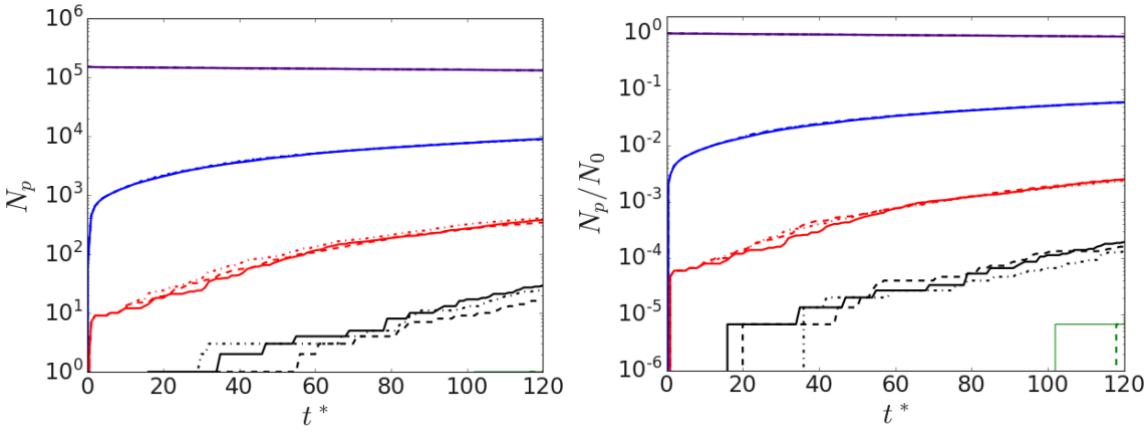

Figure 5.4: Influence of reduced surface potential on total number of agglomerates of size N_p, normalised by total number of particles as function of time, t^*. Indigo: singlets; blue: doublets; red: triplets; black: quadruplets and green: quintuplets. The number of particles normalised by total number of particles in the domain (left). —: Θ =20 mV, – –: Θ =24 mV, and –·–: Θ =16 mV.

5.2.4 Effect of inverse Debye length

Finally, the effect of the inverse Debye length, also referred to as the Debye screening length, κ, on agglomeration rate was examined. This behavioural modification, which results from the interaction of charged particles in the electrolyte solution and the surrounding fluid, is another important parameter in DLVO theory. The Debye screening length is dependent on the ionic strength of the aqueous phase, which can be modified through the addition of salts. The production of doublet, triplet, and quadruplet agglomerates in Figure 5.5 once again demonstrates that inverse Debye length has relatively little effect on the rate of agglomeration, even across a three orders of magnitude variation.

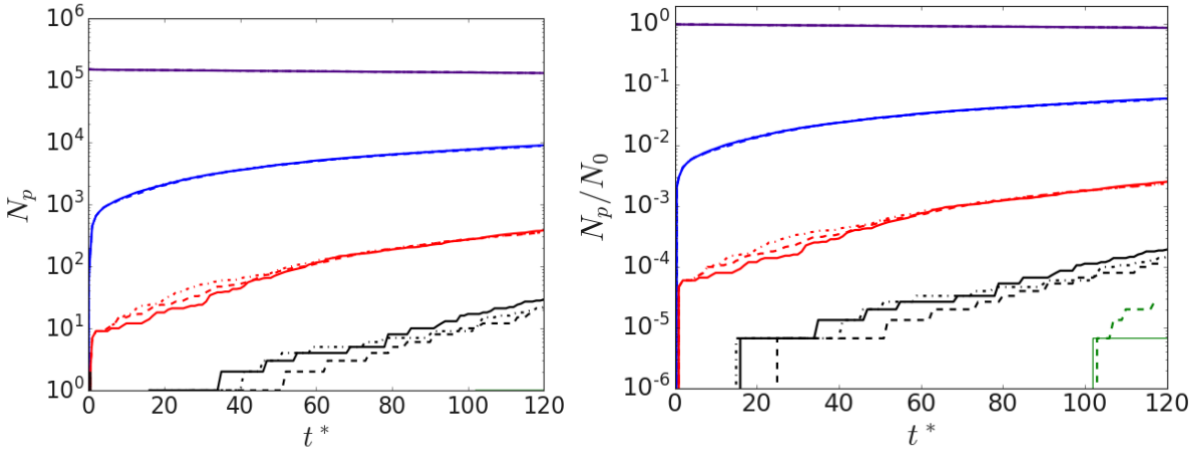

Figure 5.5: Influence of inverse Debye length on total number of agglomerates of size N_p, normalised by total number of particles as function of time, t^*. Indigo: singlets; blue: doublets; red: triplets; black: quadruplets and green: quintuplets. The number of particles normalised by total number of particles in the domain (left). —: κ =3.04 × 10^{-9}, − −: κ =3.04 × 10^{-8}, and −·−: κ =3.04 × 10^{-10}.

5.3 Modelling and simulation of energy balance-based agglomeration prediction – van der Waals interactions

According to the evidence presented above and in the previous study by Mortimer and Fairweather (2021), the influence of an electric double layer repulsion term on agglomeration dynamics is shown to be insignificant for flows of calcite particles in water. That said, the restitution coefficient, Hamaker constant and the Reynolds number have been demonstrated to exhibit the most impact on collision dynamics in Lagrangian particle tracking simulations (Njobuenwu and Fairweather, 2017). Mortimer et al. (2021) also conducted a detailed particle-resolved examination of the electric double layer in binary particle collisions and noted that the temperature and reduced surface potential have little impact on collision behaviour. Additionally, these authors found that the Reynolds number, Hamaker constant and coefficient of restitution had the strongest impacts on the interparticle interactions and consequently on collisions and agglomerations.

The restitution coefficient, Hamaker constant and Reynolds number do not feed into the electric double layer term of the full DLVO equation. Only the van der Waals' force components of the DLVO theory are responsible for post-collision cohesion, as well as the restitution coefficient, Hamaker constant, and Reynolds number variation. Therefore, in order to save time on computation, the EDL model was not applied while examining the impact of these modifications.

The same fully developed $Re_\tau = 720$ fluid flow was used to simulate four-way coupled flows with agglomeration for coefficient restitution and Hamaker constant variations using solely van der Waals interactions to determine agglomeration. The key parameters studied are the coefficient of restitution ($e_n = 0.2$, 0.4 and 0.6), the Hamaker constant ($H = 7.84$, 22.3 and 36.76 zJ), and lastly the shear Reynolds number ($Re_\tau = 360$ and 720) through additional simulations performed with a lower Re_τ. The varied simulation parameters are presented in Table 5.2, where e_n is the restitution coefficient, H is the Hamaker constant, Re_τ is the shear Reynolds number, σ is the yield pressure, and δ_0 is the minimum contact distance.

Table 5.2: Simulation mechanical and chemical properties for calcite-water agglomerating particle-laden pipe flows.

Run	**I**	**II**	**III**	**IV**	**V**	**VI**
e_n	0.4	0.2	0.6	0.4	0.4	0.4
H (zJ)	22.3	22.3	22.3	7.84	36.76	22.3
δ_0 (m)	2×10^{-10}	2×10^{-10}	2×10^{-10}	2×10^{-10}	2×10^{-10}	2×10^{-10}
σ (Pa)	3×10^{8}	3×10^{8}	3×10^{8}	3×10^{8}	3×10^{8}	3×10^{8}
Re_τ	720	720	720	720	720	360

5.3.1 Effect of variation of coefficient of restitution on collision and agglomeration

The effect of the coefficient of restitution, an important parameter which can be modified through a variety of means such as through particle coating or by adjusting the temperature of the system, is considered first. Figure 5.6 illustrates the time evolution of agglomerates of increasing size ranging from singlets to sextuplets and shows the influence of the restitution coefficient on the total number of agglomerates of size N_p as a function of t^*. Given that the agglomeration begins at time t^* = 0.01, the restitution coefficient demonstrated a fairly immediate effect on the agglomeration simulations with fixed volume fraction. At the value of the restitution coefficient employed, e_n = 0.4, the primary particle number has fallen from 150k originally injected particles to ~132k particles, or by around 12%, by the time it reaches t^* = 120. To investigate the effects of modifying the restitution coefficient on collision and agglomeration while keeping all other simulation parameters for calcite at their default values, two further simulations with e_n = 0.2 and 0.6 were performed at the same flow Reynolds number. The singlet particles were reduced from 150k particles to ~118k particles (by ~21.25%) and ~141k particles (by ~6.13%) for the restitution coefficients e_n= 0.2 and e_n= 0.6, respectively. The rate of agglomeration therefore increases, and the time required for the formation of higher-order aggregates decreases, as the restitution number decreases. When e_n= 0.2 and e_n= 0.6 simulations are compared to those with a restitution coefficient, e_n= 0.4, an additional ~9.26% of singlet particles are encouraged to aggregate for e_n= 0.2 whereas ~5.86% are discouraged from agglomeration for e_n= 0.6.

The results illustrate that the rate at which larger agglomerates are formed increases with a decrease in the normal restitution coefficient. This is due to more energy being dissipated in a collision leading to increased chances for the agglomeration condition to be satisfied. As the

simulation progresses, the existence of larger particles means the agglomeration likelihood diminishes due to larger colliding particles possessing lower van der Waals attraction and more total collision energy. Interestingly, given that the same low Stokes number of a particle was used, it appears that doublets, triplets, and other types of agglomerates develop at different rates for the three variations of restitution coefficient.

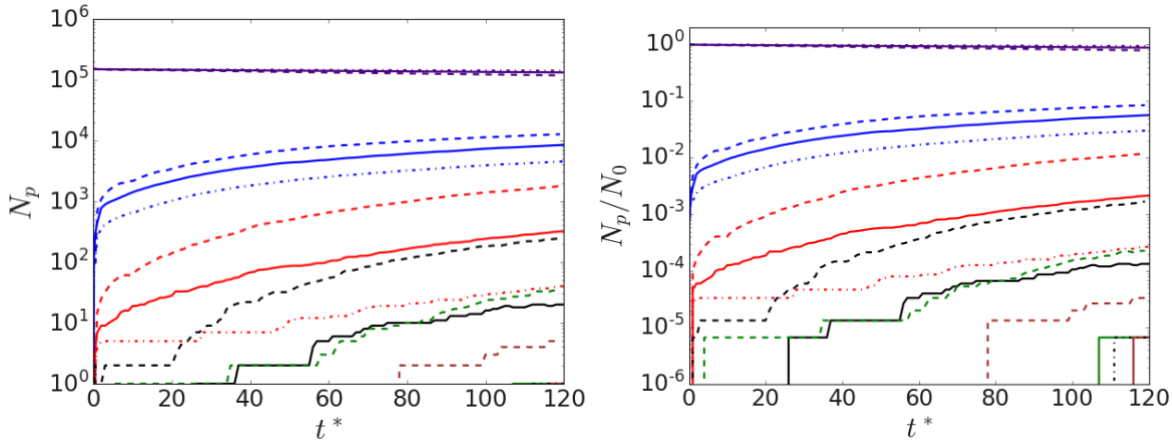

Figure 5.6: Influence of the normal restitution coefficient on total number of agglomerates of size N_p (left), and normalised by total number of particles (right), as function of time, t^*. Indigo: singlets; blue: doublets; red: triplets; black: quadruplets; green: quintuplets and brown: sextuplets. —: e_n= 0.4, − −: e_n= 0.2 and −·−: e_n= 0.6.

Figure 5.7 displays the influence of the normal restitution coefficient on the total number of cumulative particle-particle collisions, N_{col} (upper left), the total number of the cumulative particle-particle agglomerations, N_{agg} (upper right) and the temporal evolution of the agglomeration efficiency, N_{agg}/N_{col} (lower). For restitution coefficients e_n= 0.2, 0.4, and 0.6, approximately 2.5 million, 2 million, and 1.5 million individual particle-particle collisions are observed, resulting in nearly 1.88 million, over 9,500, and over 5,000 pairs of particles aggregating, respectively. The normal restitution coefficient is shown to demonstrate a significant impact on particle collisions and agglomeration; the lower the restitution coefficient, the more frequently particles collide and aggregate.

The temporal evolution of the ratio of inter-particle collisions which lead to an agglomeration event to the total number of inter-particle collisions (also called the agglomeration efficiency) is shown in Figure 5.7 (lower). There is clearly a trade-off between collision frequency and the dynamics associated with particles in various regions of the flow. For instance, close to the

wall, particles will collide with increased relative velocities due to the turbulent motion associated with that region, leading to a lower likelihood of agglomeration. In line with previous observations, the lowest coefficient of restitution leads to the greatest chance of aggregation, given a collision has already occurred, which remains steady throughout the simulation time considered.

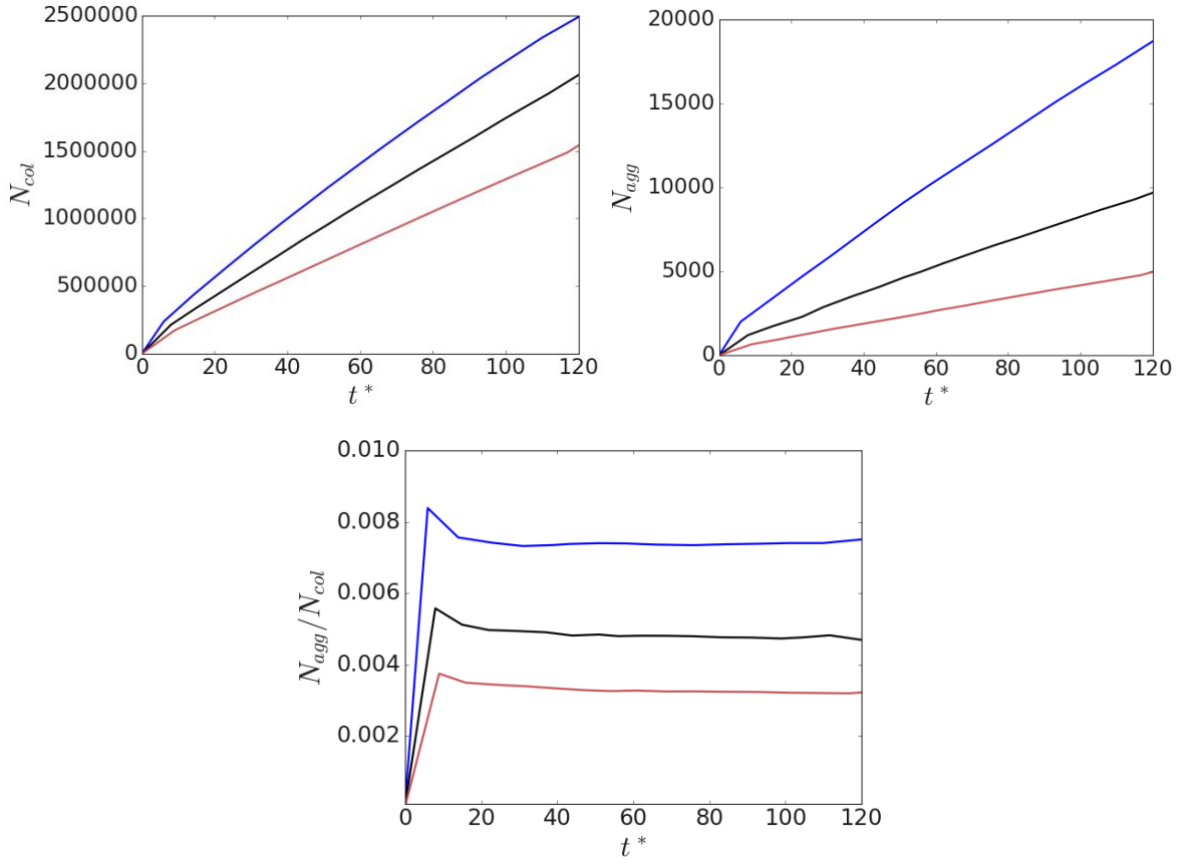

Figure 5.7: Distribution of the total number of particle-particle collisions, N_{col}, upper-left and agglomeration, N_{agg}, upper-right events. Lower is the temporal evolution of the agglomeration efficiency, N_{agg}/N_{col}. Effect of coefficient of restitution is demonstrated. Blue: e_n= 0.2; black: e_n= 0.4 and red: e_n= 0.6.

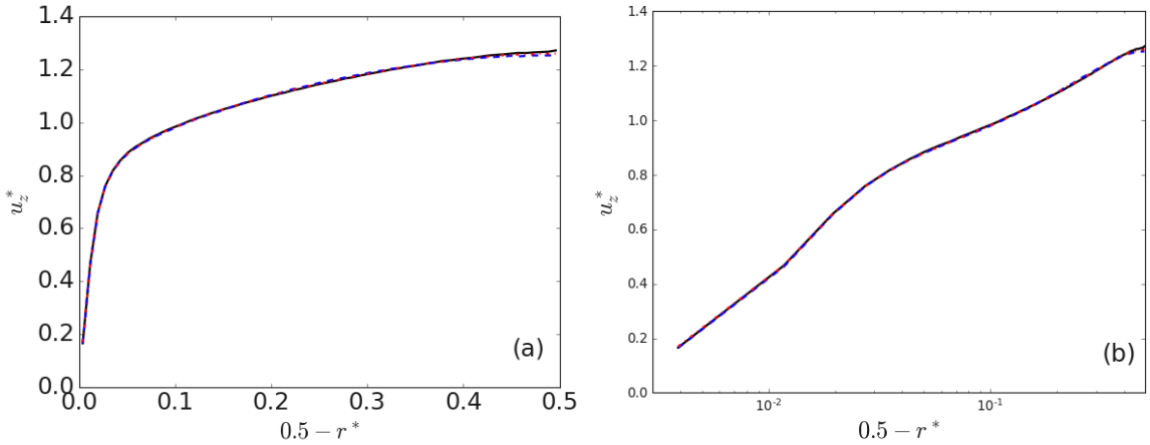

Figure 5.8: The effect of the normal coefficient of restitution on a four-way coupled flow's inner scaled statistical particle mean velocity profiles at $Re_\tau = 720$. Red (—): e_n= 0.6, black (− −): e_n= 0.4, and blue (−·−): e_n= 0.2 and (b) plotted on a logarithmic scale.

The streamwise particle mean velocity profiles predicted by different normal coefficients of restitution at the same shear Reynolds number, Re_τ=720, are shown in Figure 5.8. The restitution coefficient variation clearly has a negligible effect on the mean streamwise velocity, but near the core of the pipe, a slightly lower velocity is observed at the smallest normal coefficient of restitution. Larger particle formations usually have greater mass, resulting in slower particle acceleration and increases their inertia for a given force.

Figure 5.9 shows the root mean square of the streamwise ($u'^*_{z,rms}$), radial ($u'^*_{r,rms}$) and azimuthal ($u'^*_{\theta,rms}$) fluctuating particle velocity profiles as well as the Reynolds shear stress($< u'_z\, u'_r >^*$) at Re_τ=720 for various normal coefficient of restitution values. Again, the normal and shear stresses are essentially unaffected by the difference in the normal coefficient of restitution; however, the streamwise rms is slightly lower for the smallest normal coefficient of restitution towards the bulk flow region.

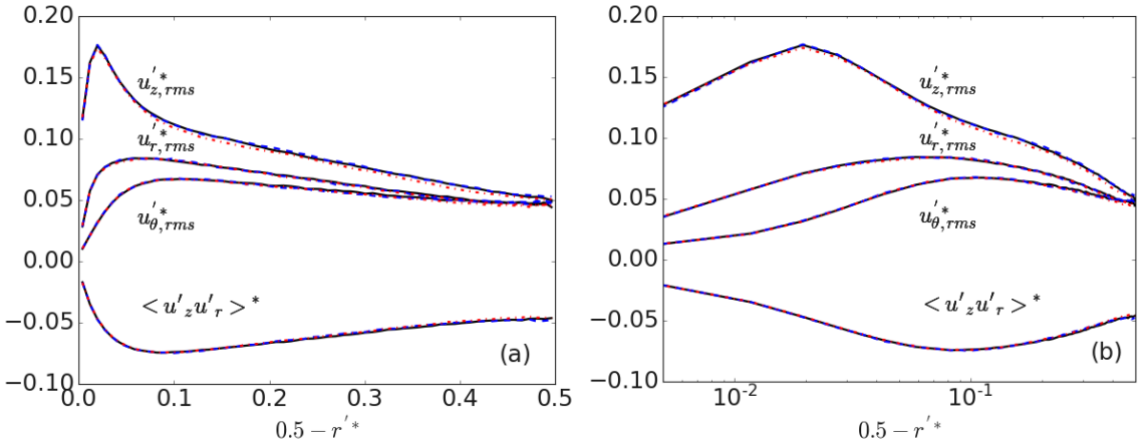

Figure 5.9: The effect of the normal coefficient of restitution on a four-way coupled flow's inner scaled statistical particle rms of streamwise, $u^*_{z,rms}$, radial, $u^*_{r,rms}$, and azimuthal, $u^*_{\theta,rms}$, velocity fluctuations and Reynolds shear stress, $< u'_z\, u'_r >^*$. Red (—): e_n= 0.6, black (− −): e_n= 0.4, and red (−·−): e_n= 0.2 and (b) plotted on a logarithmic scale.

Figure 5.10 displays the particle dynamic properties for different restitution coefficients in the viscous sublayer, buffer, log-law, and bulk flow regions of the pipe at Stokes number, St^+=1.951. These PDFs were also examined in order to gain a better understanding of the implications of changes in the restitution coefficient on the local dispersive and inter-particle interaction behaviour, and therefore on collision and agglomeration. The top left plot represents the radial direction, the top right plot represents the azimuthal direction, the lower left plot represents the particle-fluid slip velocity, and the lower right plot represents the particle velocity in the streamwise direction. The viscous sublayer and bulk regions of the flow are considerably influenced by the restitution coefficient, as evidenced by the PDFs of the particle radial velocities, although the effect is minimal in the azimuthal direction. PDFs of the slip velocity are also given in Figure 5.10 (bottom left), and these tend to increase when the restitution coefficient decreases, as would be predicted for more inertial particles. Clearly, the restitution coefficient has a significant impact on the dynamics of collision and agglomeration, particularly in the bulk region of the flow.

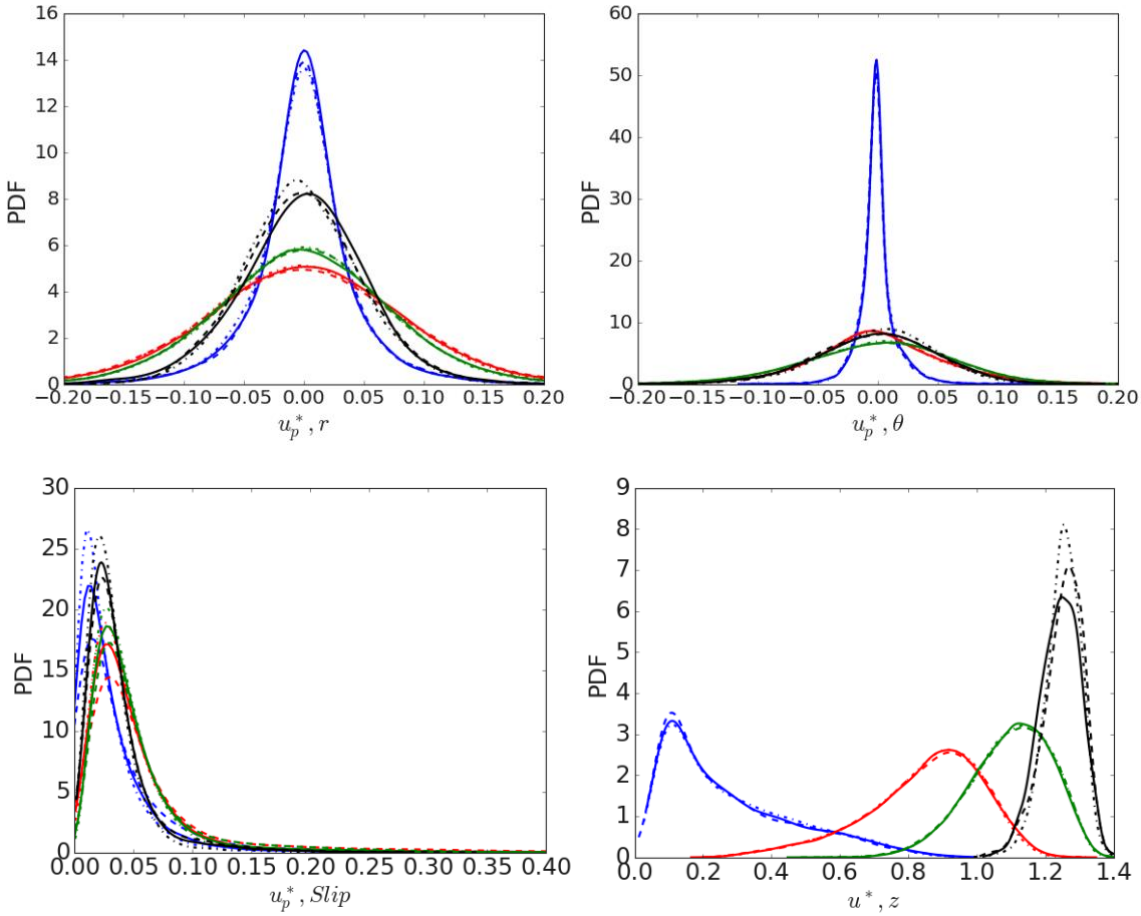

Figure 5.10: Probability density functions for the different restitution coefficients in the viscous sublayer, buffer, log-law and bulk flow regions of the pipe at $Re_\tau = 720$. Top left is the radial and right is azimuthal. Lower left is the slip velocity and right is the streamwise velocity. Blue: viscous sublayer; Red: buffer layer; Green: log-law region; Black: bulk flow. —: e_n= 0.4, − −: e_n= 0.2 and −·−: e_n= 0.6.

5.3.1.1 Temporal evolution of normal restitution coefficient, $e_n = 0.4$

Here we analyse in detail the temporal evolution of particle collision and migratory behaviour for the simulation performed with $e_n = 0.4$ (the base case). The distribution of collision events across the pipe radius is shown in Figure 5.11 (left). We observe that most of the collisions take place within the turbulent region close to the wall, with fewer collisions occurring as the pipe centreline is approached. Interestingly, Figure 5.11 (right) demonstrates that agglomeration events occur almost homogeneously over the cross-section of the pipe, with fewer aggregates forming close to the wall. For singlets, doublets and triplets, the primary particle agglomeration observed in Figure 5.12 reveals that particles are dispersed homogenously across the pipe radius, whereas for quadruplets and quintuplets, particles tend to cluster more in the middle

and centre of the pipe. The total number of primary particles decreases over time as single primary particles join together to create larger aggregates (doublets, triplets, etc.). In contrast, the development of doublets, triplets, and other aggregates increases, a pattern that was also noted by Njobuenwu and Fairweather (2017) and Breuer and Almohammed (2015).

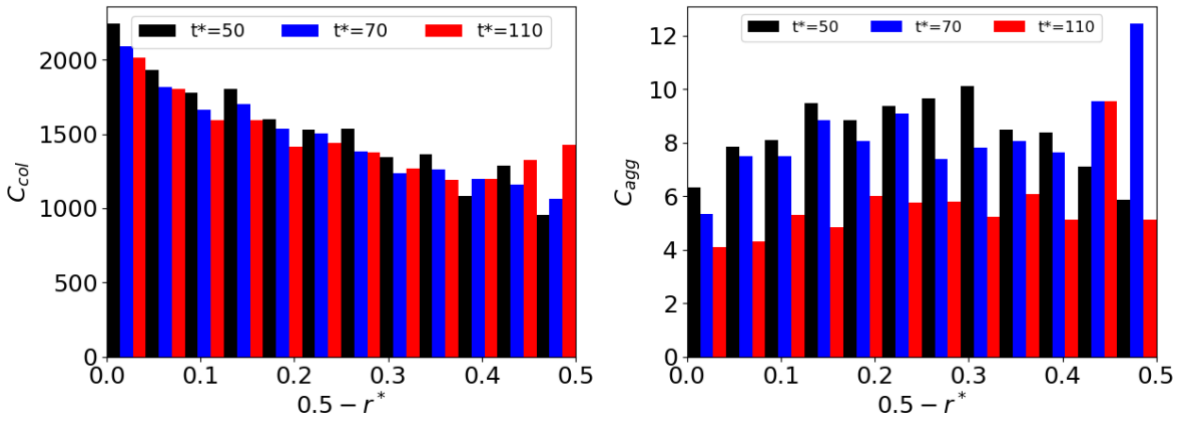

Figure 5.11: Number of collision (left) and agglomeration (right) events across the pipe radius sampled at different time t^*, normalised by volume, for normal restitution coefficient, $e_n = 0.4$.

Figures 5.13 displays the mean relative particle collision velocity (left) and the mean particle concentration profile (right) for the various restitution coefficient values. The mean relative particle collision velocity is a key parameter in collision dynamics which determines the behaviour of particles in a fluid flow. These mean relative particle collision velocities are significantly higher towards the wall and decreases exponentially towards the pipe centre. A low mean relative velocity causes greater agglomeration to occur at the pipe's centre, which agrees with earlier observations. The mean particle concentration profiles are also illustrated across the pipe at various times, with these concentrations normalised by the initially injected concentration, C_0, and total volume. The concentration is seen to be unaffected by restitution coefficient changes.

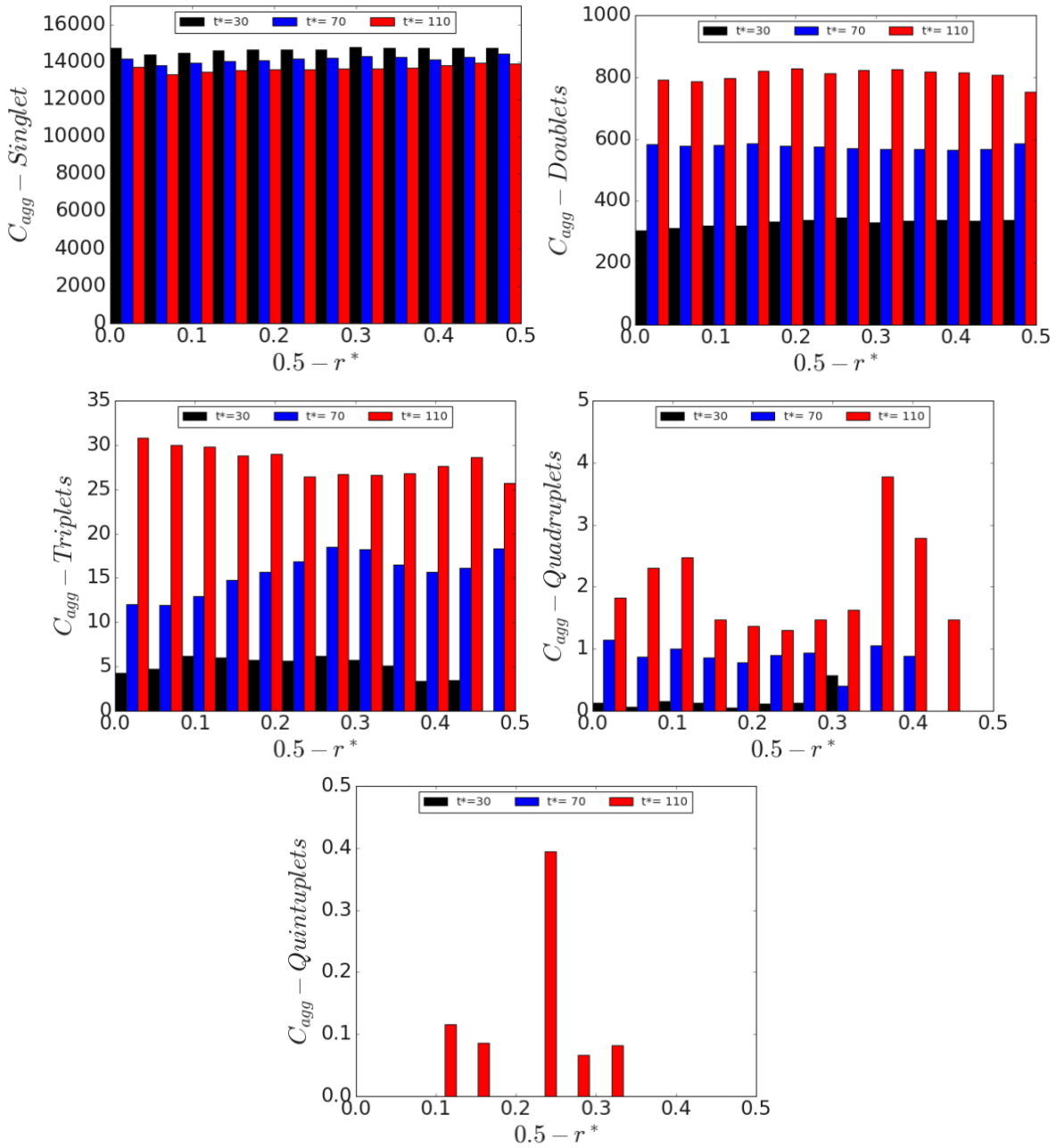

Figure 5.12: Agglomeration of primary particles (singlets, doublets etc., particles) across the pipe radius at various t^*, normalised by volume, for normal restitution coefficient, $e_n = 0.4$.

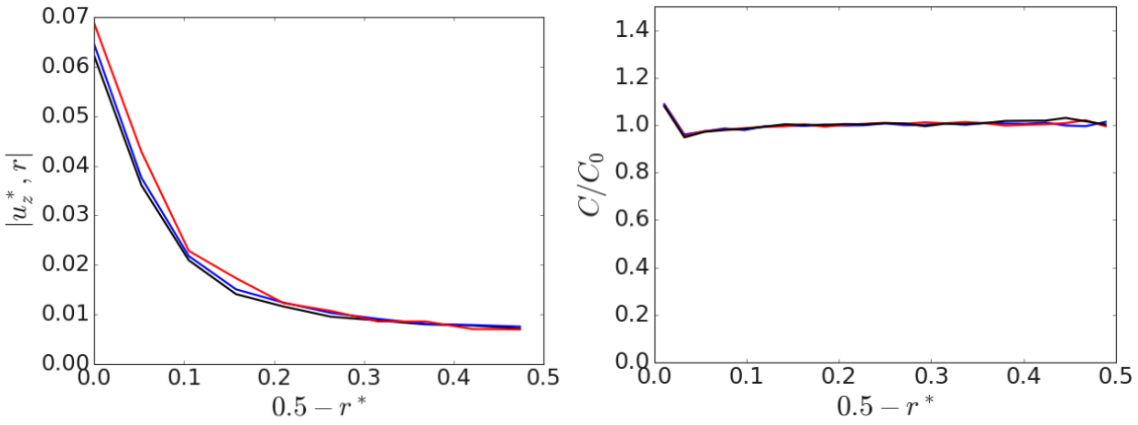

Figure 5.13: The mean relative particle collision velocity and particle concentration at different sample times across the pipe. Black: t^* = 30, blue: t^* = 70, and t^* = red: 110 for normal restitution coefficient, $e_n = 0.4$.

5.3.1.2 Temporal evolution of normal restitution coefficient, $e_n = 0.2$

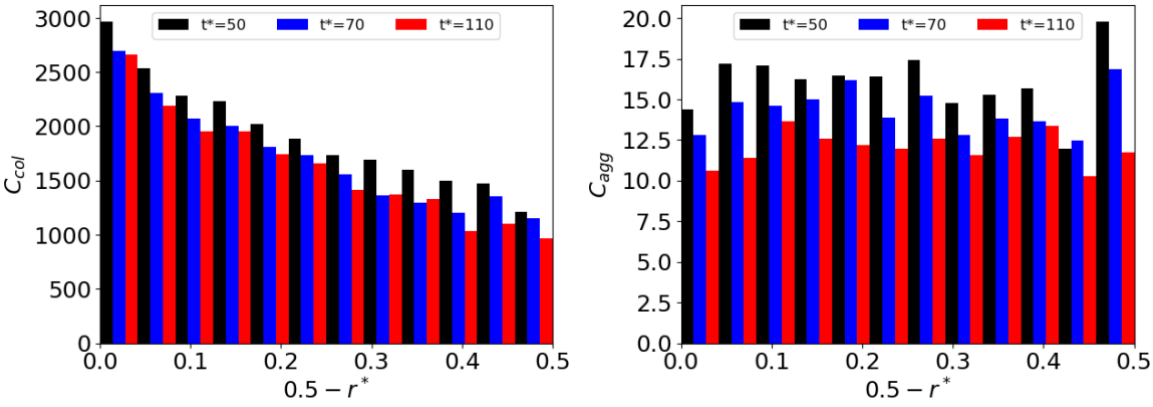

Figure 5.14: Number of collision (left) and agglomeration (right) events across the pipe radius sampled at different time t^*, normalised by volume, for normal restitution coefficient, $e_n = 0.2$.

Figure 5.14 (left) illustrates the distribution of collision events across the pipe radius at various times with a normal restitution coefficient reduction, e_n = 0.2. As the pipe centreline is approached, fewer collisions occur, and the frequency of collision occurrences is found to be higher close to the wall. Due to the high inelasticity of particle-particle collisions at low restitution coefficients, which causes particles to lose a considerable amount of kinetic energy during collision and results in a low relative velocity, particles are more prone to aggregate upon collision.

It is also interesting to note that Figure 5.14 (right) shows that agglomeration events occur almost uniformly along the pipe's cross-section at various times, with fewer aggregates developing close to the wall. The primary particle agglomeration shown in Figure 5.15 likewise

shows that particles are evenly distributed, apart from the quadruplets and quintuplets, where particles of those sizes tend to concentrate more in the middle and centre of the pipe at t^* =110.

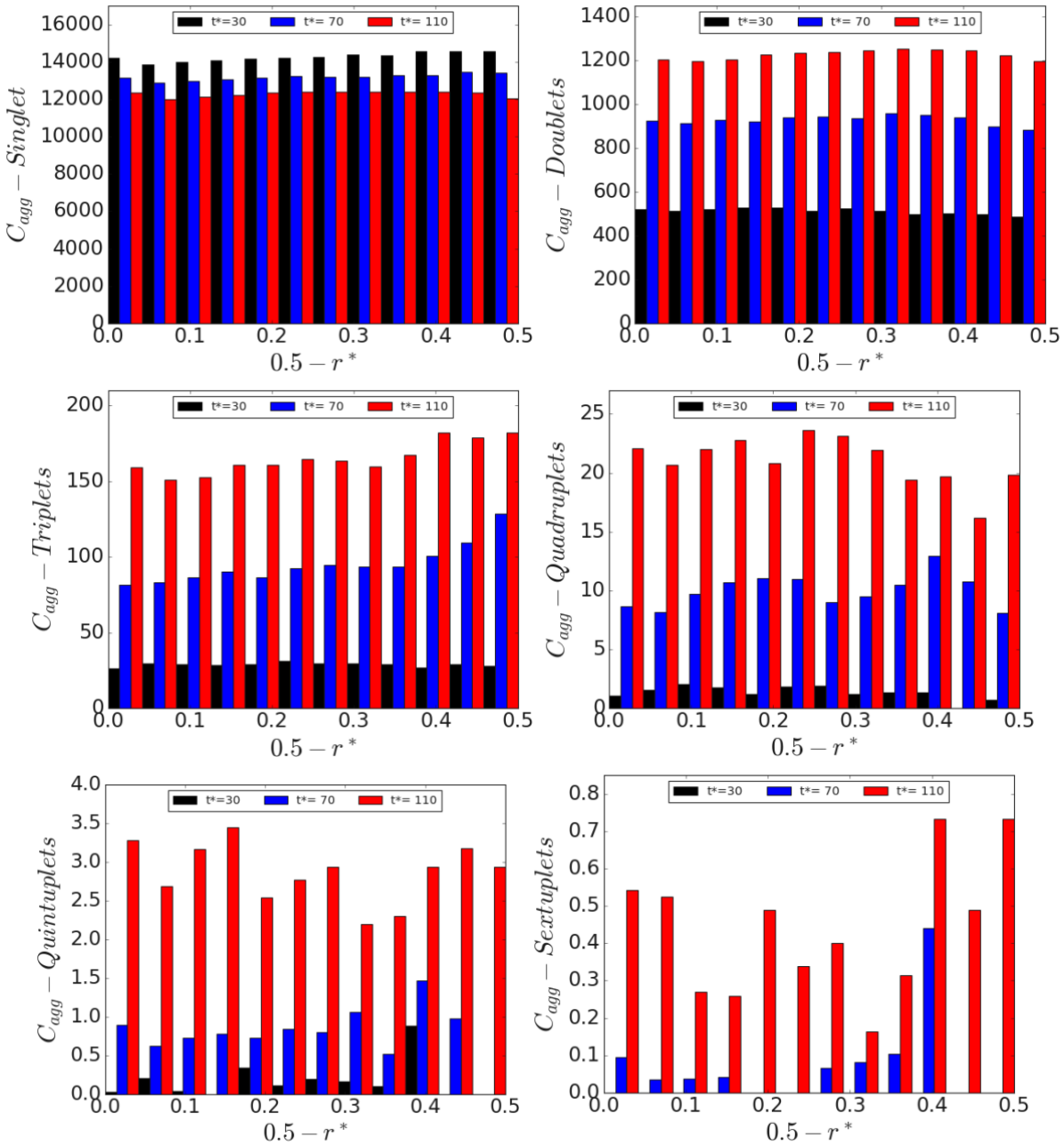

Figure 5.15: Agglomeration of primary particles (singlets, doublets etc., particles) across the pipe radius at various t^*, normalised by volume, for normal restitution coefficient, $e_n = 0.4$.

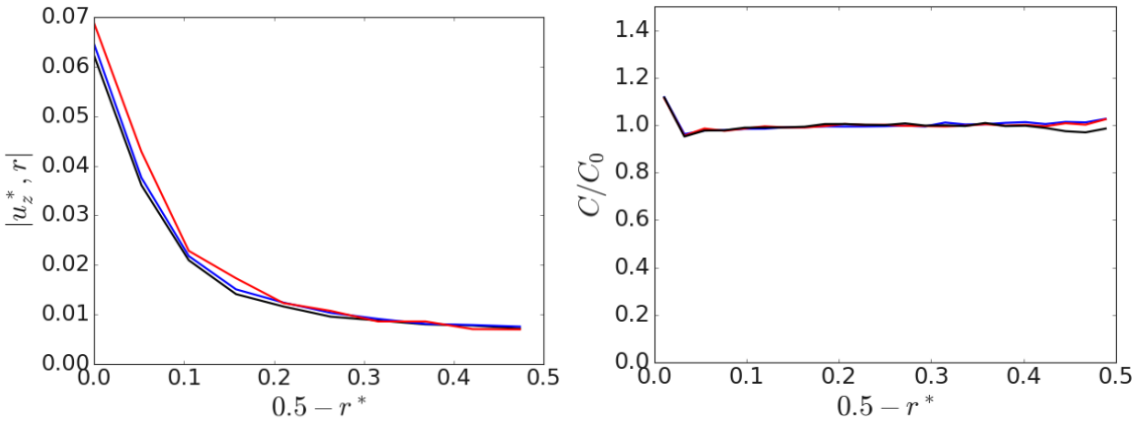

Figure 5.16: The mean relative particle collision velocity and particle concentration at different sample times across the pipe. Black: t^* = 30, blue: t^*= 70, and t^* = red: 110 for normal restitution coefficient, $e_n = 0.4$.

In agreement with the results of Figure 5.13, the predictions shown in Figure 5.16 demonstrate that mean relative particle collision velocities are significantly higher towards the wall and decrease towards the pipe centre. Additionally, mean particle concentration profiles are again unaffected by restitution coefficient changes.

5.3.1.3 Temporal evolution of normal restitution coefficient, $e_n = 0.6$

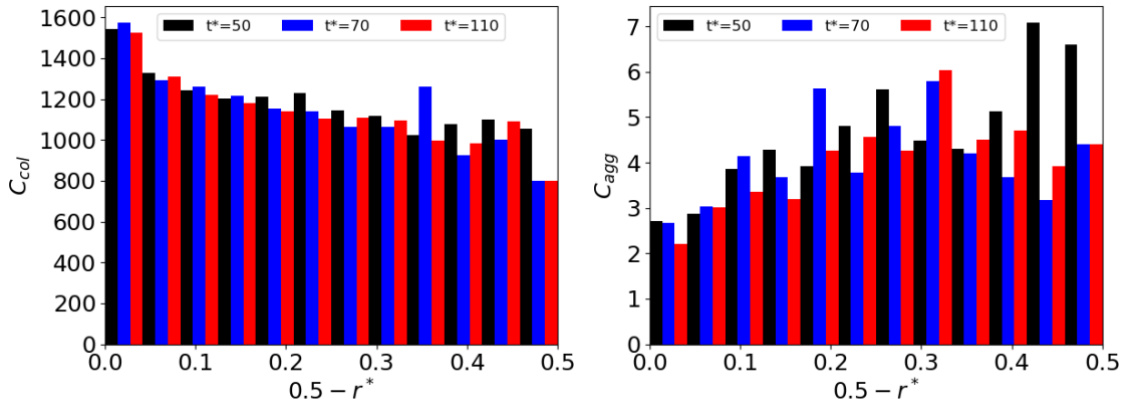

Figure 5.17: Number of collision (left) and agglomeration (right) events across the pipe radius sampled at different time t^*, normalised by volume, for normal restitution coefficient, $e_n = 0.6$.

With an increase in the normal restitution coefficient to e_n = 0.6, Figure 5.17 (left) shows the distribution of collision events across the pipe radius with time. Comparing the current higher restitution coefficient results to the previous lower ones, the number of collisions is dramatically reduced, though the shape of the distribution remains similar. Close to the wall, there are a relatively high number of collisions occurring even though the kinetic energy is

mainly conserved and the particles keep a sizable amount of their pre-collision velocity at this moderately high restitution coefficient, e_n = 0.6. Due to significantly higher mean relative particle collision velocities as compared to those for low restitution coefficients (both e_n = 0.2 or 0.4), more recoil-type behaviour and less agglomeration results when two particles collide with one another. Figure 5.17 (right) demonstrates that agglomeration events occur relatively consistently across the pipe's cross-section at different times, with fewer aggregations occurring close to the wall, in relation to the base case normal restitution coefficient, e_n = 0.4.

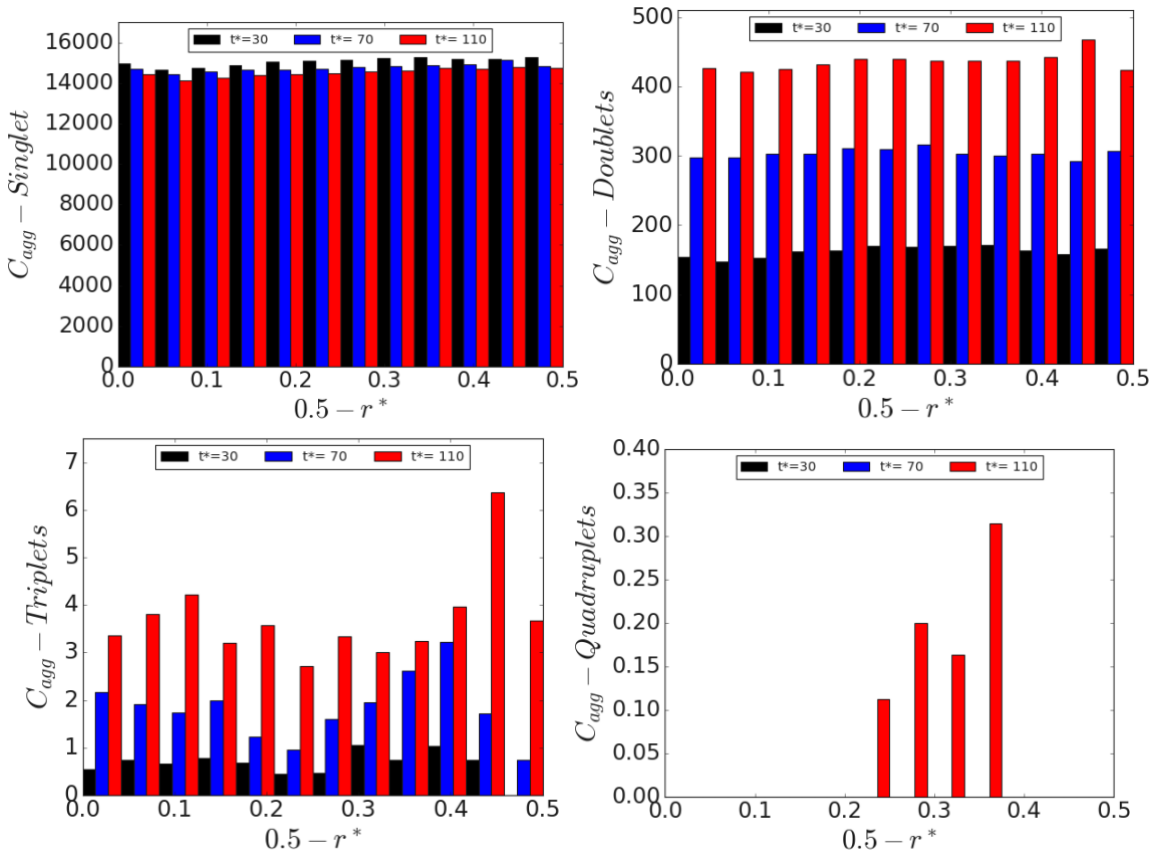

Figure 5.18: Agglomeration of primary particles (singlets, doublets etc., particles) across the pipe radius at various t^*, normalised by volume, for normal restitution coefficient, $e_n = 0.6$.

Figure 5.18 indicates that particles are uniformly distributed for singlets and doublets, but triplets and quadruplets agglomeration tend to occur more in the centre and middle of the pipe. Increasing the coefficient of restitution leads to a more homogeneous distribution of collisions across the pipe radius, with the retention of increased particle velocities caused by the collisions causing particles to separate further and reducing the chance of them re-colliding. These findings are in agreement with those observed in previous studies (Mortimer et al., 2021; Njobuenwu and Fairweather, 2017).

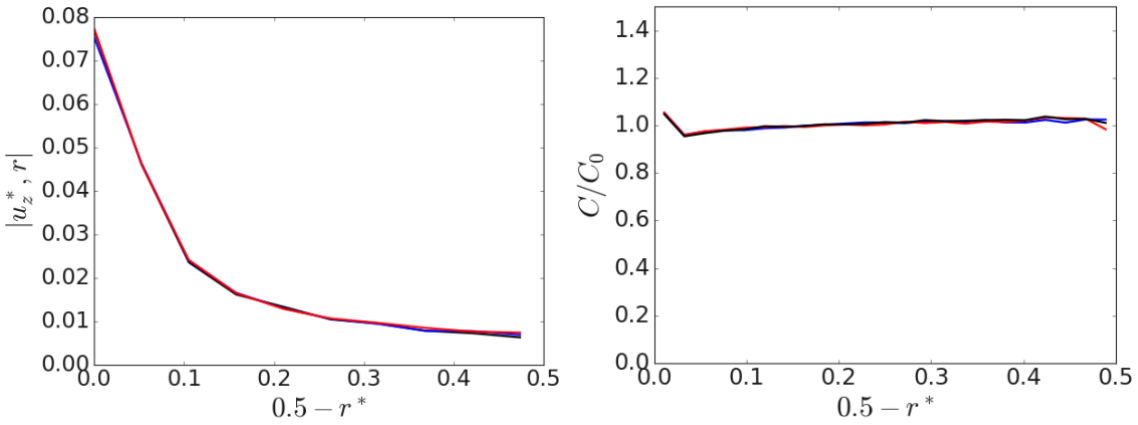

Figure 5.19: The mean relative particle collision velocity and particle concentration at different sample times across the pipe. Black: t^* = 30, blue: t^* = 70, and t^* = red: 110 for normal restitution coefficient, $e_n = 0.6$.

Lastly, and in agreement with the results of Figures 5.13 and 5.16, the predictions of Figure 5.19 show the same mean relative particle collision velocity distribution and mean particle concentration profiles, with no significant effect of restitution coefficient.

5.3.2 Effect of variation of Hamaker constant on collision and agglomeration

The Hamaker constant (denoted *H* and named after H. C. Hamaker), which quantifies particle-particle van der Waals interactions, is an important quantity to investigate when examining particle collision and agglomeration. It can be determined empirically as well as theoretically. For example, according to Lifshitz and Hamermesh's (1956) macroscopic theory, it can be computed theoretically by studying the frequency dependence of the dielectric function. The dispersion potential degrades more quickly in the retarded regime when the particle interactions are too distant from one another.

Here, the variation of the Hamaker constant is studied, a chemical parameter which modulates the strength of the van der Waals interaction between particles. It has been demonstrated in previous studies (Mortimer and Fairweather, 2021) that the Hamaker constant has an impact on the mean collision velocity of the interacting particles. Figure 5.20 demonstrates the effect of Hamaker constant on the total number of agglomerates of size N_p as a function of t^*. The generation of agglomerates with particle numbers ranging from singlets to sextuplets is observed for the highest Hamaker constant, whereas only up to quadruplet agglomerates is

observed for the lowest Hamaker constant value. This shows that as the Hamaker constant increases, so does the size of the agglomerates formed.

After 1000 timesteps ($t^* = 1$) in the simulation, the Hamaker constant's impact becomes apparent. By the time it reached $t^* = 120$, the primary particle number has decreased from 150,000 to 132,011 particles, or approximately 12%, at the value of the Hamaker constant, H = 22.3 zJ. Two further simulations were performed using the same configuration, with Hamaker constants of H = 36.76 and 7.84 zJ. Both of these modifications had a considerable impact on the frequency of collisions and agglomerations that occurred on particle contact. For the Hamaker constant H=36.76 zJ and for H=7.87 zJ, the primary particles were reduced to 118,511 particles (~21%) and 141,535 particles (~5.64%), respectively. In comparison to the Hamaker constant, H= 22.3 zJ, predictions, approximately 8% more primary particles were encouraged to agglomerate for H = 36.76 zJ, while only slightly more than 6% were discouraged for H = 7.84 zJ.

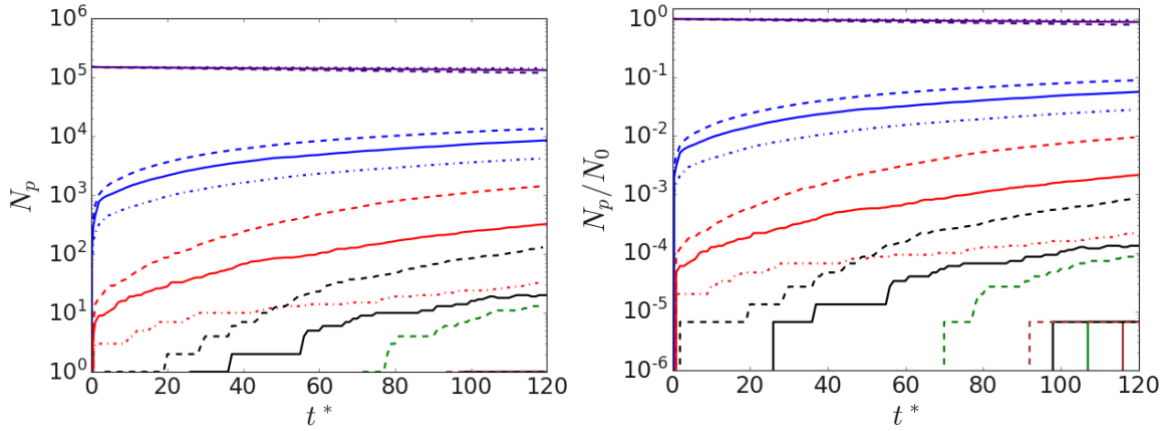

Figure 5.20: Influence of the Hamaker constant on total number of agglomerates of size N_p (left), and normalised by total number of particles (right), as function of time, t^*. Indigo: singlets; blue: doublets; red: triplets; black: quadruplets; green: quintuplets and brown: sextuplets.—: H = 22.3zJ., – –: $H = 7.84zJ$ and –·–: $H = 36.76zJ$.

The agglomeration of doublets, triplets, and so on increases with time, and the particle-particle interaction events (collision and agglomeration) were found to have a dependence on the Hamaker constant. At the end of the simulation, the total number of agglomerates observed was 2.79% (doublets), 0.022% (triplets), and 0.00067% (quadruplets) of the total primary particles for the lowest Hamaker constant, H = 7.84 zJ. Similarly, for H = 22.3 zJ, there were approximately 5.64% (for doublets), 0.216% (for triplets), 0.013% (for quadruplets), and 0.00067% (for quintuplets and sextuplets) total agglomerates. The value of H = 36.76 zJ

produced the highest agglomeration rate, which was found to be 8.88% (for doublets), 0.945% (for triplets), 0.0876% (for quadruplets), and 0. 000867% (for quintuplets and sextuplets).

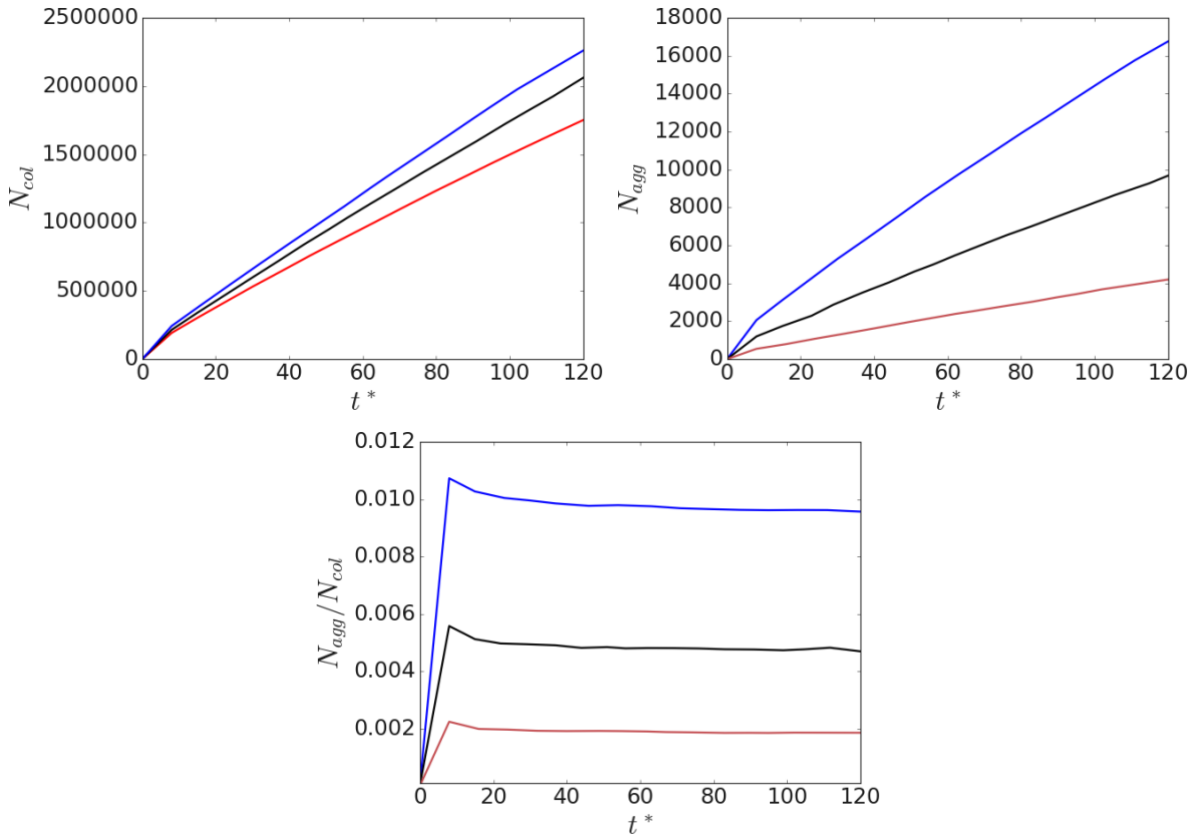

Figure 5.21: Distribution of the total number of particle-particle collisions, N_{col}, upper-left and agglomeration, N_{agg}, upper-right events. Lower is the temporal evolution of the agglomeration efficiency, N_{agg}/N_{col}. Effect of Hamaker constant is demonstrated. Blue: $H = 36.76zJ$; black: $H = 22.3zJ$ and red: $H = 7.84zJ$.

Figure 5.21 illustrates the influence of the Hamaker constant on the total number of cumulative particle-particle collisions, N_{col} (upper left) is the total number of the cumulative particle-particle collisions resulting in agglomeration, N_{agg} (upper right) and the temporal evolution of the agglomeration efficiency, N_{agg}/N_{col} (lower). The simulation was performed at a shear Reynolds number, Re_τ = 720, with restitution coefficient, e_n = 0.4 and a primary particle diameter, d_p = 100 μm. The particle density, mean yield stress, and minimum contact distance in all simulations were kept constant at $\rho_P^* = 2710$kg m^{-3}, $\sigma = 3 \times 10^8$ Pa and $\delta_0 = 2 \times 10^{-10}$ m, representing calcite particles in water. For the highest Hamaker constant, more than 2 million distinct particles interact with one another, causing more than 16,000 of them to aggregate. In general, the total number of particle collisions and agglomerations varies almost

linearly with time and has a significant dependency on the particle Hamaker constant. Higher collision frequency and higher agglomeration are produced by larger Hamaker constants. This supports the finding that an increase in the Hamaker constant has a significant impact on the likelihood of collisions and potential agglomerations.

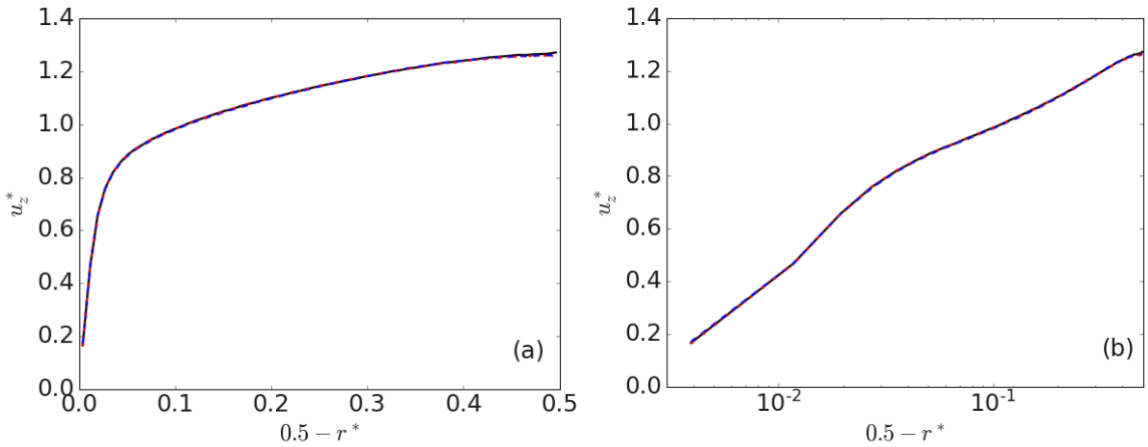

Figure 5.22: The effect of the Hamaker constant on a four-way coupled flow's inner scaled statistical particle mean velocity profiles at $Re_\tau = 720$. Red (—): $H = 7.84\ zJ$, black (− −): $H = 22.3\ zJ$, and blue(−·−): $H = 36.76\ zJ$ and (b) plotted on a logarithmic scale.

Figure 5.22 illustrates the mean streamwise particle velocities for the various Hamaker constants (H = 7.84 zJ, 22.3 zJ and 36.76 zJ) at the same shear Reynolds number, Re_τ=720. Again, the LPT was applied in these simulations to take into consideration the four-way coupling between the particles and the fluid. The mean streamwise velocities are unaffected by the Hamaker constant variation. Figure 5.23 shows the root mean square of the streamwise, $u^*_{z,rms}$, radial, $u^*_{r,rms}$, and azimuthal, $u^*_{\theta,rms}$, fluctuating particle velocity profiles as well as the Reynolds shear stress, $< u'_z\, u'_r >^*$, at Re_τ=720 for various Hamaker constants. The normal and shear stresses are unaffected by the difference in the Hamaker constant; however, the streamwise rms is slightly lower for highest Hamaker constant towards the bulk flow region.

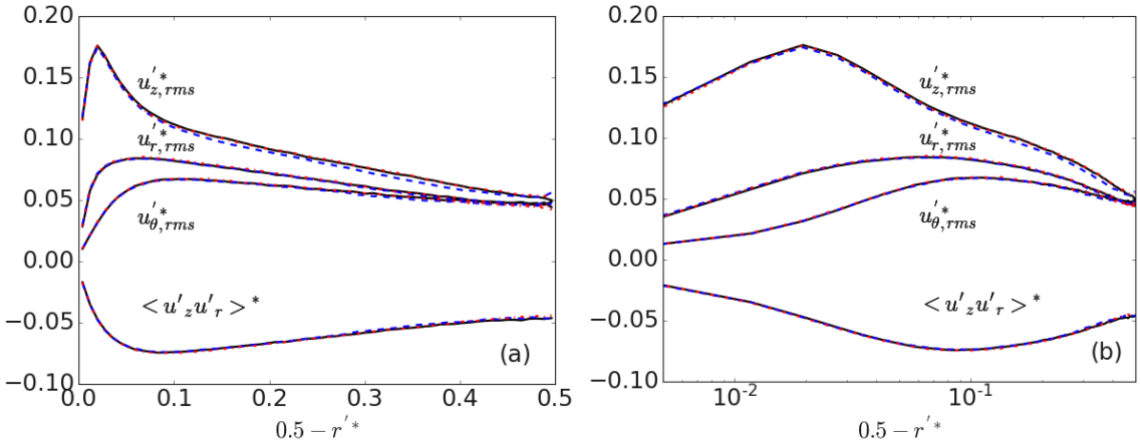

Figure 5.23:The effect of the Hamaker constant on a four-way coupled flow's inner scaled statistical particle RMS of streamwise, $u'^{*}_{z,rms}$, radial, $u'^{*}_{r,rms}$, and azimuthal, $u'^{*}_{\theta,rms}$, velocity fluctuations and Reynolds shear stress, $< u'_z\, u'_r >^*$. Red (—): $H = 7.84\ zJ$, black (− −): $H = 22.3\ zJ$, and blue (−·−): $H = 36.76\ zJ$ and (b) plotted on a logarithmic scale.

Figure 5.24 illustrates the influence of Hamaker constant on PDFs of various dynamic properties in the viscous sublayer, buffer, log-law, and bulk flow regions of the pipe at Stokes number, St^{+}=1.951. These statistical distributions were again examined in order to gain more insight into the dynamics of the particle-particle contact as well as the likelihood that specific interactions would lead to collisions and agglomerations depending on how the Hamaker constant affects the formation of agglomerates which subsequently modifies the inertial dynamics. The radial particle velocity is presented in the upper-left plot, the azimuthal velocity is presented in the upper-right plot, the particle-fluid slip velocity is presented in the lower-left plot, and the particle velocity in the streamwise direction is presented on the lower-right plot. Dynamics within the bulk region of the flow are seen to be considerably influenced by the Hamaker constant where inertial forces are likely to have a more significant impact, as evidenced by the PDFs of the particle radial, streamwise velocity and slip velocity, although the effect is minimal in the azimuthal direction. The effect of Hamaker constant in the viscous sublayer, buffer and log-law regions of the flow were insignificant in the radial, azimuthal directions and for the streamwise velocity since in this region the interactions are dominated by shear forces and fluid viscosity.

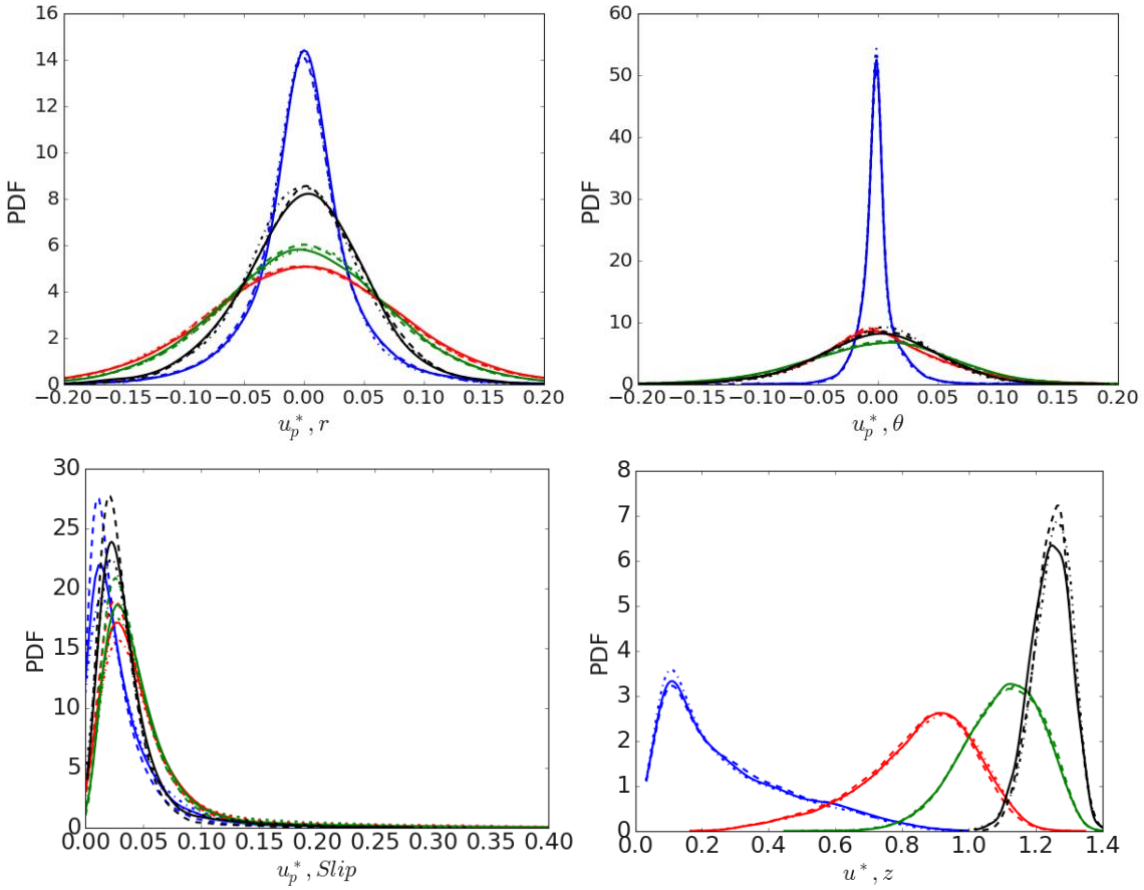

Figure 5.24: Probability density function for the different Hamaker constant in the viscous sublayer, buffer, log-law and bulk flow regions of the pipe at $Re_\tau = 720$. Top left is the radial and right is azimuthal. Lower left is the slip velocity and right is the streamwise velocity. Blue: viscous sublayer; Red: buffer layer; Green: log-law region; Black: bulk flow. —: $H = 7.84$, − −: $H = 22.3$, and −·−: $H = 36.76$.

5.3.2.1 Hamaker constant, H =7.84zJ

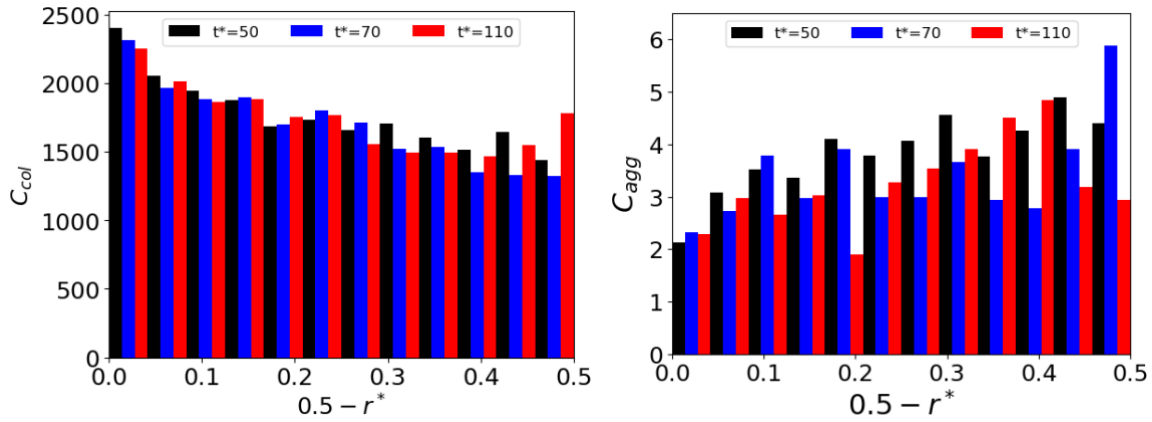

Figure 5.25: Number of collision (left) and agglomeration (right) events across the pipe radius sampled at different times t^*, normalised by volume, for Hamaker constant, H = 7.84zJ.

Figures 5.25 displays the distribution of collision (left) and agglomeration (right) occurrences across the pipe radius at various time intervals for a Hamaker constant, H = 7.84 zJ. Although there are significantly more particle collisions near the wall at this low Hamaker constant, there is less agglomeration of primary particles observed as a result of the weak van der Waals forces (low Hamaker constant). The agglomerates of the singlets, doublets, triplets, and quadruplets produced after simulation times t^* = 30, 70, and 100 are compared in Figure 5.26. For the various agglomeration sizes, the production of a doublet is observed at t^* =30 across the pipe, while few triplets are created near the pipe's wall and central regions of the flow, but by t^*=70, a greater proportion of particles form as triplets. By t^* = 100, there are more doublets, triplets, and quadruplets forming.

Figure 5.27 shows the mean relative particle collision velocity (left) and the particle concentration profile (right) for a Hamaker constant of, H = 7.84zJ. The mean relative particle velocities are higher close to the wall and exponentially lower as they approach the centre of the flow. The effect of time is generally minimal, and the relative particle velocities stay constant throughout the time period examined. There is also no change in the concentration profile with time, which approximates a constant line at $C/C_0 = 1$.

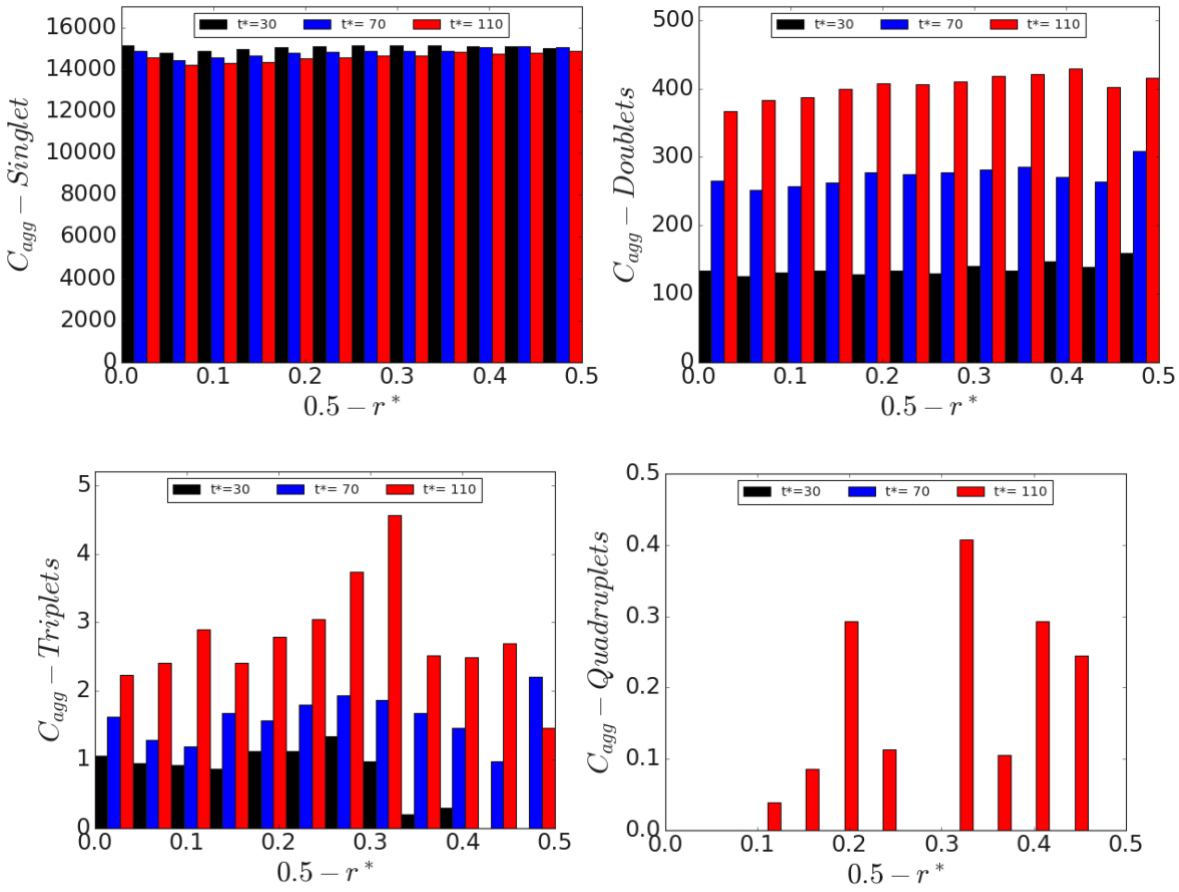

Figure 5.26: Agglomeration of primary particles (singlets, doublets etc., particles) across the pipe radius at various t^*, normalised by volume, for Hamaker constant, $H = 7.84$zJ.

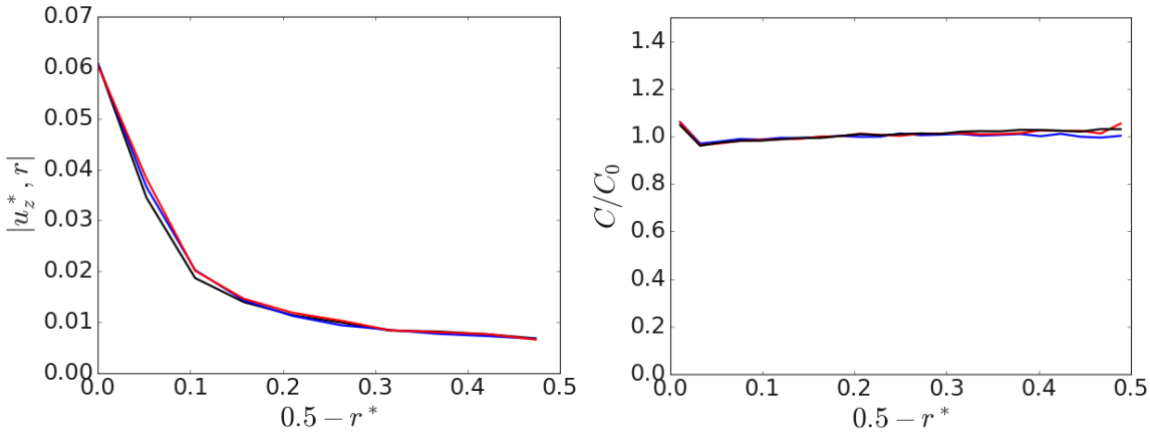

Figure 5.27: The mean relative particle collision velocity and particle concentration at different sample time across pipe. Black: t^* = 30, blue: t^* = 70, and red: t^* = 110 for Hamaker constant, $H =$ 7.84zJ.

5.3.2.2 Hamaker constant, $H = 22.3$zJ

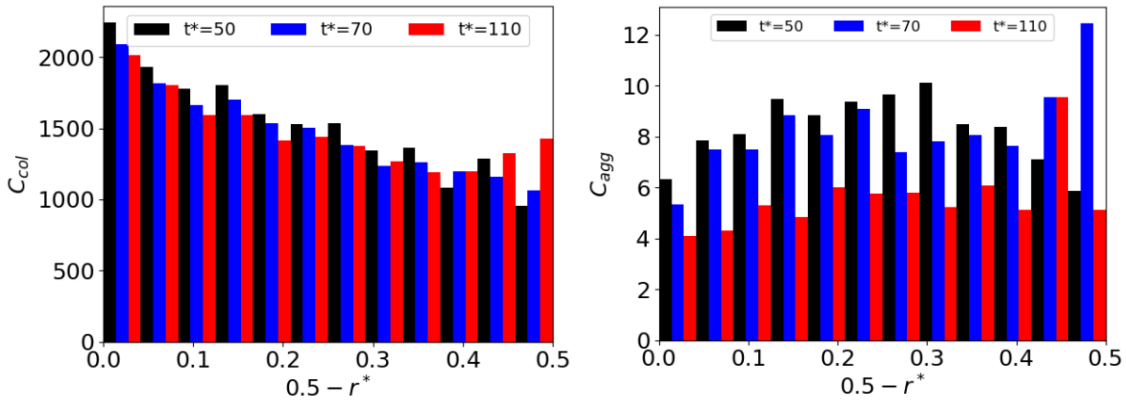

Figure 5.28: Number of collision (left) and agglomeration (right) events across the pipe radius sampled at different time t^*, normalised by volume, for Hamaker constant, $H = 22.3$zJ.

Figure 5.28 shows the time evolution of collision (left) and agglomeration (right) events across the pipe radius for a Hamaker constant, $H = 22.3$zJ, which was sampled at $t^* = 50$, 70, and 110. This time, with the Hamaker constant of $H = 22.3$zJ, there are more particle collisions near the wall and there is also significantly greater agglomeration of primary particles detected across the pipe. The number of primary particles and the generation of doublets, triplets, quadruplets, and quintuplet particles are shown in Figure 5.29 sampled at $t^* = 30$, 70, and 110. Increasing the Hamaker constant to $H = 22.3$zJ significantly increases the possibility of doublet, triplet, and other particle agglomerate production. By $t^* = 110$, it is evident that an increasing number of particles are clumping together and agglomerating, encouraging the growth of quadruplets and quintuplets.

The results of Figure 5.30 confirm those of Figure 5.27, with high mean relative particle velocities close to the wall and decreasing as the central regions of the pipe are approached. Likewise, there is no change in the concentration profile with time. Comparing Figures 5.27 and 5.30, there is also no impact of Hamaker constant on the results.

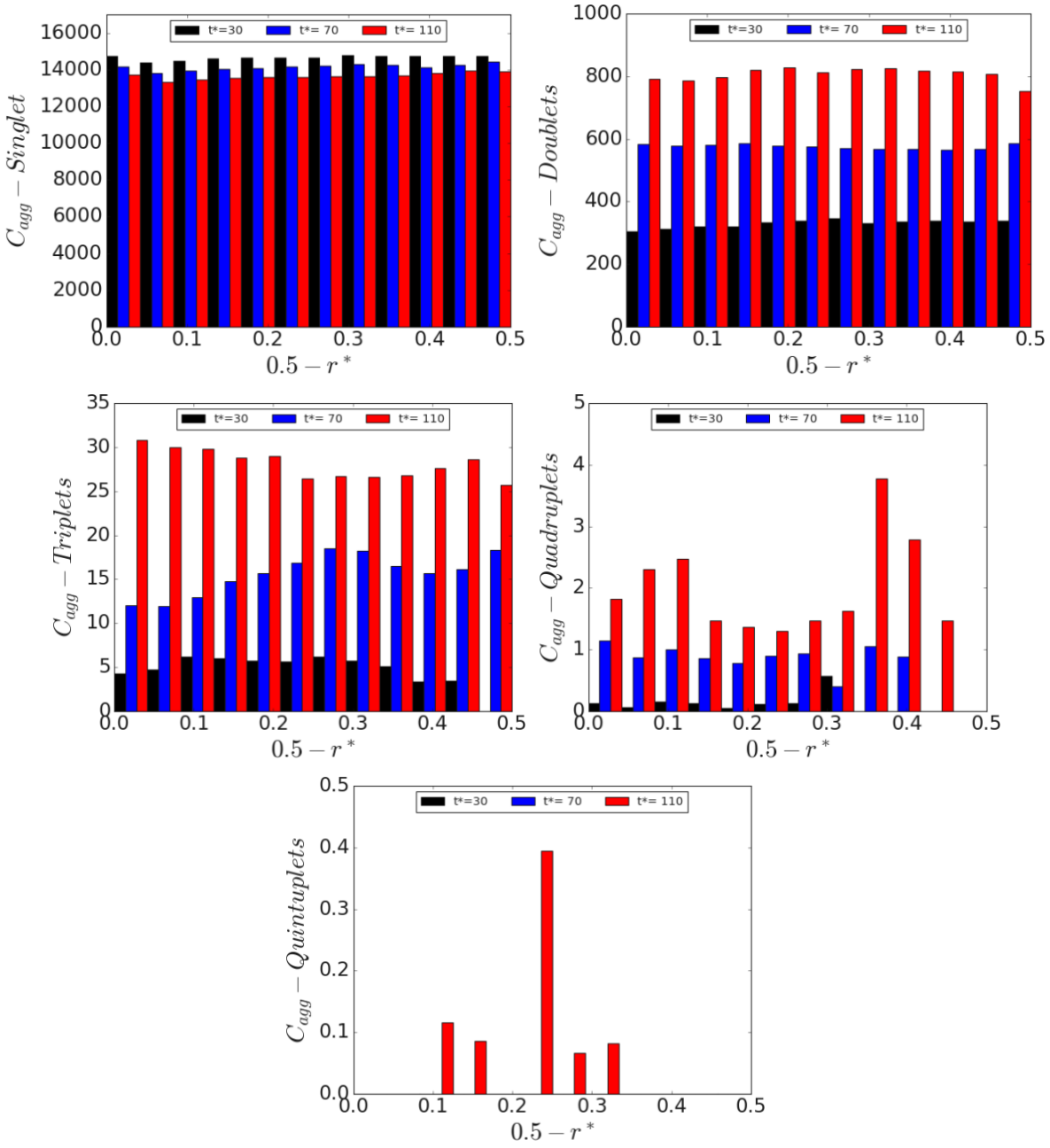

Figure 5.29: Agglomeration of primary particles (singlets, doublets etc., particles) across the pipe radius at various t^*, normalised by volume, for Hamaker constant, $H = 22.3$zJ.

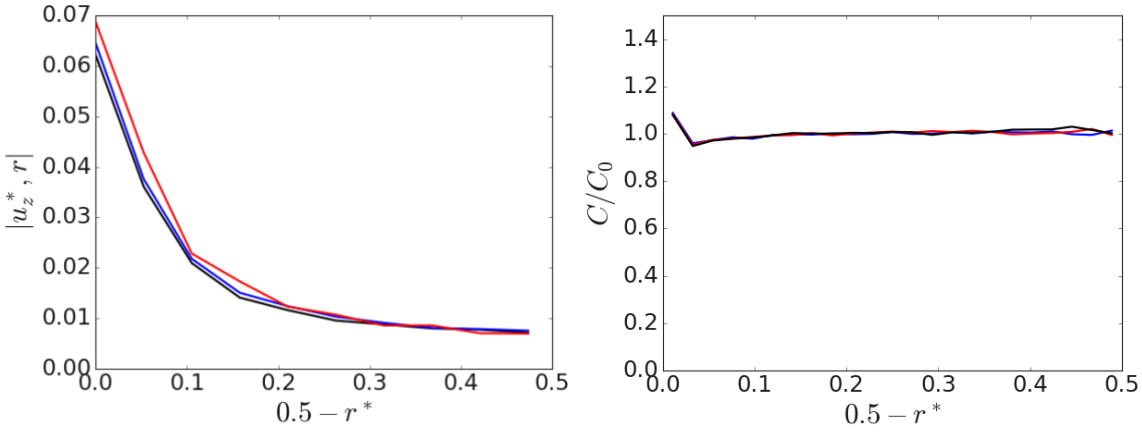

Figure 5.30: The mean relative particle collision velocity and particle concentration at different sample times across the pipe. Black: t^* = 30, blue: t^* = 70, and red: t^* = 110 for Hamaker constant, H = 22.3 zJ.

5.3.2.3 Hamaker constant, H = 36.76zJ

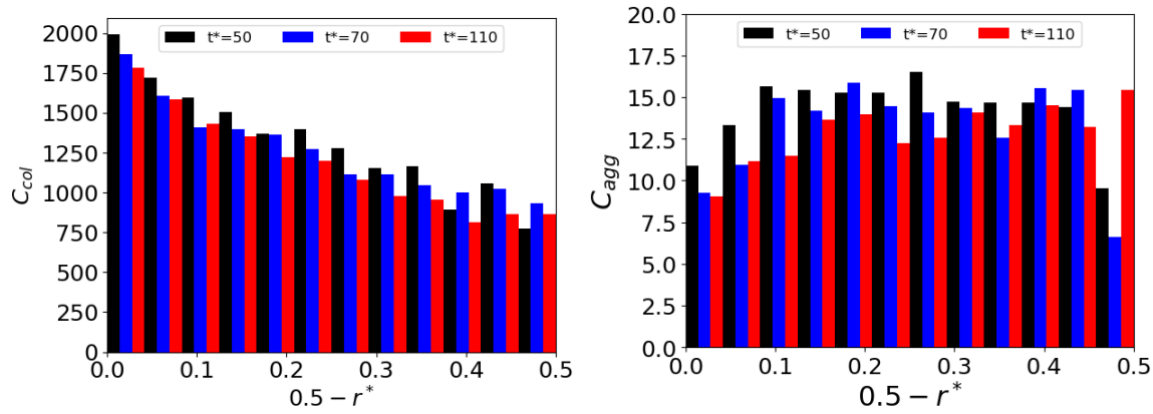

Figure 5.31: Number of collision (left) and agglomeration (right) events across the pipe radius sampled at different time t^*, normalised by volume, for Hamaker constant, H = 36.76zJ.

In this case, compared to the other two cases (H = 7.84zJ and 22.3zJ) studied, there are substantially more collisions and agglomerates formed for the highest Hamaker constant, H = 36.76zJ, as shown in Figure 5.31. Figure 5.32 demonstrates that an increase in Hamaker constant also accelerates the rate of depletion of the primary particles, leading to an increase in the number of doublets, triplets, and other agglomerates. The generation of doublet particles is greatly affected by the modification of the Hamaker constant, which is typically associated with larger van der Waals interactions between particles. Over time, doublets formed more often along the pipe's radius, indicating that the attraction forces holding the particles together are stronger. When compared to the other two cases considered, the Hamaker constant, H =

36.76zJ, produces significantly more triplet and quadruplet particles. Even though they are few in number, quintuplet and sextuplet particle formation is also observed in this flow.

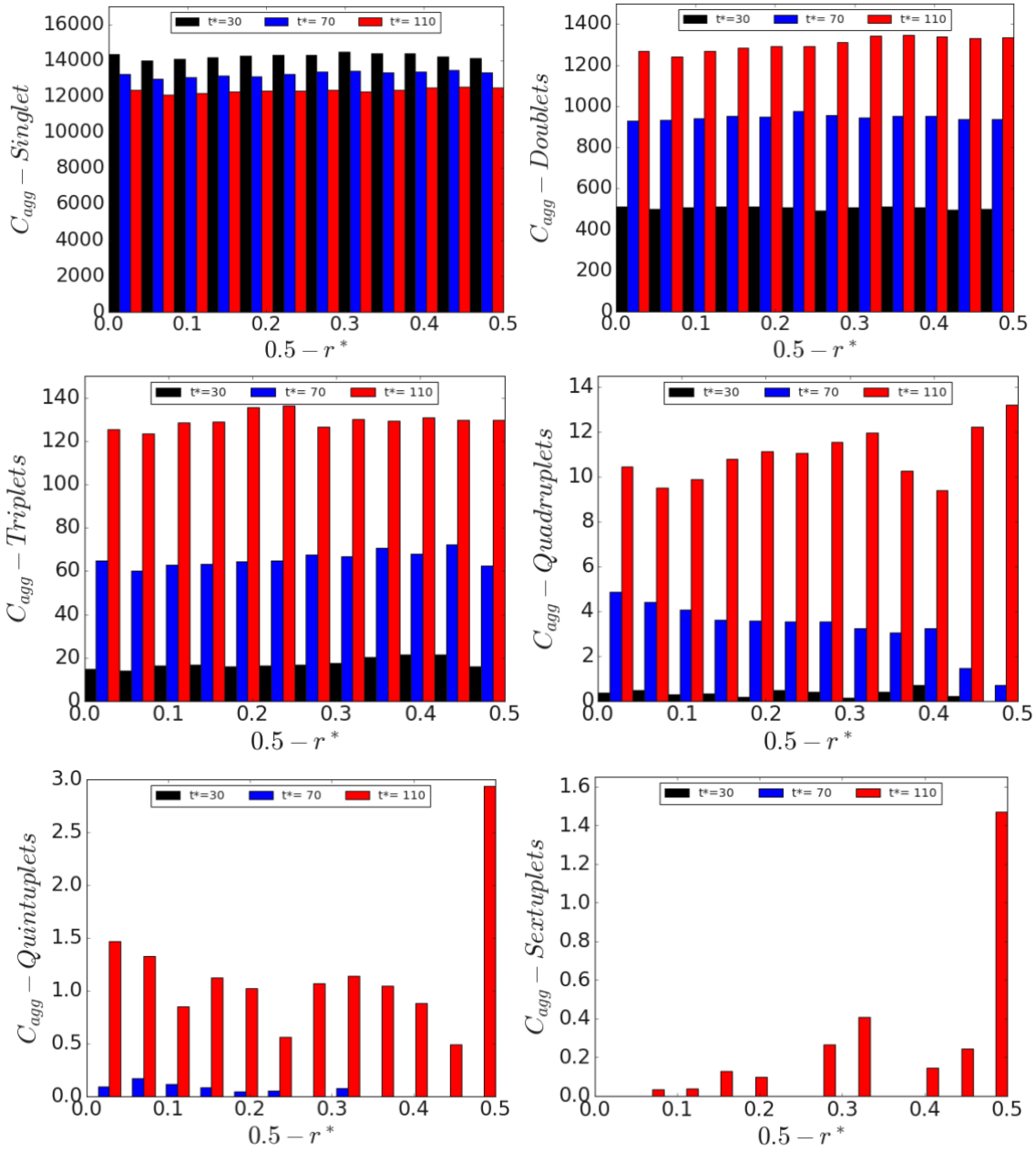

Figure 5.32: Agglomeration of primary particles (singlets, doublets etc., particles) across the pipe radius at various t^*, normalised by volume, for Hamaker constant, $H = 36.76$zJ.

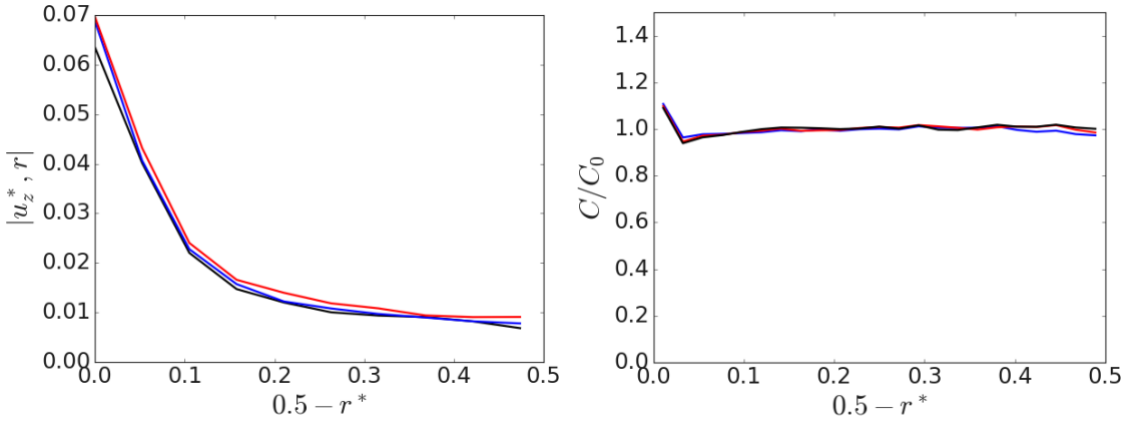

Figure 5.33: The mean relative particle collision velocity and particle concentration at different sample time across pipe. Black: t^* = 30, blue: t^* = 70, and red: t^* = 110 for Hamaker constant, $H =$ 36.76zJ.

Figures 5.33 shows the mean relative particle collision velocity (left) and the particle concentration profile (right) for a Hamaker constant of 36.76zJ. Comparing these results with those in Figures 5.27 and 5.30, the qualitative form of the profiles is the same in all cases, and the effect of varying the Hamaker constant is generally minimal.

In all cases, the Hamaker constant affects the van der Waals forces between particles, with increased interactions and a tendency to collide observed closer to the pipe wall. Particles are more likely to collide when the Hamaker constant increases because it is increases the strength of the van der Waals forces, especially in regions where particles are affected by attraction forces. Agglomeration events across the pipe radius were sampled at various times, as shown in Figures 5.25, 5.28, and 5.31. All three Hamaker constant cases show relatively constant agglomeration over the pipe cross-section at different times, with less agglomeration towards the pipe wall. Figures 5.26, 5.29 and 5.32 show that particles are evenly distributed for singlets, doublets, and triplets in all three cases. However, for quadruplets through to sextuplets, agglomeration tends to occur more in the middle or central regions of the pipe.

5.3.3 Effect of Reynolds number on collision and agglomeration

Finally, to determine how the flow Reynolds number affects particle behaviour, the flow's pressure gradient was reduced on order to achieve a $Re_\tau = 360$ flow, performed using the same computational mesh. Figure 5.34 illustrates the impact of decreasing the Reynolds number on the evolution of the number of agglomerates of size N_p. Again, the formation of agglomerates with constituent numbers ranging from singlets to sextuplets was found for $Re_\tau = 720$, whereas only quadruplets were seen for the lower Reynolds number. It is also observed that there is an increased agglomeration rate for the higher Reynolds number. This is again observed in Figure 5.35, which illustrates that particles are more likely to agglomerate, given a collision has already occurred, for the high Reynolds number case. This is likely due to the fact that the turbulent region is thinner at increased Reynolds numbers, and since most agglomeration takes place in the bulk flow region, there is a greater chance of particles encountering each other with similar velocities, increasing the chances of agglomeration.

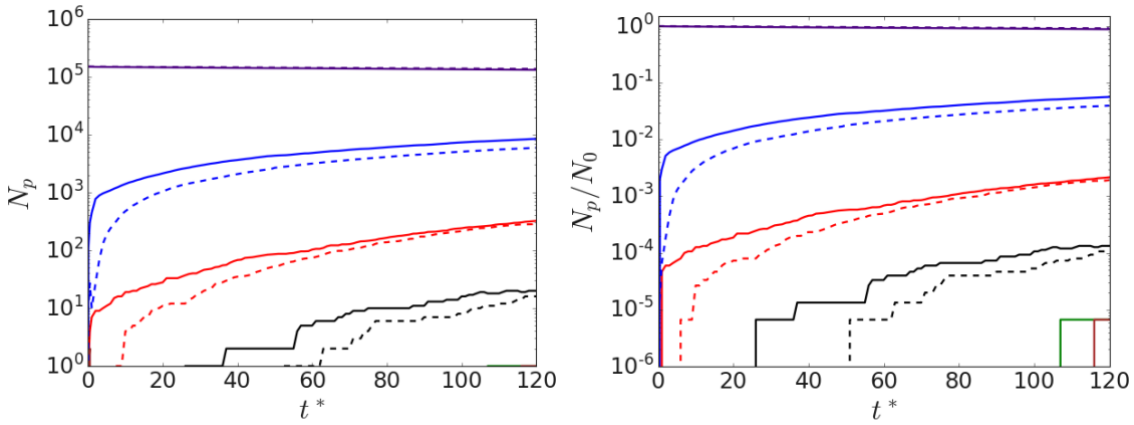

Figure 5.34 Influence of the Reynolds number on total number of agglomerates of size N_p (left), and normalised by total number of particles (right), as function of time, t^*. Indigo: singlets; blue: doublets; red: triplets; black: quadruplets; green: quintuplets and brown: sextuplets. —: Re_τ= 720, – –: Re_τ= 360.

At Reynolds number Re_τ = 720, almost 2 million individual particles interact with one another, resulting in the formation of aggregates of approximately 9672 particles, while at Reynolds number Re_τ = 360, over 1.8 million particle-particle collisions and 6651 agglomeration events are observed. Overall, the number of particle collisions and agglomerations typically varies approximately linearly with time and significantly depends on the Reynolds number. The highest Reynolds number results in increasing collision frequency and agglomeration.

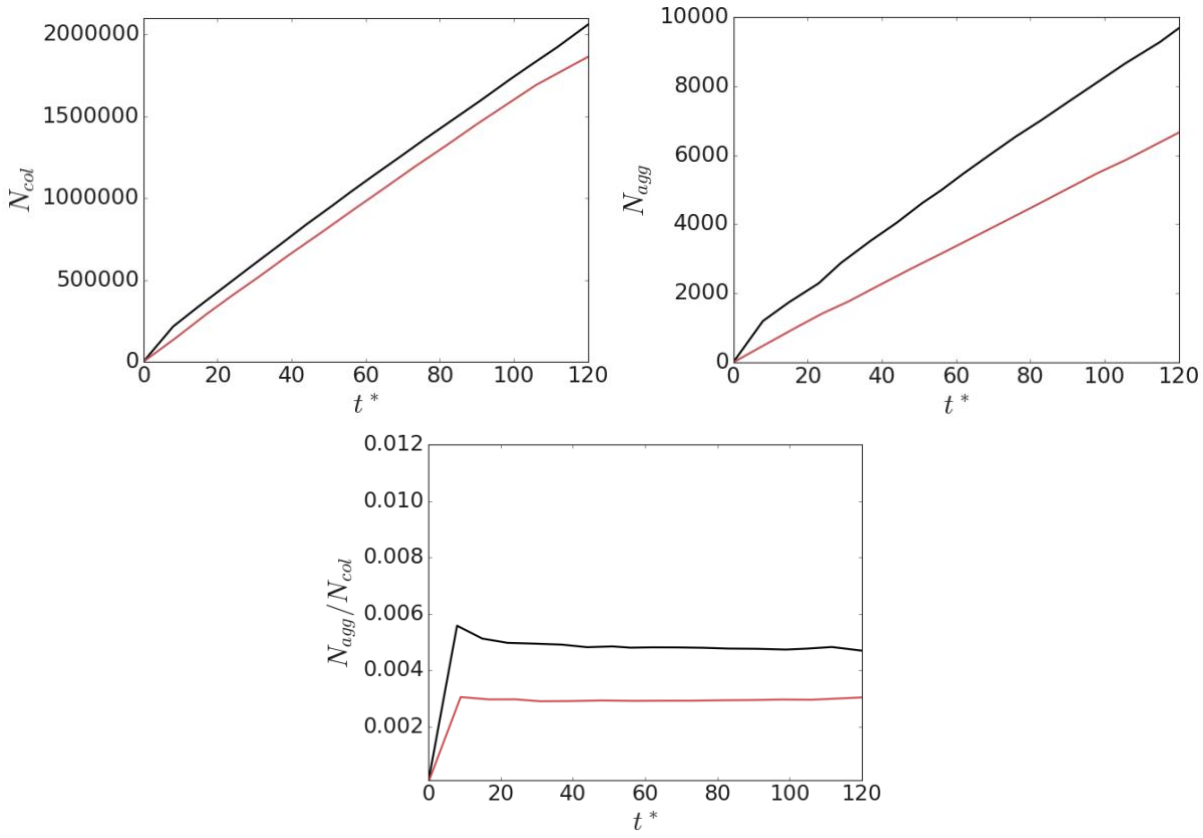

Figure 5.35: Distribution of the total number of particle-particle collision, N_{col}, upper-left and agglomeration, N_{agg}, upper-right events. Lower is the temporal evolution of the agglomeration efficiency, N_{agg}/N_{col}. Effect of Reynolds number is demonstrated. Black: Re_τ= 720 and red: Re_τ= 360.

Figure 5.36 illustrates the mean streamwise particle velocities for shear Reynolds number, Re_τ=720 and 360. The Reynolds number variation clearly affects the mean streamwise particle velocities because the fluid centreline velocity is reduced with an increase in Reynolds number. Figure 5.37 shows the root mean square of the streamwise ($u'^*_{z,rms}$), radial ($u'^*_{r,rms}$) and azimuthal ($u'^*_{\theta,rms}$), fluctuating particle velocity profiles as well as the Reynolds shear stress, $< u'_z\, u'_r >^*$ at Re_τ=720 and 360. The variation in Reynolds number has an impact on all normal and shear stresses in all flow regions with a shrinking of the width of the turbulent region with increased Reynolds number.

The influence of Reynolds number on the PDFs of dynamics particle properties in the viscous sublayer, buffer, log-law, and bulk flow regions of the pipe is shown in Figure 5.38. The radial particle velocity is presented in the upper-left plot, the azimuthal velocity is presented in the upper-right plot, the particle-fluid slip velocity is presented in the lower-left plot, and the particle velocity in the streamwise direction is presented on the lower-right plot. Reynolds

number has a significant influence on all regions of the flow, with high Reynolds number causing the PDFs of particle distributions to be more stretched, extending over a wider range of velocities.

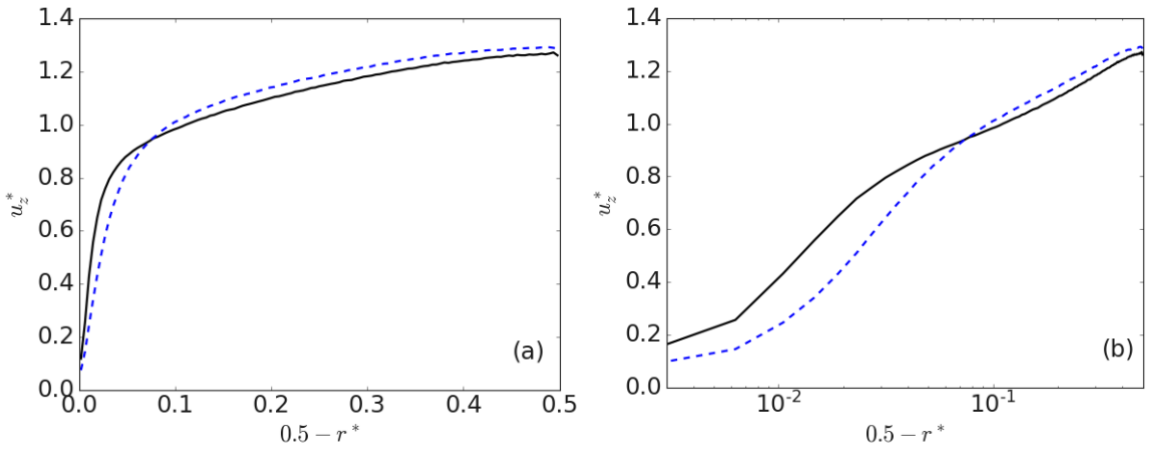

Figure 5.36: The effect of the Reynolds number on a four-way coupled flow's inner scaled statistical particle mean velocity profiles. Black: Re_τ= 720 and blue: Re_τ= 360 and (b) plotted on a logarithmic scale.

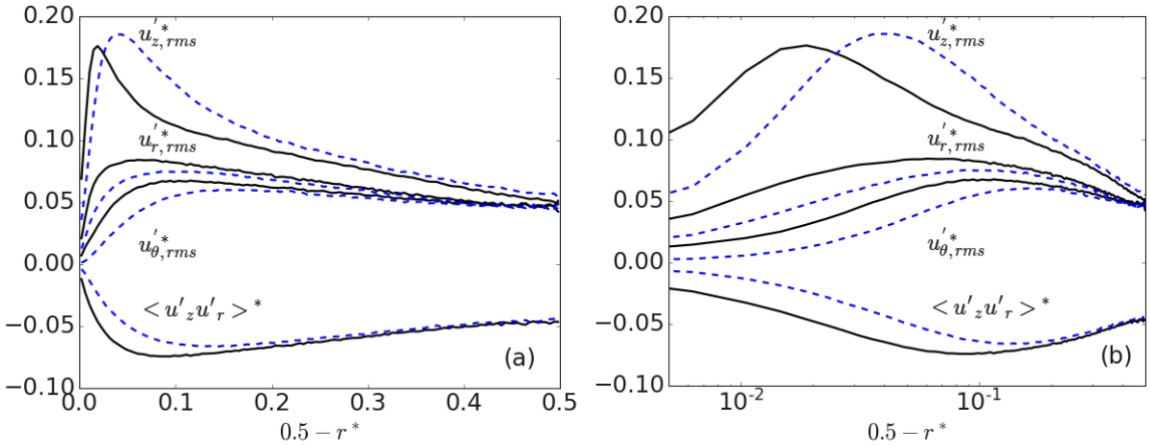

Figure 5.37: The effect of the Reynolds number on a four-way coupled flow's inner scaled statistical particle rms of streamwise, $u'^*_{z,rms}$, radial, $u'^*_{r,rms}$, and azimuthal, $u'^*_{\theta,rms}$, velocity fluctuations and Reynolds shear stress, $< u'_z\, u'_r >^*$. Black (− −): Re_τ= 720, and blue (−·−): Re_τ= 360 and (b) plotted on a logarithmic scale.

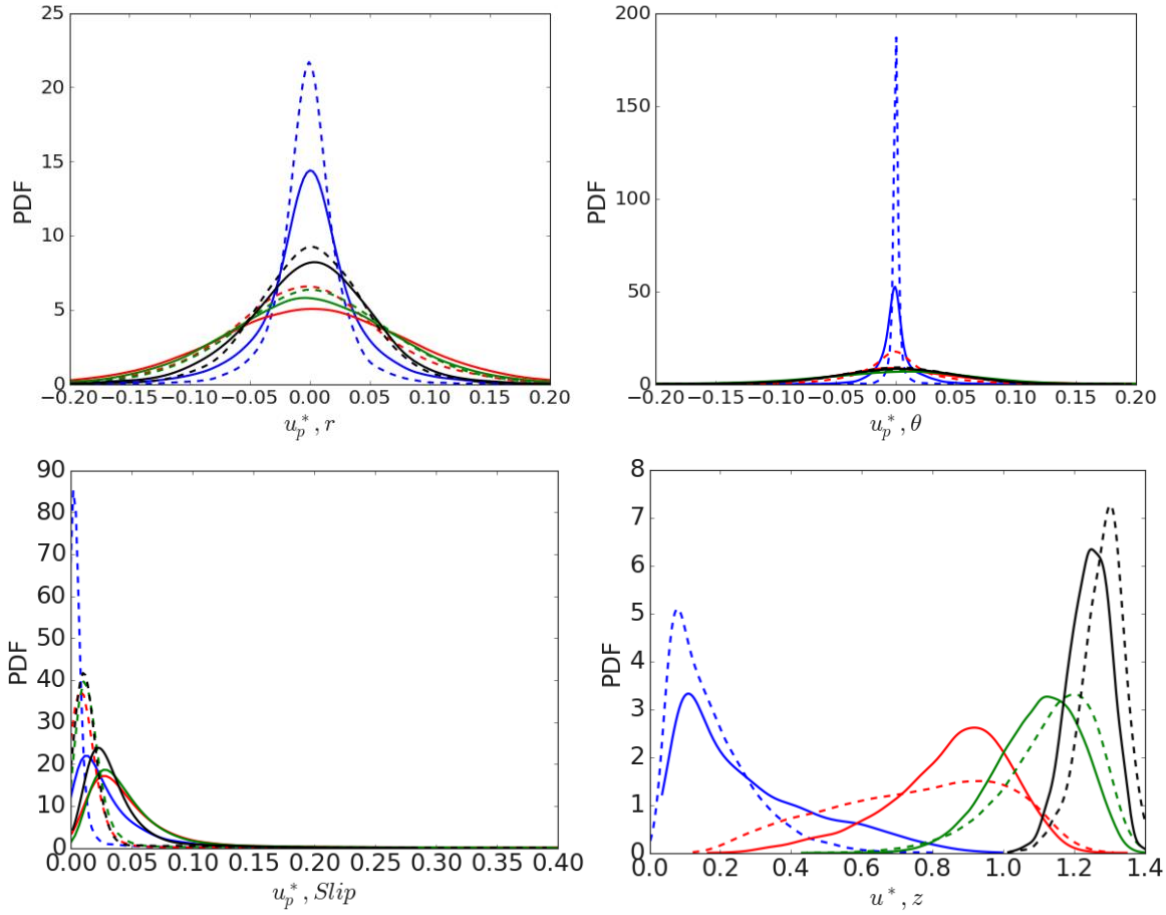

Figure 5.38: Probability density function for the different Reynolds number in the viscous sublayer, buffer, log-law and bulk flow regions of the pipe. Top left is the radial and right is azimuthal. Lower left is the slip velocity and right is the streamwise velocity. Blue: viscous sublayer; Red: buffer layer; Green: log-law region; Black: bulk flow. − −: Re_τ= 360 and —: Re_τ= 720.

5.3.3.1 Shear Reynolds number of 360

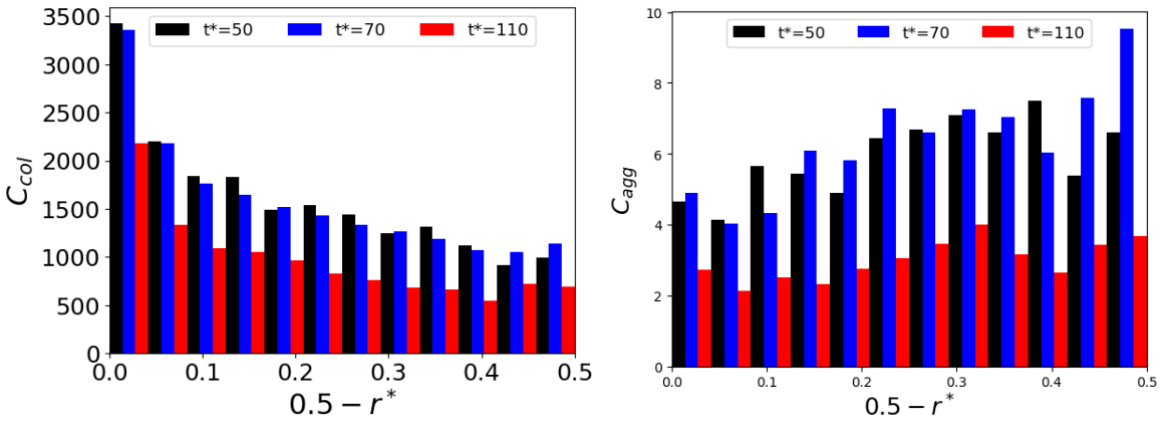

Figure 5.39: Number of collision (left) and agglomeration (right) events across the pipe radius sampled at different time t^*, normalised by volume.

Figure 5.39 shows the impact of modifying the Reynolds number to a lower value on the concentration of collision and agglomeration events across the pipe radius sampled at various times t^*. Evidently, for Re_τ=360, the collision rate along the wall is extraordinarily high and gradually drops with time, whereas the agglomeration rate is more uniform. At this lower Reynolds number, Re_τ=360, agglomerates form with constituent numbers ranging from singlets to quadruplets, as shown in Figure 5.40, whereas sextuplets were observed for the higher Reynolds number, Re_τ=720. Figures 5.41 shows the mean relative particle collision velocity (on the left) and the mean particle concentration profile (on the right) for Reynolds numbers $Re_\tau = 360$ with the trend in these profiles conforming with earlier findings and demonstrating little variation with simulation time.

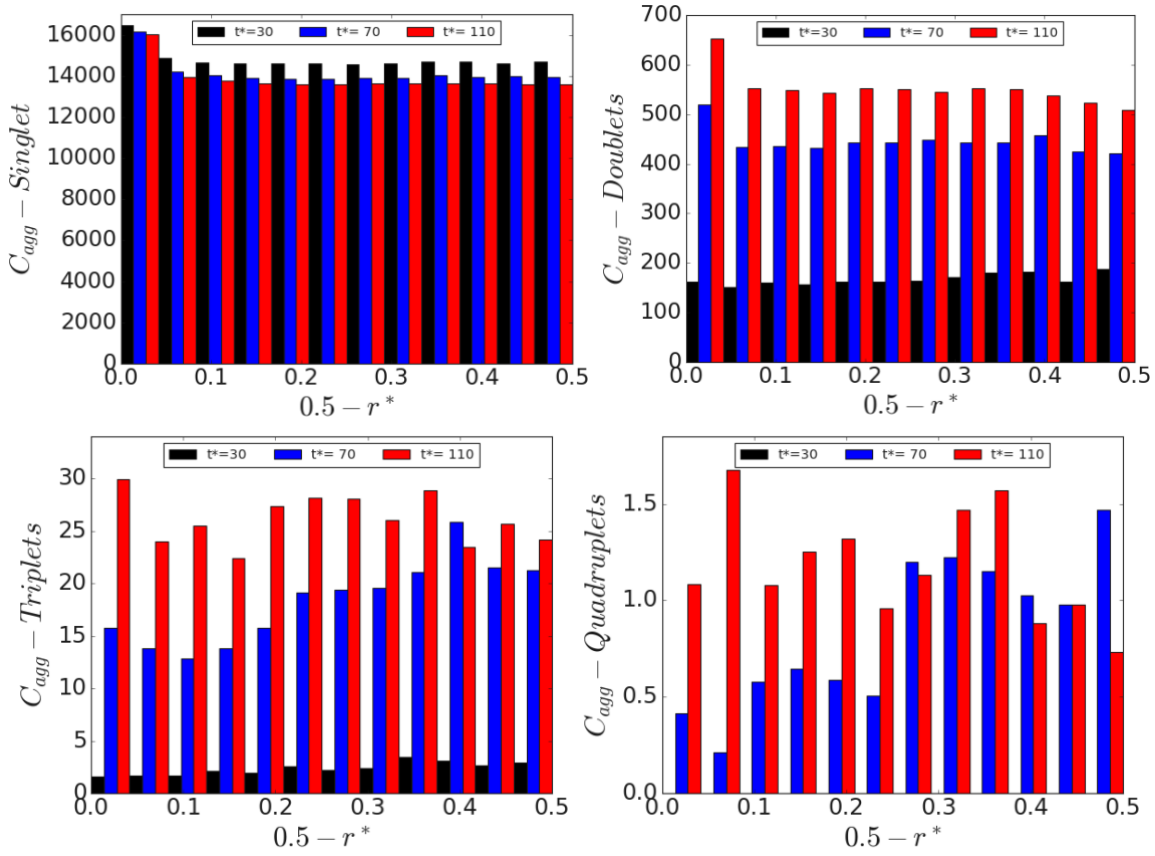

Figure 5.40: Agglomeration of primary particles (singlets, doublets etc., particles) across the pipe radius at various t^*, normalised by volume.

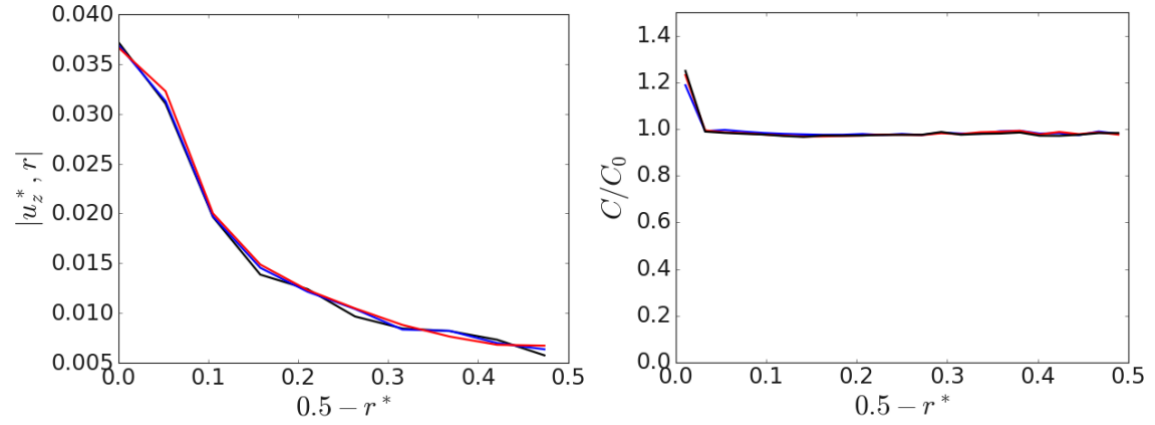

Figure 5.41: The mean relative particle collision velocity and particle concentration at different sample times across pipe. Black: t^* = 30, blue: t^* = 70, and red: t^*= 110 for Reynolds number, Re_τ = 360.

5.3.3.2 Shear Reynolds number of 720

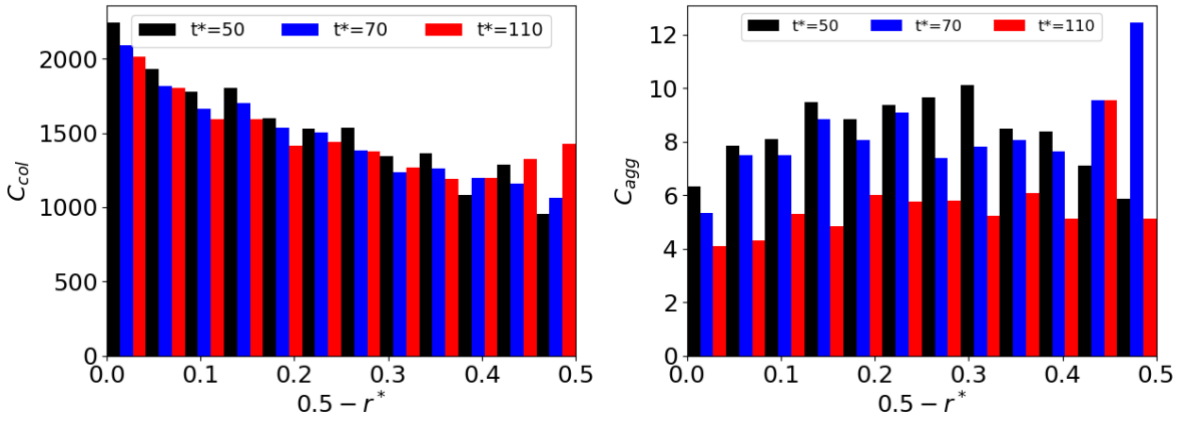

Figure 5.42: Number of collision (left) and agglomeration (right) events across the pipe radius sampled at different time t^*, normalised by volume.

Figure 5.42 shows the distribution of collision events across the pipe radius at different time for a Reynolds number Re_τ= 720. Compared to the results of Figure 5.39, as the Reynolds number increases, the influence of turbulent fluctuations becomes more prominent, leading to increased dispersion of particles, even at relatively low Stokes numbers, St^+ = 1.951. In a fluid flow, the Reynolds number has a substantial impact on how particles behave, which in turn influences collision and agglomeration. Due to the flow's chaotic nature, turbulence increases collision rates and tendencies towards agglomeration at higher Reynolds numbers. It is important to note that at t^* = 50 and 70, a higher-than-expected number of collisions are seen close to the wall for the lower Reynolds number case, as noted above, due to the reduction in turbulent fluctuations in this flow.

Figure 5.42 (right) shows the agglomeration occurrences across the pipe radius. At different times, the agglomeration rate across the pipe cross-section is relatively uniform, with less agglomeration near the pipe wall. Particles are homogenously dispersed for singlets, doublets, and triplets in both Reynolds number cases, as seen in Figures 5.40 and 5.43. However, agglomeration seems to happen more frequently in the middle or centre of the pipe for quadruplets and quintuplets.

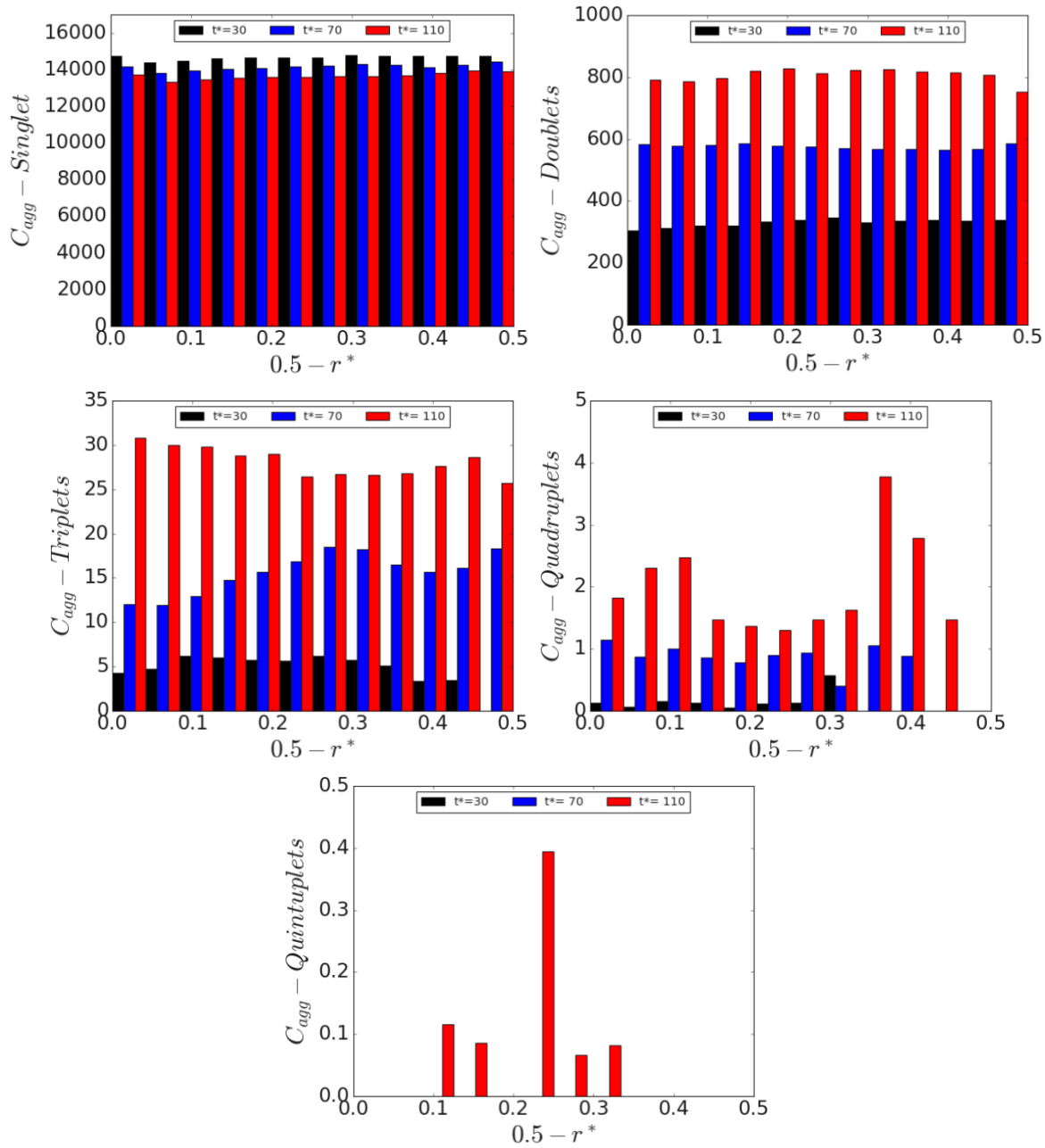

Figure 5.43: Agglomeration of primary particles (singlets, doublets etc., particles) across the pipe radius at various t^*, normalised by volume.

Figures 5.44 again shows the mean relative particle collision velocity and the mean particle concentration profile for the higher Reynolds number case, with the trend in these profiles conforming with earlier findings. Comparing Figures 5.41 and 5.44, the relative velocity and concentration profile are seen to be unaffected significantly by changes to the Reynolds number.

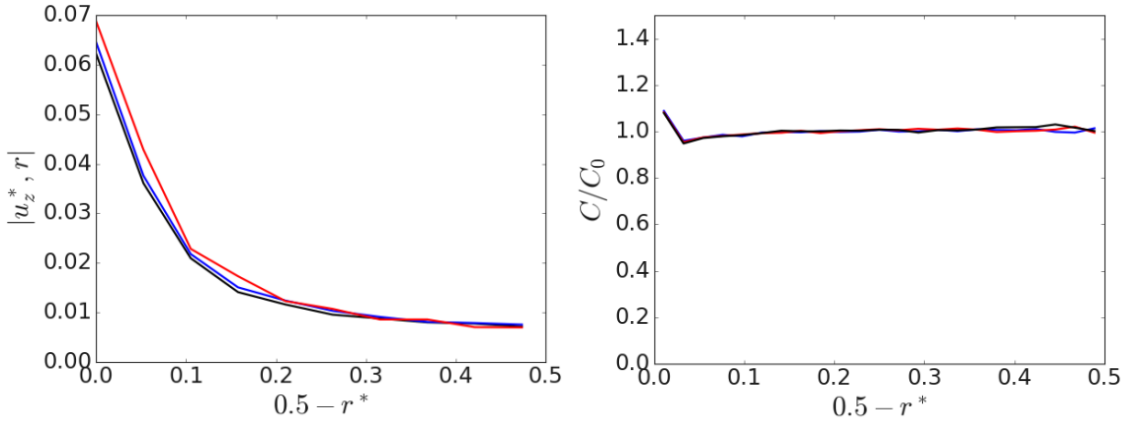

Figure 5.44: The mean relative particle collision velocity and particle concentration at different sample times across pipe. Black: t^* = 30, blue: t^* = 70, and red: t^*= 110 for Reynolds number, Re_τ = 720.

5.4 Summary of behavioural modification techniques

Here we compare and summarise the influence each parameter studied has on the particle-laden flow dynamics and agglomeration behaviour. Figure 5.45 illustrates how the Hamaker constant, Reynolds number, and normal restitution coefficient affect the time-dependent number of particles within the agglomerates as the simulation progresses. In all cases, the number of singlet particles decreases over time while the number of doublets, triplets, and quadruplets increases as the simulation progresses. At the start of the simulation 150,000 singlet particles were present at t^* = 0, however by t^* =1, the number of particles begin to steadily decrease with each parameter modulating the rate at which this occurs. The rate of decrement of the singlet particles depends on the main parameters of van der Waal's and collision interactions that were investigated. This behaviour is also shown to be dependent on the flow conditions, as well as the chemical and material properties.

For the smallest normal restitution coefficient, e_n = 0.2, up to quadruplet particles were found at t^* =1, whereas up to triplet particles were seen for the higher Hamaker constant, H = 36.76 zJ. This suggests that both a low restitution coefficient and high Hamaker constant have a substantial impact on the rate of agglomeration, providing the most agglomeration out of all the systems studied. By the time t^* = 60, the number of singlets had decreased by 12.15% for the restitution coefficient, e_n = 0.2, 6.64% for e_n = 0.4, and 3.45% for e_n = 0.6. The Hamaker constant, H = 36.76zJ, had decreased by 12.05%, H = 7.84zJ, had decreased by 3.10%, and the lowest Reynolds number, Re_τ = 360, had decreased by 3.36%. One intriguing observation is

that reducing the Reynolds number by half does not always result in a 50% reduction in agglomeration rate. This also applies to the formation of particles with doublets, triplets, and so forth.

The most evident finding from the analysis is that the lowest restitution coefficient has the largest effect on agglomeration behaviour, followed by the highest Hamaker constant. According to these results, we can infer that the Hamaker constant, restitution coefficient and Reynolds number all have an impact on singlet particles reduction. At t^* = 120, for e_n = 0.2, more than 21% of singlet particles had become either doublets, triplets, or quadruplet particles; for e_n = 0.4, this number was closer to 12%; and for e_n = 0.6, the highest restitution coefficient, it was 6.13%. For the highest Hamaker constant (H = 36.76 zJ) nearly 21% of singlet particles formed doublets or large agglomerates, while for the lowest Hamaker constant (H = 7.84 zJ) this was 5.64%. 8.54% of particles for Re_τ = 360 were found to form doublets, triplets, or quadruplets, according to the simulation results.

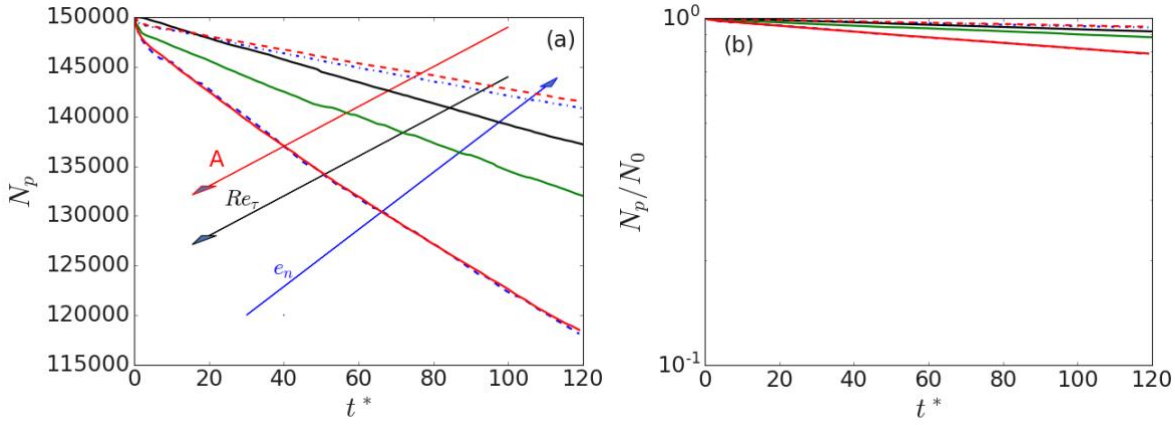

Figure 5.45: (a) Influence of the normal restitution coefficient, Hamaker constant and Reynolds number on total number of single particles, and (b) normalised by total number of particles, as function of time, t^*. Base case: —: e_n= 0.4, H = 22.3zJ, Re_τ = 720. – –: e_n= 0.6, –·–: e_n= 0.2; —: H = 36.76zJ, – –: H = 7.84zJ and —: Re_τ =360.

In all cases, the number of doublet particle agglomerates (Figure 5.46) is inversely proportional to the number of singlet particles; the formation of these agglomerates is initially observed at t^* = 1 and continues to grow over time. Comparing the highest Hamaker constant (8.88%) to the lowest restitution coefficient, e_n = 0.2 (8.44%), it appears that the formation of doublet particles is slightly higher. This is due to the evolution of doublet particles into triplet and quadruplet particles, as observed in Figure 5.40. For e_n = 0.2, almost 1% of the particles are

triplets, compared to 0.945% at H = 36.76 zJ. The triplet particle agglomerate (Figure 5.47) is first noticed at t^* = 1 except for at Reynolds number, Re_τ= 360. The quadruplet particle agglomerate is seen later in the simulation, at t^* =120, for the lowest Hamaker constant and highest restitution coefficient. There are usually considerably more doublet particles than triplet or quadruplet agglomerates, and this disparity is shown to grow over time, since at early times collisions between doublets and other particles are much less likely. In fact, there are more primary particles that could develop into doublets than doublets that could evolve into triplets and larger agglomerates. As previously stated, the agglomerates in all cases are spread uniformly, limiting the possibility of larger agglomerates forming at the rate of the doublets. These findings also demonstrate that the highest restitution coefficient and lowest Hamaker constant were related to the lowest agglomeration rate. Additionally, it appears that far longer simulation runs are required before large numbers of triplet and quadruplet particle agglomerates can develop (Figures 5.47 and 5.48). Regardless, for all important interaction parameters that have been examined in this chapter, the number of agglomerates and their size increase over time. These findings are consistent with previous research by Afkhami et al. (2013), Njobuenwu and Fairweather (2017), and Mortimer et al. (2020).

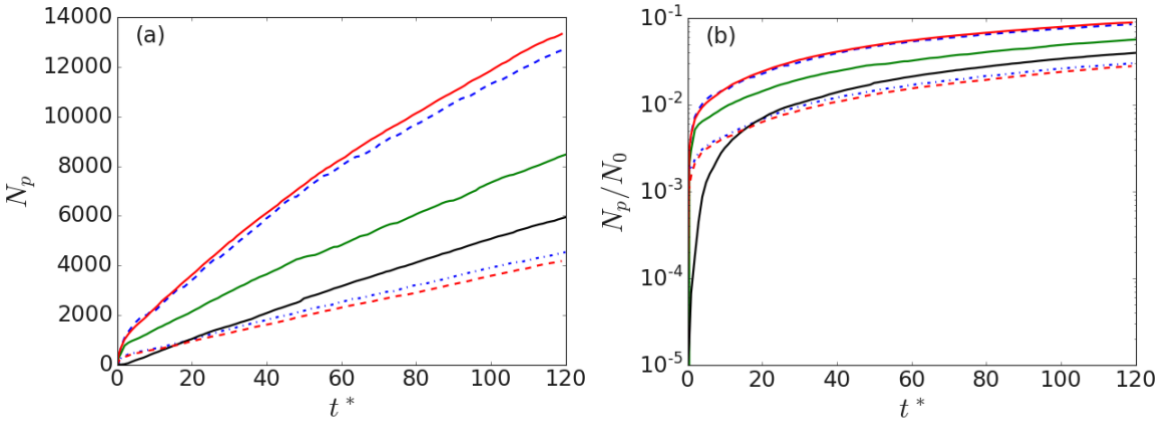

Figure 5.46: Influence of the normal restitution coefficient, Hamaker constant and Reynolds number on total number of two particle agglomerates (doublets), and (b) normalised by total number of particles, as function of time, t^*. Base case: —: e_n= 0.4, H = 22.3zJ, Re_τ = 720. – –: e_n= 0.6, —·—: e_n= 0.2; —: H = 36.76zJ, – –: H = 7.84zJ and —: Re_τ =360.

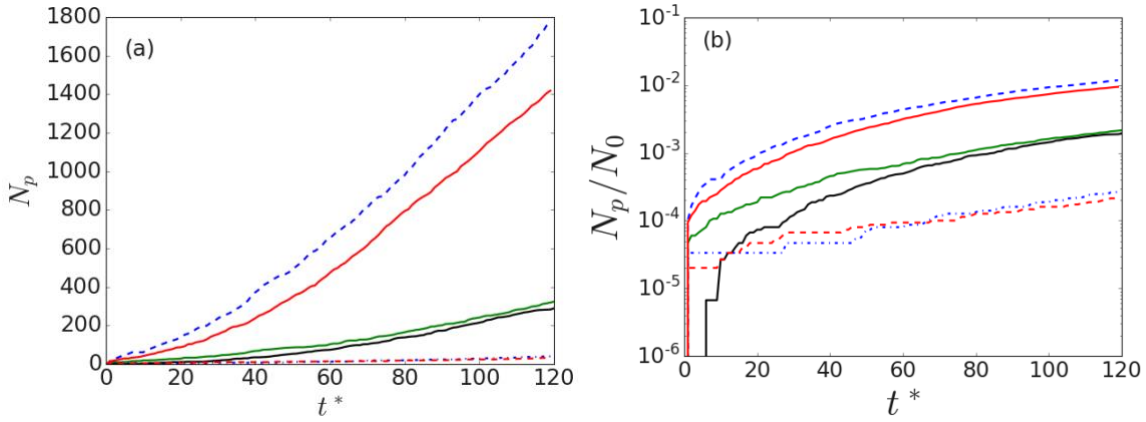

Figure 5.47: Influence of the normal restitution coefficient, Hamaker constant and Reynolds number on total number of three particle agglomerates (triplets), and (b) normalised by total number of particles, as function of time, t^*. Base case: —: e_n= 0.4, H = 22.3zJ, Re_τ = 720. – –: e_n= 0.6, —·—: e_n= 0.2; —: H = 36.76zJ, – –: H = 7.84zJ and —: Re_τ =360.

Table 5.3 displays the total number of agglomerates of different size at intervals of 30,000 (t^* = 30) timesteps, as well as the percentage decrement of primary particles and increments for doublets or larger particles. Additional research is needed to understand how a high Hamaker constant combined with a low restitution coefficient, or a low Hamaker constant combined with a high restitution coefficient, affects collision and agglomeration rates. The combined extremes of the agglomerates were not investigated due to time constraints and excessively extended simulation times.

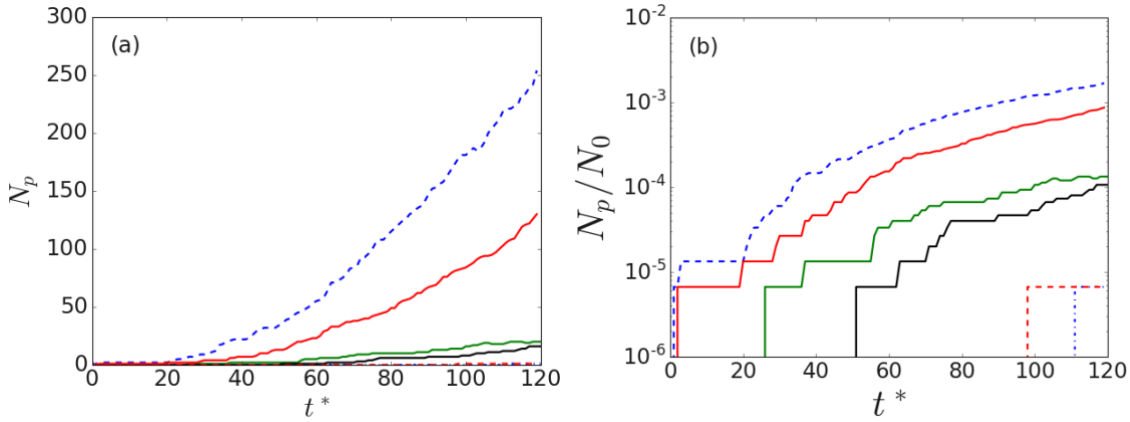

Figure 5.48: Influence of the normal restitution coefficient, Hamaker constant and Reynolds number on total number of four particle agglomerates (quadruplets), and (b) normalised by total number of particles, as function of time, t^*. Base case: —: e_n= 0.4, H = 22.3zJ, Re_τ = 720. – –: e_n= 0.6, —·—: e_n= 0.2; —: H = 36.76zJ, – –: H = 7.84zJ and —: Re_τ =360.

Table 5.3: The total number of agglomerates of size N_p at different t^*.

Agglomerates		Simulations					
		$e_n = 0.2$	$^{**}e_n = 0.4$	$e_n = 0.6$	H (zJ) = 7.84	H (zJ) =36.76	$Re_\tau = 360$
$t^* = 1$	Singlets	148557	149083	149468	149541	148604	149980
	Percentage decreased (%)	0.962	0.611	0.355	0.306	0.931	0.036
	Doublets	697	448	260	225	677	10
	Percentage increased (%)	0.465	0.3	0.173	0.15	0.451	0.018
	Triplets	15	7	4	3	14	0
	Percentage increased (%)	0.01	0.005	0.0027	0.002	0.0093	0
	Quadruplets	1	0	0	0	0	0
	Percentage increased (%)	0	0	0	0	0	0
$t^* = 30$	Singlets	139988	144001	147191	147398	139645	147188
	Percentage decreased (%)	6.67	4	1.87	1.735	6.9	1.875
	Doublets	4630	2933	1394	1286	4937	1388
	Percentage increased (%)	3.09	1.96	0.929	0.857	3.29	0.925
	Triplets	237	43	7	10	155	12
	Percentage increased (%)	0.158	0.029	0.0047	0.0067	0.103	0.008
	Quadruplets	9	1	0	0	4	0
	Percentage increased (%)	0.006	0.0006	0	0	0.00267	0
$t^* = 60$	Singlets	131772	140033	144825	145344	131932	143446
	Percentage decreased (%)	12.152	6.64	3.45	3.104	12.05	4.369
	Doublets	8017	4819	2568	2307	8277	3164
	Percentage increased (%)	5.34	3.21	1.71	1.538	5.518	2.109
	Triplets	653	103	12	14	474	74
	Percentage increased (%)	0.44	0.069	0.0087	0.0093	0.316	0.0493
	Quadruplets	55	5	0	0	23	1
	Percentage increased (%)	0.037	0.0033	0	0	0.0153	0.00067
$t^* = 90$	Singlets	124681	136119	142832	143450	124880	140243
	Percentage decreased (%)	16.88	9.25	4.78	4.367	16.75	6.505
	Doublets	10537	6617	3548	3245	10994	4605
	Percentage increased (%)	7.02	4.41	2.37	2.16	7.33	3.07
	Triplets	1190	201	24	20	948	173
	Percentage increased (%)	0.79	0.134	0.016	0.0133	0.632	0.115
	Quadruplets	147	11	0	0	67	7
	Percentage increased (%)	0.098	0.0073	0	0	0.045	0.0047
$t^* = 120$	Singlets	118127	132011	140798	141535	118511	137187
	Percentage decreased (%)	21.25	11.99	6.13	5.64	20.99	8.542
	Doublets	12667	8463	4539	4181	13322	5941
	Percentage increased (%)	8.44	5.64	3.026	2.787	8.88	3.961
	Triplets	1775	324	40	33	1418	289
	Percentage increased (%)	1.18	0.216	0.027	0.022	0.945	0.193
	Quadruplets	254	20	1	1	130	16
	Percentage increased (%)	0.17	0.0133	0.0007	0.00067	0.0867	0.0106

** Base case with $e_n = 0.4, H(\text{zJ}) = 22.3$ and $Re_\tau = 720$.

5.5 Conclusions

This chapter has considered the impact of various behavioural modification techniques within wall-bounded turbulent pipe flows. Prior to these simulations, extensive single- and multi-phase simulations were validated against previous studies with good agreement obtained. To establish the effects of behavioural modification techniques, a range of turbulent pipe flows with different particle electrochemical and fluid properties were simulated. The use of modifications to the fluid and solid particle properties to promote desired outcomes such as reducing particle agglomeration have been considered. This has entailed the implementation of two-way and four-way coupling between the particles and the fluid flow, as well as the incorporation of models for particle interaction and agglomeration.

To predict particle aggregation caused by collision interactions, an energy-balance based agglomeration determination technique was employed in conjunction with four-way coupling. The variation of influential parameters including the reduced surface potential, inverse Debye length, temperature of suspension, the restitution coefficient, Hamaker constant and Reynolds number were studied to determine the impact of behavioural modification effects. These modifications alter particle interactions by influencing various terms in the Derjaguin-Landau Verwey-Overbeek (full DLVO) theory interaction potentials.

From the analysis, it can be concluded that the electric double layer has an insignificant effect on collision and agglomeration rate. One of the more significant findings to emerge from this study is that the size and rate at which various agglomerates are formed has an inverse relationship to the restitution coefficient. Furthermore, we observe that collisions take place more frequently close to the pipe wall, though this does not appear to have much influence on the agglomeration event distribution, which is relatively homogeneous throughout the pipe. The aforementioned phenomena, in which the frequency of collisions increases in close proximity to the pipe wall while having minimal impact on the distribution of agglomeration events, can be comprehended by considering the fluid dynamics and particle behaviour. When compared to the centre of the pipe, the fluid velocity gradient near the wall is significantly larger. Analysis of the magnitude of relative particle collision velocities throughout the pipe revealed that particles colliding in the bulk region of the flow have substantially lower relative velocities than those near the wall, favouring agglomeration. On the other hand, collisions taking place in the viscous and buffer regions have increased relative velocities and hence

collision kinetic energy (backed up by Fig. 5.44), reducing the chance of agglomeration in favour of rebound events.

Similar studies have been performed for Hamaker constant and Reynolds number variation. The evidence from this study suggests that Hamaker constant and Reynolds number have a large impact on particle-particle interaction. Both collision and agglomeration rates have a linear dependency on the Hamaker constant and Reynolds number across the pipe. The analysis shows that a higher Hamaker constant increases the rate at which agglomeration takes place, and that the Reynolds number also increases the likelihood of collision and agglomeration, despite enhanced turbulence leading to more ballistic collisions. The present study has been one of the first attempts to thoroughly examine the impact of various terms in DLVO theory on collision and agglomeration rate in a pipe geometry. Further research should be carried out to investigate the combination of cases that resulted in high collision and agglomeration rates (such as low restitution coefficient, high Hamaker constant, and high Reynolds number) and those that resulted in low collision and agglomeration rates (such as high restitution coefficient, low Hamaker constant, and low Reynolds number).

6 PREDICTION OF CRITICAL DEPOSITION VELOCITIES

6.1 Introduction

In this chapter, particle-laden turbulent pipe flows are studied using DNS and/or LES of the continuous phase in combination with LPT to provide insights on methods for prediction of the critical deposition velocity at various particle Stokes numbers. In the present literature, there is a notable lack of DNS-LES based simulations of particle-laden flows that take into consideration both particle-fluid and particle-particle interactions (four-way coupling), particularly in cylindrical geometries. Furthermore, as discussed in the literature review, no previous modelling studies have examined the onset of deposition or prediction of the critical deposition velocity in such flows, with most deposition studies being experimental. However, in practice, it is challenging to study *in situ* the flows that are common in the processing of nuclear waste due to high costs and difficulties with the logistics of using intrusive methods. This emphasises the necessity for non-invasive studies, such as those conducted through computational simulation. The main objective of this research is to develop and facilitate predictive techniques of use in industry, to promote safer, more affordable waste management and decommissioning. For radioactive waste management to be effective, pond and silo sludge behaviour needs to be understood and modelled, and for its waste retrieval it is critical to characterise how sludges and slurries containing dense particles would disperse throughout a pipe and potentially deposit during transportation. Of great importance is the ability to predict the flow rates necessary to keep the particles suspended, hence the ability to predict this parameter is a major aim of this chapter. Volume fractions of up to 0.025 (or concentration of particles for mono-dispersed flows) have been examined in this Chapter; however, the model can handle much larger volume fractions, but only extremely slowly. It should be noted, however, that in transporting sludges and slurries for further processing within industry, particle concentration is generally restricted for safety reasons and to avoid criticality.

Rice (2013) and subsequently Rice et al. (2020) investigated the settling and deposition behaviour of suspensions of dense particles in closed cylindrical pipes using ultrasonic methods. In their experiments, a range of parameters were considered, though pipe diameter was not. The onset of deposition and resuspension based on fundamental properties was studied. In their experiments, parameters that are difficult to vary were excluded, such as the role of particle size distribution or polydispersity and packing fraction, although the influence of pipe diameter, *D*, was also not considered. Rice et al. (2020) proposed two ways of evaluating the critical deposition velocity: to monitor and record the onset of particles depositing as the flow rate is lowered, and to observe and monitor particles resuspending from a deposited bed as the flow rate is increased. The authors argued that these were equivalent and represented different ways to obtain the same critical deposition velocity.

In the literature, the critical deposition velocity is described in several ways. The two definitions that are most frequently used are the minimum flow velocity needed to prevent solid particles from depositing, or the velocity that corresponds to the least amount of pressure loss across the pipe. We define the critical deposition velocity as the flow velocity at which particles first start to deposit out in a flow. This occurs when the forces causing the particles to deposit towards the lower walls of the pipe (in a horizontal pipe flow) outweigh the forces keeping them suspended in the fluid. Such phenomena can be caused by a combination of fluid characteristics, particle size and density, and volume fraction. Understanding and accurately predicting the critical deposition velocity would be useful for optimising nuclear waste processing procedures, and better system designs to reduce particle deposition.

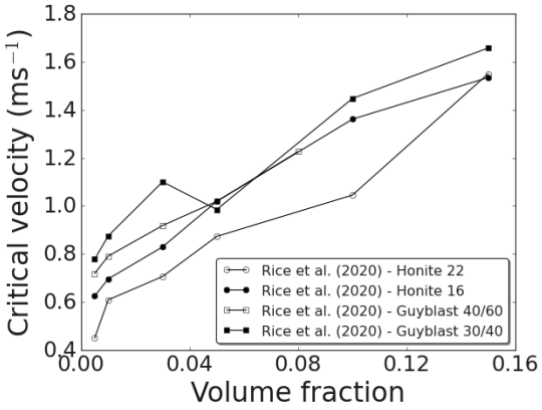

Figure 6.1: Rice et al.'s (2020) original data for variation of critical deposition velocity, V_c, with volume fraction, ϕ_p, of suspended solids for four particle species.

Figure 6.1 shows the experimental results of Rice et al. (2020) for four different particle types, plotting the critical deposition velocity against volume fraction. The four particle species examined in the acoustic bed depth measurements were Honite 16 (d_P = 41 μm), Honite 22 (d_P = 77 μm), Guyblast 40/60 (d_P = 468 μm) and Guyblast 30/40 (d_P = 691 μm) and the critical velocity was established through monitoring resuspension as the flow rate increased. Honite is a soda-lime glass bead, whilst Guyblast is a urea-based thermoset resin.

6.2 The Oroskar and Turian correlation

In an effort to relate the characteristics of the flow to the critical deposition velocity, a correlation, Eq. (6.1), was developed through studies on slurry transport flows by Oroskar and Turian (1980). An analysis based on balancing the energy required to suspend particles in a flow with that derived from the dissipation of an appropriate fraction of the turbulent eddies was used and subsequently fitted to a wide range of experimental critical deposition velocity data. Their correlation may be stated as:

$$\frac{V_c}{\sqrt{gd_P(s-1)}} = 1.85\left(\frac{d_P}{D}\right)^{-0.378}\phi^{0.1536}(1-\phi)^{0.3564}\left(\frac{D\rho_f\sqrt{gd_P(s-1)}}{\mu}\right)^{0.09} \quad (6.1)$$

Here, μ is the fluid dynamic viscosity, g the acceleration due to gravity, V_c the critical deposition velocity, d_P the particle diameter, D the pipe diameter, ρ_f the density of fluid phase, ϕ the particle phase volume fraction and s the density ratio, $s = \rho_s/\rho_f$. This has been used to collapse Rice's et al. (2020) experimental dataset.

Figure 6.2 shows the experimental resuspension datasets of Rice et al. (2020) and Yan (2010) collapsed against the correlation of Eq. (6.1). Note that the data of Yan (2010) is used here to include data from different diameter pipes. Although there is fair agreement between the Oroskar and Turian (1980) correlation and the experimental datasets from Yan (2010) and Rice et al. (2020), the model does not accurately represent the behaviour at low solids loadings. To attempt to improve this correlation using a larger range of datasets, in this chapter, a novel correlation model is developed and validated using data from resuspension and deposition experiments in order to account for both low and high solids loadings, and to evaluate whether Rice at al.'s (2020) contention that evaluating the critical deposition velocity from the onset of particles depositing as the flow rate is lowered, or as they resuspend from a deposited bed as

the flow rate is increased, is valid. The authors argued that these were equivalent and represented different ways to obtain the same critical deposition velocity.

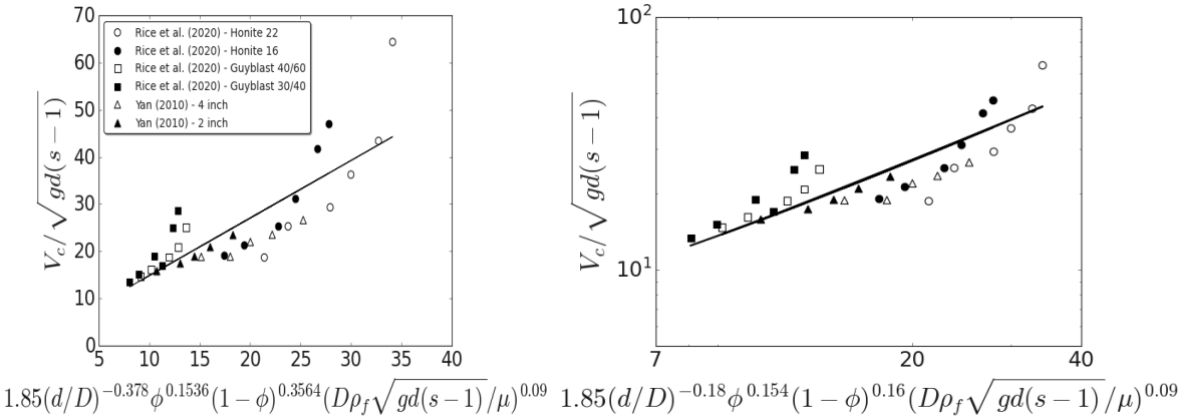

Figure 6.2: Resuspension datasets collapsed using the Oroskar and Turian (1980) correlation.

It should be noted that although alternative correlations to that of Oroskar and Turian (1980) exist, all were found to fit the Rice et al. (2020) and Yan (2010) datasets to a similar level of accuracy.

6.3 Dimensional analysis

To obtain the improved correlation, a dimensional analysis technique was employed. The dimensional analysis was performed based on the Buckingham Pi (π) theorem rules (Sonin, 2004). The pertinent variables are defined using the base dimensions of mass, length, and time, referred to as the {MLT} system. Dimensional quantities are then used as repeated variables in each step before all required Pi's are solved for. The functional relationship is expressed as $\Pi_1 = f(\Pi_2, \Pi_3, \Pi_4 \ldots)$. The critical velocity can be expressed as a function of its dependent variables as follows:

$$V_c = f(d, D, \phi, (\rho_s - \rho_f)g, \rho_f, \mu) \tag{6.2}$$

where the following definitions stand:

$\mu = [ML^{-1}T^{-1}]$ – dynamic viscosity

$g = [LT^{-2}]$ – acceleration due to gravity

$V_c = [LT^{-1}]$ – critical deposition velocity

$d = [L]$ – particle diameter

$D = [L]$ – pipe diameter

$Q_s = [L^3T^{-1}]$ – solid-phase volumetric flow rate

$Q_f = [L^3T^{-1}]$ – fluid-phase volumetric flow rate

$\rho_s = [ML^{-3}]$ – density of solid phase

$\rho_f = [ML^{-3}]$ – density of fluid phase

Note that the volume fractions and density ratios are already in their non-dimensional forms, i.e. $\phi_p = [1], s = \frac{\rho_s}{\rho_f}[M^0L^0T^0] = [1]$. There are 7 pertinent variables and three primary dimensions involved, {MLT}. Thus, four pi groups $(7 - 3 = 4)$ are required to solve the functional relationship. We may obtain the first two Pi parameters through the observations:

$$\Pi_1 = d/D \tag{6.3}$$

$$\Pi_2 = \phi \tag{6.4}$$

We choose to eliminate the following variables, D and ϕ, since they were already used in Π_1 and Π_2. Now, we are left with $V_c, d, (\rho_s - \rho_f)g, \rho_f, \mu$:

$$\begin{aligned}\Pi_3 = & [V_c][d]^a \left[(\rho_s - \rho_f)g\right]^b \left[\rho_f\right]^c \\ = & [LT^{-1}][L]^a[ML^{-3}LT^{-2}]^b[\mathrm{M}L^{-3}]^c.\end{aligned} \tag{6.5}$$

The exponents a, b and c are computed by setting all the exponents to zero, i.e., M^0, L^0, T^0, therefore:

$$\Pi_3 = V_c/\sqrt{gd(s-1)} \tag{6.6}$$

Finally,

$$\begin{aligned}\Pi_4 = & [\mu][d]^a\left[(\rho_s - \rho_f)g\right]^b\left[\rho_f\right]^c \\ = & [ML^{-1}T^{-1}]\,[L]^a[ML^{-3}LT^{-2}]^b[\mathrm{M}L^{-3}]^c.\end{aligned} \tag{6.7}$$

Therefore,

$$\Pi_4 = D\rho_f\sqrt{gd(s-1)}/\mu \tag{6.8}$$

When Π_3 is written as a function of the other Pi components, we obtain $\Pi_3 = f(\Pi_1, \Pi_2, \Pi_4)$ which is:

$$\frac{V_c}{\sqrt{gd(s-1)}} = f(\frac{d}{D}, \phi \text{ and } \frac{D\rho_f\sqrt{gd(s-1)}}{\mu}). \tag{6.9}$$

To develop a functional relationship, the above equation is set to:

$$\frac{V_c}{\sqrt{gd(s-1)}} = i_0 \left(\frac{d}{D}\right)^{i_1} \phi^{i_2} (1-\phi)^{i_3} \left(\frac{D\rho_f\sqrt{gd(s-1)}}{\mu}\right)^{i_4}. \tag{6.10}$$

Values for $i_0 - i_4$ were determined by fitting to the Rice et al. (2020) and Yan (2010) datasets by regression. The following new model was derived using Eq. (6.10) through linear regression:

$$\frac{V_c}{\sqrt{gd(s-1)}} = 1.85 \left(\frac{d}{D}\right)^{-0.18} \phi^{0.154} (1-\phi)^{0.16} \left(\frac{D\rho_f\sqrt{gd(s-1)}}{\mu}\right)^{0.09}. \tag{6.11}$$

The datasets present in Figure 6.1 were collapsed using the dimensional analysis model described above to obtain the results shown in Figure 6.3. From this point forward, the variable *X* also represents the RHS of Eq. (6.11) for simplicity.

6.4 Application of the improved critical deposition velocity correlation

6.4.1 Experimentally obtained particle deposition and resuspension datasets

Rice et al. (2020) investigated each particle species based on the same pipe diameter, $D = 42.6$ mm. To include the pipe diameter dependency in the above expression, the Yan (2010) experimental resuspension datasets were also included in developing the correlation. Yan

(2010) used $D = 50.8$ mm and $D = 101.6$ mm with small, grained sand particles without fines. Figure 6.3 depicts the Rice et al. (2020) and Yan (2010) experimental resuspension datasets collapsed against the present empirical correlation model, Eq. (6.11). Most of the Rice et al. (2020) and Yan's (2010) predicted critical deposition velocities are in line with the present correlation model predictions.

The disparities between the values that are observed and the values that a model (linear regression) predicts are referred to as residuals in Table 6.1. Residual analysis is widely used to assess a model's fit to data. Large residuals indicate that the model is missing some important information from the data. Using the residuals to identify trends, one can identify areas where the model underperforms and potentially improve it. For predictions of the correlation of Oroskar and Turian's (1980), the residual is seen to higher for every experimental resuspension dataset considered. In the case of the present model, the residual is significantly reduced showing better correlation of the available data.

Table 6.1: Experimental resuspension dataset's average residuals.

Experimental resuspension datasets	Oroskar and Turian (1980) average absolute residuals	Present model average residuals
Rice et al. (2020) - Honite 22	1.52	1.03
Rice et al. (2020) - Honite 16	0.24	0.002
Rice et al. (2020) - Guyblast 40/60	1.85	0.19
Rice et al. (2020) - Guyblast 30/40	3.32	0.84
Yan (2010) - 4 inch	5.94	3.6
Yan (2010) - 2 inch	1.6	0.024
Average	2.41	0.95

To test Rice's et al. (2020) contention that one can evaluate the deposition velocity from the onset of particle resuspension or deposition, experimental predictions from both deposition and resuspension experiments were also plotted against the same empirical correlation. Parzonka et al. (1981) examined the impact of solids concentration and particle size on the onset of deposition in a horizontal pipe flow. The authors considered three different pipe diameters, $D = 50.8$ mm, 103 mm and 202 mm to investigate the critical deposition velocity. These velocities were experimentally established using two different approaches, utilising both direct visual observation of the flow pattern in clear tubes and indirect observations utilising the

measured pressure gradient. The authors found that both particle size and pipe diameter had significant impact on the measured critical deposition velocity.

Al-Lababidi et al. (2012) used $D = 103$ mm and low particle (sand) volume fractions, $\phi_p =$ 0.000016 - 0.000538. The authors observed that stable sand dunes close to the lower wall of the pipe were formed by scouring dunes. Using pipe diameters of 19.05 mm and a variety of volume fractions, up to 20% solid concentration, Sinclair (1962) also examined the critical deposition velocity. The velocity was determined by visually viewing particles that remained stationary on the bottom of the tube. The author further confirmed that the deposition velocity is influenced by both the solid's concentration and particle diameter.

Graf et al. (1970) conducted research to establish the critical deposition velocity in solid-liquid mixtures. This research employed adaptable technology that enabled a thorough examination of the critical velocity through a transparent pipe segment. The experiments were conducted by utilising horizontal pipes with 101.6 mm and 152.4 mm diameter, and two uniform sands with d = 880 μm and d = 450 μm. The authors determined the critical velocity by observation through a plastic test section and by measuring the decrease in the fluid's total energy as it travelled through the pipe – commonly referred to as head loss curves.

Figure 6.4 gives the results of the deposition-only experimental datasets plotted against the present correlation. As can be observed from Figures 6.3 and 6.4, the correlation provides reasonable agreement in both cases, i.e. the contention proposed by Rice et al. (2020) is generally correct. Figure 6.5 compares the deposition-based datasets along with series 7 from the findings of Parzonka et al. (1981) to the current empirical correlation. In this study, the pipe diameter was enlarged to 207 mm and a significantly high-volume fraction was used in the series 7 experiments, which resulted in very high critical deposition velocities. The present correlation appears to underpredict Parzonka et al.'s (1981) series 7 findings, however the results show more agreement on the log scale, indicating reasonable order-of-magnitude agreement. Finally, in Figure 6.6, all of the resuspension and deposition-based data for the critical deposition velocity are compared against the current correlation. Overall, the current model fits well considering that the different experimental studies used a large range of volume fractions, particle diameters, and density ratios, and most importantly different ways to establish the critical deposition velocity.

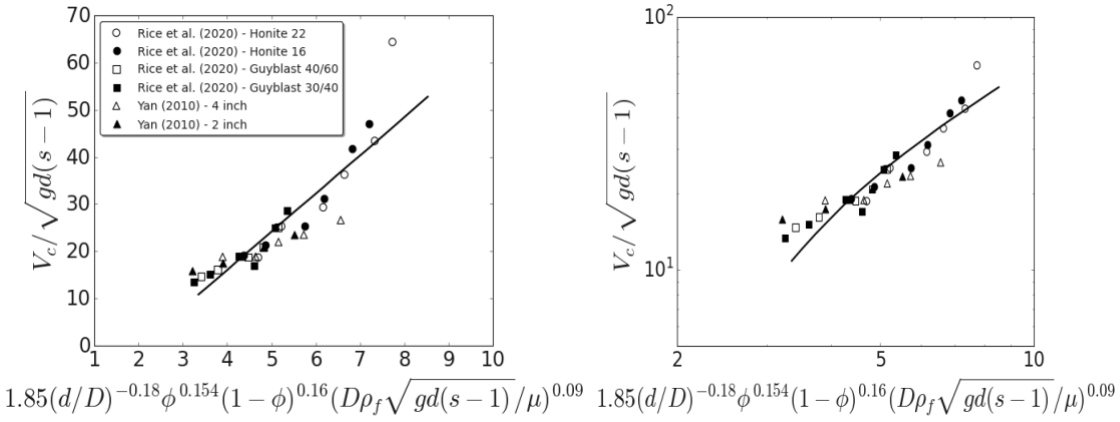

Figure 6.3: Resuspension datasets collapsed using present empirical correlation, Eq. (6.11).

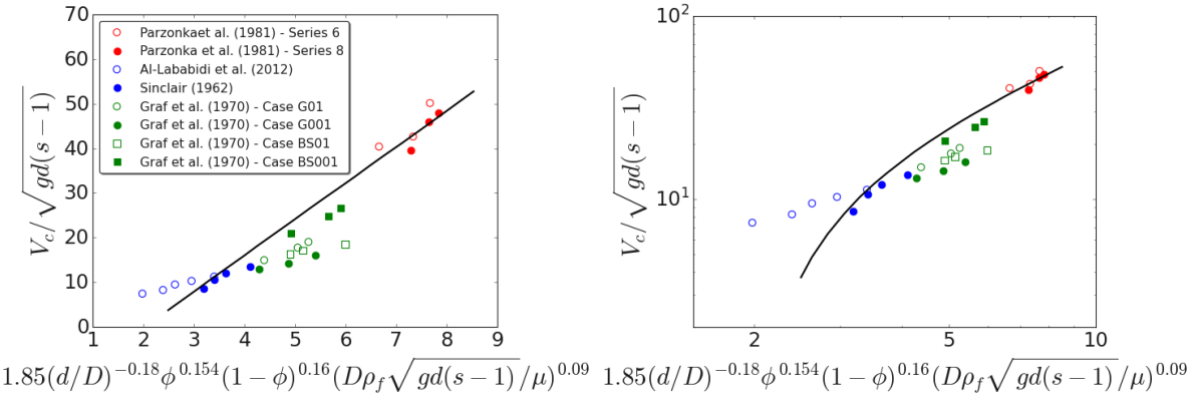

Figure 6.4: Deposition datasets collapsed using present empirical correlation, Eq. (6.11).

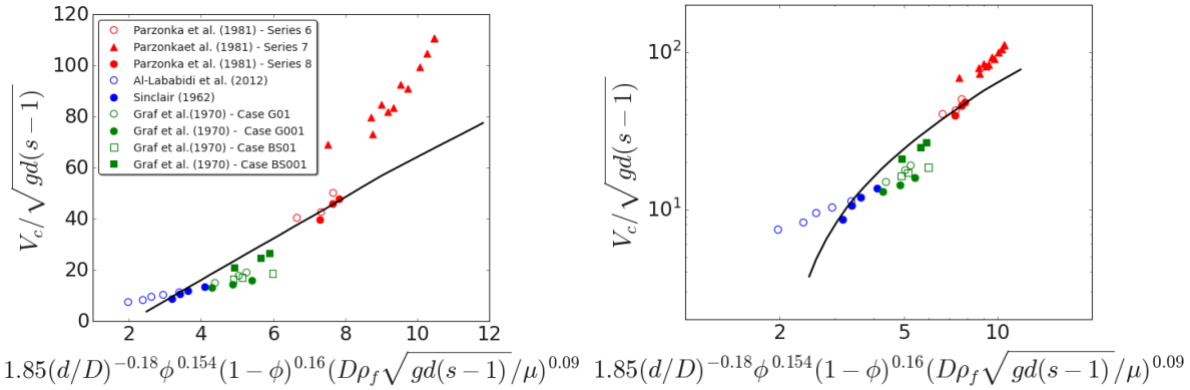

Figure 6.5: Deposition datasets (including series 7 of Pakzonka et al. (1981)) collapsed using present empirical correlation, Eq. (6.11).

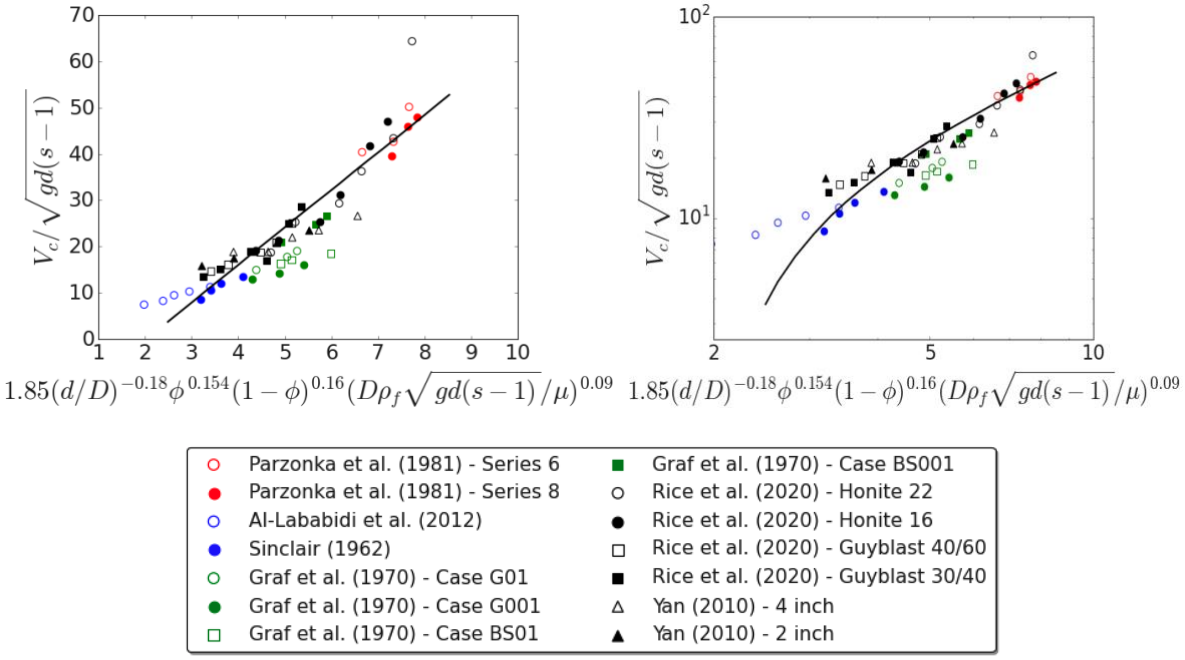

Figure 6.6: Critical deposition velocity predictions using both deposition and resuspension experimental datasets collapsed using present empirical correlation, Eq. (6.11).

6.4.2 LPT simulations for prediction of the critical deposition velocity

To generate simulation predictions, and to test the improved correlation against computational findings, depositing pipe flows are simulated with the DNS-LPT and LES-LPT approaches. Here we aim to assess whether the overall model will predict in line with the present developed correlation. In this study we consider a larger range of particle Stokes numbers and higher values corresponding to X (the RHS of Eq. (6.11)) to evaluate the applicability range of the method of predicting the critical particle deposition velocity.

At moderate to high Stokes numbers, such as those considered here, particle-turbulence interaction plays an important role in particle migration, with phenomena such as preferential concentration and turbophoresis dominating particle motion towards and away from the pipe wall. The dependence of deposition velocity on Stokes number is therefore non-trivial, though it is expected that both turbophoresis and increased gravitational forces would cause larger Stokes numbers to deposit earlier than lower ones. Previous experimental and computational studies indicate that the critical deposition velocity is a function of many parameters, though we have chosen to focus on Stokes number for this study to identify the effects of interaction with the turbulence. For the $St^+ = 1.2$, 5.5, 7.2, 11.11 and 16.78 simulations, all the parameters listed in Table 6.1 were maintained constant except the Stokes number (obtained by modifying

the density-ratio). Later, these Stokes numbers are subsequently utilised to compute an average volume coverage in the lower region of the pipe and to predict the critical deposition velocity based on the particle volume fraction in that region. They are additionally used to assess other means of obtaining the critical deposition velocity from the simulations.

Fully developed particle-laden turbulent pipe flows with Reynolds numbers ranging from $Re_\tau = 720$ to 21,600 were performed, with the conveying flow rate decreased regularly until particle deposition occurred. As previously stated, the particles were injected throughout the computational domain at initially random positions and assigned the surrounding interpolated fluid velocity at the beginning of the simulation. In the simulations, 105,000 to 2 million particles with spherical diameter $d_P = 50$ μm to 370 μm and volume fraction of $\phi_p = 7{\times}10^{-4}$ to 0.025 were considered. In all cases, it should be emphasised that all the forces, including lift, drag, gravity, pressure gradient and virtual mass, were taken into consideration and the gravitational force was applied in the vertical direction for the horizontal pipe flow. The dispersion function and mean displacement of the particles were also monitored to determine the extent of particle vertical migration, with the dispersion function (Fairweather and Yao, 2009), $D^*_{y(t)}$, defined as:

$$D^*_{y(t)} = \left(\sum_{i=1}^{N_p} \frac{(y^*_{i(t)} - y^*_{m(t)})^2}{N_p} \right)^{1/2} \tag{6.12}$$

with $y^*_{i(t)}$ the particle displacement in the vertical direction, $y^*_{m(t)}$ the mean vertical particle position, sampled across the entire domain, and N_p the total number of particles. Table 6.1 presents the simulation parameters implemented in the present study.

The first five four-way coupled flows were simulated using the fully developed $Re_\tau = 720$ flow whilst varying the Stokes number, and the flow rate was then steadily reduced until particle deposition took place. To achieve this, the pressure gradient along the pipe was lowered over time by 2% every 2000 time-steps ($t^* = 2$). To initialise the simulations, 105k particles were distributed randomly throughout the pipe domain and the same timestep of $\Delta t^* = 0.001$ was used in all these simulations. In all five cases, the same particle volume fraction was used, $\phi_p = 7 \times 10^{-4}$. The particle parameters were a diameter of 50 μm with a density ratio ranging from 1.7 to 23.3 chosen to obtain the Stokes numbers, $St^+ = 1.2$, 5.55, 7.2, 11.11 and 16.78.

Their bulk Stokes response times were 0.028, 0.125, 0.163, 0.251 and 0.379, respectively. The time interval between pressure drops is therefore significantly greater than the response bulk Stokes number to ensure the particles have enough time to suitably adjust to the modified flow.

We were able to compute particles up to 2 million with a volume fraction of 2.5% using the current University of Leeds Advanced Research Computer (ARC) or high-performance computing (HPC) on 32 standard cores. Although the ARC is capable of processing tens of millions of particles, beyond 2 million particles a larger memory request is required to facilitate the need of storing GBs of particle data. The waiting time for high memory in the ARC is then much longer. For this reason, we have restricted the number of particles to less than 2 million. LES-LPT simulations were then performed to cover higher values corresponding to the RHS of Eq. (6.11). An overlapping DNS-LPT and LES-LPT case was performed for a shear Reynolds number of 720 at around 4.2 of the RHS of Eq. (6.11), which is highlighted in light grey in Table 6.1. The same volume fraction, density ratio, number of particles, and particle diameter configuration were utilised in these concurrent simulations. A relatively large bulk Reynolds number (100k to 600k) was employed to attain values over 5 corresponding to the RHS of Eq. (6.11). These were performed using LES in order to reduce compute times given the limitations of increased grid density in DNS.

Table 6.2: Particle phase parameters for DNS/LES-LPT simulations for prediction of critical deposition velocity. Light-grey indicates the overlapping DNS/LES simulation, performed to ensure agreement between DNS and LES predictions.

Parameter	**Value**								
Shear Stokes number, St^+	1.7	5.5	7.2	11.1	16.78	17.63	2656	3187	5684
Particle diameter, d_p	50 µm	50 µm	50 µm	50 µm	50 µm	50 µm	200 µm	370 µm	300 µm
Particle diameter, d_p^*	0.005	0.005	0.005	0.005	0.005	0.0063	0.0062	0.0105	0.0061
Axial length	12.5D	12.5D	12.5D	12.5D	12.5D	12.5D	12.5D	12.5D	12.5D
Number of particles, N_p	105000	105000	105000	105000	105000	84480 0	1998894	385819	1936905
Bulk stokes number, St_B	0.028	0.125	0.163	0.251	0.379	0.392	4.887	14.343	29.35
Bulk Reynolds number, Re_B	11700	11700	11700	11700	11700	11700	300000	100000	600000
Shear Reynolds number, Re_τ	720	720	720	720	720	720	12700	4714	21600
Density ratio, ρ_p^*	1.71	7.71	10	15.42	23.3	15.42	7.71	23.3	23.3
Volume fraction, ϕ_p	0.0007	0.0007	0.0007	0.0007	0.0007	0.011	0.025	0.024	0.024
Simulation timestep, Δt^*	0.001	0.001	0.001	0.001	0.001	0.001	0.001	0.001	0.001

6.4.3 Effects of Stokes number on particle deposition dynamics – DNS

Figure 6.7 shows the mean streamwise velocity profile and the effects of the non-dimensionalised pressure gradient reduction with time, with the latter used to drive the reduction in mass flow through the pipe in order to reduce the effects of flow velocity and turbulence on suspending the particles and to encourage particle deposition. As expected, the streamwise mean velocity component decreased with time since the flow rate reduced gradually as the pressure gradient was reduced.

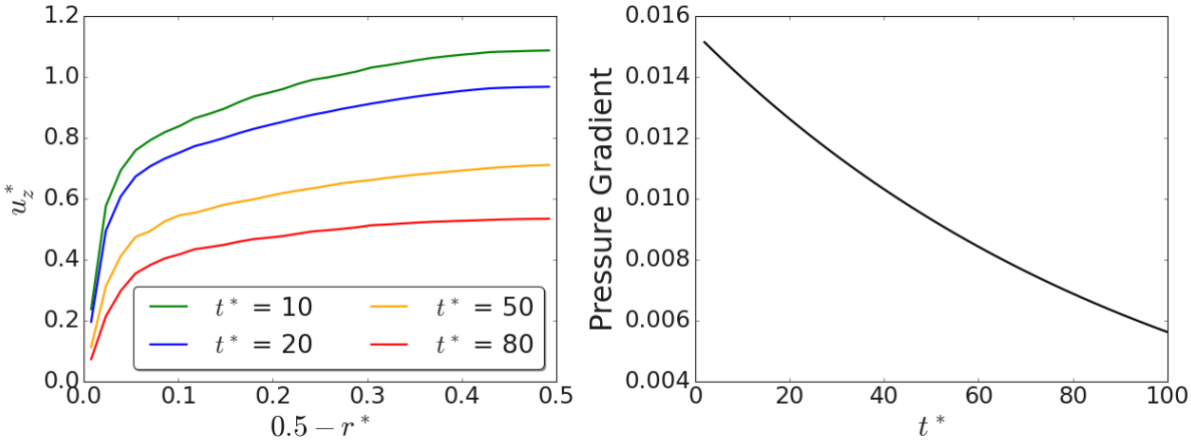

Figure 6.7: (a) Mean axial velocity at different t* and (b) prescribed non-dimensional pressure gradient.

Figure 6.8 depicts the particle dispersion function, $D^*_{y(t)}$, and the mean displacement of the particle position, $y^*_{m(t)}$, over time for four Stokes number particles. Due to the particle's inertia being less relevant than the viscous forces, the lowest Stokes number, $St^+ = 1.2$, examined did not deposit even after $t^* = 100$. These particles continue to be evenly dispersed in the flow for an extended period of time without depositing, with the deposition timescales much larger than those relevant in industrial flows. For the second lowest Stokes number considered, there is an initial increase in the dispersion function, likely due to an initial transient process where turbophoresis and wall-migration is dominant, and before gravitational acceleration can take hold. This is less apparent for the increased Stokes numbers but there is still evidence of this process. Eventually, both the particle dispersion and mean vertical position drop significantly faster with time for the higher Stokes number particles. This is due to the higher gravitational forces attributed to the increased density-ratio which cause the particles to accelerate faster in the negative vertical direction.

As the simulation evolves, and particles begin to reach the bottom of the pipe, and the gradient in the mean vertical position decreases towards zero, since accumulation in the lower region prohibits further reduction in this quantity. For the second lowest Stokes number particles, $St^+ = 5.55$, the dispersion still remains high, indicating that though they have deposited slightly, on average they are still well dispersed throughout the pipe domain. At the highest Stokes number, $St^+ = 16.78$, the particle dispersion and their mean vertical position decrease considerably faster with time than for the second lower Stokes number case. This is due to the increased gravitational force causing the particles to accelerate in the negative vertical direction at an increased rate. For the particles of $St^+ = 5.55$, the rate of migration towards the lower

half of the pipe is much slower when compared to the $St^+ = 16.78$ case. In all circumstances, by time $t^* = 40$, the mean vertical velocity averages out to zero. In general, for large Stokes numbers, the mean vertical position and particle dispersion drop more quickly over time.

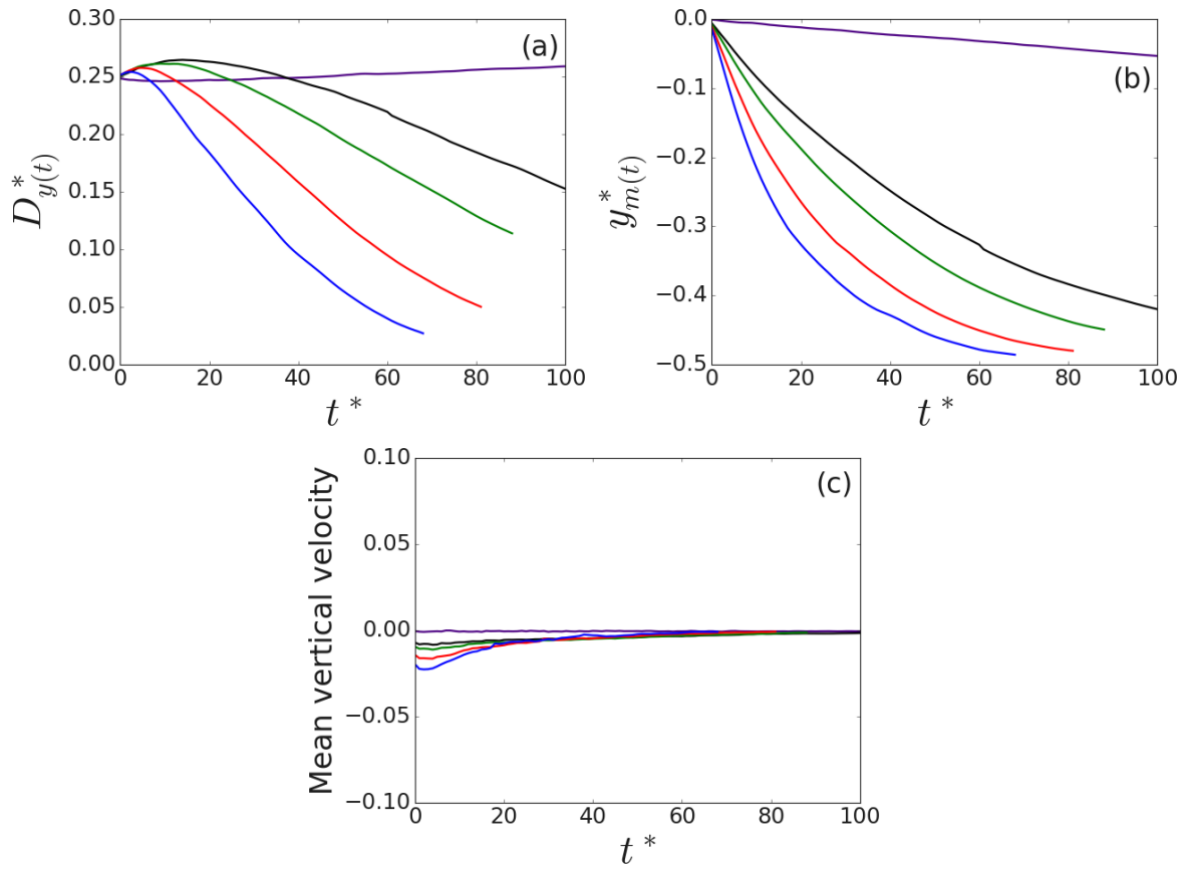

Figure 6.8: (a) Dispersion function in vertical direction, (b) mean vertical position of particles and (c) mean vertical velocity. Indigo: $St^+ = 1.22$, black: $St^+ = 5.5$; green: $St^+ = 7.2$; red: $St^+ = 11.11$; blue: $St^+ = 16.78$.

Probability density functions (PDFs) of particle dynamic properties for each Stokes number were also analysed to further understand the local dispersive and wall-interaction behaviour of the particles. Figure 6.9 illustrates the PDFs for each Stokes number considered. The top left plot (a) is for the particle velocity in the streamwise direction, the top right plot (b) considers the vertical velocity of the particles, the lower left plot (c) is the particle-fluid slip velocity, and the lower right plot (d) is the vertical position of the particles.

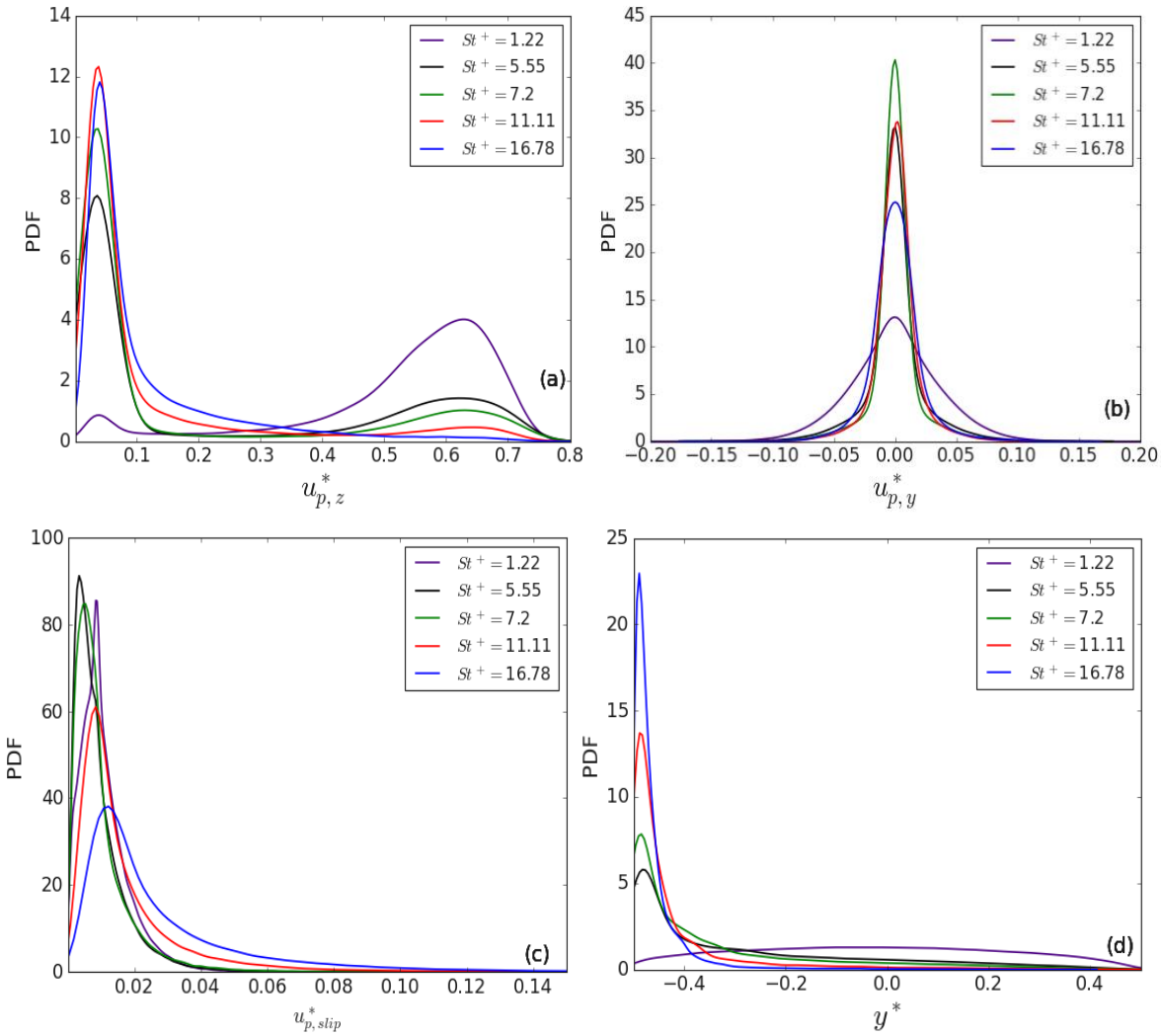

Figure 6.9: Probability density functions of particle dynamic properties: (a) streamwise velocity, (b) vertical velocity, (c) slip velocity, and (d) vertical position. Indigo: $St^+ = 1.22$, black: $St^+ = 5.5$; green: $St^+ = 7.2$; red: $St^+ = 11.11$; blue $St^+ = 16.78$ at t*=50.

Considering the streamwise velocity, for low Stokes number particles, there are two regimes observed: particles confined along the wall which reside in low-speed streaks (or have formed beds), or higher speeds in the bulk region of the flow, as demonstrated by the PDFs. For very low Stokes number particles, $St^+ = 1.2$, this separation is most evident, as there are still many particles within the bulk of the flow. The streamwise velocity of these particles is therefore split tin two regimes, where particles possessing low speeds (those trapped in the wall region) are low in number whilst at higher speeds (those in the bulk of the flow) their number is larger than the other Stokes number cases considered. The high Stokes number particles do not exhibit this behaviour, with the majority of particles existing at low velocities due to their proximity to the lower wall of the pipe, underlining the importance of flow and particle interactions within the wall-region such as particle preferential concentration in low speed streaks (as seen later in

Figs. 6.12 to 6.17), and particle interaction with near-wall turbulence structures which, through sweep and ejection events, modulate the particle flux towards the wall.

PDFs of the particles' vertical velocity are also presented, demonstrating that the low Stokes number particles exhibit a wide range of such velocities across the pipe, although centred on zero, whilst the high Stokes number particles tend to possess a more limited velocity range. There is, however, a slight skew towards positive values for all the high Stokes number velocity PDFs due to the influence of gravity. PDFs of the slip velocity are shown in Fig. 6.9(c) which tend to increase as the Stokes number increases, as would be expected for these more inertial particles. The low Stokes number particles possess the smallest and lowest range of slip velocities, with particles tending to more easily follow the flow streamlines. That said, the distribution is still wide, since gravitational effects tend to decouple the particle velocities from the local flow velocities. As the Stokes number is increased, the distribution widens further, with particles further decoupling from the flow and sampling velocities different to their surrounding local fluid as gravity accelerates them through the different wall-normal regions of the pipe flow. Finally, PDFs of the vertical position of the particles is also considered, with the high Stokes particles occupying much greater negative positions, in line with previous observations. The vertical position shows a much reduced spread in locations for increasing Stokes number demonstrating increasing particle concentrations close to the wall, whilst the lowest Stoks number particles are seen to be evenly distributed across the pipe.

Mean particle concentration profiles are illustrated in Fig. 6.10 for all four Stokes numbers across the pipe at various times. The concentrations were normalised by the initially injected concentration, C_0, and total volume, with the initial concentration profile a straight line at $C/C_0 = 1$ due to random initial injection. Even by $t^* = 10$, wall-accumulation has begun to take places for all Stokes numbers considered with the exception of the $St^+ = 1.22$ particles. Examining the two extreme Stokes number cases, particles are seen to migrate towards the lower wall region and to ultimately deposit on the lower wall of the pipe, with the near-wall concentration of the $St^+ = 16.78$ particles higher than those predicted for the lower Stokes number case, St^+ =5.5.

Interestingly, particles in the bulk of the pipe flow are relatively homogeneously distributed, likely since particles which occupy the bulk flow region tend to remain there and when

depositing will tend to fall with similar rates. As time evolves, in all cases the particles are observed to flow towards the lower wall and eventually deposit in the near-wall region. However, it is evident that the particles are more concentrated along the wall with larger Stokes numbers.

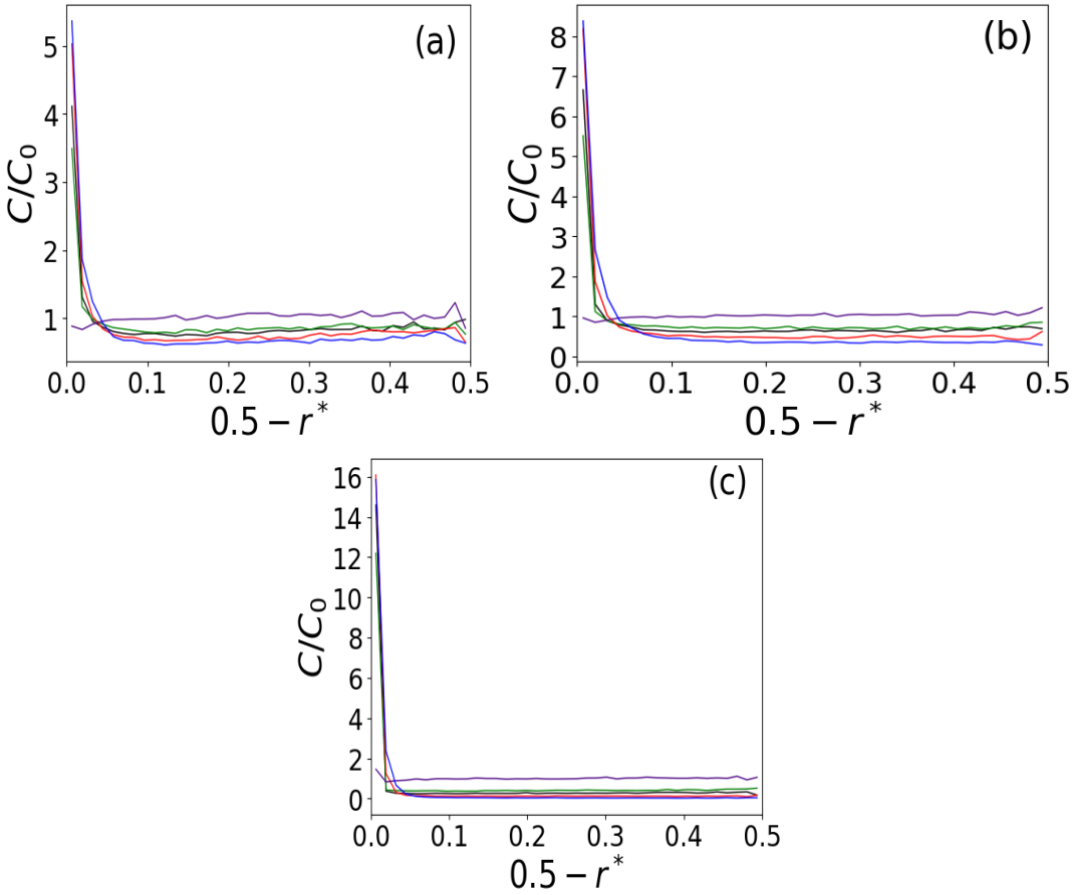

Figure 6.10: Mean particle concentration of particles normalised by initial concentration. Indigo: $St^+ = 1.22$; black: $St^+ = 5.5$; green: $St^+ = 7.2$; red: $St^+ = 11.11$; blue: $St^+ = 16.78$. (a) at t^* = 10, (b) at t^* = 20 and (c) at t^* = 50.

6.4.3.1 Deposition at $St^+ = 1.22$

To provide a more thorough perspective of the migration of particles to the near-wall region and their eventual deposition at the bottom of the pipe, the temporal evolution of instantaneous particle distributions are presented below. Figure 6.11 plots the positions of particles in the vertical direction, y^*, along the pipe, z^* (on a plane through the pipe centreline), and close to the wall ($0.49 \leq r^* \leq 0.5$), x^* variation with z^*, as well as 3D views with time for $St^+ = 1.22$. Note that the streamwise direction, z^*, against spanwise direction, x^*, plots of the instantaneous particle distributions were filtered to only include particles in the negative vertical direction, $y^* < 0$, and then close to the wall, $0.49 \leq r^* \leq 0.5$, in the lower half of the pipe. These plots show that for low Stokes numbers, the particles remained suspended, which is consistent with the findings in Figure 6.10. With increasing time, the particles remain suspended in the fluid and do not migrate to the lower portions of the pipe, even by $t^* = 110$.

The particles are relatively equally dispersed throughout the computational domain, presenting virtually little indication of their position within low-speed streaks. This shows a balance between buoyant forces acting to keep the particles suspended and gravity acting to pull the particles downward. These observations are in-line with the calculated dispersion function and mean particle position values shown in Fig. 6.8, which remain constant. It is important to highlight, however, that even for particles with the lowest Stokes numbers and the weakest interactions with the pipe wall, these will create deposited beds over longer timescales. As a result, it is possible that a waste-processing particle transport system could exhibit more such behaviour for very long pipe flows.

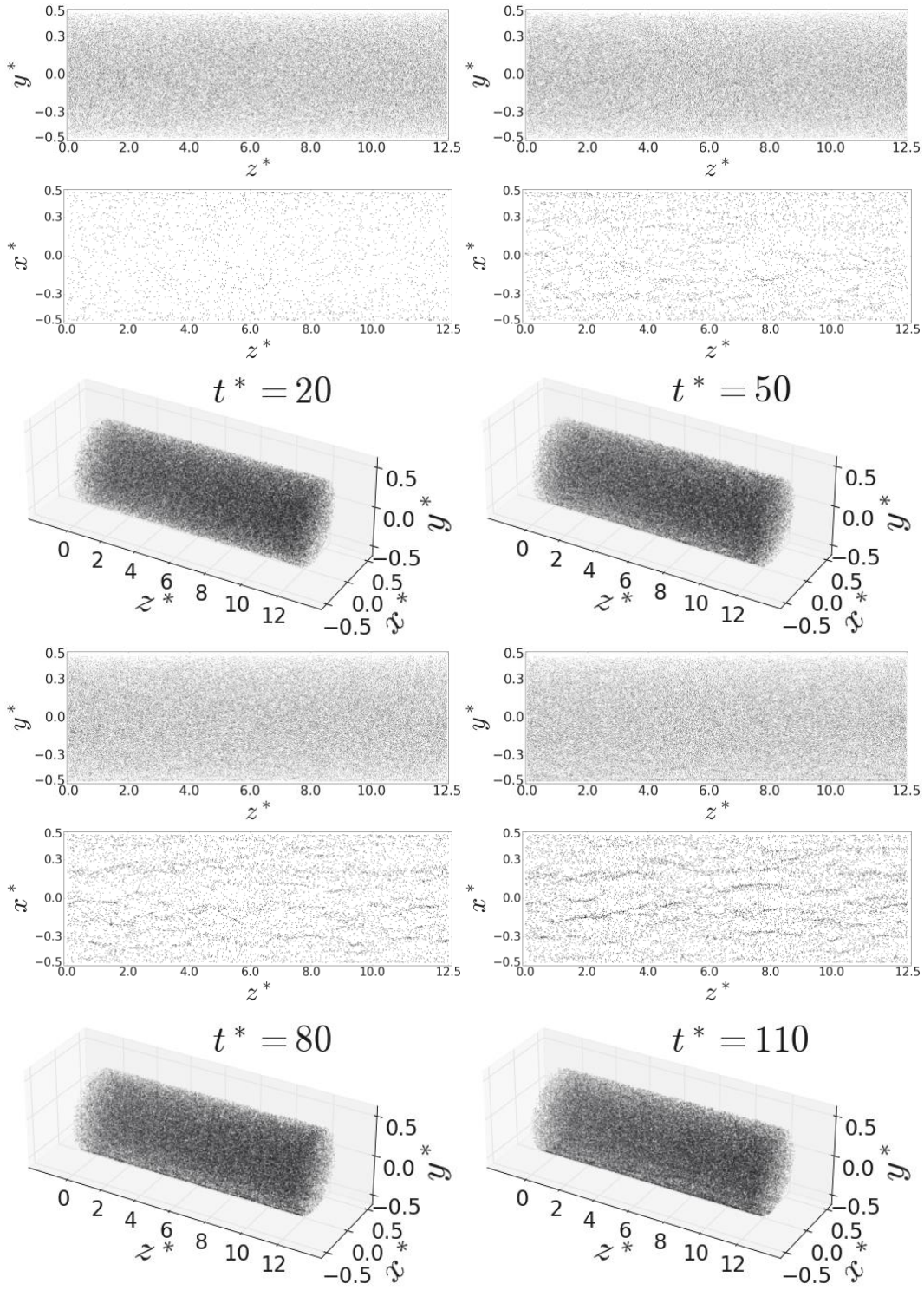

Figure 6.11: Instantaneous plots of particle positions in the vertical direction, y^* variation with z^*, and close to the wall ($0.49 \leq r^* \leq 0.5$) in the lower half of the pipe, x^* variation with z^*, with time for $St^+ = 1.2$ particles. Three-dimensional views also illustrated. Top left $t^* = 20$; top right $t^* = 50$; lower left $t^* = 80$; and lower right $t^* = 110$.

6.4.3.2 Deposition at $St^+ = 5.5$

Figure 6.12 shows the instantaneous positions of particles on a vertical plane through the pipe centre with time, and close to the wall ($0.49 \leq r^* \leq 0.5$) in the lower half of the pipe, as well as a 3D plot, for the $St^+ = 5.5$ particles. At the start of the simulation, upon injection of the particles, the particles are homogeneously dispersed throughout the computational domain. As time evolves, particle migration to the lower sections of the pipe occurs. By $t^* = 40$ the particles appear to form structures on the floor of the pipe. This is consistent with previous studies in channels and pipes where preferential concentration is observed for shear Stokes numbers between 5 and 50 (Mortimer et al., 2019).

Particles migrating to this region will interact with low-speed streaks present in the fluid, which reduces their momentum, hindering their ability to resuspend into the flow, particularly under the influence of gravity. By $t^* = 80$, more particles are present in these regions of preferential concentration, and dune-like structures begin to form further along the bottom wall of the pipe. Since four-way coupling is accounted for, particles travelling into occupied streaks may bounce off particles already present, meaning unoccupied streaks further along the pipe are more likely candidates for occupancy. It is also observed that by this time, most of the particles are present in the lower half of the pipe.

Figure 6.13 displays the positions of particles in the vertical direction, y^*, along with kernel a density estimation with marginal values at $t^* = 20$, 50 and 80 for $St^+ = 5.5$ particles. Initially, the particles are relatively evenly distributed within the computational domain, but with increasing time, migration to the lower regions of the pipe occurs. By $t^* =$50 a visible bed is not formed, although the majority of the particles have migrated towards the bottom of the pipe and formed dune-like structures, however by $t^* = 80$ a particle bed appears to have formed. This can be seen more clearly by the marginal plots and these observations are in-line with the mean particle concentration in Fig 6.10, as well as the dispersion function and mean particle position plots in Fig 6.8. In these, from approximately $t^* = 20$, the number of particles starts to deviate from the lower Stokes number case, $St^+ = 1.2$, and as time increases particle deposition proceeds at a significantly higher rate. The streamwise marginal distribution remains constant throughout the pipe and over time, as expected due to the periodic nature of the flow.

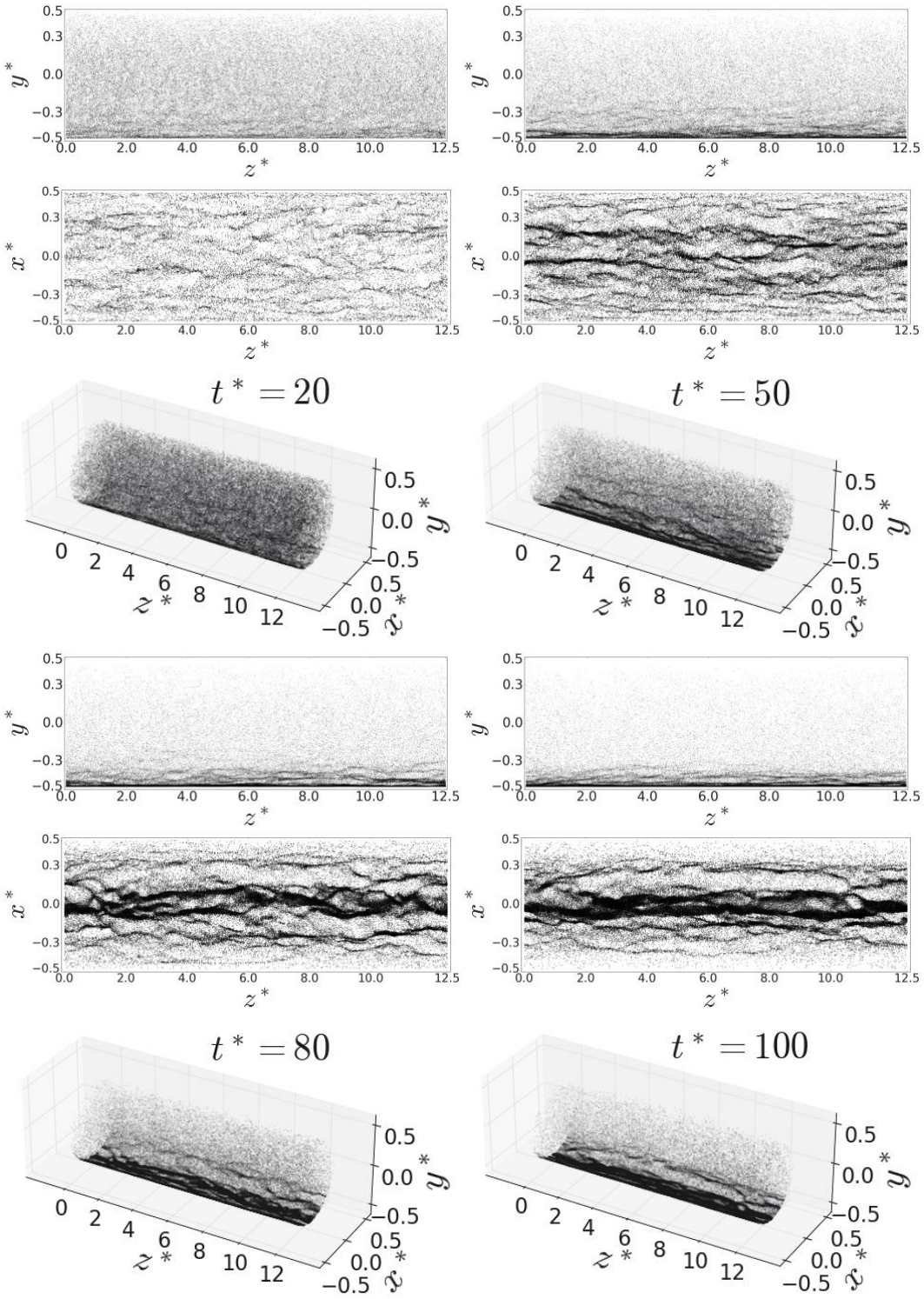

Figure 6.12: Instantaneous plots of particle positions in the vertical direction, y^* variation with z^*, and close to the wall ($0.49 \leq r^* \leq 0.5$) in the lower half of the pipe, x^* variation with z^*, with time for $St^+ = 5.5$ particles. Three-dimensional views also illustrated. Top left $t^* = 20$; top right $t^* = 50$; lower left $t^* = 80$; and lower right $t^* = 110$.

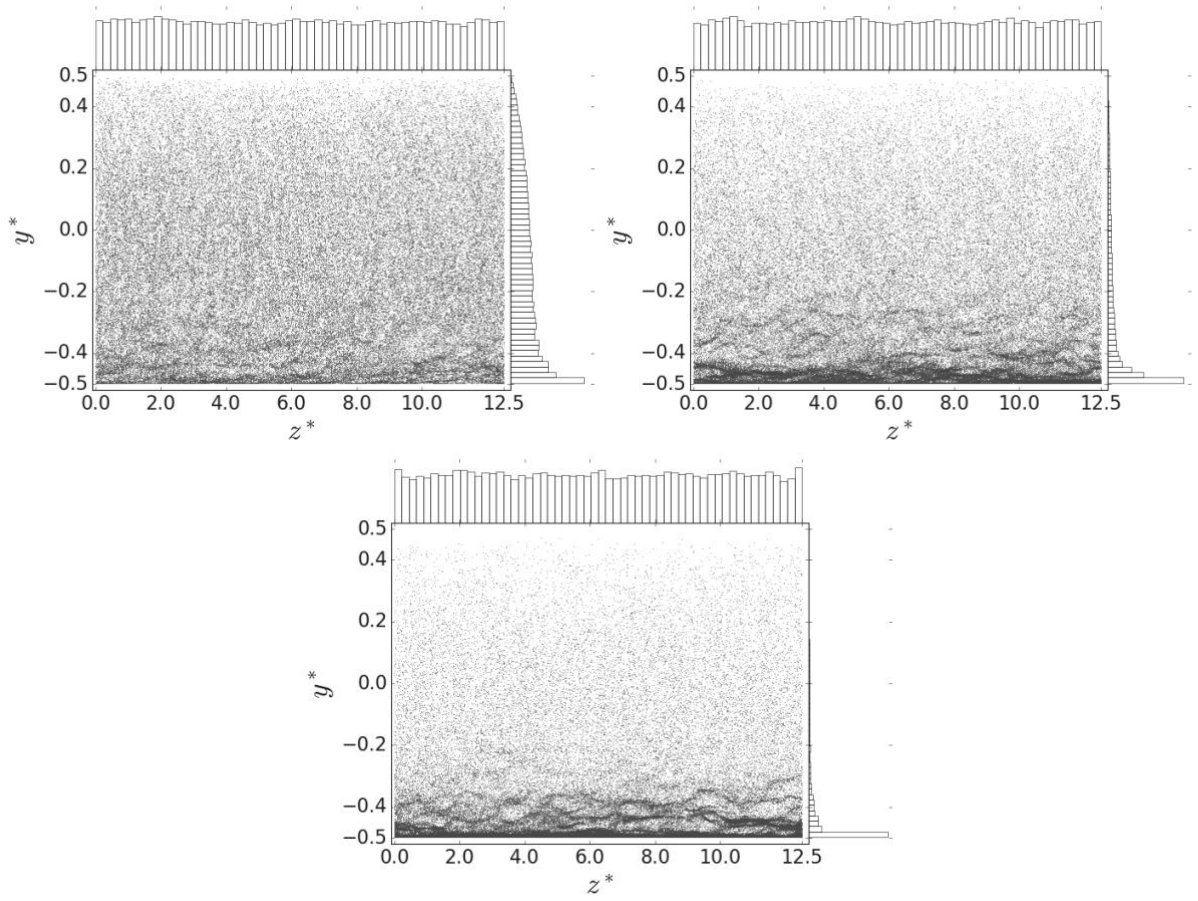

Figure 6.13: Instantaneous plots of particle vertical position with time and kernel density estimation with marginal plots for $St^+ = 5.5$. Top left: $t^* = 20$; top right: $t^* = 50$ and lower: $t^* = 80$.

6.4.3.3 Deposition at $St^+ = 7.2$ and $St^+ = 11.11$

Similarly in Figures 6.14 and 6.15 at the beginning of the simulation, the particles are spread uniformly throughout the computational domain. The near-wall concentration of the particles increases with Stokes number, and it is observed that the particles migrate towards the lower wall region before depositing at the bottom of the pipe. However, in the Stokes number, St^+=11.1 case, by $t^* = 80$ a particle bed appears to have formed. With increasing time, the majority of the particles migrate to the lower sections of the pipe in both cases. A bed, on the other hand, does not form in the Stokes number, St^+=7.2 case, despite the fact that most of the particles have moved towards the wall-region of the pipe and created dune-like formations similar to those present in the $St^+ = 5.5$ simulation at t^* = 80. For the St^+=11.1 simulation, the dispersion function starts to vary from the second- and third- lowest Stokes number cases, St^+= 5.5 and 7.2, at about t^* = 10 and the particle deposition rate rises at a noticeably faster rate as time increases.

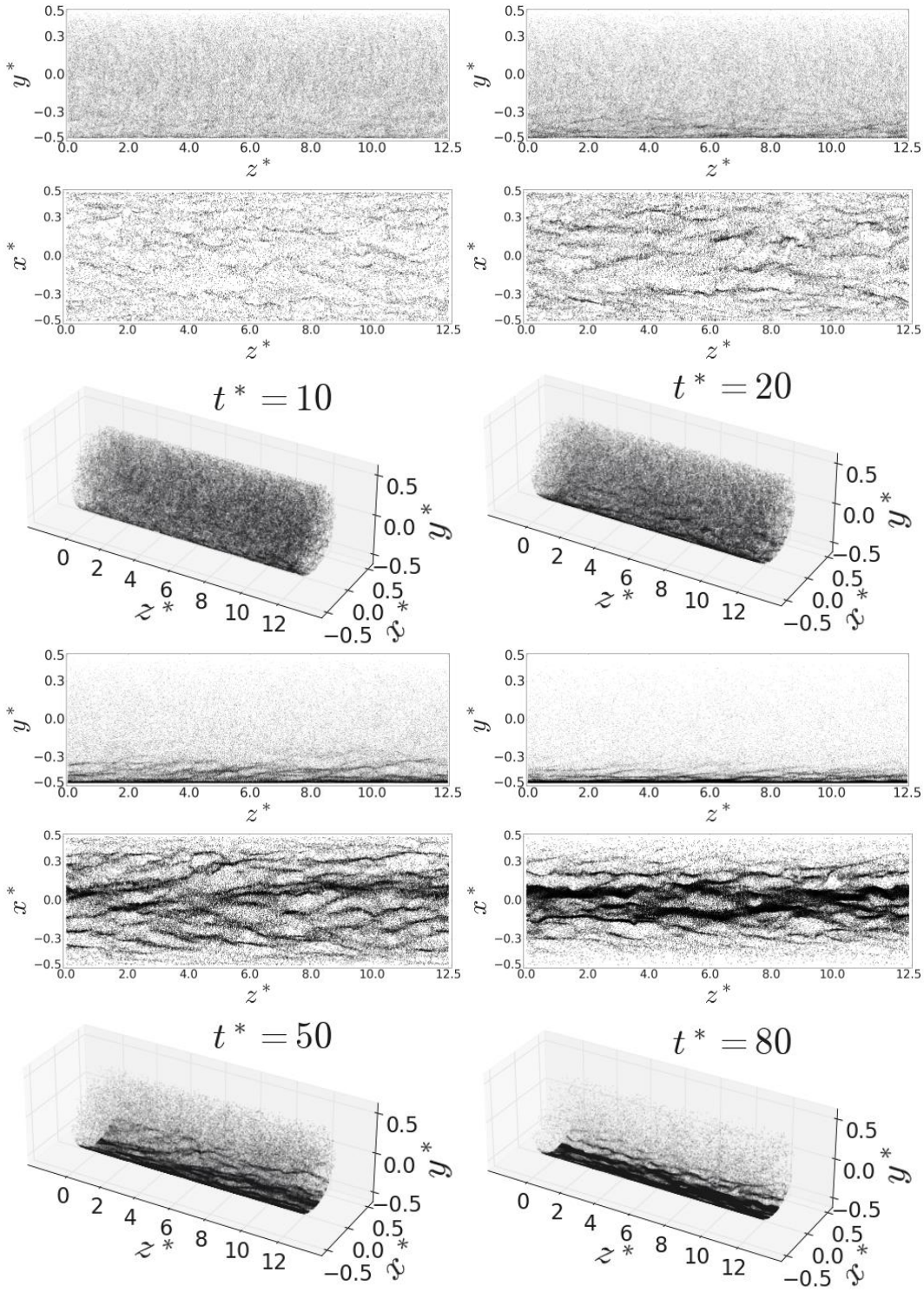

Figure 6.14: Instantaneous plots of particle positions in the vertical direction, y^* variation with z^*, and close to the wall ($0.49 \leq r^* \leq 0.5$) in the lower half of the pipe, x^* variation with z^*, with time for $St^+ = 7.2$ particles. Three-dimensional views also illustrated. Top left $t^* = 10$; top right $t^* = 20$; lower left $t^* = 50$; and lower right $t^* = 80$.

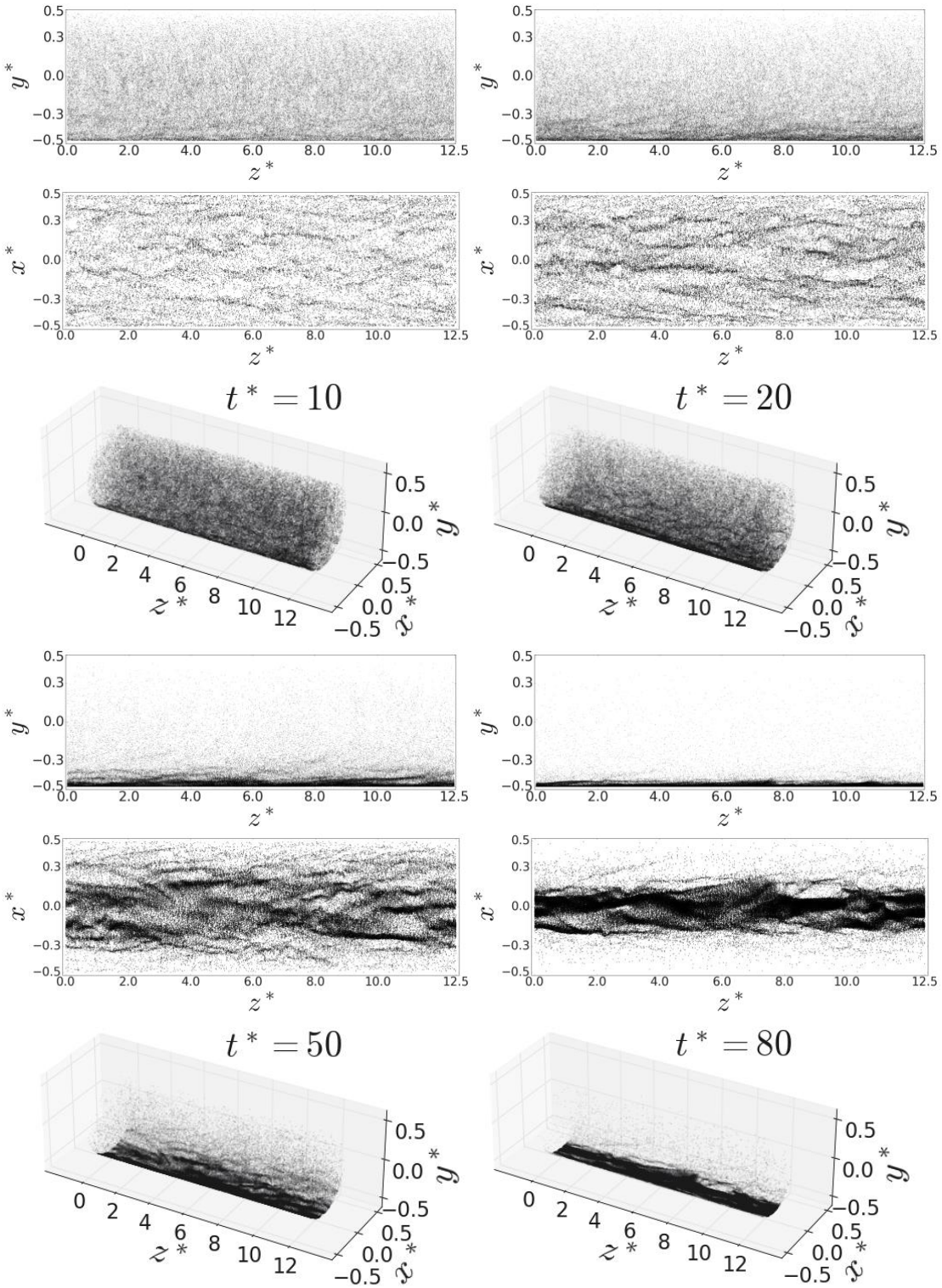

Figure 6.15: Instantaneous plots of particle positions in the vertical direction, y^* variation with z^*, and close to the wall ($0.49 \leq r^* \leq 0.5$) in the lower half of the pipe, x^* variation with z^*, with time for $St^+ = 11.11$ particles. Three-dimensional views also illustrated. Top left $t^* = 10$; top right $t^* = 20$; lower left $t^* = 50$; and lower right $t^* = 80$.

6.4.3.4 Deposition at $St^+ = 16.78$

For the highest Stokes number particles simulated initially using DNS, $St^+ = 16.78$, the effects of preferential concentration are less evident, with a more homogeneous bed forming rather than the characteristic structures resembling low-speed streaks, as observed in Fig. 6.16. This process continues up to t^* =70, by which point the upper half of the pipe is largely devoid of particles. The lack of interaction with low-speed streaks is of interest, since previous studies indicate most prominent preferential concentration taking place at Stokes numbers close to 25 (Mortimer et al., 2019). This underlines the important role gravity has to play, as the increased density ratio decouples the particles from the local flow field, allowing them to accelerate and travel through the streaks, dominant over the drag forces they would experience as they enter those regions. These findings are also consistent with the computed dispersion function and mean particle position values shown in Figure 6.8, which show that higher Stokes number particles begin to deviate from the lower Stokes number case around $t^* = 5$ and that particle deposition accelerates noticeably with time, scaling with the Stokes number. Further evidence for these observations is illustrated in Figure 6.17, which shows particle positions in the vertical direction, y^*, as well as an estimate of kernel densities of particle positions with marginal values at t^* = 20, 50, and 70. As time passes, the formation of a particle bed on the pipe close to the wall becomes increasingly noticeable; this bed formation may eventually act as a layer for further particle deposition.

Figure 6.18 illustrates the total number of particles in the vertical direction with increasing time for $St^+ \cong 5.55$ and 16.78. The smallest and largest Stokes numbers considered thus far, $St^+ \cong$ 5.55 and 16.78, were chosen for in-depth analysis considering previous resuspension experimental datasets. By t^* = 10, there is minimal variation in the symmetrical distribution of the particles between the two cases; however, by t^*= 20, deviation of behaviour is evident. A higher right-skewed (positive) distribution is observed for the higher Stokes number. This reinforces the earlier finding that particle deposition is sensitive to Stokes number, with increasing Stokes number particles depositing at higher flow velocities. By time t^*=50, the majority of the particles are present within the lower-half of the pipe, indicating particle migration towards the lower wall regions and, eventually, deposition on the pipe's lower wall. At increased Stokes numbers the particles possess lower critical deposition velocities, confirming the above findings that in general high Stokes number particles have a greater tendency to form particle beds.

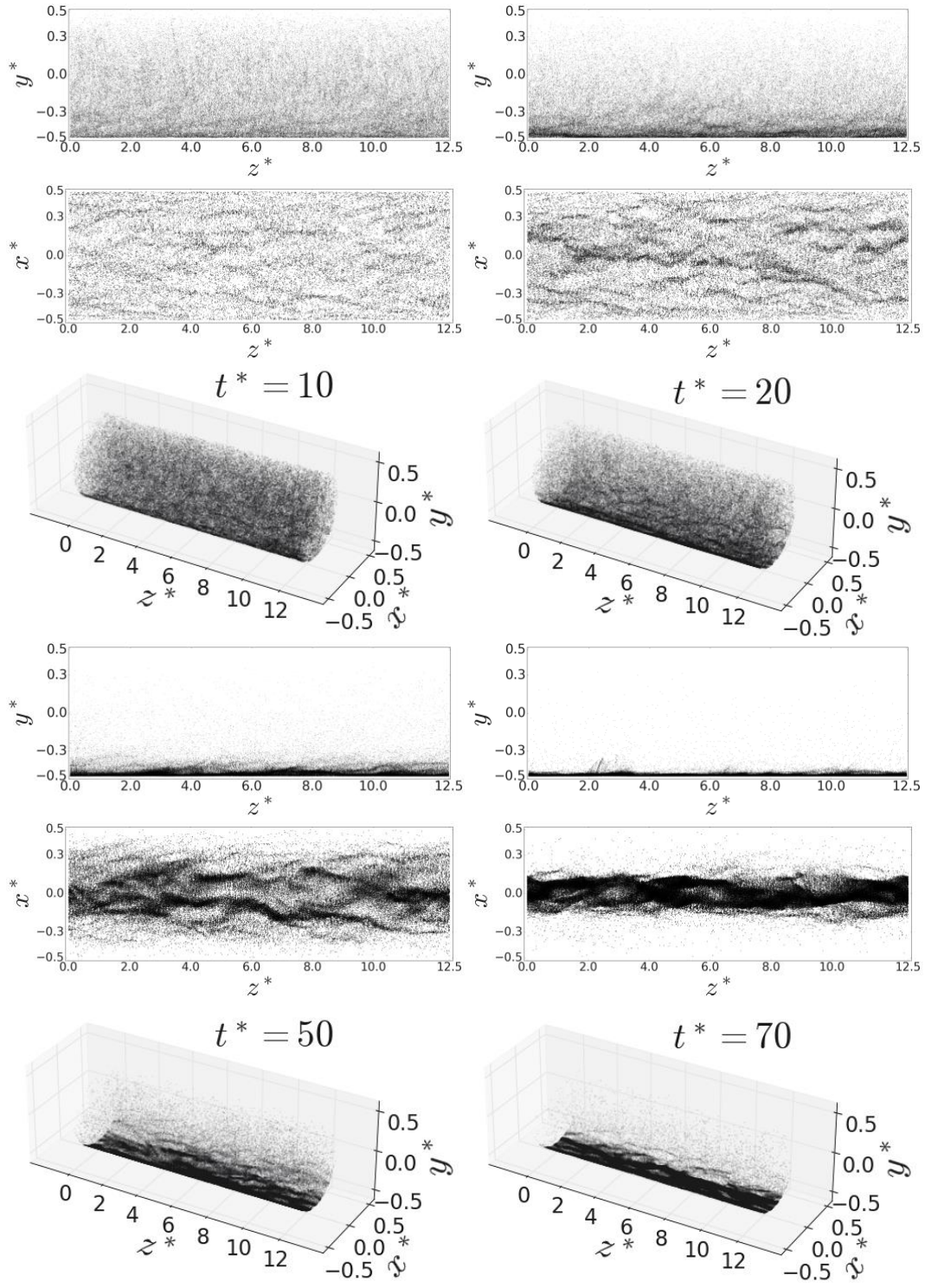

Figure 6.16: Instantaneous plots of particle positions in the vertical direction, y^* variation with z^*, and close to the wall ($0.49 \leq r^* \leq 0.5$) in the lower half of the pipe, x^* variation with z^*, with time for $St^+ = 16.78$ particles. Three-dimensional views also illustrated. Top left $t^* = 10$; top right $t^* = 20$; lower left $t^* = 50$; and lower right $t^* = 70$.

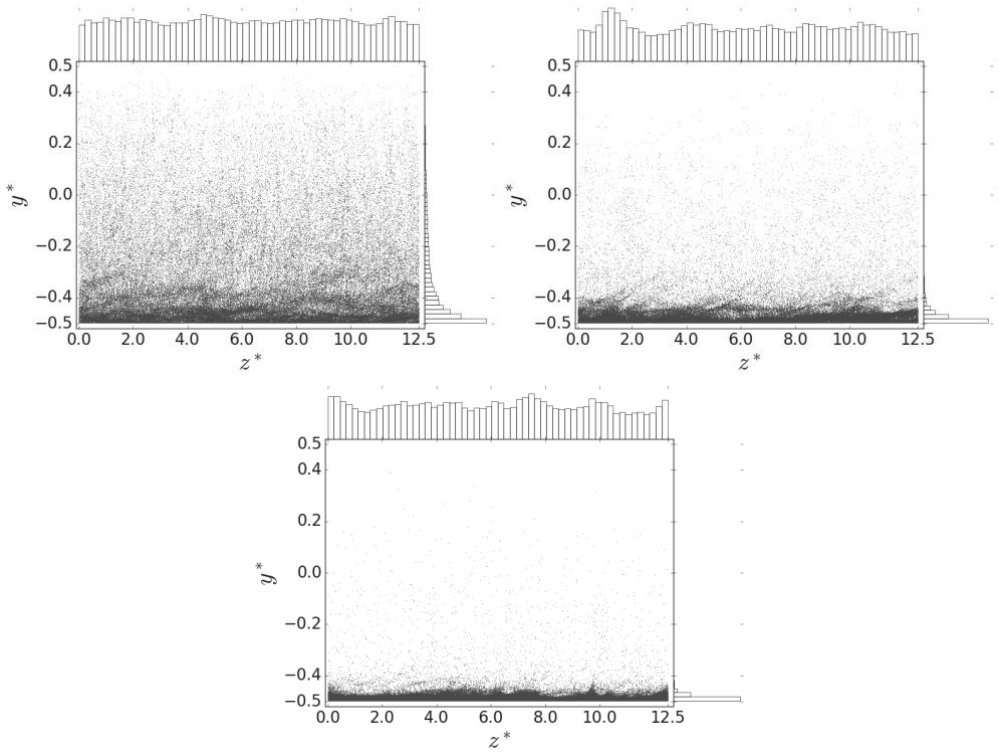

Figure 6.17: Instantaneous plots of particle vertical position with time and kernel density estimation with marginal plots for $St^+ = 16.78$. Top left: $t^* = 20$; top right: $t^* = 50$ and lower: $t^* = 70$.

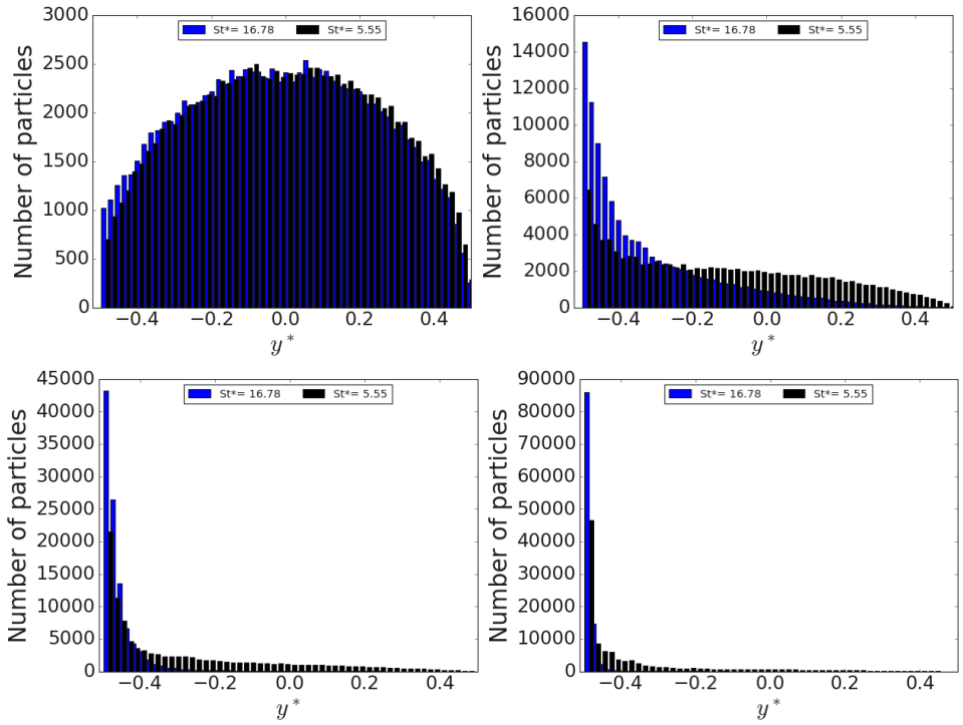

Figure 6.18: Total number of particles in a vertical direction with time, Top left $t^* = 10$; top right $t^* = 20$; lower left $t^* = 50$; and lower right $t^* = 70$ for $St^+ = 16.78$ and $t^* = 80$ for $St^+ = 5.5$.

6.4.3.5 Deposition (DNS) at $St^+ = 17.63$

Results for this Stokes number were derived using DNS in order to allow an evaluation of the accuracy of LES-based predictions. These results are considered further in the following section.

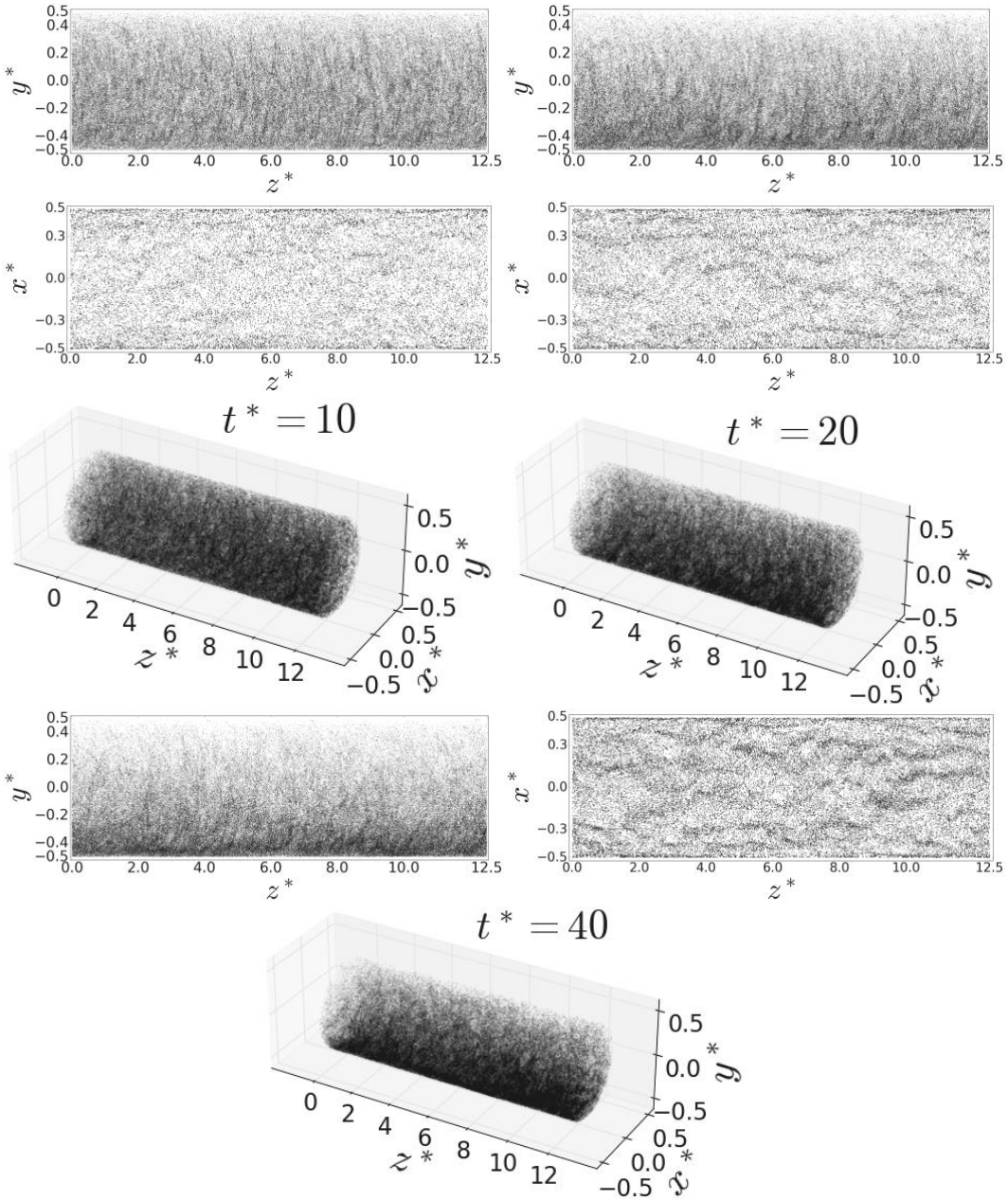

Figure 6.19: Instantaneous plots of particle positions in the vertical direction, y^* variation with z^*, and close to the wall ($0.49 \leq r^* \leq 0.5$) in the lower half of the pipe, x^* variation with z^*, with time for $St^+ = 17.63$ particles. Three-dimensional views also illustrated. Top left $t^* = 10$; top right $t^* = 20$; lower $t^* = 40$.

6.4.4 Effects of Stokes number on particle deposition dynamics – LES

In order to test whether the overall model will accurately predict the onset of deposition in accordance with the aforementioned correlation at increased Reynolds numbers and bulk flow rates, four additional depositing pipe flows were simulated using the LES-LPT code over a range of X values (4.2, 5, 6 and 6.5) spanning the Stokes number range, St^+ = 17.63, 3187, 2656, and 5684. As before, the flow velocity was gradually reduced until particle deposition took place in fully developed particle-laden turbulent pipe flows at shear Reynolds numbers of Re_τ = 720, 4,714, 12,700, and 21,600. The flows were once again driven by a slowly reducing pressure gradient in the streamwise direction, as outlined in the methodology section. As noted above, an overlapping DNS simulation was also performed for the Re_τ = 720, St^+ = 17.63 case.

Due to the high concentration and large number of particles utilised in the LES-LPT turbulent pipe flow simulations, it is difficult to observe the behaviour of the instantaneous particle distributions. As a result, every eighth particle position for the X = 4.2 case, third particle for X = 5, and nineteenth particle for X = 6 and 6.5 are plotted to approximately match with the concentrations of the original DNS-based simulations described in Section 6.4.3 where the total number of particles was 105k. A similar analysis was conducted, and the particle instantaneous positions for each simulation are presented in Figure 6.19 (DNS), and Figures 6.20 through Figure 6.23 (LES). The latter figures demonstrate that particles with much larger Stokes numbers have trajectories that diverge from the fluid flow because their inertia increases their probability of deposition and collision with the pipe wall. Although difficult to see in the results of Figures 6.20 to 6.23, because of the reduced number of particles plotted, deposited beds similar to those observed in the DNS-based simulations, e.g. Figure 6.16, were observed. This is also confirmed by the analysis given in the following section. Additionally, the overlapping DNS-LES cases, Figures. 6.19 and 6.20, are found to be qualitatively similar. A more quantitative comparison is also included in the following section.

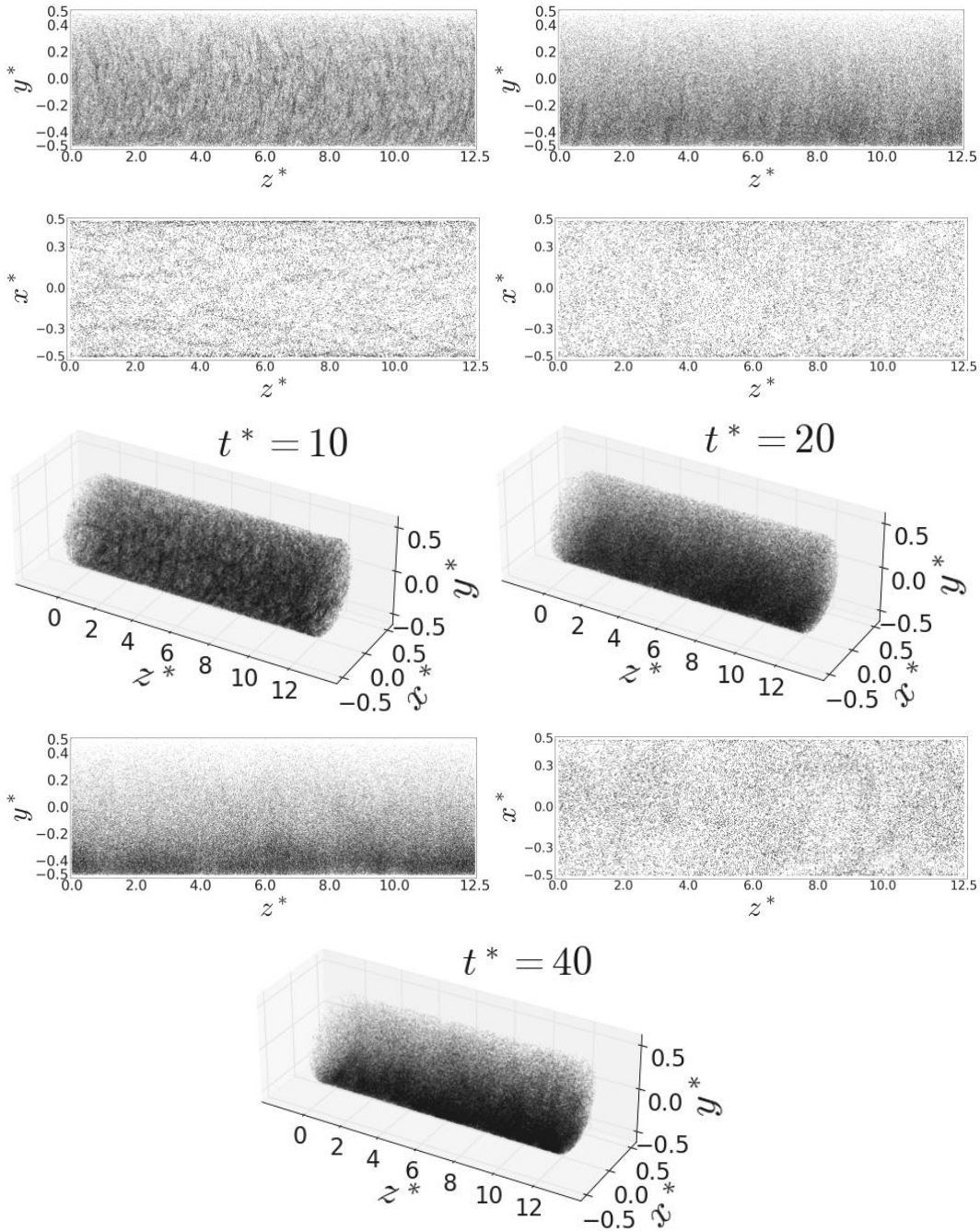

Figure 6.20: Instantaneous plots of particle positions in the vertical direction, y^* variation with z^*, and close to the wall ($0.49 \leq r^* \leq 0.5$) in the lower half of the pipe, x^* variation with z^*, with time for $St^+ = 17.63$ particles. Three-dimensional views also illustrated. Top left $t^* = 10$; top right $t^* = 20$; lower $t^* = 40$.

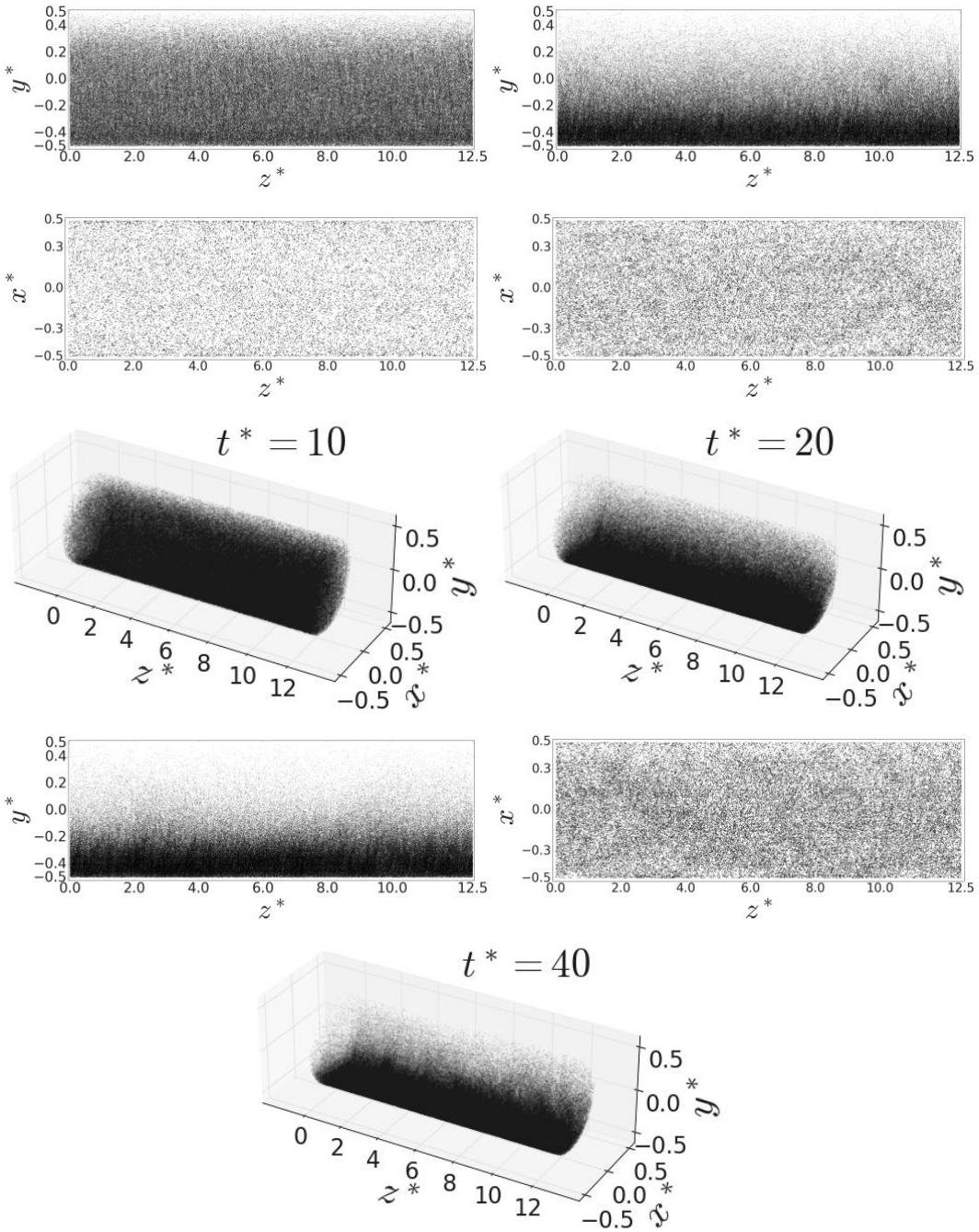

Figure 6.21: Instantaneous plots of particle positions in the vertical direction, y^* variation with z^*, and close to the wall ($0.49 \leq r^* \leq 0.5$) in the lower half of the pipe, x^* variation with z^*, with time for $St^+ = 2656$ particles. Three-dimensional views also illustrated. Top left $t^* = 10$; top right $t^* = 20$; lower $t^* = 40$.

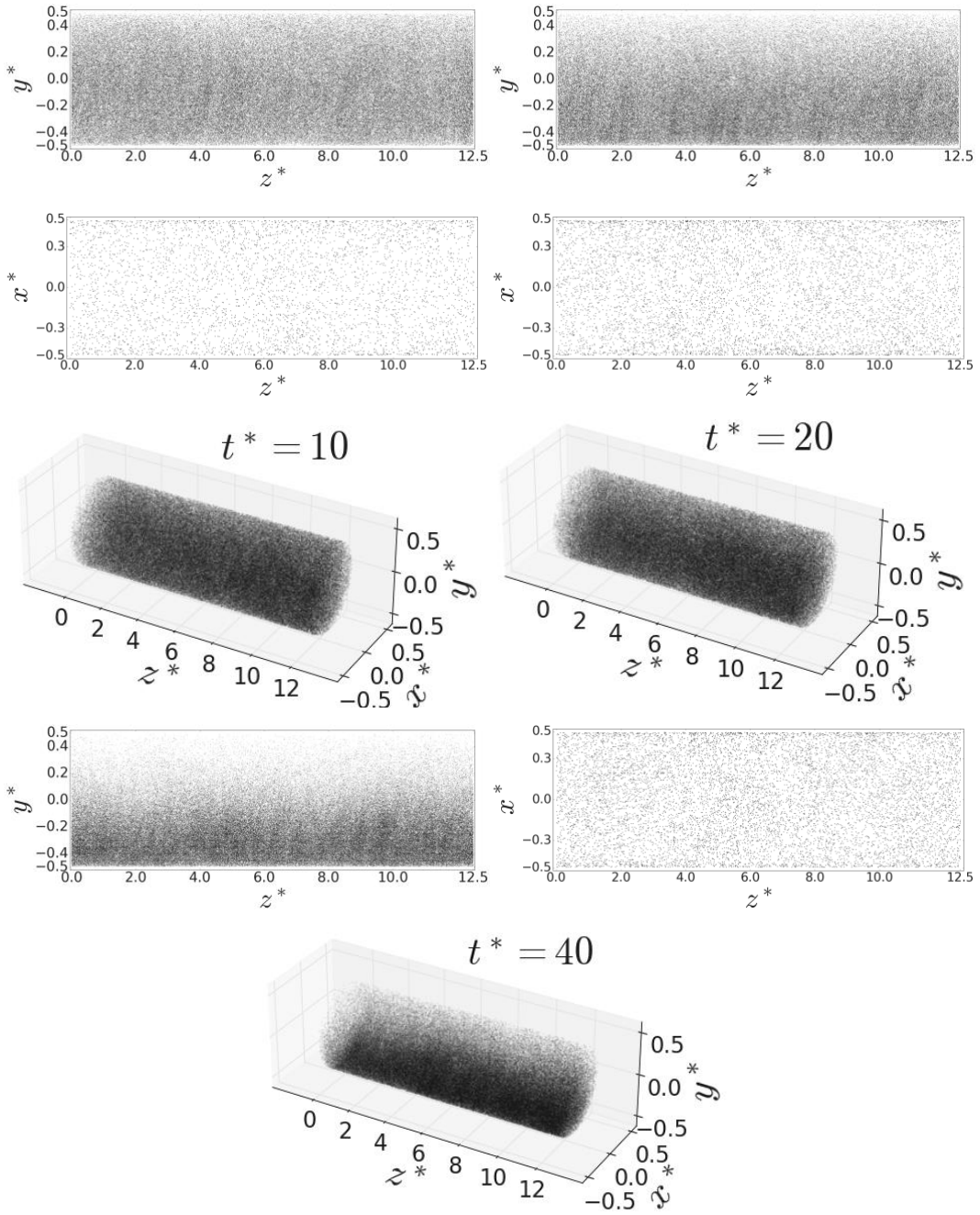

Figure 6.22: Instantaneous plots of particle positions in the vertical direction, y^* variation with z^*, and close to the wall ($0.49 \leq r^* \leq 0.5$) in the lower half of the pipe, x^* variation with z^*, with time for $St^+ = 3187$ particles. Three-dimensional views also illustrated. Top left $t^* = 10$; top right $t^* = 20$; lower $t^* = 40$.

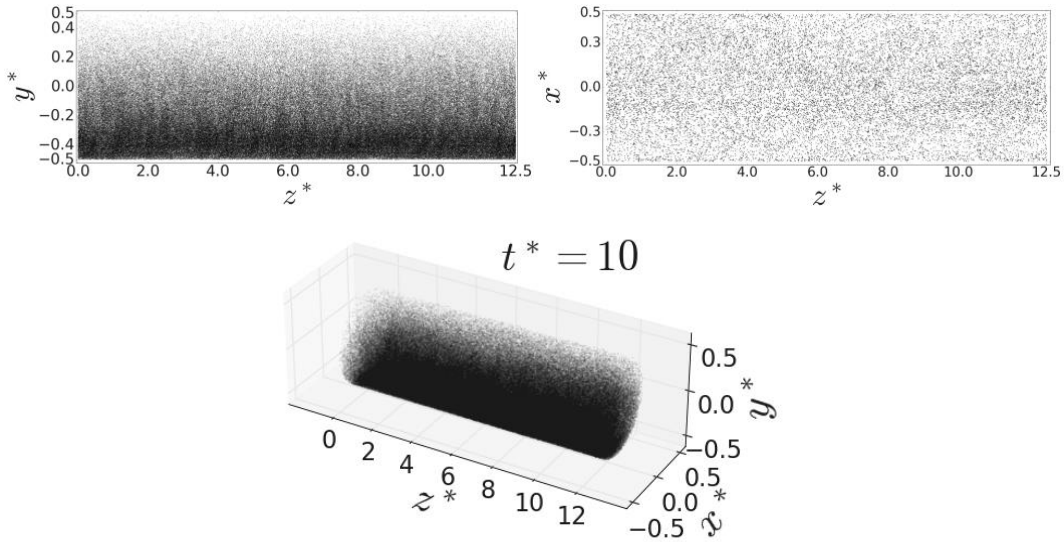

Figure 6.23: Instantaneous plots of particle positions in the vertical direction, y^* variation with z^*, and close to the wall ($0.49 \leq r^* \leq 0.5$) in the lower half of the pipe, x^* variation with z^*, with time for $St^+ = 5684$ particles. Three-dimensional views also illustrated. $t^* = 10$.

6.4.5 Critical deposition velocity predictions

The physical space inhabited by a group of individual particles, or the volume occupied by those particles, can be estimated using:

$$V_p = N_p \frac{4}{3}\pi {r_p}^3 \tag{6.13}$$

Here, V_p is the volume occupied by the particles, N_p is the number of particles and r_p is the radius of the particles.

The volume of the near-wall region used below to identify a deposited bed is defined as follows:

$$V_R = \frac{1}{2}\theta\left(r^2 - (\mathrm{r} - 2d_p^*)^2\right)L \tag{6.14}$$

where r is the radius of the pipe (0.50), L is the length of the pipe, d_p^* is the particle diameter, and θ in the plane of the pipe cross-section defines the segment of the pipe chosen for analysis. The value of θ used for the analysis using $-0.5 \leq x^* \leq 0.5$ was π and for $-0.2 \leq x^* \leq 0.2$ it was 2.3. Results derived for $-0.5 \leq x^* \leq 0.5$ therefore correspond to a segment of pipe

equal to its lower half, and $-0.2 \leq x^* \leq 0.2$ to a segment more closely reflecting the lower regions of the pipe.

The V_p/V_R value, which was calculated over time for each simulation, represents the volume occupied by particles as a percentage of the volume of the region close to the wall. The four deposited DNS Stokes number ($St^+ = 5.55$, 7.2, 11.11 and 16.78) simulations were used to calculate the average volume coverage. It was evident from instantaneous plots of particle positions in the spanwise direction that the majority of the particles accumulated at $-0.2 \leq x^* \leq 0.2$ (see Figure 6.16, for example), thus we estimated the volume coverage in this range and also in the full spanwise direction, which was $-0.5 \leq x^* \leq 0.5$. The computed volume coverages at which deposition was predicted to occur for $-0.2 \leq x^* \leq 0.2$ is approximately 2.83% and for $-0.5 \leq x^* \leq 0.5$ approximately 3.83%. These averages were established through comparison with predictions of the correlation of experimental data derived earlier, i.e. to be in agreement with the predictions of that correlation. These values correspond to around 80% of the particles having migrated towards the bottom of the pipe in both cases. In the remaining simulations, deposition was considered to have occurred when volume coverages were equal to 2.83% or 3.83% over the same volumes. Thus, these four initial simulations are used to define when a deposited bed has occurred through comparisons with the derived correlation, and hence with experimental data.

Particle-turbulence interaction plays an important role in particle migration towards the wall. Turbophoresis and increased gravitational force are expected to cause high Stokes number particles to deposit earlier than lower ones, however, the dependence of critical deposition velocity on Stokes number is large. The critical deposition velocities, determined by monitoring the particle concentrations in the lower regions of the pipe until the particles began to form high-concentration regions there, as described above, were u^* = 0.4289, 0.52, 0.69 and 0.7573 for the $St^+ \cong 5.55$, 7.2, 11.11 and 16.78 particles, respectively. Similar velocities were obtained by Rice et al. (2020).

Figure 6.24 (left) shows the ratio of the volume occupied by particles to the volume of the near-wall region, V_p/V_R, in the lower half of the pipe with time for the $-0.5 \leq x^* \leq 0.5$ (left) and for $-0.2 \leq x^* \leq 0.2$ (right) cases. As the Stokes number is increased, the rate at which the near-wall volume is occupied by particles increases, with the mean pressure gradient slowly decreasing in all cases accounting for the reduction in Reynolds number. It is also important to

note that the volume of the region capable of holding particles decreases over time. As the simulations evolved, the mean flow velocity was measured over time. Here we have considered two different average volume coverages as an indicator that beds (or dune-like structures) have formed, indicating the onset of deposition.

All the present DNS- and LES-based predictions computed using both averages of 2.83% and 3.83% were then determined to establish whether these averages could be applied over the full range of condition considered, and whether they could be used as a basis for predicting bed formation and hence the critical deposition velocity. The results are given in Figure 6.25 where all the simulation predictions are seen to be in strong agreement with the correlation developed earlier. Also, in comparison with the experimental deposition and resuspension datasets, the present simulations more closely align with the correlation, with significantly less scatter in the results. It should also be noted that the four original DNS-based predictions used to obtain the averages noted, all at $X \sim 3$, are in close agreement with the correlation.

As an alternative method of establishing the critical deposition velocity, a similar approach was taken, but now where predictions were based on the deposition of particles out of the upper regions of the pipe. Again, the original four DNS-based predictions were used to evaluate particle migration from the upper regions of the pipe, and these were found to be in reasonable agreement with the correlation when more than 97.6 percent of the particles had migrated below a level equivalent to the upper $1/8^{th}$ of the pipe. Figure 6.26 depicts particle deposition predictions in terms of the volume percentage of particles in the upper region of the pipe. The average percentage of 97.6% of particles removed from this region corresponds to 0.000211% (V_p/V_R) particles having migrated towards the bottom of the pipe. The volume occupied by the particles in this region is seen to fluctuate at the beginning of the simulations for the $St^+ = 2656$ and $St^+ = 3187$ cases, however all the predictions begin to show deposition by approximately $t^* = 25$. Due to their high Stokes numbers, which reduces their sensitivity to the fluid flow and increases their response time and dominating inertia, these particles exhibit more bouncing or rebounding after colliding with other particles or the pipe wall, and these effects are likely responsible for the initial fluctuations.

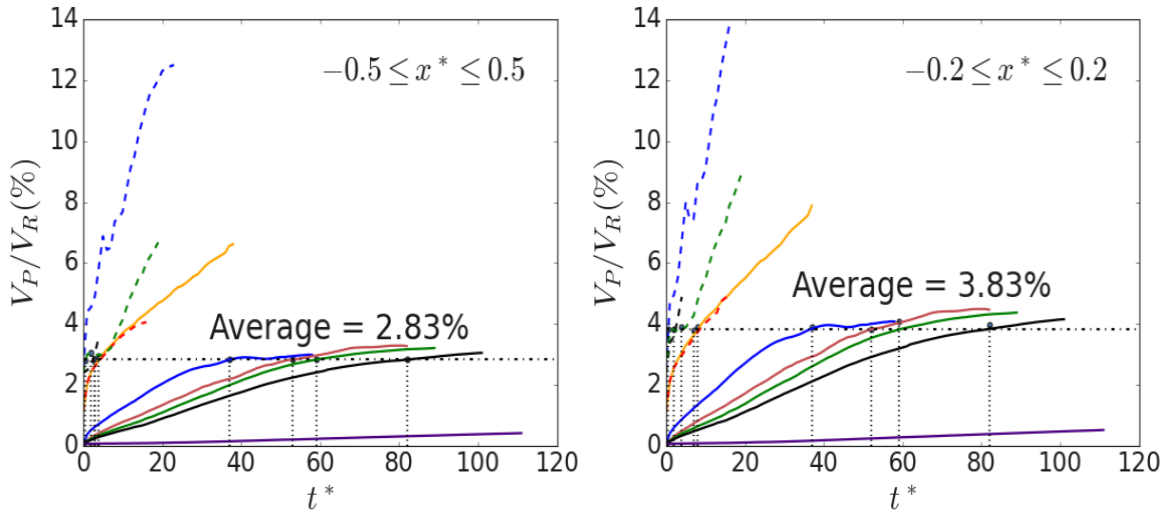

Figure 6.24: Critical deposition velocity prediction volume coverage, $0.49 \leq r* \leq 0.5$. Indigo: $St^+ = 1.2$ or $X = 2.54$, black: $St^+ = 5.5$ or $X = 2.81$, green: $St^+ = 7.2$ or $X = 3.84$, red: $St^+ = 11.11$ or $X = 2.91$, blue: $St^+ = 16.78$ or $X = 2.96$, gold: $St^+ = 17.63$ or $X = 4.2$, red (dashed): $St^+ = 17.63$ or $X = 4.2$, green (dashed): $St^+ = 3187.2$ or $X = 5.0$, blue (dashed): $St^+ = 2655.67$ or $X = 6$, black (dashed): $St^+ = 5684.4$ or $X = 6.5$.

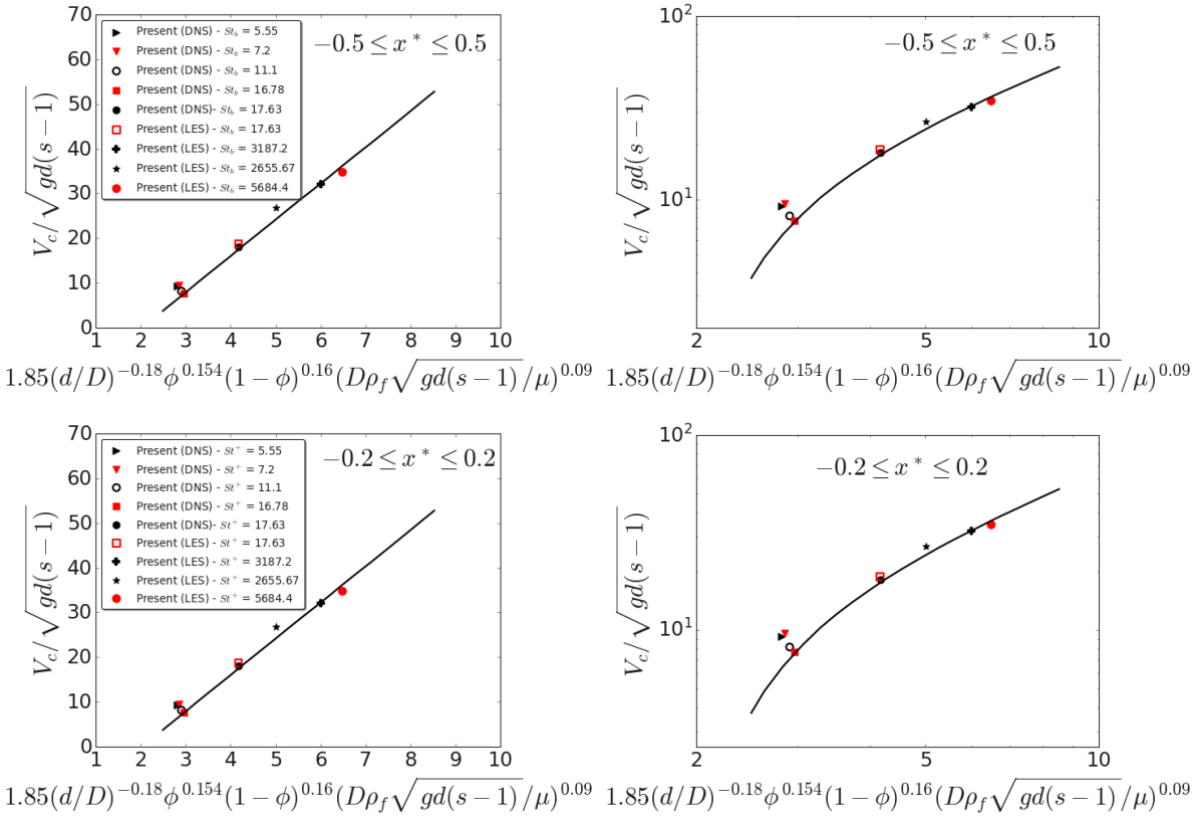

Figure 6.25: Present critical deposition velocity predictions at different Stokes number plotted against the empirical correlation – deposition to form particle bed.

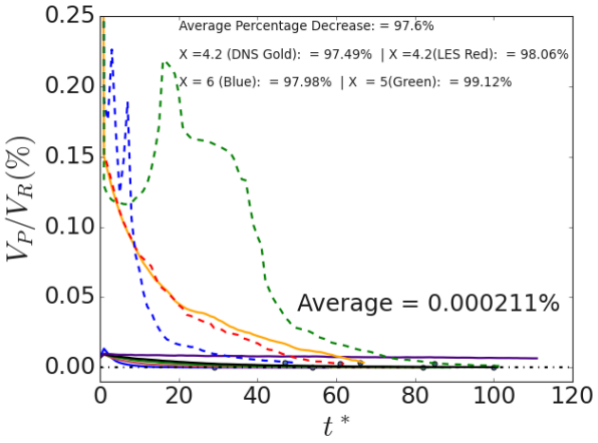

Figure 6.26: Critical deposition velocity prediction volume coverage at top of pipe. Indigo: $St^+ = 1.2$ or X = 2.54, black: $St^+ = 5.5$ or X =2.81, green: St^+ = 7.2 or X = 3.84, red: $St^+ = 11.11$ or X = 2.91, blue: $St^+ = 16.78$ or X =2.96, gold: St^+ = 17.63 or X = 4.2, red (dashed): St^+ = 17.63 or X = 4.2, green (dashed): $St^+ = 3187.2$ or X = 5.0, blue (dashed): $St^+ = 2655.67$ or X = 6.

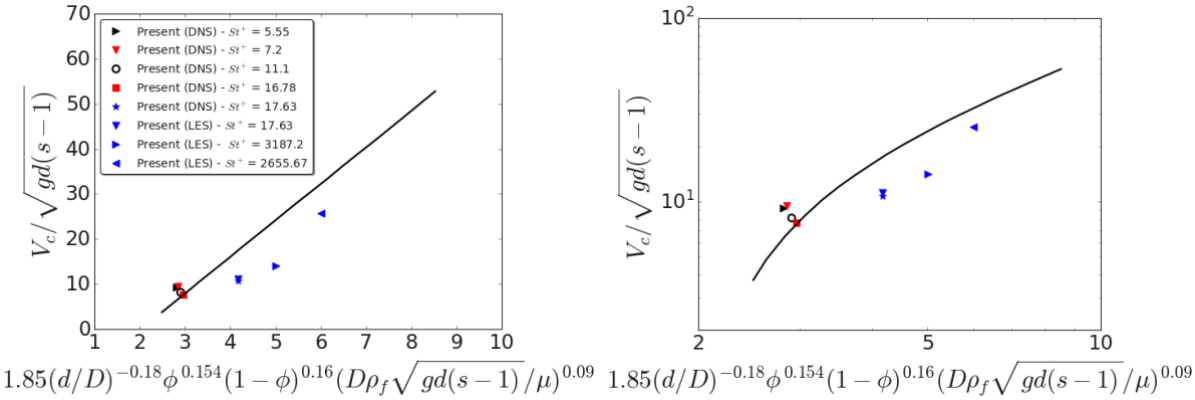

Figure 6.27: Present critical deposition velocity prediction at different Stokes number plotted against the empirical correlation – migration from upper pipe region.

Figure 6.27 shows predictions of the critical deposition velocity based on the above analysis of particles migrating from the upper regions of the pipe compared with the derived empirical correlation. Some significant underestimation of the correlation is seen in these results, although deviations from the correlation are not significantly different, in terms of scatter, than those observed earlier when comparing experimental resuspension and deposition datasets with the correlation.

Finally, Figure 6.28 shows all the present simulation predictions in comparison with the derived correlation. Overall, there is a strong consistency between the simulation results, the correlation and the experimental datasets on which it was based. However, predictions of critical

deposition velocity based on the formation of beds in the lower regions of the pipe are seen to be in far better agreement with the correlation, and hence this method provides the most accurate means of identifying the critical deposition velocity.

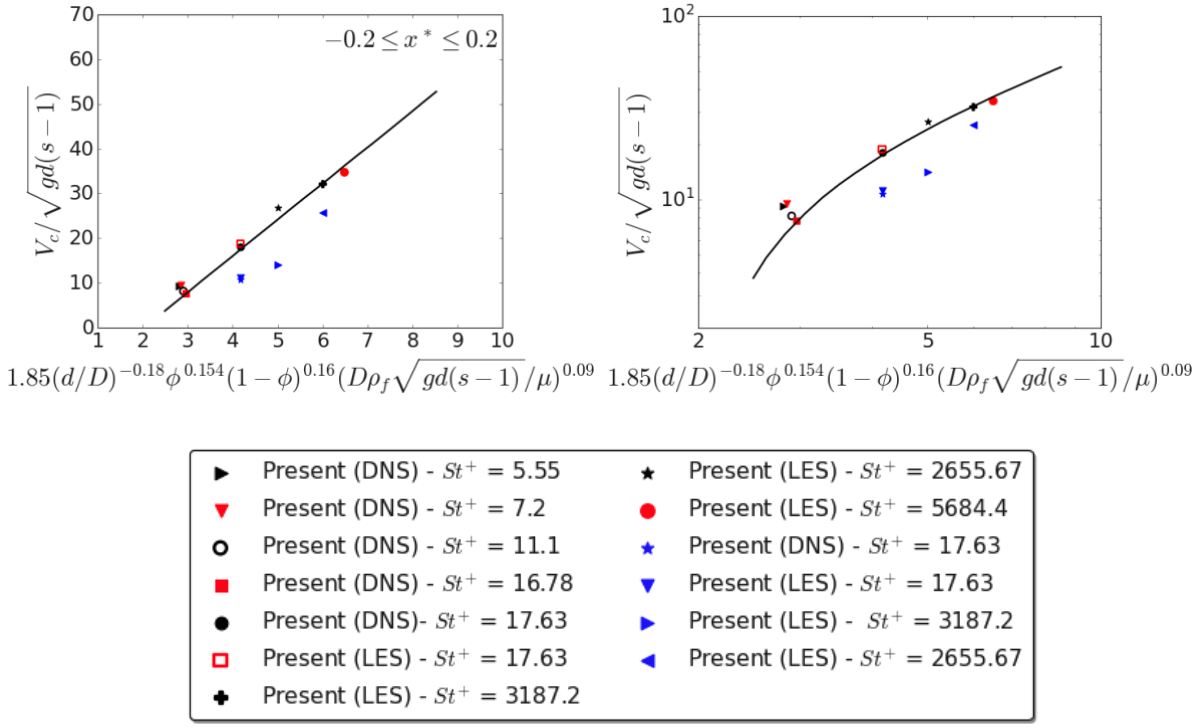

Figure 6.28: All present critical deposition velocity prediction at different Stokes numbers plotted against the empirical correlation. The blue symbols represent predictions based on particles migrating from the upper pipe region.

6.5 CONCLUSIONS

In this Chapter, the effect of particle Stokes number on particle deposition within a wall-bounded turbulent pipe flow was considered. The onset of particle deposition in particle-laden turbulent pipe flows has been studied using four-way coupled DNS-LPT and LES-LPT approaches. Fully resolved turbulent pipe flows over a range of shear Reynolds number Re_τ =720 to 21,600 were employed, with the flow rate reduced slowly with time, and methodologies proposed to predict the critical deposition velocity. The predictions have been validated through comparison with literature experimental datasets, represented by a correlation shown to be in good agreement with literature data obtained from both particle resuspension and deposition experiments. The prediction method was most successfully tested using the present simulations to analyse particle concentrations in the lower regions of the pipe, where particles were demonstrated to form dune-like structures and beds in the near-wall region, with this approach used to determine the critical deposition velocity. These simulations were performed at different Stokes numbers based on shear units, spanning a large range from $St^+ = 1.2$ to 5,684.

Overall, the present predictions using a deposition-onset identifier as a near-wall region volume occupancy fraction of ~2.83% produced critical deposition velocities in-line with the derived empirical correlation and also critical velocities established through particle resuspension experiments. The particle critical deposition velocity was shown to be sensitive to Stokes number, such that high Stokes number particles begin to deposit at higher flow rates. This was seen most clearly in particle dispersion function and particle mean displacement analysis, which showed that while the dispersion initially increased in all cases, it is soon reduced as the particles approached the lower pipe wall and began to form deposited beds. Instantaneous plots of particle positions showed that while lower Stokes number particles formed dune-like structures, interacting with the low-speed streaks in the near-wall region, increased Stokes number particles did not exhibit this behaviour, with their slip velocities and gravitational forces high enough such that their motion was decoupled from the local flow. In this case, more homogeneously distributed beds were observed to be formed.

The conclusions above were further reinforced by a study of particle dynamics that examined probability density functions for particle positions, streamwise and vertical velocities, and slip

velocities. Consideration of vertical positions showed that particles with high Stokes numbers typically had a larger tendency to form more concentrated beds faster.

Analysis of particle migration from the upper regions of the pipe as a means of predicting the critical deposition velocity was demonstrated to be less effective than the bed deposition approach, and underestimated the derived correlation due to the long time periods needed for particles to migrate to the lower regions of the pipe ($7/8^{th}$ of the diameter), and additionally the very low concentrations needing to be reached. This approach did, however, still provide adequate predictions of the critical velocity.

In general, the newly developed correlation can be used to accurately estimate critical deposition velocity profiles for resuspension or deposition-based datasets, and appears to more accurately correlate such datasets than existing correlations. Additionally, the DNS- and LES-based simulation approach can also be used as a valuable tool in predicting critical deposition velocities where no relevant experimental data exist. Given the considerable complexity of nuclear waste sludge flows and slurries inherent in waste processing and post-operational clean out operations, the performance of the present correlation and simulation-based prediction methods are extremely promising.

7 CONCLUSIONS AND RECOMMENDATIONS FOR FURTHER WORK

7.1 Conclusions

To address the challenges present in particle-laden transport processes in the nuclear industry, a comprehensive computational study of behavioural modification techniques and deposition in suspension waste pipe flows has been performed. Pipe-like geometries are widely used to transport legacy radioactive material between ponds, silos and temporary storage facilities as part of nuclear waste processing activities in the UK and elsewhere. These procedures most frequently entail high flow rates, inducing turbulent flow, and raising the likelihood of particle-particle collisions and wall deposition while also increasing the risk of aggregate build-up and pipe blockages. The present work aimed to generate further understanding of these systems, and to provide a means to improve designs, essential for carrying out waste management and post-operational clean-out (POCO) operations effectively and at reduced cost. Two major foci of this work are that of the ability to modify such flows (behavioural modification), as well as to generate improved predictive methods for identifying the critical deposition velocity, though the insight obtained further allows nuclear waste management operations to benefit from improved computational predictions of particle dispersion, particle-particle interaction, deposition, and agglomeration within turbulent pipe flows.

When compared to other computational techniques like RANS or LES for investigating fluid dynamics, DNS has a number of advantages. DNS provides extremely precise results without any modelling approximations by resolving all pertinent spatial and temporal scales of fluid motion. In addition, compared to coarser-resolution techniques, DNS offers comprehensive details regarding flow structures, turbulence statistics, and energy transfer mechanisms, providing greater insights into complex fluid flow phenomena. By solving the governing

equations of fluid motion directly without the need for turbulence models, DNS improves prediction capabilities and removes uncertainty related to model assumptions.

In predicting the continuous phase, three turbulent shear Reynolds numbers, Re_τ = 277, 360, and 720 (based on the pipe diameter), were used for direct numerical simulations of fully developed turbulent pipe flows. The descriptive fluid flow equations were solved using the fully parallelisable Nek5000 DNS solver, which is a high-order weighted residual approach with excellent accuracy and low numerical dispersion and dissipation. In order to validate the effectiveness of the code employed, profiles of mean velocity, normal stress, and shear stress within the flows were analysed. The continuous phase solver predictions for turbulent pipe flows at each Reynolds number were compared against previous simulations from the literature and experimental datasets to ensure their accuracy. The results of the present single-phase validations were reported in Chapter 4, alongside relevant literature datasets. The present work was shown to be in excellent agreement with all validation cases. Where possible, several experimental and DNS datasets were used to compare with the current simulations for the case of incompressible and Newtonian fluid flows.

To explore and study the trajectories and emergent behaviour of large numbers of dispersed solid particles, the DNS was coupled with a Lagrangian particle tracker. A fourth order Runge-Kutta technique was utilised to solve the particle equations of motion for each particle at each time-step, concurrently with the fluid solver. Contributions from drag, shear lift, virtual mass, pressure gradient and gravity forces (where applicable) were considered when calculating the particle acceleration. In the fully developed fluid flow domain, the particles were randomly injected, initialising their velocities to their spectrally interpolated fluid velocity at their location at the start of the particle simulation. The interactions of particles with the impenetrable pipe wall were assumed to be elastic. Periodic boundary conditions and no-slip conditions were applied to either extent of the streamwise direction and the radial distance at the wall, respectively. After time-evolving the simulation through sufficient integration to provide the particles with enough response time (t^*=20) to adapt to the fluid flow environment, statistical data were gathered for examination, analysis, and comparison with literature results. A simulation was performed at Re_τ = 277 to validate the four-way coupled LPT solver, and the results were directly compared with the predictions of Vreman (2007). This reference study considered the dispersion of glass beads in a turbulent pipe flow and as such, the parameters

were set identical between both systems. Good agreement was found between the current four-way coupled results of the mean particle velocity and stress components and the four-way DNS predictions of Vreman (2007), despite the much-enhanced numerical resolution used in the present work. An additional simulation was carried out at $Re_\tau = 360$ which examined the effects of particles on the continuous phase (two-way coupling) as well as further validating the coupled DNS and LPT solver. The predictions were directly compared with the DNS results of Rani et al. (2004), in which the presence of particles inside the same flow configuration was considered. The one-way and four-way mean and root-mean-square of the axial, radial, and azimuthal fluctuating velocity profiles, as well as the mean Reynolds shear stress, were compared, with both sets of findings exhibiting strong agreement. When using four-way coupling, turbulence attenuation was also observed, tending to be most apparent in the bulk flow region, and was discovered to be of a similar magnitude to that of the comparison research. All comparisons performed show statistically strong agreement with previous DNS and experimental datasets, building confidence in the further predictions performed and insight generated in this work.

To elucidate the dynamics associated with the particles' local dispersive and wall-interaction behaviour, PDFs of particle dynamic characteristics for both one-way coupled and four-way coupled particle-laden flows were also examined. Comparing the four-way coupled simulation to the one-way coupled simulation, the PDFs for the former showed a greater range of particle radial, azimuthal, and streamwise velocity components. The viscous sublayer of the flow exhibited a wider velocity spread for the one-way coupled results, and higher particle concentrations close to the wall were observed. Gravitational effects were shown to cause a slight bias towards negative velocities in all cases. Additionally, the mean particle concentration profiles for one-way coupled simulations as well as four-way coupled simulations within the turbulent pipe flow were examined. In the one-way coupled simulation compared to the four-way coupled case, more particles were seen close to the wall as a result of the high Stokes number utilised. The simulations employed to validate the data from Rani et al. (2004) and Vreman (2007) were compared, which considered particles with high Stokes numbers, $St^+ = 58$ and 79, respectively. It was found that higher particle Stokes numbers resulted in a greater wall accumulation, attributed to the effects of turbophoresis, which caused the more inertial particles to migrate towards the wall at an increased rate. Due to the fact that four-way coupling tends to hinder the wall-accumulation process, most likely as a result of

particle collisions generating slightly greater rms velocity fluctuations, one-way coupling was found to produce increased near-wall concentrations, compared to four-way coupling.

The literature review identified a notable lack of modelling research specifically addressing particle-particle interactions (four-way coupling) in cylindrical geometries, with studies utilising agglomeration mechanisms in such extremely limited. In order to generate knowledge to improve this situation, and after having performed an extensive validation which showed strong agreement for both the single-phase and particle-phase predictive methodologies, the simulation approaches were further used to examine the effects of potential behavioural modification techniques on long-term emergent phenomena such as particle collision and agglomeration rates. A variety of particle-laden pipe flows were simulated by utilising the fully-developed particle-laden turbulent pipe flow with shear Reynolds number based on pipe diameter, Re_τ = 720, and a high volume fraction, ϕ_p =1×10^{-3}. The use of behavioural modification to tune fluid and solid particle characteristics to promote desirable outcomes, such as encouraging or discouraging particle collisions and agglomeration, was investigated. This necessitated implementing two-way and four-way coupling between the particles and the fluid flow, as well as incorporating particle collision and agglomeration models. Particle aggregation resulting from collision interactions between particles in the flow was predicted using an energy-balance based agglomeration determination technique and four-way coupling. The aim was to assess the effects of various electrochemical and physical characteristics on collision and agglomeration processes. The impact of behavioural modification effects was hence explored by varying important parameters in the Derjaguin-Landau Verwey-Overbeek (DLVO) theory interaction potentials. By modifying the DLVO attraction or repulsion terms, these modifications altered the way particles interact. Mechanical and hydrodynamic effects were accounted for through modification of the normal restitution coefficient, as well as the Reynolds number, while the van der Waals attraction was studied in relation to modification of the Hamaker constant. Regarding electric double layer repulsion, the variation of key parameters such as the reduced surface potential, inverse Debye length, and suspension temperature were investigated.

The analysis concluded that the impact of the electric double layer on collision and agglomeration rates was negligible, attributable to the large particle diameters investigated in comparison to the effective range of the repulsive forces. The charge on a 100μm diameter

particle's surface is hence insufficient to repel particles and to effectively reduce the kinetic energy of the collision. It was demonstrated that the particle-particle interaction dynamics are greatly influenced by the restitution coefficient, and that the number of particle collisions, N_{col}, and the number of agglomeration events, N_{agg}, both rise with time, t^*. It was determined that the size and rate at which larger agglomerates form has an inverse relationship to the restitution coefficient. Additionally, it was observed that collisions occur more frequently towards the pipe wall. However, the distribution of agglomeration events in the pipe radial direction was shown to be uniform. The number of collisions, the number of those collisions leading to agglomeration (also known as the agglomeration efficiency), and the temporal evolution of agglomeration efficiency (doublets, triplets and so on) all increase with decreasing the coefficient of restitution.

Particle-resolved studies demonstrated that particle-particle interactions (collision and agglomeration) are sensitive to the modification of the Hamaker constant and the Reynolds number (Mortimer and Fairweather, 2021). The results of the present work showed agreement, demonstrating that the long-term bulk behaviour is strongly influenced by both parameters. Both the Hamaker constant and Reynolds number were shown to have a significant influence on the collision and agglomeration rates within a pipe. In spite of increased turbulence inducing more ballistic collisions, the study demonstrates that a higher Hamaker constant increases the rate at which agglomeration occurs and that the Reynolds number also raises the probability of collision and agglomeration. In general, the sensitivity of collision and agglomeration events to the specified simulation parameters influenced both the production of high constituent number particle agglomerates as well as the reduction of primary singlets particles. It was discovered that the production of doublet particles occurred slightly more frequently at the highest Hamaker constant, H = 36.76 zJ, than at the lowest restitution coefficient, e_n = 0.2. This is due to the fact that doublet particles develop into triplet and quadruplet particles more quickly when the restitution coefficient is low. These results lead to the conclusion that the Reynolds number, the Hamaker constant, and the restitution coefficient all influence the decrease of singlet particles and the increase of doublets, triplets, and larger particle agglomerates, with the lowest restitution coefficient having the largest influence on agglomeration behaviour and the highest Hamaker constant having the second-largest influence.

Another key aim of the work was to determine how the flow rate or Reynolds number affects the onset of particle deposition, of use in designing processes where avoidance of this behaviour is critical. The effects of particle Stokes number on the settling and deposition dynamics of particle-laden turbulent pipe flows was also studied. To provide a theoretical foundation for prediction of the critical deposition velocity, a dimensional analysis was performed, collapsing various deposition and resuspension literature datasets to form an improved empirical correlation compared to others available in the literature. The predictive model was validated through comparison with many experimental datasets from the literature. The results for both the experimental datasets for resuspension and deposition were well correlated by the derived correlation. Rice et al. (2020) suggested two methods for determining the critical deposition velocity. The primary way is defined as the velocity at which particles first begin to deposit out of a flow as the Reynolds number is reduced. The alternative approach is by measuring the flow velocity at which particle resuspension from the pipe floor occurs, as the Reynolds number is increased. The authors claimed that both methods were equivalent and represented different ways to determine the critical deposition velocity. In correlating data from both resuspension and deposition datasets, the developed correlation works confirms Rice et al.'s (2020) contention is generally correct. Furthermore, the predictive methodology was further evaluated using both the experimental data as well as simulation results performed to determine the critical deposition velocity directly.

The onset of particle deposition using four-way coupled DNS-LPT and LES-LPT based simulations of particle-laden flows, particularly in cylindrical topologies, has very rarely been studied in the literature. To address this using the presented methodology, four-way coupled DNS-LPT and LES-LPT simulations were performed to investigate deposition in particle-laden turbulent pipe flows. To target sets of parameters across the full range covered in the correlation comparisons, four fully developed particle-laden pipe flows were first driven to a steady state at shear Reynolds numbers Re_τ = 720, 4714, 12700 and 21600. To reduce the flow rate such that deposition would occur, the constant pressure gradient driving force term was gradually reduced by two per cent every 2000 timesteps (t^* = 2). Various particle Stokes numbers based on shear units spanning a large range from $St^+ = 1.2$ to 5684 were simulated using fully developed flow field solutions as initial conditions. The gravitational force was applied in the vertical direction for a horizontal pipe flow, and the conveying flow rate was then decreased as detailed above allowing particle deposition to eventually occur. A method for identification of

the critical deposition velocity was also developed by assessing the concentration of particles in the lower regions of a pipe, where particles were shown to form dune-like structures and deposited beds in the near-wall region as the simulations progressed. These simulations were compared to the derived empirical correlation to establish the coverage by particles of the lower regions of the pipe which corresponded to the critical deposition velocity, thereby providing a means of determining the latter velocity under different flow conditions and particle characteristics.

The results of Stokes number $St^+ =$ 1.22, 5.55, 7.2, 11.11 and 16.78 investigations demonstrated that particle deposition is highly sensitive to the particle Stokes number, with increasing Stokes number particles depositing at higher flow velocities. The particle dispersion function and particle mean displacement were shown to decrease significantly faster with time for larger Stokes number particles due to the increasing gravitational force acting on the particles. This analysis additionally demonstrated that, although dispersion initially increased in each case, it quickly decreased as the particles approached the bottom pipe wall and started to form deposited beds. Based on a thorough analysis of the Stokes numbers $St^+ \cong$ 5.55 and 16.78, it can be deduced that by t^* = 10 there is little difference in the symmetrical distribution of the particles between the two cases; nevertheless, by t^*= 20, there was clear divergence of behaviour. By time t^* =50, the majority of the particles were in the lower half of the pipe, indicating that particles begin to deposit at higher flow rates. Temporal evolution of particle concentration profiles showed that particles fell towards the lower wall region, and eventually deposited on the floor of the pipe, with a particle bed forming for higher Stokes numbers. In contrast, instantaneous plots of particle positions at lower Stokes number, showed a bed was not formed, although the majority of the particles did form dune-like structures on the floor of the pipe. The previously reported findings were further supported by a study of the particle dynamics that investigated probability density functions of particle positions and velocities. Particles with higher Stokes numbers were found to have lower critical deposition velocities, confirming prior findings that high Stokes number particles have a greater propensity to form particle beds.

The simulation predictions yielded critical deposition velocities that are consistent with the empirical correlation developed as well as critical velocities established through resuspension and deposition experiments at roughly 2.83% ($-0.2 \leq x^* \leq 0.2$) or 3.83% ($-0.5 \leq x^* \leq$

0.5) particle volume occupancy close to the pipe walls. This computed average volume coverage was used to identify the point at which around 80% (average = 2.83%) of the particles had moved towards the pipe's bottom. As the Stokes number was increased, the rate at which the near-wall region volume was occupied increased. Overall, there was a high degree of consistency between the simulation findings, the empirical correlation, and hence the experimental datasets from which it was developed; the analysis shows that all of the present simulation predictions were consistent with the developed correlation. Due to the lengthy times needed for 97% particles to migrate to the lower regions of the pipe, it was found that using particle migration from the upper regions of the pipe as a method of estimating the critical deposition velocity was less effective than using the bed deposition strategy. The former results showed some considerable underestimation of the correlation, although the scatter of the deviations from the correlation was not statistically different from that of the experimental datasets for resuspension and deposition used to derive the correlation. As a result, the development of beds in the lower portions of the pipe, which was observed to be in much better agreement with the correlation, appears to be the most accurate technique to predict the critical deposition velocity, which was considerably more accurate than the alternative approach.

7.2 Recommendations for further work

This study examined various behavioural modification techniques for particle transport and interaction in pipe flows. The present work successfully investigated the effects of various potential behavioural modification techniques on particle dispersion and agglomeration by utilising a fully coupled DNS-LPT approach. With the exception of the Reynolds number variation study, which used an Re_τ = 360 flow, all simulations of behavioural modification were performed using the same shear Reynolds number, Re_τ = 720, isolating the effects of the parameters of interest from those caused by turbulence. As it was observed that Reynolds number has a substantial impact on particle-particle interaction, the current DNS-LPT model should be extended to turbulent flows at higher Reynolds numbers, wherein collisions may be more frequent, and particle-turbulence interaction may play a more important role.

The fact that the particle sizes and shapes observed in nuclear slurry flows are often polydispersed and inhomogeneous adds another layer of complexity, with particle sizes generally ranging from 1 μm to 1 mm. Only 100 μm diameter particles were used in the present

simulations (although the particle Stokes number was varied); hence, it would be beneficial to investigate particle size variations as well as polydispersity in cylindrical geometries. The results of previous studies in channel flows have demonstrated that a wide range of various particle-fluid and interparticle interaction processes can be observed depending on particle size (Njobuenwu and Fairweather, 2017). Furthermore, particles are rarely fully spherical; they can also consist of more complex structures like needles, discs, and other shapes. To anticipate the effects of both polydispersity and non-sphericity on the subsequent flow dynamics and aggregation properties, and to more accurately represent industrial flows, the present DNS-LPT algorithms should be extended. To ascertain the various interaction orientations, velocities, and angular velocities that are present in non-spherical multiphase pipe flows, a comparable DNS-LPT study should be performed.

It was demonstrated that it is feasible to develop behavioural modification strategies based on the results obtained when significant fluid flow and particle characteristics were altered. It is important to conduct more research to examine the interactions between cases with high collision and agglomeration rates (such as low restitution coefficient, high Hamaker constant, and high Reynolds number) and cases with low collision and agglomeration rates (such as high restitution coefficient, low Hamaker constant, and low Reynolds number). Furthermore, the behavioural modification techniques studied did so under the assumption of zero gravity; this means that additional research that takes gravitational acceleration into account in determining particle trajectories could have important consequences that could either promote or discourage interparticle agglomeration through the interplay between the hydrodynamic and inertial forces.

Additionally, it was also demonstrated that the Stokes number affects the critical deposition velocity, since it was observed that high Stokes number particles deposit at greater flow rates. Due to the proximity of the particles, when they have moved towards the bottom of the pipe, there are likely to be more complex collision and agglomeration events. It would therefore be worthwhile to examine the simulation of behavioural modification techniques in conjunction with particle deposition simulations.

Despite the present work generating a lot of understanding surrounding the dynamics and behavioural modification of particle-laden pipe flows, there are still unanswered questions surrounding how the fluid and particulate phases will behave over long timeframes and in more

complex geometries. It would be beneficial to conduct additional research using these methods for a variety of simulated particle-laden pipe flows with parameters, initial conditions and geometries tailored to those relevant to the transport of nuclear waste. These could include implementing pipes with bends and pre-deposited beds. Elucidating the dynamics of mechanisms such as particle dispersion, turbulence modulation, particle deposition and collision and agglomeration would be very helpful in determining how the behavioural modification approaches affect the bulk properties of more complex systems in order to predict potential issues and improve understanding of these flows. Additionally, examining particle resuspension from solid beds would also be beneficial in waste processing system design as a potential means of removing deposited beds from pipes and preventing their complete blockage.

Methodologies were developed for this study which employed DNS in conjunction with LPT, which offers a high level of predictive accuracy for studying waste transport systems. They also hold a great deal of promise for the generation of knowledge regarding the development and application of behavioural modification techniques in flows. This study could be broadened to examine other behavioural modification techniques, perhaps including additional phases. For instance, the addition of polymer additives is a promising way to encourage agglomeration through flocculation, and it is possible to use the injection of flocculation agents to improve particle deposition which is desirable in some waste processing applications. Low-particle number interactions could also be studied on a fundamental scale using the immersed boundaries method in conjunction with DNS.

Finally, although the model developments described have made use of experimental data where available, there is clearly a dearth of such data for use in model formulation and validation. Future research would significantly benefit from the provision of experimental data relevant to all the studies reported in this thesis, and to the proposed studies recommended in this section.

8 REFERENCES

Adams J. F. W. (2011). Particle deposition, dispersion and Re-suspension behaviour in turbulent square duct and circular pipes flows. Thesis, University of Leeds.

Ahmari.H and Kabir. S.M.I.K. (2020). Applied fluid mechanics lab manual. Mavs Open Press, Arlington.

Alexander LG, Coldren CL. (1951). Droplet transfer from suspending air to duct walls. Industrial & Engineering Chemistry. 43, pp.1325-1331.

Aly, A., Trupp, A. and Gerrard, A. (1978). Measurements and prediction of fully developed turbulent flow in an equilateral triangular duct. Journal of Fluid Mechanics. 85(1), pp.57-83.

Al-Lababidi, S., Yan, W. and Yeung, H. (2012). Sand transportations and deposition characteristics in multiphase flows in pipelines. ASME. J. Energy Resour. Technol.-ASME. 134, pp.034501.

Boersma, B.J. (2011). Direct numerical simulation of turbulent pipe flow up to a Reynolds number of 61,000. In: Journal of Physics: Conference Series: IOP Publishing, p042045.

Borée, J. and Caraman, N. (2005). Dilute bidispersed tube flow: Role of interclass collisions at increased loadings. Physics of Fluids. 17(5), p055108.

Bremhorst, K. and Walker, T. (1973). Spectral measurements of turbulent momentum transfer in fully developed pipe flow. Journal of Fluid Mechanics. 61(1), pp.173-186.

Breuer, M., Alletto, M. and Flow, F. (2012). Efficient simulation of particle-laden turbulent flows with high mass loadings using LES. International Journal of Heat and Fluid Flow. 35, pp.2-12.

Breuer, M. and Almohammed, N. (2015). Modeling and simulation of particle agglomeration in turbulent flows using a hard-sphere model with deterministic collision detection and enhanced structure models. International Journal of Multiphase Flow. 73, pp.171-206.

Caraman, N., Borée, J. and Simonin, O. (2003). Effect of collisions on the dispersed phase fluctuation in a dilute tube flow: Experimental and theoretical analysis. Physics of Fluids. 15(12), pp.3602-3612.

Cai, S., Liang, J., Gao, Q., Xu, C. and Wei, R. (2020). Particle image velocimetry based on a deep learning motion estimator. IEEE Transactions on instrumentation and measurement, 69(6), pp. 3538-3554.

Cenedese A., Costantini A., and Romano, G. P. (1992). LDA spectral measurements in a turbulent boundary layer. Experimental Thermal and Fluid Science, 5(3), pp. 281-289.

Cenedese A., Romano G. P., and Di Felice F. (1991). Experimental testing of Taylor's hypothesis by L.D.A. in highly turbulent flow. Experiments in Fluids, 11, pp. 351-358.

Choi,Y.D., Chung, M.K. (1983). Analysis of turbulent gas – solid suspension in a pipe. Journal of Fluids Engineering., 105, pp.329 – 334.

Clift, R. G. (2005). Bubbles, drops, and particles. Courier Corporation.

Comte-Bellot, G. (1976). Hot-wire anemometry. Annual Review of Fluid Mechanics. 8(1), pp.209-231.

Dandy, D. A. and Dwyer, H.A. (1990). A sphere in shear flow at finite Reynolds number: effect of shear on particle lift, drag, and heat transfer. Journal of Fluid Mechanics. 216, pp.381-410.

Davies, J.T. (1987). Calculation of critical velocities to maintain solids in suspension in horizontal pipes. AIChE Journal. 42(7), pp.1667-1679.

Deardorff, J.W. (1970). A numerical study of three-dimensional turbulent channel flow at large Reynolds numbers. Journal of Fluid Mechanics. 41(2), pp.453-480

Den Toonder, J. M., Hulsen, J. , M. A., Kuiken, G. D. C. and Nieuwstadt, F. T. M. (1997). Drag reduction by polymer additives in a turbulent pipe flow: numerical and laboratory experiments. Journal of Fluid Mechanics. 337, pp.1193-231.

Den Toonder, J. and Nieuwstadt, F. (1997). Reynolds number effects in a turbulent pipe flow for low to moderate Re. Physics of Fluids. 9(11), pp.3398-3409.

Demuren, A.O. and Rodi, W. (1984). Calculation of Turbulence-Driven Secondary Motion in Non-Circular Ducts. Journal of Fluid Mechanics. 140(3), pp.189-222.

Derjaguin, B. and Landau, L. (1941). Theory of the stability of strongly charged lyophobic sols and of the adhesion of strongly charged particles in solutions of electrolytes. Acta Physicochim. URSS. 14(6), pp.633-662.

Durst, F., Melling, A. and Whitelaw, J.H. (1976). Principles and practice of laser-Doppler anemometry. NASA STI/Recon Technical Report A. 76.

Eckelmann H. (1974). The structure of the viscous sublayer and the adjacent wall region in a turbulent channel flow. Journal of Fluid Mechanics 65(3), pp. 439-459.

Eggels, J., Unger, F., Weiss, M., Westerweel, J., Adrian, R., Friedrich, R. and Nieuwstadt, F. (1994). Fully developed turbulent pipe flow: a comparison between direct numerical simulation and experiment. Journal of Fluid Mechanics. 268(1), pp.175-210.

Eggels, J., Westerweel, J., Nieuwstadt, F. and Adrian, R. (1993). Direct numerical simulation of turbulent pipe flow. Applied Scientific Research. 51(1), pp.319-324.

Ekambara, K., Sanders, R. S., Nandakumar, K. and Masliyah, J. H. (2009). Hydrodynamic simulation of horizontal slurry pipeline flow using ANSYS. CFX. Ind. Eng. Chem. Res, 48, pp.8159-8171.

El Khoury, G.K., Schlatter, P., Noorani, A., Fischer, P.F., Brethouwer, G. and Johansson, A.V. (2013). Direct numerical simulation of turbulent pipe flow at moderately high Reynolds numbers. Flow, turbulence and combustion. 91(3), pp.475-495.

Elghobashi, S. (1991). Particle-laden turbulent flows: direct simulation and closure models. Applied Scientific Research. 48(3-4), pp.301-314.

Elghobashi, S. (1994). On predicting particle-laden turbulent flows. Applied Scientific Research. 52(4), pp.309-329.

Elghobashi, S. (2007). An Updated classification map of particle-laden turbulent flows. In: IUTAM symposium on computational approaches to multiphase Flow: Proceedings of an IUTAM Symposium held at Argonne National Laboratory, October 4-7, 2004: Springer Science & Business Media, p.3.

Fairweather, M. and Yao, J. (2009). Mechanisms of particle dispersion in a turbulent, square duct flow. AIChE journal. 55(7), pp.1667-1679.

Fan, J. X., Zhang, L. Cheng, K. Cen. (1997). Numerical simulation and experimental study of two-phase flow in a vertical pipe. Aerosol Science and Technology. 27, pp.281 – 292.

Ferrante, A. and Elghobashi, S. (2003). On the physical mechanisms of two-way coupling in particle-laden isotropic turbulence. Physics of Fluids. 15(2), pp.315- 329.

Fischer, P. F., Lottes, J. W. and Kerkemeier, S. G. Nek5000, (2008). http://nek5000.mcs.anl.gov (accessed 12th November 2021).

Forney, L.J. and Spielman, L.A. (1974). Deposition of coarse aerosols from turbulent flow. Journal of Aerosol Science. 5(3), pp.257-271.

Friedlander, S. and Johnstone, H. (1957). Deposition of suspended particles from turbulent gas streams. Industrial & Engineering Chemistry. 49(7), pp.1151-1156.

Fukagata K. and Kasagi N. (2002) Highly Energy-Conservative Finite Difference Method for the Cylindrical Coordinate System. Journal Computational Physics. 181 (2), pp.478– 498.

Gavrilakis, S. (1992). Numerical simulation of low-Reynolds-number turbulent flow through a straight square duct. Journal of Fluid Mechanics. 244, pp.101-129.

Germano, M., Piomelli, U., Moin, P. and Cabot, W.H. (1991). A dynamic subgrid- scale eddy viscosity model. Physics of Fluids. 3(7), pp.1760- 1765.

Gessner, F.B. and Jones, J.B. (1965). On Some Aspects of Fully-Developed Turbulent Flow in Rectangular Channels. Journal of Fluid Mechanics. 23, pp.689-713.

Gessner, F.B., Po, J. and Emery, A. (1979). Measurements of developing turbulent flow in a square duct. Turbulent Shear Flows I. Springer, pp.119-136.

Gillies, R. G. and Shook, C. A. (1994). Concentration distributions of sand slurries in horizontal pipe flow. Part. Sci. Technol. 12, pp.45-69.

Gillies, R. G. and Shook, C. A. (2000). Modelling high concentration settling slurry flows. Canadian journal of Chemical Engineering. 78, pp.709-716.

Gillies, R. G., Schaan, J., Sumner, R. J., Mckibben, M. J. and Shook, C. A. (2000). Deposition velocities for Newtonian slurries in turbulent flow. Canadian journal of Chemical Engineering. 78, pp.704-708.

Gillies, R. G., Shook, C. A and Wilson, K. C. (1991). An improved two layer model for horizontal slurry pipeline flow. Canadian journal of Chemical Engineering. 69, pp.173-178.

Gillies, R. G., Shook, C. Aand XU, J. H. (2004). Modelling heterogeneous slurry flows at high velocities. Canadian journal of Chemical Engineering. 82, pp.1060-1065.

Gnanamanickam E. P., Nottebrock B., Große S., Sullivan J. P., and Schröder W. (2013). Measurement of turbulent wall shear-stress using micro-pillars. Measurement Science and Technology, 24(12).

Große, S. and Schröder, W. (2008). Dynamic wall-shear stress measurements in turbulent pipe flow using the micro-pillar sensor MPS 3. International Journal of Heat and Fluid Flow. 29(3), pp.830-840.

Guha, D., Ramachandran, P.A. and Dudukovic, M.P. . (2007). Flow field of suspended solids in a stirred tank reactor by Lagrangian tracking. Chemical Engineering Science. 62(22), pp.6143-6154.

Hill, R.J. (1978). Models of the scalar spectrum for turbulent advection. Journal of Fluid Mechanics. 88(3), pp.541-562.

Hultmark, M., Bailey, S. C. C. and Smits, A. J. (2010). Scaling of near-wall turbulence in pipe flow. Journal of fluid Mechanics. 649, pp.103-113.

Hultmark, M., Vallikivi, M., Bailey, S. C. C. and Smits, A. J. (2012). Turbulent pipe flow at extreme Reynolds numbers. Phys. Rev. Lett. 108.

Joung Y, Choi SU, Choi JI. (2007). Direct numerical simulation of turbulent flow in a square duct: analysis of secondary flows. Journal of Engineering mechanics. 133, pp.213.

Kajishima, T. and Miyake, Y. (1992). A discussion on eddy viscosity models on the basis of the large eddy simulation of turbulent flow in a square duct. Computers & Fluids. 21(2), pp.151-161.

Kreplin, H.P. and Eckelmann, H. (1979). Behavior of the three fluctuating velocity components in the wall region of a turbulent channel flow. Physics of Fluids. 22(7), pp.1233-1239.

Kuerten, J.G. and Vreman, A. (2015). Effect of droplet interaction on droplet-laden turbulent channel flow. Physics of Fluids. 27(5), pp.053304.

Laufer, J. (1951). Investigation of turbulent flow in a two-dimensional channel. Thesis, California Institute of Technology.

Laufer, J. (1954). The structure of turbulence in fully developed pipe flow. National Advisor Committee for Aeronautics. pp.1174.

Lawn, C. (1971). The determination of the rate of dissipation in turbulent pipe flow. Journal of Fluid Mechanics. 48(3), pp.477-505.

Lee I.B., Pascual J., Hong S.W., Seo I.H., Kwon K.S., Bartzanas T. and Kacira M. (2013).The past, present and future of CFD for agro-environmental applications. Computers and Electronics in Agriculture. 93, pp. 168-183.

Lee, J. and Lee, C. (2015). Modification of particle-laden near-wall turbulence: Effect of Stokes number. Physics of Fluids. 27(2), p023303.

Lee, S. and Durst, F. (1982). On the motion of particles in turbulent duct flows. International Journal of Multiphase Flow. 8(2), pp.125-146.

Li, A. and Ahmadi, G. (1992). Dispersion and deposition of spherical particles from point sources in a turbulent channel flow. Aerosol Science and Technology. 16(4), pp.209-226.

Li, A., Ahmadi, G., Bayer, R.G. and Gaynes, M.A. (1994). Aerosol particle deposition in an obstructed turbulent duct flow. Journal of Aerosol Science. 25(1), pp.91-112.

Lifshitz E.M. and Hamermesh M. (1956). The theory of molecular attractive forces between solids. Reprinted from Soviet Physics JETP 2. 73, pp. 329-349.

Li, J., Wang, H., Liu, Z., Chen, S. and Zheng, C. (2012). An experimental study on turbulence modification in the near-wall boundary layer of a dilute gas-particle channel flow. Experiments in Fluids. 53(5), pp.1385-1403.

Lilly, D.K. (1967). The representation of small-scale turbulence in numerical simulation experiments. Proceedings of IBM Scientific Computing Symposium on Environmental Sciences, IBM Data Processing Division, White Plains, New York. pp.195–210.

Li, Q., Song, J., Li, C., Wei, Y. and Chen, J.(2013). Numerical and experimental study of particle deposition on inner wall of 180° bend. Powder Technology. 237, pp.241-254.

Li, Y., McLaughlin, J.B., Kontomaris, K. and Portela, L. (2001). Numerical simulation of particle-laden turbulent channel flow. Physics of Fluids. 13(10), pp.2957-2967.

Lin, J.T. (1972). Velocity spectrum of locally isotropic turbulence in the inertial and dissipation ranges. Physics of Fluids. 15(1), pp.205-207.

Liu B.Y.H. and Agarwal, J.K. (1974). Experimental Observation of Aerosol Deposition in Turbulent Flow. Journal of Aerosol Science. 5, pp. 145-155.

Liu, B.Y.H, Berglund, R.N. and Agarwal, J.K. (1974). Experimental studies of optical particle counters. Atmospheric Environment. 8(7), pp.717-732.

Madabhushi, R.K. and Vanka, S. (1991). Large eddy simulation of turbulence-driven secondary flow in a square duct. Physics of Fluids. 3(11), pp.2734-2745.

Marchioli C., Fantoni M., and Soldati A. (2010). Orientation, distribution, and deposition of elongated, inertial fibers in turbulent channel flow. Physics of Fluids, 22, 033301

Marchioli, C., Giusti, A., Salvetti, M. V. and Soldati, A. (2003). Direct numerical simulation of particle wall transfer and deposition in upward turbulent pipe flow. International Journal of . Multiphase Flow , 29, 1017–1038.

Marchioli, C. and Soldati, A. (2002). Mechanisms for particle transfer and segregation in a turbulent boundary layer. Journal of Fluid Mechanics. 468(10), pp.283-315.

Marchioli C. and Soldati A. (2007). Reynolds number scaling of particle preferential concentration in turbulent channel flow. Advances in Turbulence XI, Springer 162 Proceedings in Physics, 117, pp.298-300.

Marchioli, C., Soldati, A., Kuerten, J., Arcen, B., Taniere, A., Goldensoph, G., Squires, K., Cargnelutti, M. and Portela, L. (2008). Statistics of particle dispersion in direct numerical simulations of wall-bounded turbulence: Results of an international collaborative benchmark test. International Journal of Multiphase Flow. 34(9), pp.879-893.

Mark, A. and van Wachem, B.G. (2008). Derivation and validation of a novel implicit second-order accurate immersed boundary method. Journal of Computational Physics. 227(13), pp.6660-6680.

Maxey, M.R. and Riley, J.J . (1983). Equation of motion for a small rigid sphere in a nonuniform flow. Physics of Fluids. 26(4) , pp.883-889.

McKeon B and Smits A. (2002). Static pressure correction in high Reynolds number fully developed turbulent pipe flow. Measurement Science and Technology. 13(10), p1608.

Mckeon, B. J., LI, J., Jiang, W., Morrison, J. F. and Smits, A. J. (2004a). Further observations on the mean velocity distribution in fully developed pipe flow. Journal of Fluid Mechanics. 501(2), pp.135-147.

Mckeon, B. J., Swanson, C. J., Zagarola, M. V., Donnelly, R. J. and Smits, A. J. (2004b). Friction factors for smooth pipe flow. Journal of Fluid Mechanics. 511, pp.41-44.

McKeon B, Li J, Jiang W, Morrison J, Smits A. (2003). Pitot probe corrections in fully developed turbulent pipe flow. Measurement Science and Technology. 14, pp.1449.

McKeon BJ, Zagarola MV, Smits AJ. (2005). A new friction factor relationship for fully developed pipe flow. Journal of Fluid Mechanics. 538, pp.429-443.

Melling, A. and Whitelaw, J.H. (1976). Turbulent-Flow in a Rectangular Duct. Journal of Fluid Mechanics. 78(23), pp.289-315.

Morinishi Y. and Tamano S. (2005). Study on differences in turbulence statistics between compressible and incompressible low-Reynolds number turbulent channel flows using semi-local scaling. JSME International Journal Series B. 48(4), pp.743-749.

Morrison, J. F., Mckeon, B. J., Jiang, W. and Smits, A. J. (2004). Scaling of the streamwise velocity component in turbulent pipe flow. Journal of Fluid Mechanics. 508, 99-131.

Mortensen, P., Andersson, H., Gillissen, J. and Boersma, B. (2008). Dynamics of prolate ellipsoidal particles in a turbulent channel flow. Physics of Fluids. 20(9), pp.093302.

Mortimer, L. F. and Fairweather, M. (2021). Assessment of behavioral modification techniques through immersed boundary method simulation of binary particle interactions in isotropic turbulence. Physics of Fluids. 33, pp.073307.

Mortimer, L. F., Njobuenwu, D.O., and Fairweather, M. (2020). Agglomeration dynamics in liquid–solid particle-laden turbulent channel flows using an energy-based deterministic approach. Physics of Fluids. 32

Mortimer, L. F., Njobuenwu, D.O., and Fairweather, M. (2019). Near- wall interparticle collision dynamics in multi-phase turbulent channel flows. Physics of Fluids. 31, pp.063302

Mortimer, L. F. (2019). Particle transport, interaction and agglomeration for nuclear reactor and nuclear waste flow applications. Thesis, University of Leeds.

Munson, B. R., Young D. F. and Okiishi, T. H. (2002). Fundamentals of Fluid Mechanics. Aerospace Engineering Iowa State, John Wiley&Sons.

NDA. (2022). 2022 UK Radioactive Waste Inventory. The Crown and Nuclear Decomissioning Authority.

Nikuradse, J. (1926). Untersuchung über die Geschwindigkeitsverteilung in turbulenten Strömungen. Vdi-verlag.

Nikuradse, J. (1929). Untersuchungen über die Strömungen des Wassers in konvergenten und divergenten Kanälen. Vdi-Verlag.

Njobuenwu, D. and Fairweather, M. (2015a). Dynamics of single, non-spherical ellipsoidal particles in a turbulent channel flow. Chemical Engineering Science. 123, pp.265-282.

Njobuenwu, D.O. and Fairweather, M. (2015b). Deterministic modelling of particle agglomeration in turbulent flow. In: ICHMT DIGITAL LIBRARY ONLINE: Begel House Inc.

Njobuenwu, D.O. and Fairweather, D. O. (2017). Simulation of deterministic energy-balance particle agglomeration in turbulent liquid-solid flows. Physics of Fluids. 29, 083301.

Oliveira, J. L. G., van der Geld, C. W. M., and Kuerten, J. G. M. (2017). Concentration and velocity statistics of inertial particles in upward and downward pipe flow. Journal of Fluid Mechanics. 822, pp.640-663.

Orlandi P. and Fatica M. (1997). Direct simulations of turbulent flow in a pipe rotating about its axis. Journal of Fluid Mechanics. 343, pp.43-72.

Oroskar, A. R. and Turian, R. M. (1980). The critical velocity in pipeline flows of slurries. AlChE Journal. 26, pp.550-558.

Owolabi B. E., Poole R. J., and Dennis D. J. C. (2016). Experiments on low-Reynolds-number turbulent flow through a square duct. Journal of Fluid Mechanics. 798, pp.398-410.

Ozcan, M., Yildirim M. and Ozturk S. (2016). Generation expansion planning scenarios to reduce natural gas dependency of Turkey. Energy Exploration & Exploitation. 34(2), pp.244-261

Pakzonka,W., Kenchington, J.M. and Charles, M.E. (1981). Hydrotransport of solids in horizontal pipes:effects of solids concentration and particle size on the deposit velocity. The Canadian journal of Chemical Engineering. 59(3), pp.291-296.

Pao, Y.H. (1965). Structure of Turbulent Velocity and Scalar Fields at Large Wavenumbers. The Physics of Fluids. 8(6), pp.1063-1075.

Patel, V. and Head, R. (1968). Reversion of turbulent to laminar flow. Journal of Fluid Mechanics. 34(2), pp.371-392.

Perry, A.E (1982). Hot-wire anemometry. Clarendon Press.

Petersen, A. (2020, 05 01). rectangleworld. Retrieved from rectangleworld: http://rectangleworld.com/blog/archives/358

Piomelli, U. and Liu, J. (1995). Large-eddy simulation of rotating channel flows using a localized dynamic model. Physics of Fluids. 7(4), pp.839-848.

Pope, S. B. (2001). Turbulent Flows. Cambridge University Press, IOP Publishing.

Portela, L. M., Cota, P. and Oliemans, R. V. A. (2002). Numerical study of the near-wall behaviour of particles in turbulent pipe flows. Powder Tech. 125(2), pp.149–157.

Prat A., Sautory T.and Navarro-Martinez S. (2020). A Priori Sub-grid Modelling Using Artificial Neural Networks. International Journal of Computational Fluid Dynamics. 34, pp.397-417.

Rani, S.L and Vanka S.P. (2000). Numerical simulation of two-way coupling effects in a particle-laden turbulent pipe flow. ASME Fluids Engineering Summer Conference. SME Fluids Engi- neering.

Rani, S.L., Winkler, C. and Vanka, S. (2004). Numerical simulations of turbulence modulation by dense particles in a fully developed pipe flow. Powder Technology. 141(1-2), pp. 80-90.

Reynolds, O. (1895). On the dynamical theory of incompressible viscous fluids and the determination of the criterion. Philosophical Transactions of the Royal Society of London. A. 186, pp.123-164.

Rice, H. P., Peakall, J., Fairweather M., Hunter, T. (2020). Extending estimation of the critical deposition velocity in solid–liquid pipe flow to ideal and non-ideal particles at low and intermediate solid volume fractions. Chemical Engineering Science. 211, p115308.

Rice, H. P., Fairweather M., Peakall, J., Hunter, T. N., Mahmoud, B. and Biggs, S. R. (2015). Constraints on the functional form of the critical deposition velocity in solid-liquid pipe flow at low solid volume fractions. Chemical Engineering Science. 126, pp.759-770.

Rice, H. P. (2013). Transport and deposition behaviour of model slurries in closed pipe flow. Thesis, University of Leeds.

Riley, K., Hobson, M., and Bence, S. (2006). Mathematical Methods for Physics and Engineering. A Comprehensive Guide (3rd ed.), Cambridge University Press.

Saffman, P. (1965). The lift on a small sphere in a slow shear flow. Journal of Fluid Mechanics. 22(2), pp.385-400.

Schiller, L. (1934). Neue quantitative Versuche zur Turbulenzentstehung. ZAMM-Journal of Applied Mathematics and Mechanics/Zeitschrift für Angewandte Mathematik und Mechanik. 14(1), pp.36-42.

Sharma, G. and Phares, D.J. (2006). Turbulent transport of particles in a straight square duct. International Journal of Multiphase Flow. 32(7), pp.823-837.

Singh, J. Rudman, M. and Blackburn, H.M. (2018). Reynolds number effects in pipe flow turbulence of generalized Newtonian fluids. Phys. Rev. Fluids 3

Smagorinsky J. (1963). General circulation experiments with the primitive equations: {I} The basic equations. Monthly Weather Review. 91, pp.99-164.

Sonin, A. (2004). A generalization of the Pi-theorem and dimensional analysis. Proc Natl Acad Sci U S A. 101(23), pp.8525-6.

Stokes, G.G. (1851). On the effect of the internal friction of fluids on the motion of pendulums. Pitt Press Cambridge.

Su, M. and Friedrich, R. (1994). Investigation of fully developed turbulent flow in a straight duct with large eddy simulation. Journal of Fluids Engineering. 116(4), pp.677-684.

Tao, B., Katz, J. and Meneveau, C. (1999). Application of HPIV data of turbulent duct flow for turbulence modeling. In 3rd ASME/JSME Joint Fluids Engineering Conference, pp.18-22.

Tracy, H.J. (1963). Turbulent flow in a three-dimensional channel. Thesis, Georgia Institute of Technology.

Tsuji, Y. and Morikawa, Y. (1982). LDV Measurements of an Air-Solid Two-Phase Flow in a Horizontal Pipe. Journal of Fluid Mechanics. 120(4), pp.385-409.

Tsuji Y, Morikawa, Y., Shiomi, H. (1984). LDV measurements of an air-solid two-phase flow in a vertical pipe. Journal of Fluid Mechanics. 139(4), pp.417-434.

Uijttewaal, W. S. and Oliemans, R. V. A. (1996). Particle dispersion and deposition in direct numerical and large eddy simulations of vertical pipe flows. Physics of Fluids , 8(10), pp.2590–2604.

van Wachem, B., Zastawny, M., Zhao, F. and Mallouppas, G. (2015). Modelling of gas–solid turbulent channel flow with non-spherical particles with large Stokes numbers. International Journal of Multiphase Flow. 68, pp.80-92.

Varaksin, A. Y., Polezhaev, Y.V. and Polyakov, A.F. (2000). Effect of particle concentration on fluctuating velocity of the disperse phase for turbu- lent pipe flow. Int. J. Heat and Fluid Flow, 21(5), pp.562 – 567.

Verwey, E.J.W. and Overbeek, J.T.G. (1955). Theory of the stability of lyophobic colloids. Journal of Colloid Science. 10(2), pp.224-225.

Vreman, A. W. (2007). Turbulence characteristics of particle-laden pipe flow. Journal of Fluid Mechanics. 584, pp.235-279.

Vreman, A. (2015). Turbulence attenuation in particle-laden flow in smooth and rough channels. Journal of Fluid Mechanics. 773(6), pp.103-136.

Vreman, A. 2016. Particle-resolved direct numerical simulation of homogeneous isotropic turbulence modified by small fixed spheres. Journal of Fluid Mechanics. 796(4), pp.40-85.

Vreman, B., Geurts, B.J., Deen, N., Kuipers, J. and Kuerten, J.G. (2009). Two-and four-way coupled Euler–Lagrangian large-eddy simulation of turbulent particle-laden channel flow. Flow, Turbulence and Combustion. 82(1), pp.47-71.

Wagner C., Hüttl T. J. and Friedrich R. J. (2001). Low-Reynolds-number effects derived from direct numerical simulations of turbulent pipe flow. Comp. Fluids 2001,30 (5),pp.581–590.

Walpot R. J. E., van der Geld C. W. M. and Kuerten J. G. M. (2007). Determination of the coefficients of Langevin models for inhomogeneous turbulent flows by three-dimensional particle tracking velocimetry and direct numerical simulation. Physics of Fluids 19, 045102

Westerweel, J., Draad, A., Van der Hoeven, J.T. and Van Oord, J. (1996). Measurement of fully-developed turbulent pipe flow with digital particle image velocimetry. Experiments in Fluids. 20(3), pp.165-177.

Winkler, C., Rani, S.L. and Vanka, S. (2004). Preferential concentration of particles in a fully developed turbulent square duct flow. International Journal of Multiphase Flow. 30(1), pp.27-50.

Winkler, C., Rani, S.L. and Vanka, S. (2006). A numerical study of particle wall-deposition in a turbulent square duct flow. Powder Technology. 170(1), pp.12-25.

Wu, X. H. and Moin. (2008). A direct numerical simulation study on the mean velocity characteristics in turbulent pipe flow. Journal of Fluid Mechanics, 608, pp.81-112.

Wu, X., Baltzer, J.R., Adrian, R.J. (2012). Direct numerical simulation of a 30R long turbulent pipe flow at $R^+ = 685$: large- and very large-scale motions. Journal of Fluid Mechanics , 698, pp.235–281.

Yan W. (2010). Sand transport in multiphase pipelines. Thesis, Cranfield University.

Yao, J. and Fairweather, M. (2010). Inertial particle resuspension in a turbulent, square duct flow. Physics of Fluids. 22(3), p033303.

Yeh, Y. and Cummins, H. (1964). Localized fluid flow measurements with an He–Ne laser spectrometer. Applied Physics Letters., 4(10), pp.176-178.

Young, J. and Leeming, A. (1997). A theory of particle deposition in turbulent pipe flow. Journal of Fluid Mechanics, 340, pp.129–159.

Zagarola, M. V. and Smits, A. J. (1998). Mean-flow scaling of turbulent pipe flow. Journal of Fluid Mechanics, 373,33-79.

Zamansky, R., Vinkovic, I. and Gorokhovski, M. (2011). DNS and LES with stochastic modelling of subgrid acceleration applied to solid particles in a high Reynolds number channel flow. In: TSFP digital library online: Begel House Inc.

Zhang H., Ahmadi G., Fan F. G., and McLaughlin J. B. (2001).Ellipsoidal particles transport and deposition in turbulent channel flows. International Journal of Multiphase Flow, 27(6), pp. 971-1009.

Zhang, J., Tao, B. and Katz, J. (1997). Turbulent flow measurement in a square duct with hybrid holographic PIV. Experiments in Fluids. 23(5), pp.373-381.

Zhao, F., George, W. and Van Wachem, B. (2015). Four-way coupled simulations of small particles in turbulent channel flow: The effects of particle shape and Stokes number. Physics of Fluids. 27(8), p083301.

Zhao, L., Andersson, H.I. and Gillissen, J. (2010). Turbulence modulation and drag reduction by spherical particles. Physics of Fluids. 22(8), p081702.

Zhu Z. (2009). Direct numerical simulation of turbulent flow in a straight square duct at Reynolds number 600. Journal of Hydrodynamics, Ser. B 21(5), pp. 600-607.

Zisselmar, R. and Molerus, O. (1979). Investigation of solid – liquid pipe flow with regard to turbulence modification. Chem. Eng. J., pp.18233 – 239.